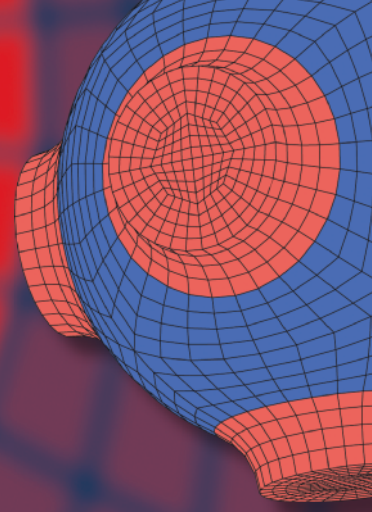


Advanced Structured Materials

Francesco Marmo
Salvatore Sessa
Emilio Barchiesi
Mario Spagnuolo *Editors*



Mathematical Applications in Continuum and Structural Mechanics

 Springer


Advanced Structured Materials

Volume 127

Series Editors

Andreas Öchsner, Faculty of Mechanical Engineering, Esslingen University of Applied Sciences, Esslingen, Germany

Lucas F. M. da Silva, Department of Mechanical Engineering, Faculty of Engineering, University of Porto, Porto, Portugal

Holm Altenbach , Faculty of Mechanical Engineering, Otto von Guericke University Magdeburg, Magdeburg, Sachsen-Anhalt, Germany

Common engineering materials reach in many applications their limits and new developments are required to fulfil increasing demands on engineering materials. The performance of materials can be increased by combining different materials to achieve better properties than a single constituent or by shaping the material or constituents in a specific structure. The interaction between material and structure may arise on different length scales, such as micro-, meso- or macroscale, and offers possible applications in quite diverse fields.

This book series addresses the fundamental relationship between materials and their structure on the overall properties (e.g. mechanical, thermal, chemical or magnetic etc.) and applications.

The topics of *Advanced Structured Materials* include but are not limited to

- classical fibre-reinforced composites (e.g. glass, carbon or Aramid reinforced plastics)
- metal matrix composites (MMCs)
- micro porous composites
- micro channel materials
- multilayered materials
- cellular materials (e.g., metallic or polymer foams, sponges, hollow sphere structures)
- porous materials
- truss structures
- nanocomposite materials
- biomaterials
- nanoporous metals
- concrete
- coated materials
- smart materials

Advanced Structured Materials is indexed in Google Scholar and Scopus.

More information about this series at <https://link.springer.com/bookseries/8611>


Francesco Marmo · Salvatore Sessa ·
Emilio Barchiesi · Mario Spagnuolo
Editors

Mathematical Applications in Continuum and Structural Mechanics

 Springer

Editors

Francesco Marmo 
University of Naples Federico II
Napoli, Italy

Salvatore Sessa 
University of Naples Federico II
Napoli, Italy

Emilio Barchiesi 
Università degli Studi dell'Aquila
L'Aquila, Italy

Mario Spagnuolo 
Università degli Studi dell'Aquila
L'Aquila, Italy

ISSN 1869-8433

ISSN 1869-8441 (electronic)

Advanced Structured Materials

ISBN 978-3-030-42706-1

ISBN 978-3-030-42707-8 (eBook)

<https://doi.org/10.1007/978-3-030-42707-8>

© Springer Nature Switzerland AG 2021

This work is subject to copyright. All rights are reserved by the Publisher, whether the whole or part of the material is concerned, specifically the rights of translation, reprinting, reuse of illustrations, recitation, broadcasting, reproduction on microfilms or in any other physical way, and transmission or information storage and retrieval, electronic adaptation, computer software, or by similar or dissimilar methodology now known or hereafter developed.

The use of general descriptive names, registered names, trademarks, service marks, etc. in this publication does not imply, even in the absence of a specific statement, that such names are exempt from the relevant protective laws and regulations and therefore free for general use.

The publisher, the authors and the editors are safe to assume that the advice and information in this book are believed to be true and accurate at the date of publication. Neither the publisher nor the authors or the editors give a warranty, expressed or implied, with respect to the material contained herein or for any errors or omissions that may have been made. The publisher remains neutral with regard to jurisdictional claims in published maps and institutional affiliations.

This Springer imprint is published by the registered company Springer Nature Switzerland AG
The registered company address is: Gewerbestrasse 11, 6330 Cham, Switzerland

Contents

| | | |
|----------|--|-----------|
| 1 | Usage of Guided Wave Resonance Phenomena for Defect Detection in Laminate Elastic Structures | 1 |
| | Artem Eremin, Evgeny Glushkov, Natalia Glushkova, and Rolf Lammering | |
| 1.1 | Introduction | 1 |
| 1.2 | Computational Models | 3 |
| 1.3 | Experimental Evaluation of Resonance Frequencies | 6 |
| 1.4 | Estimation of the Defect Size | 9 |
| 1.5 | Conclusion | 9 |
| | References | 10 |
| 2 | Modelling of Piezocomposites with Mechanical Interface Effects | 13 |
| | Andrey V. Nasedkin | |
| 2.1 | Introduction | 13 |
| 2.2 | Effective Moduli Method for Homogenization of Two-Phase Piezoelectric Nanocomposite | 15 |
| 2.3 | Dimensionless Homogenization Problem | 19 |
| 2.4 | Finite Element Modelling | 20 |
| 2.5 | Modelling of Representative Volume Elements | 21 |
| 2.6 | Results and Discussion | 23 |
| 2.7 | Conclusion | 27 |
| | References | 28 |
| 3 | A Mathematical Model for Bone Cell Population Dynamics of Fracture Healing Considering the Effect of Energy Dissipation | 33 |
| | Mahziyar Darvishi, Hooman Dadras, Mohammad Mahmoodi Gahrouei, Kiarash Tabesh, and Dmitry Timofeev | |
| 3.1 | Introduction | 33 |
| 3.2 | The Model | 37 |
| 3.2.1 | The Main Assumptions | 37 |
| 3.2.2 | The Governing Equations | 38 |

| | | |
|----------|--|-----------|
| 3.2.3 | The Stimulus | 39 |
| 3.2.4 | The Function $\kappa(\varphi)$ | 40 |
| 3.2.5 | The Mechanical Framework | 40 |
| 3.2.6 | Numerical Data | 42 |
| 3.2.7 | Healing of Bone | 42 |
| 3.2.8 | Dissipation | 44 |
| 3.3 | Results and Discussion | 46 |
| 3.4 | Conclusion | 47 |
| | References | 50 |
| 4 | Second Gradient Linear and Nonlinear Constitutive Models of Architected Materials: Static and Dynamic Behaviors | 53 |
| | Yosra Rahali, Hilal Reda, Benoit Vieille, Hassan Lakiss, and Jean-François Ganghoffer | |
| 4.1 | Introduction | 54 |
| 4.2 | First- and Second-Order Effective Moduli of Periodic Networks | 56 |
| 4.2.1 | Analytical Method | 60 |
| 4.2.2 | Homogenized Viscoelastic Behavior | 62 |
| 4.2.3 | Incremental Scheme | 63 |
| 4.3 | Wave Propagation Analysis Based on Nonlinear Models | 67 |
| 4.3.1 | Strain Energy Density | 67 |
| 4.4 | Conclusion | 68 |
| | References | 69 |
| 5 | An Application of Coulomb-Friction Model to Predict Internal Dissipation in Concrete | 73 |
| | Giuliano Aretusi and Alessandro Ciallella | |
| 5.1 | Introduction | 73 |
| 5.2 | A Brief Synopsis of the Employed Model | 76 |
| 5.2.1 | 3D Formulation of a Micromorphic Concrete-Based Material | 76 |
| 5.2.2 | Simplified Formulation for the Case of a Pure Compression | 78 |
| 5.3 | Numerical Simulations and Discussions | 79 |
| 5.4 | Conclusion | 81 |
| | References | 83 |
| 6 | From the Swarm Robotics to Material Deformations | 87 |
| | Paolo D'Avanzo, Alessio Ciro Rapisarda, and Salvatore Samuele Sirletti | |
| 6.1 | Introduction | 87 |
| 6.2 | Other Models in Literature | 89 |
| 6.2.1 | Position-Based Dynamics (PBD) | 90 |
| 6.2.2 | Swarm Robotics | 90 |
| 6.3 | The Model Here Proposed | 92 |
| 6.3.1 | A Recall About Graph Theory | 93 |

- 6.3.2 Constructing the Model 93
- 6.3.3 Relationship with Other Models 96
- 6.3.4 Meaning of Neighbors 98
- 6.4 Numerical Simulations 98
 - 6.4.1 Standard Simulations 104
 - 6.4.2 Second Neighborhoods and Exotic Simulations 110
- 6.5 Conclusion 115
- References 118
- 7 A Review of the Class of Bouc-Wen Differential Models
for Simulating Mechanical Hysteresis Phenomena 127**
Davide Pellecchia and Massimo Paradiso
 - 7.1 Introduction 127
 - 7.2 Modeling of Symmetric Hysteresis Loops 129
 - 7.2.1 Bouc Model and Its Modified Versions 130
 - 7.2.2 Sensitivity Analysis 131
 - 7.3 Modeling of Asymmetric Hysteresis Loops 132
 - 7.3.1 Asymmetric Bouc-Wen Models 133
 - 7.3.2 Sensitivity Analysis 135
 - 7.4 Modeling of Pinched Hysteresis Loops 136
 - 7.4.1 Pinching Bouc-Wen Models 137
 - 7.4.2 Sensitivity Analysis 139
 - 7.5 Modeling of Degrading Hysteresis Loops 140
 - 7.5.1 Degrading Bouc-Wen Models 140
 - 7.5.2 Sensitivity Analysis 142
 - 7.6 Conclusion 143
 - References 143
- 8 A Generalized Formulation of Time Integration Methods
for Nonlinear Dynamic Analysis of Hysteretic Mechanical
Systems 149**
Davide Pellecchia and Pasquale Cesarano
 - 8.1 Introduction 150
 - 8.2 Families of Time Integration Methods 151
 - 8.2.1 Nonlinear Equilibrium Equations 151
 - 8.2.2 Generalized Formulation of Time Integration
Methods 152
 - 8.3 Conventional Time Integration Methods 153
 - 8.3.1 Newmark’s Family of Methods 154
 - 8.3.2 Some Instances of the NFMs 157
 - 8.3.3 Implementation Scheme of the NFMs 158
 - 8.4 Structure-Dependent Time Integration Methods 159
 - 8.4.1 Chang’s Family of Explicit Methods 160
 - 8.4.2 Some Instances of the CFEMs 163
 - 8.4.3 Implementation Scheme of the CFEMs 163
 - 8.5 Numerical Experiments 164

| | | |
|-----------|---|------------|
| 8.5.1 | Mechanical System Properties | 165 |
| 8.5.2 | Applied Generalized External Force | 166 |
| 8.5.3 | Hysteretic Model Parameters | 166 |
| 8.5.4 | Results of the Nonlinear Time History Analyses | 166 |
| 8.6 | Conclusion | 167 |
| | References | 169 |
| 9 | Quasi-Harmonic Solutions for Transversely Isotropic Magneto-Electro-Thermo-Elasticity: A Symbolic Mathematics Approach | 173 |
| | Francesco Marmo and Massimo Paradiso | |
| 9.1 | Introduction | 173 |
| 9.2 | Field Equations | 175 |
| 9.3 | A General Solution to the Field Equations in Terms of Quasi-Harmonic Potentials | 179 |
| 9.3.1 | Inversion of the Differential Operator \mathcal{L} | 179 |
| 9.3.2 | Factorization of the Differential Equation $ \mathcal{L} \varphi = \mathbf{0}$ | 180 |
| 9.4 | Automatic Evaluation of $ \mathcal{L} $ and \mathcal{L}^* and Relevant Coefficients | 183 |
| 9.4.1 | Evaluation of $ \mathcal{L} $ | 183 |
| 9.4.2 | Evaluation of \mathcal{L}^* | 186 |
| 9.5 | Conclusion | 188 |
| | References | 188 |
| 10 | Mathematical Tools for the Seismic Analysis of Reinforced Concrete Structures: A Selected Review | 191 |
| | Cristoforo Demartino and Sicheng Zhou | |
| 10.1 | Introduction | 192 |
| 10.2 | Review of Strategies Accounting for Global Torsion in Buildings | 193 |
| 10.2.1 | Review of the Dynamic Equivalent Rotational Spectrum | 195 |
| 10.3 | Computation of Multicomponent Actions by Seismic Envelopes | 198 |
| 10.4 | Capacity Checks of Reinforced Concrete Beams | 201 |
| 10.4.1 | A General Algorithm to Perform Capacity Checks by the Supreme Envelope | 204 |
| 10.5 | Conclusions | 206 |
| | References | 208 |
| 11 | Form Finding of Shell Structures by Using Membrane Theory | 213 |
| | Francesco Marmo and Nicol o Vaiana | |
| 11.1 | Introduction | 213 |
| 11.2 | The Membrane Theory of Shells | 216 |
| 11.2.1 | Global and Local Reference Frames | 216 |

- 11.2.2 Transformation Formulas for Lengths and Areas 217
- 11.2.3 Distributed Loads and Stress Components 218
- 11.2.4 Equilibrium 220
- 11.3 Form-Finding Algorithm 222
 - 11.3.1 Discretization of the Equilibrium Equations
by the Finite Difference Method 222
 - 11.3.2 Assigning the Distribution of Projected Membrane
Stresses 226
 - 11.3.3 Evaluation of the Shell Mid-Surface Height 227
 - 11.3.4 Iterative Procedure for Assigning Projected Loads 229
- 11.4 Numerical Examples 230
 - 11.4.1 Shell with One Free Side 231
 - 11.4.2 Shell Supported at Corners 231
- 11.5 Conclusion 234
- References 235
- 12 Influence of Non-structural Components on Equivalent
Linearization of Buildings 239**

Salvatore Sessa and Luciano Rosati

 - 12.1 Introduction 239
 - 12.2 Brief Review of Tail-Equivalent Linearization 241
 - 12.3 Influence of Secondary Devices on TELS 242
 - 12.3.1 Frequency Content Comparison 243
 - 12.3.2 First Excursion Probability Comparison 246
 - 12.4 Conclusion 249
 - References 250
- 13 Do We Really Need Pantographic Structures? 253**

Mario Spagnuolo and Emilio Barchiesi

 - 13.1 Introduction 253
 - 13.2 Metamaterials Are (Natural) Materials *on Demand* 254
 - 13.3 Second Gradient Theories 256
 - 13.4 Microstructure in Continuum Mechanics 257
 - 13.4.1 The Synthesis Problem 258
 - 13.5 Why We Really Need Pantographic Structures 259
 - 13.5.1 The Existence of Pantographic Metamaterial
Motivates the Need of Second Gradient Theories 259
 - 13.5.2 A Mechanical Diode 260
 - 13.5.3 An Iterative Algorithm for Synthesising
Metamaterials 261
 - 13.6 Conclusion 262
 - References 263

Contributors

Giuliano Aretusi MeMoCS - University of L'Aquila, L'Aquila, Italy

Emilio Barchiesi International Research Center for the Mathematics and Mechanics of Complex Systems, University of L'Aquila, L'Aquila, Italy;
École Nationale d'Ingénieurs de Brest, ENIB, UMR CNRS, IRDL, Brest, France

Pasquale Cesarano CAE Technologies s.r.l. – Simulia, Centro Direzionale isola, Naples, Italy

Alessandro Ciallella DICEAA - University of L'Aquila, L'Aquila, Italy

Paolo D'Avanzo University of Naples Federico II, Naples, Italy

Hooman Dadras Department of Mechanical Engineering, Isfahan University of Technology, Isfahan, Iran

Mahziyar Darvishi Department of Mechanical Engineering, Isfahan University of Technology, Isfahan, Iran

Cristoforo Demartino Zhejiang University—University of Illinois at Urbana Champaign Institute (ZJUI), Zhejiang, Haining, PR China

Artem Eremin Institute for Mathematics, Mechanics and Informatics, Kuban State University, Krasnodar, Russia

Jean-François Ganghoffer Université de Lorraine, Metz Cedex, France

Evgeny Glushkov Institute for Mathematics, Mechanics and Informatics, Kuban State University, Krasnodar, Russia

Natalia Glushkova Institute for Mathematics, Mechanics and Informatics, Kuban State University, Krasnodar, Russia

Hassan Lakiss Faculty of Engineering, Section III, Lebanese University, Beirut, Lebanon

Rolf Lammering Institute of Mechanics, Helmut-Schmidt-University/University of the Federal Armed Forces, Hamburg, Germany

Mohammad Mahmoodi Gahrouei Department of Mechanical Engineering, Isfahan University of Technology, Isfahan, Iran

Francesco Marmo Department of Structures for Engineering and Architecture, University of Naples Federico II, Napoli, Italy

Andrey V. Nasedkin Institute of Mathematics, Mechanics and Computer Sciences, Southern Federal University, Rostov-on-Don, Russia

Massimo Paradiso Department of Structures for Engineering and Architecture, University of Naples Federico II, Naples, Italy

Davide Pellecchia Department of Structures for Engineering and Architecture, University of Naples Federico II, Naples, Italy

Yosra Rahali GPM, INSA Rouen, Université de Rouen, Saint-Étienne-du-Rouvray, France

Alessio Ciro Rapisarda University of Naples Federico II, Naples, Italy

Hilal Reda Faculty of Engineering, Section III, Lebanese University, Beirut, Lebanon

Luciano Rosati University of Naples Federico II, Napoli, Italy

Salvatore Sessa University of Naples Federico II, Napoli, Italy

Salvatore Samuele Sirletti University of Naples Federico II, Naples, Italy

Mario Spagnuolo Dipartimento di Ingegneria Civile, Ambientale e Architettura (DICAAR), Università degli Studi di Cagliari, Cagliari, Italy; International Research Center for the Mathematics and Mechanics of Complex Systems, University of L'Aquila, L'Aquila, Italy

Kiarash Tabesh Department of Mechanical Engineering, Isfahan University of Technology, Isfahan, Iran

Dmitry Timofeev Dipartimento di Ingegneria e Scienze dell'Informazione e Matematica, Università degli Studi dell'Aquila, L'Aquila, Italy

Nicoló Vaiana Department of Structures for Engineering and Architecture, University of Naples Federico II, Napoli, Italy

Benoit Vieille GPM, INSA Rouen, Université de Rouen, Saint-Étienne-du-Rouvray, France

Sicheng Zhou Zhejiang University—University of Illinois at Urbana Champaign Institute (ZJUI), Zhejiang, Haining, PR China

Chapter 1

Usage of Guided Wave Resonance Phenomena for Defect Detection in Laminate Elastic Structures



Artem Eremin, Evgeny Glushkov, Natalia Glushkova, and Rolf Lammering

Abstract Since the values of natural scattering resonance frequencies strongly depend on the size and shape of the scatterer, it seems worthwhile to use this information for the enhancement of damage characterization capabilities of SHM systems. In this chapter, potential possibility of such approach is demonstrated and discussed in the example of guided wave interaction with a flat bottom hole in a metallic plate that simulates deep pitting corrosion. A good agreement of the theoretically predicted and experimentally obtained scattering resonance frequencies has confirmed the capability of this approach, which is illustrated by examples of the defect's size reconstruction.

Keywords Resonance frequency · Scattering · Structural health monitoring · Corrosion · Guided wave

1.1 Introduction

Elastic guided waves (GW) have become a recognized structural health monitoring (SHM) tool for elongated laminate structures manufactured from metals and polymer composites (Lammering et al. 2018). The presence of scattered GWs in the sensor-acquired signals is considered as an indication of the developing structure-specific

A. Eremin (✉) · E. Glushkov · N. Glushkova
Institute for Mathematics, Mechanics and Informatics, Kuban State University, Stavropolskaya st. 149, 350040 Krasnodar, Russia
e-mail: eremin_a_87@mail.ru

E. Glushkov
e-mail: evg@math.kubsu.ru

N. Glushkova
e-mail: nvg@math.kubsu.ru

R. Lammering
Institute of Mechanics, Helmut-Schmidt-University/University of the Federal Armed Forces, Holstehofweg 85, 22043 Hamburg, Germany
e-mail: rolf.lammering@hsu-hh.de

macroscopic damage. However, the damage evaluation process is complicated by multiple diffraction patterns of GW interaction with structural features. Therefore, the knowledge of any damage-specific wave characteristics that could be extracted from the measured signals would allow for the enrichment of quantification opportunities of SHM systems.

As a non-destructive evaluation method, GW can be useful also for damage recognition for the newest class of artificial composites with microstructure also called metamaterials (Barchiesi et al. 2018, 2020c; Del Vescovo and Giorgio et al. 2014) with mechanical properties that cannot be found in nature. These (macroscopic) properties are mainly determined by the micro- or nanostructure of the considered metamaterial rather than by the chemical and physical properties of the materials constituting it at the microscopic level. An example of mechanical metamaterials is a pantographic structure (dell'Isola et al. 2017, 2016a, b, c, 2019a, b; Placidi et al. 2017, 2016, Spagnuolo et al. 2020, 2021; Barchiesi et al. 2020a, b; Turco and Barchiesi 2019). In order to account for multiscale mechanical interactions, which take place for metamaterials, higher order gradient continuum theories can be a choice (Alibert et al. 2013; Auffray et al. 2013; dell'Isola et al. 2015, 2016a, b, c, 2012; Rahali et al. 2015; Sciarra et al. 2007). The methodologies involving GW may also be used in a synergetic way with other experimental (Vaiana et al. 2017), numerical (Vaiana et al. 2019, 2021; Serpieri et al. 2018; Sessa et al. 2018; Greco et al. 2018; Marmo et al. 2018), and analytical (Marmo et al. 2020, 2016; Trotta et al. 2016) aspects.

A phenomenon of GW resonance interaction with localized obstacles is among the potential candidates for the enrichment of quantification opportunities of SHM systems (Glushkov et al. 2012, 2015a, b; Solodov 2017). It is characterized by the capturing of incident wave energy in the defect's vicinity and its prolonged localization with a gradual re-emission at near-real diffraction resonance frequencies (eigenfrequencies of the corresponding defect-structure boundary value problem). Since these frequencies strongly depend on the defect's type, shape, and location, they may, if being detected, enhance damage characterization capabilities of SHM systems.

In this chapter, a theoretical and experimental study of the GW resonance interaction with circular flat-bottom holes (FBH) simulating deep pitting corrosion in metallic structures is presented. Employing semi-analytical and mesh-based numerical tools, the existence of near-real resonance diffraction frequencies is predicted, and their strong dependence on the damage severity is shown. Experimental investigations performed with surface-mounted piezoelectric wafer active sensors and contactless laser Doppler vibrometry (LDV) confirm the values of the computed eigenfrequencies and the corresponding amplitude localization patterns (eigenforms). Predicted prolonged GW re-emission is also clearly observed, providing the possibility of resonance frequency estimation using the spectral and time-frequency analysis of signals acquired by remote sensors. Some test examples of damage geometry reconstruction through the minimization of the discrepancy between the measured data and numerical results are presented and discussed.

1.2 Computational Models

(a) Analytically based approach

To study complex resonance frequencies f_n of the diffraction problem, two approaches have been implemented. In the first case, approximate plate theories are employed to simulate GW diffraction by a circular FBH of radius R and depth d in an opened waveguide of thickness H (Fig. 1.1). The Mindlin approach is used for antisymmetric wave motion (i.e., modes A0, A1, and SH1) and the Poisson theory handles the lowest order compressional waves (fundamental symmetric S0 and shear horizontal SH0 modes) (Cegla et al. 2008; Grahn 2008; Vemula and Norris 1997). In the framework of these theories, the components of the displacement vector $\mathbf{u}(\mathbf{x}) = \{u_x, u_y, u_z\}$ where $\mathbf{x} = \{x, y, z\}$ are approximated by linear functions of the transverse coordinate z . In cylindrical coordinates $\{r, \theta, z\}$, his approximation takes the form

$$u_r = u_{r,S} - z\Pi_r, u_\theta = u_{\theta,S} - z\Pi_\theta, u_z = w \quad (1.1)$$

where $u_{r,S}(r, \theta)$ and $u_{\theta,S}(r, \theta)$ are radial and angular displacement components governed by the equations of the Poisson theory while $w(r, \theta)$, $\Pi_r(r, \theta)$ and $\Pi_\theta(r, \theta)$ are vertical and rotation components obtained from the Mindlin theory. The time-harmonic motion $\mathbf{u} \cdot \exp(-i\omega t)$ is further assumed; the vector $\mathbf{u}(\mathbf{x}, \omega)$ is the frequency spectrum of a transient wave field, $\omega = 2\pi f$ angular frequency, and f is frequency.

The displacement functions can be expressed in terms of scalar potentials:

$$u_{r,S} = \frac{\partial\phi}{\partial r} + \frac{1}{r} \frac{\partial\psi}{\partial\theta}, u_{\theta,S} = \frac{1}{r} \frac{\partial\phi}{\partial\theta} - \frac{\partial\psi}{\partial r}, \quad (1.2)$$

$$w(r, \theta) = w_1(r, \theta) + w_2(r, \theta), \quad (1.3)$$

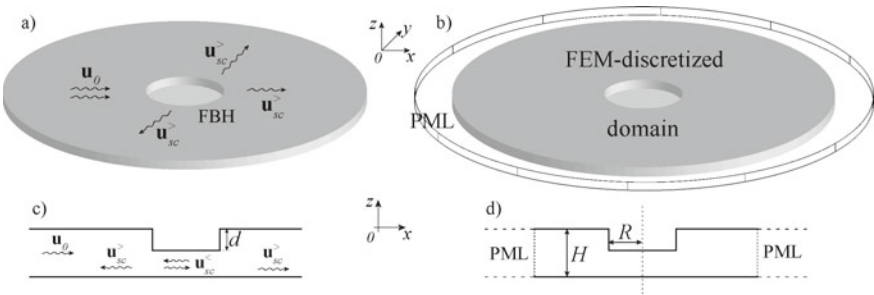


Fig. 1.1 General view of the problem geometry: (a)—analytically based simulation, (b)—mesh-based discretization; cross-sections by xOz plane in the case of the plate theory approximation (c) and FEM-PML approach (d)

$$\Pi_r = A_1 \frac{\partial w_1}{\partial r} + A_2 \frac{\partial w_2}{\partial r} + \frac{1}{r} \frac{\partial V}{\partial \theta}, \quad \Pi_\theta = A_1 \frac{1}{r} \frac{\partial w_1}{\partial \theta} + A_2 \frac{1}{r} \frac{\partial w_2}{\partial \theta} + \frac{\partial V}{\partial r}.$$

The potential functions ϕ , ψ , w_1 , w_2 , V obey the Helmholtz equations with the wavenumbers k_p , k_s , k_1 , k_2 , k_3 standing for S0, SH0, A0, A1, and SH1 modes, respectively. These quantities as well as the constants A_1 , A_2 in Eq. (1.3) are expressed via the elastic constants of the plate (Cegla et al. 2008; Grahn, 2008; Vemula and Norris 1997).

Considering the interaction of the incident disturbance $\mathbf{u}_0(\mathbf{x}, \omega)$ with the FBH, the total wavefield could be split into two different parts—one is for the region outside the defect ($r > R$) and the other is for the area $r < R$ below the FBH:

$$\mathbf{u}(\mathbf{x}, \omega) = \begin{cases} \mathbf{u}_0 + \mathbf{u}_{sc}^>, & r > R, -H/2 < z < H/2, \\ \mathbf{u}_{sc}^<, & r < R, -H/2 < z < H/2 - d. \end{cases} \quad (1.4)$$

Here, $\mathbf{u}_{sc}^>(\mathbf{x}, \omega)$ is the scattered field in the outer region, $\mathbf{u}_{sc}^<(\mathbf{x}, \omega)$ is the motion getting inside the FBH. The relation (1.4) produces analogous decompositions for the potentials entering the total field $\mathbf{u}(\mathbf{x}, \omega)$. Recalling the problem geometry, it is convenient to expand them in Bessel/Hankel series with unknown coefficients:

$$\{\phi^>, \psi^>\} = H \sum_{m=-\infty}^{\infty} \{a_m, b_m\} H_m^{(1)}(\{k_p^H, k_s^H\}r) e^{im\theta}, \quad (1.5)$$

$$\{\phi^<, \psi^<\} = H \sum_{m=-\infty}^{\infty} \{f_m, g_m\} J_m(\{k_p^{H-d}, k_s^{H-d}\}r) e^{im\theta},$$

$$\{w_1^>, w_2^>, V^>\} = \sum_{m=-\infty}^{\infty} \{c_m, d_m, e_m\} H_m^{(1)}(\{k_1^H, k_2^H, k_3^H\}r) e^{im\theta}, \quad (1.6)$$

$$\{w_1^<, w_2^<, V^<\} = \sum_{m=-\infty}^{\infty} \{h_m, i_m, j_m\} J_m(\{k_1^{H-d}, k_2^{H-d}, k_3^{H-d}\}r) e^{im\theta}.$$

The superscripts H and $H - d$ indicate whether the wavenumber is for the outer plate or FBH; a_m, \dots, j_m are unknown coefficients.

If the incident field \mathbf{u}_0 is known (e.g., a plane A0 or S0 wave upcoming from infinity), the expansion coefficients are obtained from the linear algebraic equations resulting from the substitution of expansions (1.5), (1.6) into the boundary conditions at the FBH border $r = R$. The latter include the continuity conditions for all displacements, forces, and moments as well as the coupling conditions arising from the fact that the neutral axis of the FBH is offset from the neutral axis of the plate material surrounding it (Cegla et al. 2008; Glushkov et al. 2018). Such coupling allows for considering mode conversion phenomenon (i.e., A0–S0 and vice-versa conversion) conditioned by the non-symmetry of the obstacle.

Due to the orthogonality of circumferential orders in Eqs. (1.5), (1.6), the equations for estimating a_m, \dots, j_m can be set up for each integer circumferential order m . Therefore, the problem is reduced to the infinite set of 10×10 linear algebraic equations with respect to the unknowns $a_m, b_m, c_m, d_m, e_m, f_m, g_m, h_m, i_m, j_m$. Their solution quickly converges and only the lowest circumferential orders could be preserved. In general, the truncation number in the corresponding series depends on the FBH size and characteristic wavelengths of the incoming and scattered fields. In the computations presented below, the convergence is achieved with 9 lowest circumferential orders.

Scattering resonance frequencies f_n could be formally evaluated as singular points in the complex frequency plane of the corresponding set of homogeneous algebraic systems (i.e., searching for the zeros of their determinants). However, such an approach turned up being numerically unstable. Alternatively, the incident field in the form of plane A0 or S0 wave is considered, truncated set of algebraic systems is solved, and f_n are approximated by the frequencies, which provide unbounded growth of displacements in the FBH region, employing expansions (1.5) and (1.6).

(b) Finite element analysis

A more sophisticated three-dimensional case is studied with the finite element method (FEM). The FEM is applied to a bounded specimen of thickness H containing all the defects, which is enclosed by perfectly matched layers (PML) to simulate an open waveguide (Fig. 1.1c) (Hein et al. 2012) (COMSOL 5.3). Although the built-in solver yields many spurious complex eigenfrequencies intrinsic to finite bodies, the required scattering resonance poles, remaining in the open guide, could be straightforwardly selected since their imaginary parts are sufficiently small ($|\text{Im } f_n| \ll \text{Re } f_n$) and the corresponding eigenforms are strongly localized in the FBH.

To compare the performance of the implemented approaches and investigate the influence of the FBH geometric parameters on the diffraction eigenfrequencies, a waveguide of thickness $H = 2$ mm manufactured from aluminium (Young's modulus $E = 70$ GPa, Poisson coefficient $\nu = 0.33$, and density $\rho = 2700$ kg/m³) is considered. The obtained results (trajectories of complex resonance frequencies) are summarized in Fig. 1.2. The left subplot corresponds to the fixed obstacle depth $d = 1.75$ mm and the varying radius R ; in the right one, on the contrary, the radius $R = 2.5$ mm is constant while the depth d varies. With the increase of damage severity (larger values of either R or d parameters), the number of almost real resonance poles in the frequency range considered increases while the magnitude of their imaginary parts decreases. Moreover, monotonous dependence of resonance frequencies f_n from the obstacle geometry parameters is observed, which confirms their potential for damage characterization. Regarding the model comparison, the results obtained with both approaches are consistent with each other; hence, the simplified 2D plate-based model is capable of the reliable evaluation of resonance frequencies for a relatively broad range of the parameters R and d .

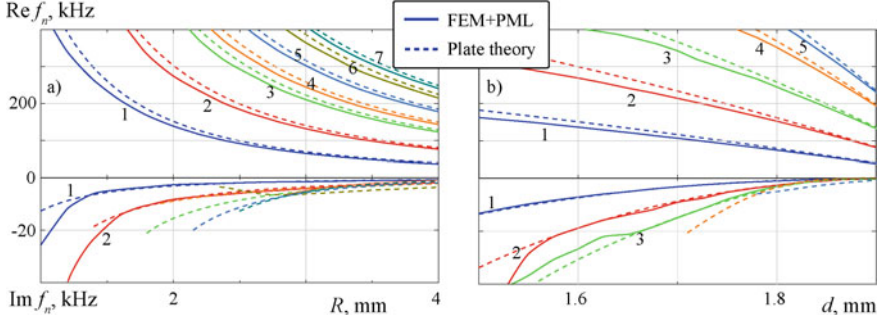


Fig. 1.2 Dependencies of complex resonance frequencies from FBH geometry parameters

1.3 Experimental Evaluation of Resonance Frequencies

Preliminary experimental investigations have been carried out with an aluminium plate sample of dimensions $400 \times 300 \times 2 \text{ mm}^3$ containing a circular FBH of radius $R = 2.45 \text{ mm}$ and depth $d = 1.68 \text{ mm}$. Guided waves are generated by prolonged rectangular piezoelectric wafer active sensors (PWAS) of the dimensions $5 \times 30 \times 0.25 \text{ mm}^3$. It is adhered to the specimen 70 mm away from the FBH in such a way that the elongated PWAS side is parallel to the Oy axis of the introduced Cartesian coordinate system (see Figs. 1.1 and 1.4). Transient out-of-plane displacement velocity $v_z(\mathbf{x}, t)$ is measured on the plate surface by a Polytec PSV-500 one-dimensional scanning laser Doppler vibrometer.

Theoretical resonance frequencies are evaluated in advance, and the first four of them (f_n , $n = 1, 2, 3, 4$), obtained by both models, are summarized in the first two rows of Table 1.1. Corresponding localization patterns (eigenforms) at the FBH in the open waveguide are shown in Fig. 1.3. As expected, the location and number of nodal points change with the increase of n .

Since a considerable increase of the oscillation amplitude is expected at the resonance frequencies, a straightforward way to experimentally reveal their presence is to measure transient oscillations inside the FBH and select such frequencies f_n^{exp} at which strong local maxima of the signal spectra are observed (Glushkov et al. 2015a, b). Preliminarily, the analysis of the corresponding theoretical eigenforms (Fig. 1.3a) suggests that a few measurement points located at the FBH bottom could be enough for the estimation and selection of f_n^{exp} values. In accordance with the

Table 1.1 The first four predicted and measured resonance frequencies of the circular FBH

| Employed approach | f_1 , kHz | f_2 , kHz | f_3 , kHz | f_4 , kHz |
|-------------------|-------------|-------------|-------------|-------------|
| Plate theory | 127.4–5.2i | 255.1–13.5i | 398.2–22.8i | 455.9–13.8i |
| FEM + PML | 112.4–3.7i | 223.7–10.5i | 351.5–17.8i | 407.3–9.3i |
| Experiment | 116.3 | 223.7 | 362.1 | 421.5 |

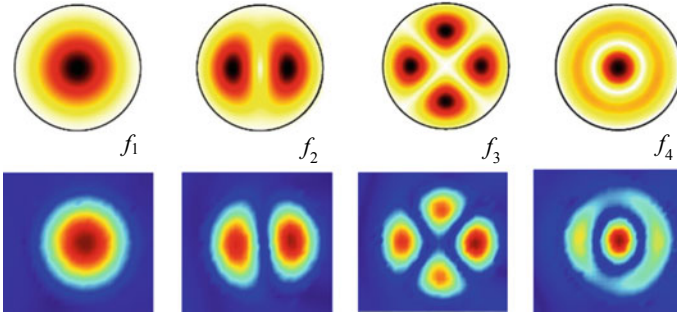


Fig. 1.3 Computed (upper row) and measured (lower row) resonance localization patterns (amplitudes of out-of-plane velocities on the FBH surface) for the first four resonance frequencies

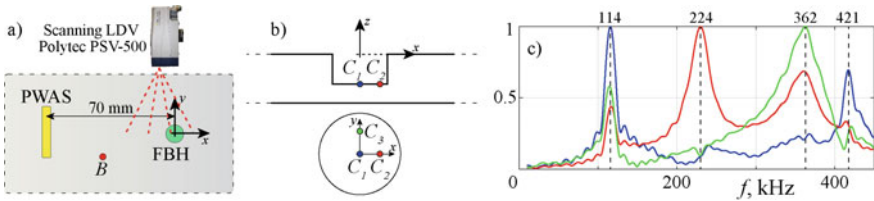


Fig. 1.4 Sketch of the experimental setup (a); points on the FBH surface for the frequency spectrum evaluation (b); normalized spectra of the signals measured at these points (blue line—point C1, red line—C2, green line—C3) (c)

antinode patterns, the local maxima of the frequency response at the central point $C1(0,0)$ (Fig. 1.4b) are expected at the first and fourth resonance frequencies, the point $C2(R/2,0)$ can provide the value of f_2^{exp} , while the third resonance frequency f_3^{exp} should be dominant at the location $C3(0,3R/4)$. To check this assumption, the PWAS is excited with a broadband rectangular $1 \mu s$ pulse voltage, and the velocities $V_z(x, t)$ are measured at the proposed points $C1-C3$. The evaluated spectra $|v_z(x, f)|$ are summarized in Fig. 1.4c, and all the four expected local maxima are clearly visible. Moreover, their location on the frequency axis is in good agreement with the predicted values f_n (the last row and the first two rows in Table 1.1, correspondingly).

Within the SHM concept, the wave signals are measured at a limited set of distributed active/passive sensors. Therefore, it is important to understand whether the resonance frequencies f_n^{exp} can be detected outside the damaged region. Since the resonance interaction of the incident GW with the FBH is characterized by a prolonged localization of the wave motion at the obstacle with a gradual re-emission into the structure, the presence of such narrow-band oscillations in the wave signals measured at some remote points might serve as a reliable resonance indicator. To illustrate such a possibility, transient wave signals have been measured at point $B(-35.5, -15.4)$ mm located aside from the straight path between the PWAS and FBH (Fig. 1.4).

Figure 1.5 a gives an example of the shape of the velocity signal $v_z(x, t)$ obtained at this point for the broadband $2 \mu\text{s}$ PWAS excitation. From this plot, it is difficult to distinguish the waves scattered by the FBH from the initial PWAS generated signal and spurious reflections from the specimen boundaries. Therefore, time–frequency analysis based on the continuous Gabor wavelet transform has been applied (Kishimoto et al. 1995). The corresponding normalized scalogram truncated for better contrast to the 0.5-level is provided in Fig. 1.5b. The incident waves are pronounced here as a dark broad vertical segment appearing at $0.02\text{--}0.04$ ms. Recalling dispersion properties of fundamental antisymmetric mode A0 in a 2 mm aluminium layer and considering the location of point B, the dark area at 0.06 ms is identified as the wavefield scattered by the defect. Multiple reflections from boundaries arrive at point B from $t = 0.115$ ms (yellow area in the low-right corner of the plot). Therefore, the wavefields re-emitted from the defect due to the trapped mode phenomena might manifest themselves in the time interval between these two events, i.e., for $t \in (0.065, 0.113)$ ms (denoted by the vertical dashed-dotted lines in Fig. 1.5a, b). Some elongated patterns within this segment are already visible in Fig. 1.5b. The spectrum of this part of the measured signal is shown in Fig. 5c. It indicates the presence of two strong local maxima at the frequencies $\tilde{f}_1 = 117$ kHz and $\tilde{f}_2 = 224$ kHz, which coincide with the first two f_n^{exp} determined above. The latter is believed to serve as an illustration of the capability for the damage scattering resonance frequency estimation with sensing points located away from the damaged area.

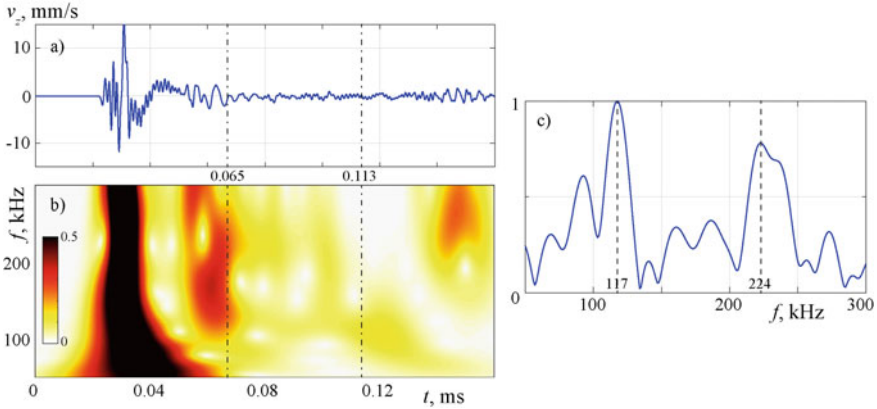


Fig. 1.5 Remote estimation of resonance frequencies. (a) Example of velocity signal (broadband $2 \mu\text{s}$ PWAS excitation); (b) corresponding normalized scalogram; the spectrum of the measured part for t between 0.065 and 0.113 ms is plotted in (c)

Table 1.2 Measured and reconstructed radius and depth of a circular FBH for two experimental samples

| Waveguide thickness H , mm | Measured radius R , mm | Measured depth d , mm | Identified radius, mm | Identified depth, mm |
|------------------------------|--------------------------|-------------------------|-----------------------|----------------------|
| 2 | 2.46 | 1.68 | 2.72 | 1.64 |
| 3 | 2.76 | 2.6 | 2.9 | 2.66 |

1.4 Estimation of the Defect Size

In this section, we discuss a possible application of the diffraction resonance phenomenon for damage sizing. The geometry of a circular FBH is parametrized by the radius R and depth d . The task is to estimate these two parameters from the values of several first resonance frequencies. A natural way for solving this problem is to construct a quadratic discrepancy functional between N experimental f_n^{exp} and computed f_n eigenfrequencies

$$Err(R, d) = \sum_{n=1}^N (f_n - f_n^{exp})^2 \quad (1.6)$$

and to minimize it with respect to the R and d variables, e.g., by employing the microgenetic algorithm (Krishnakumar 1989).

The results of damage geometry reconstruction for the initial experimental sample and the thicker second one ($H = 3$ mm) are given in Table 1.2. Here, the first three experimental resonance frequencies have served as an input, and the numerical evaluation of theoretical f_n has been performed within the analytically based model. Disregard its relative simplicity, the estimated values of R and d are in good agreement with the results measured by the digital micrometer.

1.5 Conclusion

Resonance phenomena accompanying the interaction of elastic GWs with local thickness changes in the form of circular FBH are investigated. The parametric analysis performed within the approximate plate theory and FEM-PML computational model has shown the presence of almost real natural scattering resonance frequencies and revealed the general influence of FBH geometry parameters on their distribution in the complex frequency plane. Experimental LDV measurements have confirmed a strong and prolonged wave motion localized at the obstacle at the predicted resonance frequencies. The possibility of resonance frequency estimation using wave signals acquired at off-damage locations as well as the reconstruction of damage

geometry relying on the experimental eigenfrequencies is illustrated by numerical and experimental examples for some specific samples.

Acknowledgements This work is supported by the Russian Science Foundation (Project No. 17-11-01191).

References

- Alibert JJ, Seppecher P, dell’Isola F (2003) Truss modular beams with deformation energy depending on higher displacement gradients. *Math Mech Solids* 8(1)
- Auffray N, dell’Isola F, Eremeyev V, Madeo A, Rosi G (2013) Analytical continuum mechanics à la Hamilton-Piola: least action principle for second gradient continua and capillary fluids. *Math Mech Solids*
- Barchiesi E, Spagnuolo M, Placidi L (2018) Mechanical metamaterials: a state of the art. *Math Mech Solids*
- Barchiesi E, dell’Isola F, Hild F, Seppecher P (2020b) Two-dimensional continua capable of large elastic extension in two independent directions: asymptotic homogenization, numerical simulations and experimental evidence. *Mech Res Commun* 103
- Barchiesi E, Eugster SR, dell’isola F, Hild F (2020c) Large in-plane elastic deformations of bi-pantographic fabrics: asymptotic homogenization and experimental validation. *Math Mech Solids* 25(3):739–767
- Barchiesi E, Yang H, Tran CA, Placidi L, Müller WH (2020a) Computation of brittle fracture propagation in strain gradient materials by the FEniCS library. *Math Mech Solids*
- Cegla FB, Rohde A, Veidt M (2008) Analytical prediction and experimental measurement for mode conversion and scattering of plate waves at non-symmetric circular blind holes in isotropic plates. *Wave Motion* 45:162–177
- Del Vescovo D, Giorgio I (2014) Dynamic problems for metamaterials: review of existing models and ideas for further research. *Int J Eng Sci* 80:153–172
- dell’Isola F, Seppecher P, Madeo (2012) A How contact interactions may depend on the shape of Cauchy cuts in Nth gradient continua: approach “à la D’Alembert”. *Z Für Angew Math Und Phys* 63(6)
- dell’Isola F, Andreaus U, Placidi L (2015) At the origins and in the vanguard of peridynamics, non-local and higher-gradient continuum mechanics: An underestimated and still topical contribution of Gabrio Piola. *Math Mech Solids* 20(8)
- dell’Isola F, Della Corte A, Giorgio I (2016a) Higher-gradient continua: the legacy of Piola, Mindlin, Sedov and Toupin and some future research perspectives. *Math Mech Solids*
- dell’Isola F, Della Corte A, Greco L, Luongo A (2016b) Plane bias extension test for a continuum with two inextensible families of fibers: a variational treatment with Lagrange multipliers and a perturbation solution. *Int J Solids Struct*
- dell’Isola F, Giorgio I, Pawlikowski M, Rizzi N (2016) Large deformations of planar extensible beams and pantographic lattices: heuristic homogenization, experimental and numerical examples of equilibrium. *Proc R Soc A* 472(2185)
- dell’Isola F, Cuomo M, Greco L, Della Corte A (2017) Bias extension test for pantographic sheets: numerical simulations based on second gradient shear energies. *J Eng Math*
- dell’Isola F, Seppecher P, Alibert JJ, Lekszycki T, Grygoruk R, Pawlikowski M, Steigmann D, Giorgio I, Andreaus U, Turco E, Gołaszewski M, Rizzi N, Boutin C, Eremeyev VA, Misra A, Placidi L, Barchiesi E, Greco L, Cuomo M, Cazzani A, Della Corte A, Battista A, Scerrato D, Eremeeva IZ, Rahali Y, Ganghoffer JF, Müller W, Ganzosch G, Spagnuolo M, Phaff A, Barcz K,

- Hoschke K, Neggers J, Hild F (2019) Pantographic metamaterials: an example of mathematically driven design and of its technological challenges. *Continuum Mech Thermodyn* 31(4):851–884
- dell’Isola F, Seppecher P, Spagnuolo M, Barchiesi E, Hils F, Lekszycki T, Giorgio I, Placidi L, Andreaus U, Cuomo M, Eugster SR, Pfaff A, Hoschke K, Langkemper R, Turco E, Sarikaya R, Misra A, De Angelo M, D’Annibale F, Bouterf A, Pinelli X, Misra A, Desmorat B, Pawlikowski M, Dupuy C, Scerrato D, Peyre P, Laudato M, Manzari L, Göransson P, Hesch C, Hesch S, Franciosi P, Dirrenberger J, Maurin F, Vangelatos Z, Grigoropoulos C, Melissinaki V, Farsari M, Muller W, Abali BE, Liebold C, Ganzosch G, Harrison P, Drobnicki R, Igumnov L, Alzahrani F, Hayat T (2019) Advances in pantographic structures: design, manufacturing, models, experiments and image analyses. *Continuum Mech Thermodyn* 31(4):1231–1282
- Glushkov E, Glushkova N, Golub MV, Moll J, Fritzen CP (2012) Wave energy trapping and localization in a plate with a delamination. *Smart Mater. Struct.* 21
- Glushkov E, Glushkova N, Eremin A, Lammering R (2015) Trapped mode effects in notched plate-like structures. *J Sound Vib* 358:142–151
- Glushkov EV, Glushkova NV, Eremin AA, Lammering R (2015b) Guided wave propagation and diffraction in plates with obstacles: resonance transmission and trapping mode effects. *Phys Procedia* 70:447–450
- Glushkov E, Glushkova N, Eremin A, Lammering R (2018) Trapped modes and resonance wave transmission in a plate with a system of notches. *J Sound Vib* 412:360–371
- Grahn T (2008) Lamb wave scattering from a circular partly through-thickness hole in a plate. *Wave Motion* 37:63–80
- Greco F, Luciano R, Serino G, Vaiana N (2018) A mixed explicit-implicit time integration approach for nonlinear analysis of base-isolated structures. *Ann Solid Struct Mech* 10(1–2):17–29
- Hein S, Koch L, Nannen L (2012) Trapped modes and Fano resonances in two-dimensional acoustical duct cavity systems. *J Fluid Mech* 692:257–287
- Kishimoto K, Inoue H, Hamada M, Shibuya T (1995) Time frequency analysis of dispersive waves by means of wavelet transform. *J Appl Mech* 62:841–846
- Krishnakumar K (1989) Micro-genetic algorithms for stationary and non-stationary function optimization. In: *Proceedings SPIE 1196 intelligent control and adaptive systems*. Rodriguez G, Philadelphia, PA, United States
- Lammering R, Gabbert U, Sinapius M, Schuster T, Wierach P (eds) (2018) *Lamb-wave based structural health monitoring in polymer composites*. Springer International Publishing AG, Cham, Switzerland
- Marmo F, Sessa S, Rosati L (2016) Analytical solution of the Cerruti problem under linearly distributed horizontal loads over polygonal domains. *J Elast* 124(1):27–56. <https://doi.org/10.1007/s10659-015-9560-3>
- Marmo F, Toraldo F, Rosati A, Rosati L (2018) Numerical solution of smooth and rough contact problems. *Meccanica* 53:1415–1440. <https://doi.org/10.1007/s11012-017-0766-2>
- Marmo F, Sessa S, Vaiana N, De Gregorio D, Rosati L (2020) Complete solutions of three-dimensional problems in transversely isotropic media. *Continuum Mech Thermodyn* 32(3):775–802. <https://doi.org/10.1007/s00161-018-0733-8>
- Placidi L, Barchiesi E, Turco E, Rizzi NL (2016) A review on 2D models for the description of pantographic fabrics. *Z Für Angew Math Phys* 67(5)
- Placidi L, Andreaus U, Giorgio I (2017) Identification of two-dimensional pantographic structure via a linear D4 orthotropic second gradient elastic model. *J Eng Math*
- Rahali Y, Giorgio I, Ganghoffer JF, dell’Isola F (2015) Homogenization à la Piola produces second gradient continuum models for linear pantographic lattices. *Int J Eng Sci* 97
- Sciarra G, dell’Isola F, Coussy O (2007) Second gradient poromechanics. *Int J Solids Struct* 44(20)
- Serpieri R, Sessa S, Rosati L (2018) A MITC-based procedure for the numerical integration of a continuum elastic-plastic theory of through-the-thickness-jacketed shell structures. *Compos Struct* 191:209–220. <https://doi.org/10.1016/j.compstruct.2018.02.031>

- Sessa S, Marmo F, Vaiana N, Rosati L (2018) A computational strategy for eurocode 8-compliant analyses of reinforced concrete structures by seismic envelopes. *J Earthquake Eng* <https://doi.org/10.1080/13632469.2018.1551161>
- Solodov I (2017) Resonant ultrasonic activation of damage: application for diagnostic imaging. *Res Nondestruct Eval* 28:28–44
- Spagnuolo M, Franciosi P, dell’Isola F (2020) A Green operator-based elastic modeling for two-phase pantographic-inspired bi-continuous materials. *Int J Solids Struct* 188:282–308
- Spagnuolo M, Yildizdag ME, Andreaus U, Cazzani AM (2021) Are higher-gradient models also capable of predicting mechanical behavior in the case of wide-knit pantographic structures? *Math Mech Solids* 26(1):18–29
- Trotta S, Marmo F, Rosati L (2016) Analytical expression of the Eshelby tensor for arbitrary polygonal inclusions in two-dimensional elasticity. *Compos B Eng* 106:48–58. <https://doi.org/10.1016/j.compositesb.2016.09.010>
- Turco E, Barchiesi E (2019) Equilibrium paths of Hencky pantographic beams in a three-point bending problem. *Math Mech Complex Syst* 7(4):287–310
- Vaiana N, Spizzuoco M, Serino G (2017) Wire rope isolators for seismically base-isolated lightweight structures: experimental characterization and mathematical modeling. *Eng Struct* 140:498–514. <https://doi.org/10.1016/j.engstruct.2017.02.057>
- Vaiana N, Sessa S, Marmo F, Rosati L (2019) Nonlinear dynamic analysis of hysteretic mechanical systems by combining a novel rate-independent model and an explicit time integration method. *Nonlinear Dyn* 98(4):2879–2901. <https://doi.org/10.1007/s11071-019-05022-5>
- Vaiana N, Sessa S, Rosati L (2021) A generalized class of uniaxial rate-independent models for simulating asymmetric mechanical hysteresis phenomena. *Mech Syst Signal Process* 146: 106984 <https://doi.org/10.1016/j.ymsp.2020.106984>
- Vemula C, Norris AN (1997) Flexural wave propagation and scattering on thin plates using Mindlin theory. *Wave Motion* 26:1–12

Chapter 2

Modelling of Piezocomposites with Mechanical Interface Effects



Andrey V. Nasedkin

Abstract This investigation is devoted to the determination of the material properties of piezoelectric mixed composites with stochastically distributed inclusions or pores and with mechanical imperfect interface, which simulates the nanoscale effects. Finite element package ANSYS was used to simulate the representative volume element and to calculate the effective material properties of piezocomposite material. This approach is based on the theory of effective moduli, the representative volumes simulation and the finite element technologies. The contact boundaries between the materials of different phases were covered by the surface elastic shell elements with membrane stress option in order to take the interface effects into account. As an example, the results of the effective moduli calculation for a porous ferrohard piezoceramics were presented. The results have shown that the surface stresses on the pore boundaries could have a significant effect on the values of the effective stiffness moduli and little effect on the values of the effective piezomoduli and dielectric permittivities.

Keywords Piezoelectricity · Porous piezoceramics · Effective moduli · Nanomechanics · Surface stress · Interphase boundary · Finite element method

2.1 Introduction

Piezoelectric composite materials are widely used for the manufacture of high-tech devices for hydroacoustics, nondestructive testing, medical diagnostics and therapy, level and flow measurement, consumer, automotive and aerospace industries. The analysis of these materials shows that the material properties remain to be the essential limiting factor in the development of the most effective piezoelectric transducers. A lot of new nanostructured piezoelectric composite materials, which were developed in the recent years, have a range of important advanced features, such as the possibilities

A. V. Nasedkin (✉)

Institute of Mathematics, Mechanics and Computer Sciences, Southern Federal University, Rostov-on-Don, Russia

© Springer Nature Switzerland AG 2021

F. Marmo et al. (eds.), *Mathematical Applications in Continuum and Structural Mechanics*, Advanced Structured Materials 127, https://doi.org/10.1007/978-3-030-42707-8_2

of controllable variation of the functional characteristics within a wide range and the ultra-low mechanical quality factor.

Furthermore, it should be noted that the simulation of composite micro- and nano-materials has specific features. It is known that some nanomaterials have unconventional physical properties that significantly differ from the characteristics of usual macrosized bodies. For example, the known experimental fact is the stiffness increases with the reduction of the nanoobject sizes. One of the factors responsible for this behaviour can be the surface effect. As research of the recent years shows, for the bodies of submicro- and nano-sizes, the surface stresses play an important role and influence the deformation of the bodies. In connection to this, an interesting problem can arise from the extension of this approach to the nanostructured piezoelectric composite materials (Dai et al. 2011; Fang et al. 2018; Huang and Yu 2006; Pan et al. 2011; Park et al. 2011; Wang et al. 2014, 2016a, b; Zhao et al. 2016). Therefore, here it is logical to consider not only the mechanical surface effects but also the surface effects for electric fields (Eremeyev and Nasedkin 2017; Nasedkin 2017).

Theoretical investigations of piezoelectric and magnetoelectric nanosized materials with surface effects and imperfect interface models were also presented in (Dai et al. 2011; Pan et al. 2011; Eremeyev and Nasedkin 2017; Gu et al. 2014a, b; Gu and Qin 2014; Nasedkin et al. 2014), etc. Formulae for the effective shear modulus of a fiber reinforced piezoelectric composite was obtained in (Xiao et al. 2011) using a self-consistent method. Investigations of effective moduli for nanosized piezoelectric composites were continued in (Wang et al. 2014; Nasedkin 2017; Chen 2008; Gu et al. 2015; Malakooti and Sodano 2013), etc.

The study of piezoelectric composite materials may also be linked to the reasoning and methodologies used for other complex materials. More specifically, it has been shown in literature that variational approaches have many epistemological and heuristic advantages (dell'Isola et al. 2020; dell'Isola and Placidi 2011). This kind of approach has been successfully applied to model complex materials (Placidi et al. 2019; Pideri and Seppecher 1997; Barchiesi et al. 2018; Camar-Eddine and Seppecher 2001; Milton et al. 2009; Alibert et al. 2003; Turco et al. 2019a, 2020), especially for the so-called metamaterials (dell'Isola et al. 2019a, b; Placidi et al. 2018a, b, 2020; Turco et al. 2019b; Spagnuolo et al. 2020, 2021; Spagnuolo, 2020). Many application fields may be found, such as structural mechanics (Vaiana et al. 2021, 2019; Sessa et al. 2015, 2017, 2018a, b, 2019a, 2019b; Serpieri et al. 2018; Cricri et al. 2015).

In the present work, the models of two-phase piezoelectric composite materials are developed in the framework of classic continuum approaches of solid mechanics and methods of composite mechanics. Similarly (Nasedkin 2019) these models are used to construct more complicated models of the micro- and nano-sized piezoelectric bodies that additionally take into account the surface or interphase mechanical boundary conditions.

We use an integrated approach to the determination of the effective moduli of nanoporous piezoelectric composites with stochastically distributed porosity. In order to take into account nanoscale level at the borders between material and pores, the Gurtin–Murdoch model of surface stresses are used. ANSYS finite element

package was used to simulate the representative volume elements and to calculate the effective moduli. This approach is based on the theory of effective moduli of composite mechanics, simulation of the representative volumes and the finite element method. Here, we adopt that the contact boundaries between material and pores are covered by the surface membrane elements in order to take the surface stresses into account.

2.2 Effective Moduli Method for Homogenization of Two-Phase Piezoelectric Nanocomposite

Let Ω be a representative volume element of a two-phase composite piezoelectric material with nanodimensional inclusions or pores; $\Omega = \Omega^{(1)} \cup \Omega^{(2)}$; $\Omega^{(1)}$ is the volume occupied by the primary material of the first phase (matrix); $\Omega^{(2)}$ is the set of the volumes occupied by the material of the second phase (inclusions or pores); $\Gamma = \partial \Omega$ is the external boundary of the volume Ω Γ^s is the set of frontier surfaces of materials with different phases ($\Gamma^s = \partial \Omega^{(1)} \cap \partial \Omega^{(2)}$); \mathbf{n} is the external unit normal vector to the boundary, outward with respect to $\Omega^{(1)}$, i.e., to the region occupied by the primary material; $\mathbf{x} = \{x_1, x_2, x_3\}$ is the vector of the Cartesian coordinates. We suppose that the volumes $\Omega^{(1)}$ and $\Omega^{(2)}$ are filled with different piezoelectric materials. Then in the framework of linear static theory of piezoelectricity we have the following system of equations:

$$\sigma_{ij,j} = 0, D_{i,i} = 0, \sigma_{ij} = c_{ijkl}^E \varepsilon_{kl} - e_{kij} E_k, D_i = e_{ikl} \varepsilon_{kl} + \varepsilon_{ik}^S E_k \quad (2.1)$$

$$\varepsilon_{ij} = (u_{i,j} + u_{j,i})/2, E_i = -\varphi_{,i} \quad (2.2)$$

where σ_{ij} are the components of the second rank stress tensor $\boldsymbol{\sigma}$; ε_{ij} are the components of the second rank strain tensor $\boldsymbol{\varepsilon}$; D_i are the components of the electric flux density vector \mathbf{D} ; E_i are the components of the electric field vector \mathbf{E} ; u_i are the components of the displacement vector \mathbf{u} ; φ is the function of electric potential; c_{ijkl}^E is the fourth rank tensor of elastic stiffness moduli at constant electric field; e_{ikl} is the third rank tensor of piezoelectric moduli; ε_{ik}^S is the second rank tensor of dielectric permittivity moduli at constant mechanical strain; $c_{ijkl}^E = c_{ijkl}^{E(m)}$, $e_{ikl} = e_{ikl}^{(m)}$, $c_{ijkl}^E = c_{ijkl}^{E(m)}$, $\varepsilon_{ik}^S = \varepsilon_{ik}^{S(m)}$, $\sigma_{ij} = \sigma_{ij}^{(m)}$, $\varepsilon_{ij} = \varepsilon_{ij}^{(m)}$, $D_i = D_i^{(m)}$, $E_i = E_i^{(m)}$, $u_i = u_i^{(m)}$, $\varphi = \varphi^{(m)}$, $\mathbf{x} \in \Omega^{(m)}$, $m = 1, 2$.

The material moduli of the piezoelectric medium have usual properties of symmetry ($c_{ijkl}^E = c_{jikl}^E = c_{klij}^E$; $e_{ikl} = e_{ilk}$; $\varepsilon_{ik}^S = \varepsilon_{ki}^S$) and positive definiteness, i.e., $\exists W_\Omega > 0, \forall \varepsilon_{ij} = \varepsilon_{ji}, E_i$:

$$U_\Omega(\varepsilon_{ij}, E_i) = (c_{ijk}^E \varepsilon_{ij} \varepsilon_{kl} + \varepsilon_{kl}^S E_k E_l)/2 \geq W_\Omega(\varepsilon_{kl} \varepsilon_{kl} + E_k E_k)/2 \quad (2.3)$$

where $U_\Omega(\varepsilon_{ij}, E_i)$ is the density of the intrinsic energy in the volume Ω .

In vector–matrix notation in R^3 the formulas (2.1), (2.2) can be rewritten in the form

$$\mathbf{L}^T(\nabla) \cdot \mathbf{T} = 0, \quad \nabla \cdot \mathbf{D} = 0, \quad \mathbf{T} = \mathbf{c}^E \cdot \mathbf{S} - \mathbf{e}^T \cdot \mathbf{E}, \quad \mathbf{D} = \mathbf{e} \cdot \mathbf{S} + \boldsymbol{\varepsilon}^S \cdot \mathbf{E} \quad (2.4)$$

$$\mathbf{S} = \mathbf{L}(\nabla) \cdot \mathbf{u}, \quad \mathbf{E} = -\nabla\varphi, \quad \mathbf{L}^T(\nabla) = \begin{bmatrix} \partial_1 & 0 & 0 & 0 & \partial_3 & \partial_2 \\ 0 & \partial_2 & 0 & \partial_3 & 0 & \partial_1 \\ 0 & 0 & \partial_3 & \partial_2 & \partial_1 & 0 \end{bmatrix}, \quad (2.5)$$

where $\mathbf{L}(\mathbf{a})$ is a matrix operator for the vector \mathbf{a} ; $\nabla = \{\partial_1, \partial_2, \partial_3\}$; $\mathbf{T} = \{\sigma_{11}, \sigma_{22}, \sigma_{33}, \sigma_{23}, \sigma_{13}, \sigma_{12}\}$ is the six-dimensional array of the stress components; $\mathbf{S} = \{\varepsilon_{11}, \varepsilon_{22}, \varepsilon_{33}, 2\varepsilon_{23}, 2\varepsilon_{13}, 2\varepsilon_{12}\}$ is the six-dimensional array of the strain components; \mathbf{c}^E is the 6×6 matrix of elastic moduli at constant electric field; \mathbf{e} is the 3×6 matrix of piezoelectric moduli; $\boldsymbol{\varepsilon}^S$ is the 3×3 matrix of dielectric permittivity moduli at constant strains; $c_{\alpha\beta}^E = c_{ijkl}^E$, $e_{i\beta} = e_{ikl}$, $\alpha, \beta = 1, 2, \dots, 6$; $i, j, k, l = 1, 2, 3$ with the correspondence law $\alpha \Leftrightarrow (ij) \sim (ji)$, $\beta \Leftrightarrow (kl) \sim (lk)$, $1 \Leftrightarrow (11)$, $2 \Leftrightarrow (22)$, $3 \Leftrightarrow (33)$, $4 \Leftrightarrow (23) \sim (32)$, $5 \Leftrightarrow (13) \sim (31)$, $6 \Leftrightarrow (12) \sim (21)$; $(\dots)^T$ is the transpose operation; $(\dots) \cdot (\dots)$ is the scalar product operation between two vectors or a matrix by vector multiplication. The matrices \mathbf{c}^E and $\boldsymbol{\varepsilon}^S$ are symmetric ($c_{\alpha\beta}^E = c_{\beta\alpha}^E$, $\varepsilon_{ik}^S = \varepsilon_{ki}^S$) and positive definite by virtue of the properties (2.3), i.e., $\exists W_\Omega > 0, \forall \mathbf{S}, \mathbf{E}$:

$$U_\Omega(\mathbf{S}, \mathbf{E}) = (\mathbf{S}^T \cdot \mathbf{c}^E \cdot \mathbf{S} + \mathbf{E}^T \cdot \boldsymbol{\varepsilon}^S \cdot \mathbf{E})/2 \geq W_\Omega(\mathbf{S}^T \cdot \mathbf{S} + \mathbf{E}^T \cdot \mathbf{E})/2 \quad (2.6)$$

In accordance with Gurtin–Murdoch model for surface stresses, we will assume that on the nanosized interphase boundaries Γ^s the following equations are satisfied:

$$\mathbf{L}^T(\mathbf{n}) \cdot [\mathbf{T}] = \mathbf{L}^T(\nabla^s) \cdot \mathbf{T}^s, \quad \mathbf{n} \cdot [\mathbf{D}] = 0, \quad \mathbf{x} \in \Gamma^s, \quad (2.7)$$

where $[\mathbf{T}] = \mathbf{T}^{(1)} - \mathbf{T}^{(2)}$ is the stress jump, etc.; ∇^s is the surface gradient operator, associated with usual spatial nabla–operator ∇ by the formula $\nabla^s = \nabla - \mathbf{n}\partial/\partial r$; r is the coordinate, measured by the normal to Γ^s ; $\mathbf{T}^s = \{\sigma_{11}^s, \sigma_{22}^s, \sigma_{33}^s, \sigma_{23}^s, \sigma_{13}^s, \sigma_{12}^s\}$ is the array of surface stresses σ_{ij}^s . Note that surface stresses σ_{ij}^s have the dimensionality (N/m) different from the dimensionality of usual stresses σ_{ij} (N/m²).

We adopt that the surface stresses \mathbf{T}^s are related only to the surface strains \mathbf{S}^s by the surface Hooke's law

$$\mathbf{T}^s = \mathbf{c}^{Es} \cdot \mathbf{S}^s, \quad \mathbf{S}^s = \mathbf{L}(\nabla^s) \cdot \mathbf{u}^s, \quad \mathbf{u}^s = \mathbf{A} \cdot \mathbf{u}, \quad \mathbf{A} = \mathbf{I} - \mathbf{nn}^* \quad (2.8)$$

where \mathbf{c}^{Es} is the 6×6 matrix of surface elastic moduli with dimensionality N/m; \mathbf{I} is the 3×3 identity matrix.

The properties of the matrix of surface elastic moduli c^{Es} are similar to the corresponding properties of the matrix c^E , i.e., $c_{\alpha\beta}^{Es} = c_{\beta\alpha}^{Es}$, and the transformed matrix \tilde{c}^{Es} in local coordinate system with the tangent ors $\boldsymbol{\tau}_1, \boldsymbol{\tau}_2$ and normal \boldsymbol{n} , has the feature of positive definiteness: $\exists W_\Gamma > 0, \forall \tilde{\boldsymbol{S}}^s = \{\tilde{S}_1^s, \tilde{S}_2^s, 0, 0, 0, \tilde{S}_6^s\}$,

$$2U_\Gamma(\tilde{\boldsymbol{S}}^s) = \tilde{\boldsymbol{S}}^{sT} \cdot \tilde{c}^{Es} \cdot \tilde{\boldsymbol{S}}^s \geq W_\Gamma \tilde{\boldsymbol{S}}^T \cdot \tilde{\boldsymbol{S}} \quad (2.9)$$

that follow from the condition of the positive definiteness of the surface mechanical energy density $U_\Gamma(\tilde{\boldsymbol{S}}^s)$ relative to surface strain $\tilde{\boldsymbol{S}}^s$.

Setting the appropriate boundary conditions on the external boundary $\Gamma = \partial \Omega$, we can find the solutions of the problems (2.4), (2.5), (2.7), (2.8) for heterogeneous piezoelectric medium in the representative volume element Ω . Then the comparison of the averaged stresses, strains, electric fluxes and electric fields with the analogous values for homogeneous medium (i.e., for the comparison medium) will allow us to determine the effective moduli for the composite material. We note that, because the piezoelectric material is an anisotropic medium, in order to determine the full set of the effective moduli it is necessary to solve several problems (2.4), (2.5), (2.7), (2.8) for different types of boundary conditions.

Here the main tasks consist in the choice of the representative volume element with the specific structure and in the choice of the boundary conditions for the heterogeneous medium and the comparison medium, as well as the technologies for solving the boundary problems for heterogeneous piezoelectric media. According to the previously developed methods for the simulation of the ordinary piezoelectric composites (Nasedkin and Shevtsova 2011, 2013), we consider analogous approaches for the piezoelectric problems with surface stresses.

For homogeneous piezoelectric comparison medium we adopt that the same Eqs. (2.4), (2.5) are satisfied with constant effective moduli $\boldsymbol{c}^{E\text{eff}}$, $\boldsymbol{e}^{\text{eff}}$ and $\boldsymbol{\epsilon}^{\text{Seff}}$, which are to be determined. In order to calculate these moduli, let us assume that on the external boundary Γ the following relations take place

$$\boldsymbol{u} = \boldsymbol{L}^T(\boldsymbol{x}) \cdot \boldsymbol{S}_0, \quad \varphi = -\boldsymbol{x} \cdot \boldsymbol{E}_0, \quad \boldsymbol{x} \in \Gamma, \quad (2.10)$$

where $\boldsymbol{S}_0 = \{S_{01}, S_{02}, S_{03}, S_{04}, S_{05}, S_{06}\}$; $S_{0\beta}$ are some constant values that do not depend on \boldsymbol{x} ; \boldsymbol{E}_0 is some constant vector. Then, $\boldsymbol{u} = \boldsymbol{L}^T(\boldsymbol{x}) \cdot \boldsymbol{S}_0$, $\boldsymbol{S} = \boldsymbol{S}_0$, $\varphi = -\boldsymbol{x} \cdot \boldsymbol{E}_0$, $\boldsymbol{E} = \boldsymbol{E}_0$, $\boldsymbol{T} = \boldsymbol{T}_0 = \boldsymbol{c}^{E\text{eff}} \cdot \boldsymbol{S}_0 - \boldsymbol{e}^{\text{eff}T} \cdot \boldsymbol{E}_0$, $\boldsymbol{D} = \boldsymbol{D}_0 = \boldsymbol{e}^{\text{eff}} \cdot \boldsymbol{S}_0 + \boldsymbol{\epsilon}^{\text{Seff}} \cdot \boldsymbol{E}_0$ will give the solution for the problem (2.4), (2.5), (2.7), (2.8), (2.10) in the volume Ω for the homogeneous comparison medium.

Let us solve now problem (2.4), (2.5), (2.7), (2.8), (2.10) for heterogeneous medium and assume that for the composite medium and for the comparison medium the averaged stresses and electric flux densities are equal, i.e., $\langle \boldsymbol{T} \rangle_{\Omega\Gamma} = \langle \boldsymbol{T}_0 \rangle_{\Omega\Gamma}$, $\langle \boldsymbol{D} \rangle_{\Omega} = \langle \boldsymbol{D}_0 \rangle_{\Omega}$. Hereinafter the angle brackets $\langle \dots \rangle_{\Omega}$ denote the values, averaged by the volume Ω , and the angle brackets $\langle \dots \rangle_{\Omega\Gamma}$ denote the values,

averaged by the volume Ω and by the interface surfaces Γ^s .

$$\langle \bullet \rangle_{\Omega} = \frac{1}{|\Omega|} \int_{\Omega} f(\bullet) d\Omega, \quad \langle \bullet \rangle_{\Omega\Gamma} = \frac{1}{|\Omega|} \left(\int_{\Omega} f(\bullet) d\Omega + \int_{\Gamma^s} f(\bullet)^s d\Gamma \right) \quad (2.11)$$

Therefore, we obtain that the equations $\mathbf{T}_0 = \mathbf{c}^{E\text{eff}} \cdot \mathbf{S}_0 - \mathbf{e}^{\text{eff}T} \cdot \mathbf{E}_0 = \langle \mathbf{T} \rangle_{\Omega\Gamma}$ and $\mathbf{D}_0 = \mathbf{e}^{\text{eff}} \cdot \mathbf{S}_0 + \mathbf{e}^{S\text{eff}} \cdot \mathbf{E}_0 = \langle \mathbf{D} \rangle_{\Omega}$ are satisfied for the effective moduli of the composite, where \mathbf{S}_0 and \mathbf{E}_0 are the given values from the boundary conditions (2.10).

Hence, even in the assumption of the anisotropy of the general form for the comparison medium, all the stiffness moduli $c_{\alpha\beta}^{E\text{eff}}$, the piezomoduli $e_{i\beta}^{\text{eff}}$ and the dielectric permittivity moduli $\varepsilon_{ij}^{S\text{eff}}$ can be computed, if we solve nine boundary value problems (2.4), (2.5), (2.7), (2.8), (2.10), having set in (2.10) only one of the components $S_{0\zeta}$ or E_{0k} ($\zeta = 1, 2, \dots, 6; k = 1, 2, 3$) not equal to zero:

– problems I – VI ($\beta = 1, 2, \dots, 6$)

$$S_{0\zeta} = S_0 \delta_{\beta\zeta}, \quad E_{0k} = 0 \Rightarrow c_{\alpha\beta}^{\text{eff}} = \langle T_{\alpha} \rangle_{\Omega\Gamma} / S_0; \quad e_{i\beta}^{\text{eff}} = \langle D_i \rangle_{\Omega} / S_0 \quad (2.12)$$

– problems VII – IX ($j = 1, 2, 3$)

$$S_{0\zeta} = 0, \quad E_{0k} = E_0 \delta_{jk} \Rightarrow e_{j\alpha}^{\text{eff}} = -\langle T_{\alpha} \rangle_{\Omega\Gamma} / E_0; \quad \kappa_{ij}^{\text{eff}} = \langle D_i \rangle_{\Omega} / E_0, \quad (2.13)$$

where δ_{ij} is the Kronecker symbol; $\alpha = 1, 2, \dots, 6; i = 1, 2, 3$.

In the case of porous piezoceramics of 6 *mm* class, in order to determine its ten independent effective moduli ($c_{11}^{E\text{eff}}, c_{13}^{E\text{eff}}, c_{33}^{E\text{eff}}, c_{44}^{E\text{eff}}, e_{31}^{\text{eff}}, e_{33}^{\text{eff}}, e_{15}^{\text{eff}}, \varepsilon_{11}^{S\text{eff}}, \varepsilon_{33}^{S\text{eff}}$), it is enough to solve only five static problems (2.4), (2.5), (2.7), (2.8), (2.10), having set one of the component $S_{0\beta}$, E_{0l} ($\beta = 1, 2, \dots, 6; l = 1, 2, 3$) in the boundary conditions (2.10) not equal to zero $k = 1, 2, 3$

$$\text{I. } S_{0\beta} = S_0 \delta_{1\beta}, \quad E_0 = 0 \Rightarrow c_{1k}^{E\text{eff}} = \langle \sigma_{kk} \rangle_{\Omega\Gamma} / S_0, \quad e_{31}^{\text{eff}} = \langle D_3 \rangle_{\Omega} / S_0, \quad (2.14)$$

$$\text{II. } S_{0\beta} = S_0 \delta_{3\beta}, \quad E_0 = 0 \Rightarrow c_{k3}^{E\text{eff}} = \langle \sigma_{kk} \rangle_{\Omega\Gamma} / S_0, \quad e_{33}^{\text{eff}} = \langle D_3 \rangle_{\Omega} / S_0, \quad (2.15)$$

$$\text{III. } S_{0\beta} = S_0 \delta_{4\beta}, \quad E_0 = 0 \Rightarrow c_{44}^{E\text{eff}} = \langle \sigma_{23} \rangle_{\Omega\Gamma} / S_0, \quad e_{15}^{\text{eff}} = \langle D_2 \rangle_{\Omega} / S_0, \quad (2.16)$$

$$\text{IV. } S_0 = 0, \quad E_{0l} = E_0 \delta_{1l} \Rightarrow e_{15}^{\text{eff}} = -\langle \sigma_{13} \rangle_{\Omega\Gamma} / E_0; \quad \varepsilon_{11}^{S\text{eff}} = \langle D_1 \rangle_{\Omega} / E_0, \quad (2.17)$$

$$\text{V. } S_0 = 0, \quad E_{0l} = E_0 \delta_{3l} \Rightarrow e_{3k}^{\text{eff}} = -\langle \sigma_{kk} \rangle_{\Omega\Gamma} / E_0; \quad \varepsilon_{33}^{S\text{eff}} = \langle D_3 \rangle_{\Omega} / E_0, \quad (2.18)$$

Thus, as we can see, the boundary value problems (2.4), (2.5), (2.7), (2.8), (2.10) with (2.12), (2.13) or with (2.14)–(2.18) differ from the usual problems of linear

piezoelectricity by the presence of the interface boundary conditions (2.7), (2.8) and the average quantities $\langle \bullet \rangle_{\Omega\Gamma}$, which are typical for the Gurtin–Murdoch model of surface stresses for nanosized bodies (Chatzigeorgiou et al. 2015; Javili et al. 2013).

Note that complete interface conditions should take into account the coupled surface electromechanical fields according to the relations that follow from (Eremeyev and Nasedkin 2017; Nasedkin 2017)

$$\mathbf{L}^T(\mathbf{n}) \cdot [\mathbf{T}] = \mathbf{L}^T(\nabla^s) \cdot \mathbf{T}^s, \mathbf{n} \cdot [\mathbf{D}] = \nabla^s \cdot \mathbf{D}^s, \quad \mathbf{x} \in \Gamma^s \quad (2.19)$$

$$\mathbf{T}^s = \mathbf{c}^{Es} \cdot \mathbf{S}^s - \mathbf{e}^{sT} \cdot \mathbf{E}^s, \quad \mathbf{D}^s = \mathbf{e}^s \cdot \mathbf{S}^s + \boldsymbol{\epsilon}^{Ss} \cdot \mathbf{E}^s, \quad \mathbf{E}^s = -\nabla^s \varphi \quad (2.20)$$

Here, however, we use the uncoupled interface conditions (2.7), (2.8), which are obtained from (2.19), (2.20) with zero surface piezomoduli and dielectric constants: $\mathbf{e}^s = 0$, $\boldsymbol{\epsilon}^{Ss} = 0$.

2.3 Dimensionless Homogenization Problem

Dimension analysis shows that the surface stiffness moduli $c_{\alpha\beta}^s$ differ in dimensionality from the corresponding values $c_{\alpha\beta}$ in the volume. Thus, in the SI system, the moduli $c_{\alpha\beta}$, as well as the stresses σ_{ij} , are measured in N/m^2 , whereas the moduli $c_{\alpha\beta}^s$, as well as the surface stresses σ_{ij}^s , are measured in N/m . Experimental data also indicate that the values of the corresponding surface and bulk quantities differ in such a way that they are comparable $c_{\alpha\beta} \sim c_{\alpha\beta}^s/d$ with typical spatial sizes d of the order 10^{-9} (m) and less. In our problem such a parameter is the specific size of inclusions or pores, and so we expect that the surface or interface effects will have an influence only if pores or inclusions are nanoscale.

Then, to ensure the accuracy of the finite element computations due to the smallness of the geometric sizes of inclusions, here it is convenient to make a transition to the dimensionless coordinates and parameters. For example, we can choose the following characteristic dimensional parameters: the minimum size a of the pores or inclusions, the stiffness modulus $c = c_{11}^E$, and the dielectric permittivity constant $\varepsilon = \varepsilon_{11}^S$. Then we can introduce the following notations:

$$\hat{x} = x/a, \hat{u} = u/a, \hat{\varphi} = \varphi/(E_d a), \quad E_d = \sqrt{c/\varepsilon}, \quad (2.21)$$

$$\hat{\mathbf{c}}^E = \mathbf{c}^E/c, \quad \hat{\boldsymbol{\epsilon}}^S = \boldsymbol{\epsilon}^S/\varepsilon, \quad \hat{\mathbf{e}} = \mathbf{e}E_d/c, \quad \hat{\mathbf{c}}^s = \mathbf{c}^s/(ac), \quad (2.22)$$

$$\hat{\mathbf{T}} = \mathbf{T}/c, \quad \hat{\mathbf{E}} = \mathbf{E}/E_d, \quad \hat{\mathbf{D}} = \mathbf{D}E_d/c, \quad \hat{\mathbf{T}}^s = \mathbf{T}^s/(ac). \quad (2.23)$$

Thus, problem (2.4), (2.5), (2.7), (2.8), (2.10) can be solved in dimensionless form for the variables (2.21)–(2.23) marked with the ‘hat’ symbol. Then after solving this problem we can return back to dimensional quantities.

2.4 Finite Element Modelling

For solving piezoelectric problems (2.4), (2.5), (2.7), (2.8), (2.10) with (2.12), (2.13) or with (2.14)–(2.18), we can pass to their weak statements and use classical finite element techniques. Let Ω_h be the region filled by the finite element mesh, $\Omega_h \subseteq \Omega$, $\Omega_h = \Omega_h^{(1)} \cup \Omega_h^{(2)}$, $\Omega_h^{(j)} \approx \Omega^{(j)}$, $\Omega_h = \cup_k \Omega^{ek}$, where Ω^{ek} is a separate piezoelectric finite element with the number k . Let also Γ_h^s be a finite element mesh from surface elements conformable with the volume mesh Ω_h , $\Gamma_h^s = \Omega_h^{(1)} \cap \Omega_h^{(2)}$, $\Gamma_h^s \approx \Gamma^s$, $\Gamma_h^s = \cup_m \Gamma_s^{em}$, Γ_s^{em} is a separate elastic surface finite element with number m and the elements Γ_s^{em} are the edges of the suitable volume elements Ω^{ek} located on the interphase boundaries.

We will use the classic Lagrangian or serendipity volume finite elements with nodal degrees of freedom of displacements and electric potentials. Note that due to the structure of the surface mechanical fields, for the elements Γ_s^{em} we can use standard shell or plate elements with elastic membrane stresses options, i.e., only with displacements nodal degrees of freedom. For these elements, we can take a fictitious unit thickness so that the surface moduli in (2.8) can be determined from the product of specially defined volume moduli and shell thickness.

For static piezoelectric problems, we can find the approximate solution $\{\mathbf{u}_h \approx \mathbf{u}, \varphi_h \approx \varphi\}$ at the finite element mesh Ω_h in the form

$$\mathbf{u}_h(\mathbf{x}) = \mathbf{N}_u^T(\mathbf{x}) \cdot \mathbf{U}, \quad \varphi_h(\mathbf{x}) = \mathbf{N}_\varphi^T(\mathbf{x}) \cdot \Phi, \quad (2.24)$$

where \mathbf{N}_u^T is the matrix of the basic or form functions for displacements, \mathbf{N}_φ^T is the row vector of the basic functions for the electric potentials, \mathbf{U} is the vector of nodal displacements and Φ is the vector of nodal electric potentials.

According to usual approach, we approximate the continuum weak statement of the piezoelectric problem in finite-dimensional spaces related to the system of basic functions \mathbf{N}_u^T , \mathbf{N}_φ^T . Substituting (2.24) and similar representations for the projecting functions into the weak statement of the piezoelectric problem for Ω_h , we get the following finite element system

$$\mathbf{K}_{uu} \cdot \mathbf{U} + \mathbf{K}_{u\varphi} \cdot \Phi = \mathbf{F}_u, \quad (2.25)$$

$$-\mathbf{K}_{u\varphi}^* \cdot \mathbf{U} + \mathbf{K}_{\varphi\varphi} \cdot \Phi = \mathbf{F}_\varphi, \quad (2.26)$$

Here, $\mathbf{K}_{uu} = \sum^a \mathbf{K}_{uu}^{ek}$, $\mathbf{K}_{u\varphi} = \sum^a \mathbf{K}_{u\varphi}^{ek}$, $\mathbf{K}_{\varphi\varphi} = \sum^a \mathbf{K}_{\varphi\varphi}^{ek}$ are the global matrices, obtained from the corresponding element matrices by ensemble operation (\sum^a).

The element matrices are given by the formulas

$$\mathbf{K}_{uu}^{ek} = \mathbf{K}_{\Omega uu}^{ek} + \mathbf{K}_{\Gamma uu}^{ek} \quad (2.27)$$

$$\mathbf{K}_{\Omega uu}^{ek} = \int_{\Omega^{ek}} \mathbf{B}_u^{eT} \cdot \mathbf{c}^E \cdot \mathbf{B}_u^e d\Omega, \quad \mathbf{K}_{\Gamma uu}^{ek} = \int_{\Gamma_s^{ek}} \mathbf{B}_{su}^{eT} \cdot \mathbf{c}^S \cdot \mathbf{B}_{su}^e d\Gamma \quad (2.28)$$

$$\mathbf{K}_{\varphi\varphi}^{ek} = \int_{\Omega^{ek}} \mathbf{B}_\varphi^{eT} \cdot \boldsymbol{\varepsilon}^S \cdot \mathbf{B}_\varphi^e d\Omega, \quad \mathbf{K}_{u\varphi}^{ek} = \int_{\Omega^{ek}} \mathbf{B}_u^{eT} \cdot \mathbf{e}^T \cdot \mathbf{B}_\varphi^e d\Omega \quad (2.29)$$

$$\mathbf{B}_u^e = \mathbf{L}(\nabla) \cdot \mathbf{N}_u^{eT}, \quad \mathbf{B}_\varphi^e = \nabla \mathbf{N}_\varphi^{eT}, \quad \mathbf{B}_{su}^e = \mathbf{L}(\nabla^s) \cdot \mathbf{A} \cdot \mathbf{N}_u^{eT}, \quad (2.30)$$

where \mathbf{N}_u^{eT} , \mathbf{N}_φ^{eT} are the matrix and the row vector of approximating basic functions, respectively, defined at separate finite elements. The vectors \mathbf{F}_u , \mathbf{F}_φ in (2.25), (2.26) are obtained from the corresponding boundary conditions (2.10) with (2.12), (2.13) or with (2.14)–(2.18).

The matrices $\mathbf{K}_{\Gamma uu}$ and $\mathbf{K}_{\Gamma uu}^{ek}$, defined by the surface stresses, are similar to the stiffness matrices for surface or interphase elastic membranes. Hence, for implementing the finite element piezoelectric analysis for the bodies with mechanical surface and interphase effects, it is necessary to have surface or interphase structural membrane elements along with ordinary solid piezoelectric finite elements.

2.5 Modelling of Representative Volume Elements

The presented approaches were implemented in the finite element software ANSYS for porous piezoceramic composites. The representative volume element $\hat{\Omega}$ in dimensionless coordinates was taken in a shape of cube divided in $\hat{L} \times \hat{L} \times \hat{L}$ geometrically equal small cubes, which were 8-node hexahedral structured solid finite elements SOLID5. As a result, in the grand cube $\hat{\Omega}$ there were n^3 hexahedral finite elements of the size $\hat{l} = \hat{L}/n$, where n was an integer. Here, we assume the following dimensional geometric values: $L = a\hat{L}$, $l = a\hat{l}$, $a = l$, i.e., the parameter a is the size of a separate finite element, and thus for a nanoporous structure the value a is the nanosize of smallest pore.

In the obtained two-phase composite, the finite elements of the first phase had material properties of the original piezoelectric material, and the pores had negligibly small material moduli. Then the elements with the pore properties were selected by the simple random method. It can be noted that such model is easy to build but it does not support the connectivity of the elements of the first phase and does not reflect the connectivity structure of the elements of the second phase (closed or open pores). Other methods that support the connectivity of the skeleton consisting of the

elements of the first phase or supporting the cluster properties for the elements of the second phase are described in (Nasedkin and Shevtsova 2013; Kudimova et al. 2018a, b; Kurbatova et al. 2018; Nasedkin and Eremeyev 2014; Nasedkin 2015).

For automatic coating of the internal boundaries of the pores, the algorithm similar to the one described in (Nasedkin et al. 2014; Nasedkin and Kornievsky 2017a, b) has been used. At first the finite elements with the pore material properties were selected. Then the external boundaries of the array of elements with the pore properties were covered by target contact elements TARGE170 using the command TSHAP, QUAD. Hence, the edges of all porous finite elements lying on the external surfaces of the set of these elements got covered by four node contact elements (TARGE170 of the shape QUAD). Then the contact elements, located on the external border of the representative volume, were deleted and the remaining finite elements were substituted by the four node shell elements SHELL63 with the membrane capabilities. As a result, all contact boundaries, where piezoelectric structural elements were in contact with pores, had been coated by the membrane finite elements for the simulation of the surface stresses effect.

We note that in order to define a membrane element in ANSYS, it is necessary to specify the stiffness moduli $c_{\alpha\beta}^m$ and the thickness h^m . As it was noted in (Nasedkin and Kornievsky 2017a, b), the membrane element in ANSYS can be used as the interface element, obtained when taking into account conditions (2.7), (2.8), when $c_{\alpha\beta}^s = h^m c_{\alpha\beta}^m$. Therefore, in ANSYS computations, the important values are the products of the stiffness moduli $c_{\alpha\beta}^m$ of the membrane element by its thickness h^m , and not the values of $c_{\alpha\beta}^m$ and h^m separately. In contrast to (Nasedkin and Kornievsky 2017a, b), here, according to the previous section, the representative volume was defined in dimensionless way where the edge of one finite element was equal to one. Therefore, the dimensioning by space parameter was equal to the minimal size of the element of the second phase a . As there is not enough data on the values of the surface moduli for different materials and this data is often contradictory, then in accordance with the investigations on other materials in the case of nanoporous piezoceramics, it was assumed that the surface stiffness moduli were connected to the volume moduli of piezoceramics by the formula $c_{\alpha\beta}^s = l_c c_{\alpha\beta}$, where $l_c = 10^{-10}$ (m). Let us also assume that $h^m = a$, $c_{\alpha\beta}^m = k^s c_{\alpha\beta}$, where k^s is the dimensionless coefficient. Then $c_{\alpha\beta}^s = h^m c_{\alpha\beta}^m = k^s a c_{\alpha\beta} = (k^s a / l_c) c_{\alpha\beta}^s$, i.e., $a = l_c / k^s$ and thus the coefficient k^s is inversely proportional to the minimal size of the pores a . Further in numerical experiments with constant surface moduli $c_{\alpha\beta}^s$ the coefficient k^s and the porosity p were varied. As it can be seen, the growth of k^s corresponds to the decrease of the minimal pore size a , where at $k^s > 1$ the value a becomes smaller than $l_c = 10^{-10}$ (m).

For the shell elements ANSYS SHELL181, it is necessary to ensure the anisotropy type, which corresponds to the anisotropy of the volume finite element. As it is known, the material properties of finite elements in ANSYS are set in the local element coordinate systems $Ox^{ek}y^{ek}z^{ek}$, whereas for the membrane element with number k the material properties in the plane $Ox^{ek}y^{ek}$ are important. For the cubic finite element with the cube elements, the edges of which are parallel to the coordinate axes of the main Cartesian coordinate system, the membrane elements can be located

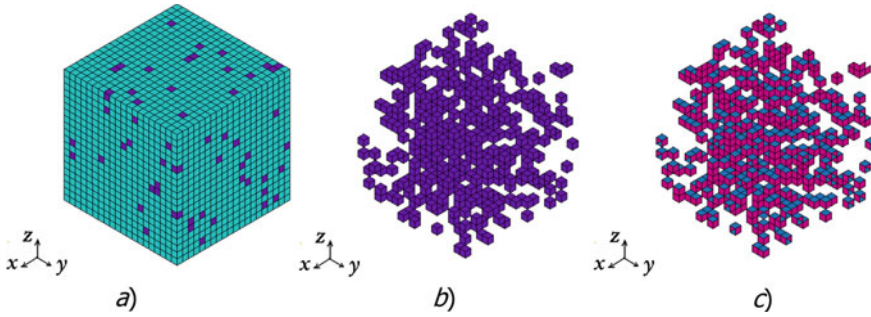


Fig. 2.1 Example of representative volume element: (a) all elements; (b) pores; (c) interphase boundaries

in the planes parallel to the planes Oxy , Oxz and Oyz . Thus, in the case of the piezoceramic material of 6 mm-class, in order to provide a correspondence between the volume anisotropy with the anisotropy of the membrane elements, it is necessary to vary the stiffness moduli of the membrane elements located perpendicular to the Oxy , which can be implemented by the way of the permutation of the initial stiffness coefficients by the rows and columns, corresponding to the axes z and y .

One example of the representative volumes is the representative volume, which consists of $20 \times 20 \times 20$ elements ($n = 20$) or the porosity $p = 5\%$, is shown in Fig. 2.1, where on the left the whole volume is shown (Fig. 2.1a); the middle figure illustrates the elements of the second phase (Fig. 2.1b); and on the right the interface membrane elements are shown (Fig. 2.1c). At that the membrane elements located perpendicular to the plane Oxy are shown in crimson, and the elements located parallel to the plane Oxy are shown in blue.

At the next stage, problems (2.4), (2.5), (2.7), (2.8), (2.10) were solved in ANSYS package. Then in the ANSYS postprocessor, the average stresses were calculated according to (2.11) both over solid and surface finite elements. In the end, using formulas (2.12)–(2.16) for the averaged stresses and electric fluxes, the effective moduli of porous piezoceramic materials with surface stresses were obtained.

We emphasize that as the pores were chosen with the help of the random number generator, every launch of the program will give different distribution of these elements. Therefore, for different location of the pores, the total area of the membranes Γ^s will change and the total stiffness of the volume will also change. However, for a not very large porosity p these effects will not have significant effect on the values of the effective moduli for each new launch of the program.

2.6 Results and Discussion

As an example we consider nanoporous piezoceramic material (material of 6 mm class). The skeleton material is the ferroelectric piezoceramics PZT-8 with the

following bulk moduli: $c_{11}^E = 14.68 \cdot 10^{10}$, $c_{12}^E = 8.108 \cdot 10^{10}$, $c_{13}^E = 8.105 \cdot 10^{10}$, $c_{33}^E = 13.17 \cdot 10^{10}$, $c_{44}^E = 3.135 \cdot 10^{10}$ (N/m²), $e_{31} = -3.875$, $e_{33} = 13.91$, $e_{15} = 10.34$ (C/m²), $\varepsilon_{11}^S = 904\varepsilon_0$, $\varepsilon_{33}^S = 561\varepsilon_0$, $\varepsilon_0 = 8.85 \cdot 10^{-12}$ (F/m). For the pores, the material constants (marked by the superscript p) were chosen equal to the following values: $c_{\alpha\beta}^{Ep} = \chi c_{\alpha\beta}^E$; $e_{i\alpha}^p = \chi e_{i\alpha}$; $\chi = 1 \cdot 10^{-10}$; $\varepsilon_{11}^{Sp} = \varepsilon_{33}^{Sp} = \varepsilon_0$.

For the analysis of the influence of the porosity and surface effect on the effective moduli, we have carried out the calculations of the effective moduli for a fixed number of the elements $n_l = 20$ along the axes of the representative volume, but for various porosity p and various but not very large values of the multiplier k^s . The results of the calculations are presented in Fig. 2.2, 2.3, 2.4 and 2.5. Here and after $r(\dots)$ denotes the relative values of the effective properties, with respect to the corresponding values of the moduli for zero porosity. For example, $r(c_{11}) = c_{11}^{\text{eff}}/c_{11}$, where c_{11}^{eff} is the effective stiffness modulus for the nanoporous PZT ceramics, which takes the surface stress into account, $c_{11} = c_{11}^E$ is the value of the stiffness modulus for an ordinary material of piezoceramics and so on. The curves 1 correspond to the

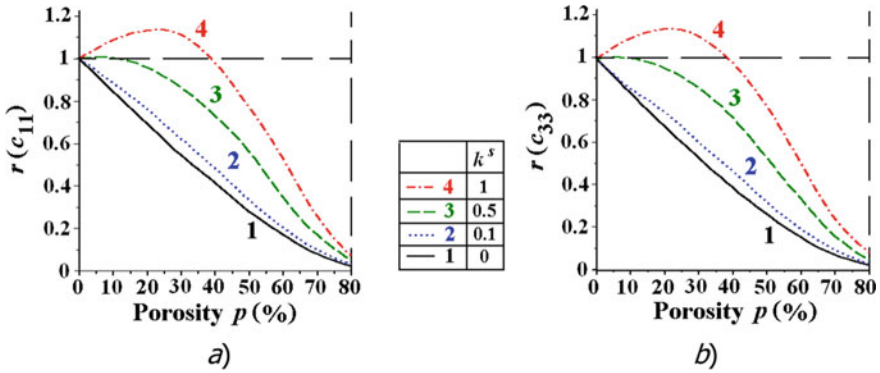


Fig. 2.2 Dependencies of the relative effective moduli c_{11}^{eff} (a) and c_{33}^{eff} (b) versus porosity

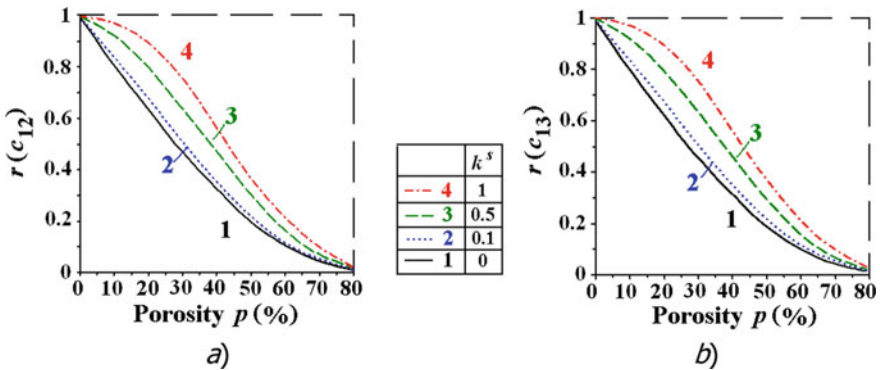


Fig. 2.3 Dependencies of the relative effective moduli c_{12}^{eff} (a) and c_{13}^{eff} (b) versus porosity

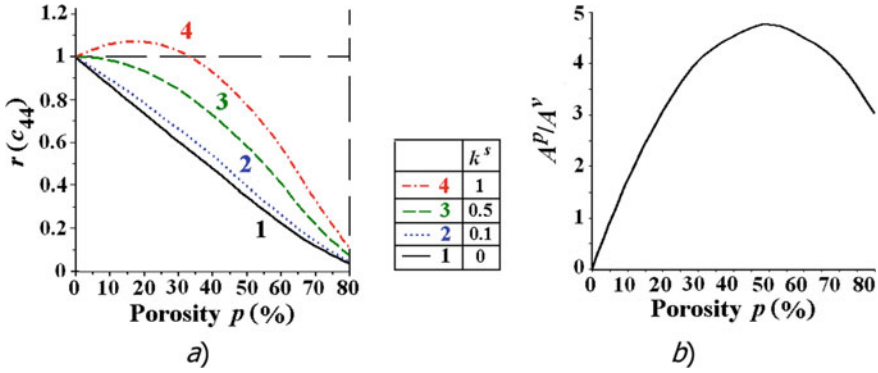


Fig. 2.4 Dependencies of the relative effective modulus c_{44}^{eff} (a) and area of interface A^P (b) versus porosity

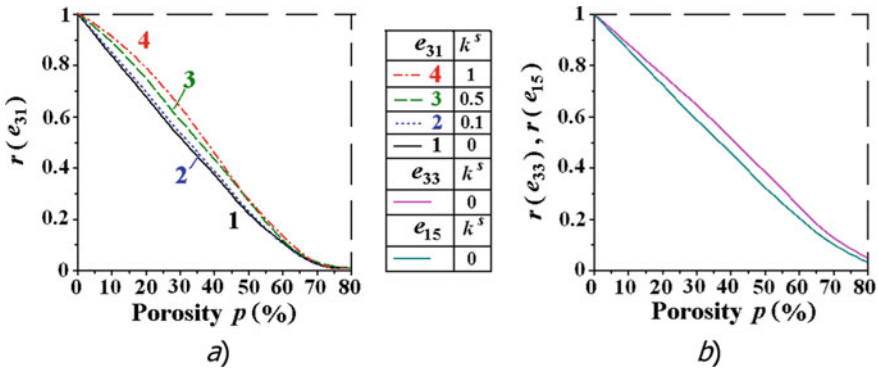


Fig. 2.5 Dependencies of the relative effective piezomoduli $e_{i\alpha}^{\text{eff}}$ versus porosity

case $k^s = 0$, the curves 2 correspond to the case $k^s = 0.1$, the curves 3 correspond to the case $k^s = 0.5$, and the curves 4 correspond to the case $k^s = 1$.

As these figures illustrate, for relatively small values of the multiplier k^s (curves 1 and 2) the surface stresses have relatively small influence on the stiffness moduli. However, for any porosity the surface stresses increase the effective stiffness of porous material. Moreover, here there is the possibility of the cases, when the nanoporous material will have greater stiffness than the corresponding dense material. Such situation can be observed for $k^s = 1$ for the stiffness moduli c_{11}^{eff} , c_{33}^{eff} , and c_{44}^{eff} with the porosity $p \leq 33\%$. Meanwhile, the stiffness moduli c_{12}^{eff} and c_{13}^{eff} do not exceed the values $c_{12} = c_{12}^E$ and $c_{13} = c_{13}^E$ correspondingly, even when $k^s = 1$.

As it was noted in (Nasedkin and Kornievsky 2017a, b; Duan et al. 2006, 2008; Eremeyev 2016; Eremeyev and Morozov 2010) and other works, the porosity and the surface stresses have opposite effects on the effective stiffness. It is obvious that the porosity growth leads to the decrease in the stiffness moduli, whereas the surface

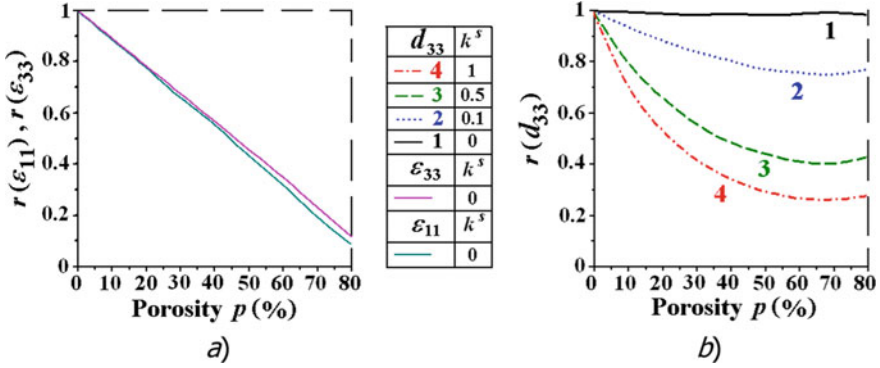


Fig. 2.6 Dependencies of the relative effective dielectric permittivities $\varepsilon_{ii}^{\text{eff}}$ (a) and piezomodulus d_{33}^{eff} (b) versus porosity

stresses increase the stiffness. For the nanoporous materials the surface stresses will grow considerably for large values of k^s , which is equivalent to the very small nanosized of pores. Moreover, for nanoporous materials initial porosity growth will lead to the growth of the area of the boundaries of the pores with surface stresses. For example, from the graph in Fig. 2.4b, it can be seen that for the considered cubic structure of the representative volume the areas of the interface boundaries grow fast at the beginning, and then their growth becomes smaller with the maximum at $p = 50\%$. The trends noted above can explain the phenomenon of the stiffness moduli increase in the nanomaterials with not very large porosity and very small nanosized of the pores [see (Nasedkin and Kornievsky 2017a, b; Duan et al. 2006, 2008; Eremeyev 2016; Eremeyev and Morozov 2010)].

Meanwhile, the uncoupled surface stresses have much less effect on the effective piezomoduli e_{31}^{eff} , e_{33}^{eff} , and e_{15}^{eff} (Fig. 2.5) and almost do not influence on the dielectric permittivities κ_{11}^{eff} and κ_{33}^{eff} (Fig. 2.6a).

As it can be seen from Fig. 2.5, the influence of the surfaces stresses is significant mostly for the relative values of the transverse piezomodulus $r(e_{31})$, whereas the curves for other piezomoduli and dielectric permittivities (Fig. 2.6a) for different multipliers k^s ($0 \leq k^s \leq 1$) almost coincide and look like one curve both in Fig. 2.5b and Fig. 2.6a.

It is obvious that the effective piezomoduli and dielectric permittivities should change more significantly, if instead of uncoupled mechanical surface stresses we take into account fully or partially coupled electromechanical surface effects using the models (Eremeyev and Nasedkin 2017; Nasedkin and Eremeyev 2014; Nasedkin 2017).

It is interesting to note that the behaviour of the thickness piezomodulus d_{33}^{eff} for the porous piezoceramic with surface stresses (Fig. 2.6b, curves 2–4), considerably differ from the behaviour of the same piezomodulus for ordinary porous piezoceramic (Fig. 2.6b, curve 1). Whereas for ordinary porous piezoceramic, the thickness piezomodulus d_{33}^{eff} almost does not depend on the porosity (Nasedkin and Shevtsova

2011, 2013; Getman and Lopatin 1996; Hikita et al. 1983; Rybyanets 2011), the fact of taking the surface stresses into account leads to the decrease of effective piezomodulus d_{33}^{eff} , which starts to increase only for highly porous piezoceramics.

The described methodology could be also applied for mixed anisotropic nanostructured composites with other connectivity types for different physico-mechanical fields, such as poroelastic, thermoelastic, magnetoelectric or magnetoelectroelastic and other types of nanocomposites. In the obtained two-phase composite, the finite elements of the first phase had material properties of the original piezoelectric material, and the pores had negligibly small material moduli. Then the elements with the pore properties were selected by the simple random method. It can be noted that such model is easy to build but it does not support the connectivity of the elements of the first phase and does not reflect the connectivity structure of the elements of the second phase (closed or open pores). Other methods that support the connectivity of the skeleton consisting of the elements of the first phase or supporting the cluster properties for the elements of the second phase are described in (Nasedkin and Shevtsova 2013; Kudimova et al. 2018a, b; Kurbatova et al. 2018; Nasedkin 2015; Nasedkin et al. 2014).

2.7 Conclusion

In the paper, the problems of the effective properties determination for the two phase piezoelectric composite with surface (interface) stresses on the interphase boundaries were considered. The applied interface conditions describe the size effects for nanostructured composites. The presented approach can be used for porous electroelastic materials, when the second phase is the set of pores, which are simulated as piezoelectric materials with negligibly small stiffness moduli and piezomodulil. The model for the calculation of the effective moduli of nanoporous ferroelectric piezoceramics PZT-8 was developed. The homogenization problems were solved numerically in finite element package ANSYS for the representative volume with uniform meshing in hexahedral piezoelectric elements with random porosity. In the constructed volume at the interface boundaries additionally, the elastic membrane elements were generated, which simulated the conditions at the interface.

For highly porous piezoelectric materials, the presented results should be corrected, due to the use of the model of the representative volume with stochastic porosity, which does not support the connectivity of the skeleton elements and does not reflect the connectivity structure for the second phase (closed or open porosity).

Further investigations can be connected with the analysis of the influence of the representative volume connectivity structures on the effective moduli of nanoporous piezoelectric materials. Such analysis can be carried out similarly to the one presented in (Nasedkin 2019; Nasedkin and Shevtsova 2011, 2013; Chatzigeorgiou et al. 2015; Kudimova et al. 2018a, b) for the composites without interface effects . Other actual

problems are the problems of the development of surface electromechanical coupled finite elements, which can be used to take into account the surface interface effects in more details in the homogenization problems for nanostructured piezoelectric composites.

Acknowledgements This research was supported by the Ministry of Science and Higher Education of the Russian Federation, project No. 9.1001.2017/4.6.

References

- Alibert JJ, Seppecher P, dell'Isola F (2003) Truss modular beams with deformation energy depending on higher displacement gradients. *Math Mech Solids* 8(1)
- Barchiesi E, dell'Isola F, Laudato M, Placidi L, Seppecher P (2018) A 1D continuum model for beams with pantographic microstructure: asymptotic micro-macro identification and numerical results. In: *Advances in mechanics of microstructured media and structures*. Springer, Cham, pp 43–74
- Camar-Eddine M, Seppecher P (2001) Non-local interactions resulting from the homogenization of a linear diffusive medium. *Comptes Rendus L'académie Sci-Ser I-Math* 332(5):485–490
- Chatzigeorgiou G, Javili A, Steinmann P (2015) Multiscale modelling for composites with energetic interfaces at the micro-or nanoscale. *Math Mech Solids* 20(9):1130–1145
- Chen T (2008) Exact size-dependent connections between effective moduli of fibrous piezoelectric nanocomposites with interface effects. *Acta Mech* 196:205–217
- Cricri G, Perrella M, Sessa S, Valoroso N (2015) A novel fixture for measuring mode III toughness of bonded assemblies. *Eng Fract Mech* 138:1–18. <https://doi.org/10.1016/j.engfracmech.2015.03.019>
- Dai S, Gharbi M, Sharma P, Park HS (2011) Surface piezoelectricity: size effects in nanostructures and the emergence of piezoelectricity in non-piezoelectric materials. *J Appl Phys* 110:104305–104307
- dell'Isola F, Seppecher P, Alibert JJ, Lekszycki T, Grygoruk R, Pawlikowski M, Steigmann D, Giorgio I, Andreaus U, Turco E, Gołaszewski M, Rizzi N, Boutin C, Eremeyev VA, Misra A, Placidi L, Barchiesi E, Greco L, Cuomo M, Cazzani A, Della Corte A, Battista A, Scerrato D, Eremeeva IZ, Rahali Y, Ganghoffer JF, Müller W, Ganzosch G, Spagnuolo M, Phaff A, Barcz K, Hoschke K, Negggers J, Hild F (2019a) Pantographic metamaterials: an example of mathematically driven design and of its technological challenges. *Continuum Mech Thermodyn* 31(4):851–884
- dell'Isola F, Seppecher P, Spagnuolo M, Barchiesi E, Hils F, Lekszycki T, Giorgio I, Placidi L, Andreaus U, Cuomo M, Eugster SR, Pfaff A, Hoschke K, Langkemper R, Turco E, Sarikaya R, Misra A, De Angelo M, D'Annibale F, Bouterf A, Pinelli X, Misra A, Desmorat B, Pawlikowski M, Dupuy C, Scerrato D, Peyre P, Laudato M, Manzari L, Göransson P, Hesch C, Hesch S, Franciosi P, Dirrenberger J, Maurin F, Vangelatos Z, Grigoropoulos C, Melissinaki V, Farsari M, Muller W, Abali BE, Liebold C, Ganzosch G, Harrison P, Drobnicki R, Igumnov L, Alzahrani F, Hayat T (2019b) Advances in pantographic structures: design, manufacturing, models, experiments and image analyses. *Continuum Mech Thermodyn* 31(4):1231–1282
- dell'Isola F, Placidi L (2011) Variational principles are a powerful tool also for formulating field theories. In: *Variational models and methods in solid and fluid mechanics*. Springer, Vienna, pp 1–15
- dell'Isola F, Seppecher P, Placidi L, Barchiesi E, Misra A (2020) 8 least action and virtual work principles for the formulation of generalized continuum models. *Discret Contin Models Complex Metamaterials* 327

- Duan HL, Wang J, Karihaloo BL, Huang ZP (2006) Nanoporous materials can be made stiffer than non-porous counterparts by surface modification. *Acta Mater* 54:2983–2990
- Duan HL, Wang J, Karihaloo BL (2008) Theory of elasticity at the nanoscale. *Adv Appl Mech* 42:1–68
- Eremeyev VA (2016) On effective properties of materials at the nano- and microscales considering surface effects. *Acta Mech* 227:29–42
- Eremeyev V, Morozov N (2010) The effective stiffness of a nanoporous rod. *Dokl Phys* 55(6):279–282
- Eremeyev VA, Nasedkin AV (2017) Mathematical models and finite element approaches for nano-sized piezoelectric bodies with uncoupled and coupled surface effects. In: Sum-batyan, M.A. (ed.) *Wave dynamics and composite mechanics for microstructured materials and metamaterials. series advanced structured materials*, vol 59. Springer, Singapore, pp 1–18
- Fang XQ, Zhu CS, Liu JX, Liu XL (2018) Surface energy effect on free vibration of nano-sized piezoelectric double-shell structures. *Phys B* 529:41–56
- Getman I, Lopatin S (1996) Theoretical and experimental investigation of the porous PZT ceramics. *Ferroelectrics* 186:301–304
- Gu ST, Qin L (2014) Variational principles and size-dependent bounds for piezoelectric inhomogeneous materials with piezoelectric coherent imperfect interfaces. *Int J Eng Sci* 78:89–102
- Gu ST, Liu JT, He QC (2014a) Piezoelectric composites: Imperfect interface models, weak formulations and benchmark problems. *Comp Mater Sci* 94:182–190
- Gu ST, Liu JT, He QC (2014b) The strong and weak forms of a general imperfect interface model for linear coupled multifield phenomena. *Int J Eng Sci* 85:31–46
- Gu ST, He QC, Pensee V (2015) Homogenization of fibrous piezoelectric composites with general imperfect interfaces under anti-plane mechanical and in-plane electrical loadings. *Mech Mater* 88:12–29
- Hikita K, Yamada K, Nishioka M, Ono M (1983) Piezoelectric properties of the porous PZT and the porous PZT composite with silicone rubber. *Ferroelectrics* 49:265–272
- Huang GY, Yu SW (2006) Effect of surface piezoelectricity on the electromechanical behaviour of a piezoelectric ring. *Phys Status Solidi B* 243(4):R22–R24
- Javili A, McBride A, Mergheima J, Steinmann P, Schmidt U (2013) Micro-to-macro transitions for continua with surface structure at the microscale. *Int J Solids Struct* 50:2561–2572
- Kudimova AB, Nadolin DK, Nasedkin AV, Oganessian PA, Soloviev AN (2018) Finite element homogenization models of bulk mixed piezocomposites with granular elastic inclusions in ACELAN package. *Mater Phys Mech* 37(1):25–33
- Kudimova AB, Nadolin DK, Nasedkin AV, Nasedkina AA, Oganessian PA, Soloviev AN (2018) Models of porous piezocomposites with 3–3 connectivity type in ACELAN finite element package. *Mater Phys Mech* 37(1):16–24
- Kurbatova NV, Nadolin DK, Nasedkin AV, Oganessian PA, Soloviev AN (2018) Finite element approach for composite magneto-piezoelectric materials modeling in ACELAN-COMPOS package. In: Altenbach, H, Carrera, E, Kulikov, G. (eds.) *Analysis and modelling of advanced structures and smart systems. Series advanced structured materials*, vol 81. Springer, Singapore, pp 69–88
- Malakooti MH, Sodano HA (2013) Multi-inclusion modeling of multiphase piezoelectric composites. *Compos Part B* 47:181–189
- Milton GW, Seppecher P, Bouchitté G (2009) Minimization variational principles for acoustics, elastodynamics and electromagnetism in lossy inhomogeneous bodies at fixed frequency. *Proc R Soc A Math Phys Eng Sci* 465(2102):367–396
- Nasedkin AV (2015) Finite element design of piezoelectric and magnetoelectric composites with use of symmetric quasidefinite matrices. In: Parinov IA, Chang S-H, Theerakulpisut S (eds) *Advanced materials—studies and applications*. Nova Science Publ, NY, pp 109–124
- Nasedkin AV (2017) Some homogenization models of nanosized piezoelectric composite materials of types ceramics—pores and ceramics—ceramics with surface effects. In: Güemes A, Benjeddou A, Rodellar J, Leng J (eds) *VIII ECCOMAS thematic conf. on smart structures and materials*,

- VI Int. conf. on smart materials and nano-technology in engineering—SMART 2017. CIMNE, Barcelona, Spain, pp 1137–1147
- Nasedkin AV (2019) Analysis of surface stress influence on the effective properties of nano-porous piezocomposites. *Probl Prochnosti I Plast-Probl Strength Plast* 81(1):5–18
- Nasedkin AV, Eremeyev VA (2014) Harmonic vibrations of nanosized piezoelectric bodies with surface effects. *ZAMM* 94:878–892
- Nasedkin AV, Kornievsky AS (2017) Finite element modeling and computer design of anisotropic elastic porous composites with surface stresses. In: Sumbatyan MA (ed.) *Wave dynamics and composite mechanics for microstructured materials and metamaterials*. Series advanced structured materials, vol 59. Springer, Singapore, pp 107–122
- Nasedkin AV, Kornievsky AS (2017) Finite element modeling of effective properties of elastic materials with random nanosized porosities. *Vycisl. meh. splos. Sred-Computational. Continuum Mech* 10(4):375–387
- Nasedkin AV, Shevtsova MS (2011) Improved finite element approaches for modeling of porous piezocomposite materials with different connectivity. In: Parinov IA (ed) *Ferroelectrics and superconductors: properties and applications*. Nova Science Publ, New York, pp 231–254
- Nasedkin AV, Shevtsova MS (2013) Multiscale computer simulation of piezoelectric devices with elements from porous piezoceramics. In: Parinov IA, Chang S-H (eds) *Physics and mechanics of new materials and their applications*. Nova Science Publ, New York, pp 185–202
- Nasedkin AV, Nasedkina AA, Remizov VV (2014) Finite element modeling of porous thermoelastic composites with account for their microstructure. *Vycisl. meh. splos. sred-Computational. Continuum Mech* 7(1):100–109
- Pan XH, Yu SW, Feng XQ (2011) A continuum theory of surface piezoelectricity for nanodielectrics. *Sci China Phys Mech Astron* 54:564–573
- Park HS, Devel M, Wang Z (2011) A new multiscale formulation for the electromechanical behavior of nanomaterials. *Comput Methods Appl Mech Eng* 200:2447–2457
- Pideri C, Seppelcher P (1997) A second gradient material resulting from the homogenization of an heterogeneous linear elastic medium. *Continuum Mech Thermodyn* 9(5):241–257
- Placidi L, Misra A, Barchiesi E (2018) Two-dimensional strain gradient damage modeling: a variational approach. *Z Angew Math Phys* 69(3):1–19
- Placidi L, Barchiesi E, Misra A (2018a) A strain gradient variational approach to damage: a comparison with damage gradient models and numerical results. *Math Mech Compl Syst* 6(2):77–100
- Placidi L, Rosi G, Barchiesi E (2019) Analytical solutions of 2-dimensional second gradient linear elasticity for continua with cubic-d 4 microstructure. In: *New achievements in continuum mechanics and thermodynamics*. Springer, Cham, pp 383–401
- Placidi L, dell'Isola F, Barchiesi E (2020) Heuristic homogenization of Euler and pantographic beams. In *Mechanics of fibrous materials and applications*. Springer, Cham, pp 123–155
- Rybyanets AN (2011) Porous piezoceramics: theory, technology, and properties. *IEEE Trans Ultrason Ferroelectr Freq Control* 58:1492–1507
- Serpieri R, Sessa S, Rosati L (2018) A MITC-based procedure for the numerical integration of a continuum elastic-plastic theory of through-the-thickness-jacketed shell structures. *Compos Struct* 191:209–220. <https://doi.org/10.1016/j.compstruct.2018.02.031>
- Sessa S, Marmo F, Rosati L (2015) Effective use of seismic response envelopes for reinforced concrete structures. *Earthquake Eng Struct Dynam* 44(14):2401–2423. <https://doi.org/10.1002/eqe.2587>
- Sessa S, Serpieri R, Rosati L (2017) A continuum theory of through-the-thickness jacketed shells for the elasto-plastic analysis of confined composite structures: theory and numerical assessment. *Compos B Eng* 113:225–242. <https://doi.org/10.1016/j.compositesb.2017.01.011>
- Sessa S, Marmo F, Rosati L, Leonetti L, Garcea G, Casciaro R (2018a) Evaluation of the capacity surfaces of reinforced concrete sections: eurocode versus a plasticity-based approach. *Meccanica* 53(6):1493–1512. <https://doi.org/10.1007/s11012-017-0791-1>

- Sessa S, Marmo F, Vaiana N, Rosati LA (2018b) Computational strategy for eurocode 8-compliant analyses of reinforced concrete structures by seismic envelopes. *J Earthquake Eng* <https://doi.org/10.1080/13632469.2018.1551161>
- Sessa S, Marmo F, Vaiana N, De Gregorio D, Rosati L (2019a) Strength hierarchy provisions for transverse confinement systems of shell structural elements. *Compos B Eng* 163:413–423. <https://doi.org/10.1016/j.compositesb.2019.01.018>
- Sessa S, Marmo F, Vaiana N, Rosati L (2019b) Probabilistic assessment of axial force–biaxial bending capacity domains of reinforced concrete sections. *Meccanica* 54(9):1451–1469. <https://doi.org/10.1007/s11012-019-00979-4>
- Spagnuolo M (2020) Circuit analogies in the search for new metamaterials: phenomenology of a mechanical diode. In: *Nonlinear wave dynamics of materials and structures*. Springer, Cham, pp 411–422
- Spagnuolo M, Franciosi P, dell’Isola F (2020) A Green operator-based elastic modeling for two-phase pantographic-inspired bi-continuous materials. *Int J Solids Struct* 188:282–308
- Spagnuolo M, Yildizdag ME, Andreas U, Cazzani AM (2021) Are higher-gradient models also capable of predicting mechanical behavior in the case of wide-knit pantographic structures? *Math Mech Solids* 26(1):18–29
- Turco E, dell’Isola F, Misra A (2019a) A nonlinear Lagrangian particle model for grains assemblies including grain relative rotations. *Int J Numer Anal Meth Geomech* 43(5):1051–1079
- Turco E, Misra A, Sarikaya R, Lekszycki T (2019b) Quantitative analysis of deformation mechanisms in pantographic substructures: experiments and modeling. *Continuum Mech Thermodyn* 31(1):209–223
- Turco E, Barchiesi E, Giorgio I, dell’Isola, F (2020) A Lagrangian Hencky-type non-linear model suitable for metamaterials design of shearable and extensible slender deformable bodies alternative to Timoshenko theory. *Int J Non-Linear Mech* 123
- Vaiana N, Sessa S, Marmo F, Rosati L (2019) Nonlinear dynamic analysis of hysteretic mechanical systems by combining a novel rate-independent model and an explicit time integration method. *Nonlinear Dyn* 98(4):2879–2901. <https://doi.org/10.1007/s11071-019-05022-5>
- Vaiana N, Capuano R, Sessa S, Marmo F, Rosati L (2021) Nonlinear dynamic analysis of seismically base-isolated structures by a novel OpenSees hysteretic material model. *Appl Sci* 11(3):900
- Wang Z, Zhu J, Jin XY, Chen WQ, Zhang Ch (2014) Effective moduli of ellipsoidal particle reinforced piezoelectric composites with imperfect interfaces. *J Mech Phys Solids* 65:138–156
- Wang KF, Wang BL, Kitamura T (2016a) A review on the application of modified continuum models in modeling and simulation of nanostructures. *Acta Mech Sin* 32:83–100
- Wang W, Li P, Jin F, Wang J (2016b) Vibration analysis of piezoelectric ceramic circular nanoplates considering surface and nonlocal effects. *Compos Struct* 140:758–775
- Xiao JH, Xu YL, Zhang FC (2011) Size-dependent effective electroelastic moduli of piezoelectric nanocomposites with interface effect. *Acta Mech* 222:59–67
- Zhao D, Liu JL, Wang L (2016) Nonlinear free vibration of a cantilever nanobeam with surface effects: semi-analytical solutions. *Int J Mech Sci* 113:184–195

Chapter 3

A Mathematical Model for Bone Cell Population Dynamics of Fracture Healing Considering the Effect of Energy Dissipation



Mahziyar Darvishi, Hooman Dadras, Mohammad Mahmoodi Gahrouei, Kiarash Tabesh, and Dmitry Timofeev

Abstract The importance of mechanical modeling has been increasing in recent years for almost every area of biological sciences. The process of bone recovery is one of the issues to be addressed within a mechanical framework. In this study, a model for the bone healing process is proposed taking into account the bone cell population as well as the effect of energy dissipation. Numerical simulations for bone under a cyclic external loading are performed in order to show predicting capabilities of the model.

Keywords Bone tissue · Bone healing · Cell population dynamics · Bone remodeling · Bone fracture healing · Energy dissipation · Mechanical modeling

3.1 Introduction

Developing mathematical models for biological phenomena is nowadays one of the most exciting research areas for scientists working on the field of modern applied mathematics. A model accurate enough can be a very powerful tool in understanding and anticipating functions of a biological system. In this study, we will focus on the bone capacity to repair itself when it is fractured, i.e. bone healing. Accurate description of this process is important for medical applications such as bone surgery or bone substitutes like prostheses, since it helps to avoid patient dependency (Sheidaei et al. 2019).

There are many factors which have to be taken into account for a proper description of the bone healing process. Such factors as, for instance, an interaction between osteoblasts and osteoclasts, and signal transmission through osteocytes are widely

M. Darvishi · H. Dadras · M. Mahmoodi Gahrouei · K. Tabesh
Department of Mechanical Engineering, Isfahan University of Technology, Isfahan, Iran

D. Timofeev (✉)
Dipartimento di Ingegneria e Scienze dell'Informazione e Matematica, Università degli Studi dell'Aquila, L'Aquila, Italy
e-mail: dmitry.timofeev@graduate.univaq.it

© Springer Nature Switzerland AG 2021
F. Marmo et al. (eds.), *Mathematical Applications in Continuum and Structural Mechanics*, Advanced Structured Materials 127,
https://doi.org/10.1007/978-3-030-42707-8_3

addressed in the literature (Klein-Nulend et al. 2012; Baiotto and Zidi 2004). But effects of osteophytes as well as stem cell responsibilities in the process have not been properly discussed yet. The more accurate and comprehensive the model is, the better one understands the healing process in bones. In this study, a model to describe healing process is presented improving the work in Giorgio et al. (2017d) by considering effects of energy dissipation as well as a width of a fracture gap.

Nowadays, bio-material implants in bone for big fractures are widely used in orthopedic, jaw, skull surgery, and dental implantation (Giorgio et al. 2017c) to replace a missing bone or to treat bone fractures. However, small cracks and gaps in a bone tissue are naturally being fixed during the process of healing, since the new bone cells would refill the gaps without any use of implanted materials and scaffolds.

Approximately 10–20% of bone mass is water. A significant proportion (30–40%) of the dry weight is constituted by organic components of an extra-cellular matrix and the remaining part (60–70%) consists of inorganic mineral salts such as micro-crystalline hydroxyapatite (Della Corte et al. 2019). Each bone cell has a specific effect on the healing process. Osteoblasts are derived from mesenchymal stem progenitors that are located close to the bone surface. They are growing cells which synthesize and secrete organic components of the matrix. Osteocytes act as a kind of mechanical sensors controlling calcium and phosphate levels in the microenvironment. They detect exerted mechanical forces and transform them into a biological activity (mechano-transduction). Osteocytes are in control of synthesis/resorption activities in bone tissues by sending a proper signal to adjacent cells. This is essential in establishing a connection between mechanical stimuli and bone healing. Osteoclasts are giant, motile cells with multiple nuclei and they play a major role in matrix resorption during bone growth and remodeling (Lekszycki and dell'Isola 2012). All of these factors have to be taken into account in order to develop a proper formal description of bone formation and resorption. The formulation of our model can be a link between what happens in a bone at the cellular level, and the macro-mechanical properties of a bone tissue (Della Corte et al. 2019).

The modeling problem for the mechanical behavior of living tissues has been confronted by many researchers. In this context, we can refer to the pioneering work by Wolff (1892). In recent years, the discovery of osteocytes led us to develop better and more advanced bone-tissue models. Bone healing studies are divided into the following two categories: the studies that consider the bone tissue at macro-scale and micro-level, respectively. Models assuming the linear Cauchy isotropic material were the simplest mechanical models at the macro-scale point of view which were capable to explain dry bone tissue under a constant load in a short period of time (Della Corte et al. 2019). A time-dependent theory for the remodeling in the case of a bone subjected to the daily loading history was presented using this concept (Lekszycki and dell'Isola 2012). In 2011, a continuum poro-elastic mixture model was presented including an interaction between bone tissues and biocompatible materials (Andreas et al. 2015). That model considered bone as a porous material and suggested an explanation of a stimulus in its formulation (Lekszycki and dell'Isola 2012). Also, a second gradient, two-solid, continuum mixture with variable masses was proposed to describe effects of microstructure on mechanically driven bone

remodeling mixed with bio-resorbable material and it is shown that the microstructural effects on the overall process of remodeling both natural bone and bio-material may be non-negligible (Madeo et al. 2012). The bone tissue synthesis and resorption were explained in a mixture model of bone tissue and bio-resorbable material including mass density. Later a new model was developed by Andreaus et al. (2015) providing a range of bio-mechanical parameters for residual regions of bio-materials which remain in remodeled bone. Another model investigated the mixture model of Lekszycki and dell'Isola (2012) with a biological stimulus of nonlocal nature playing a role in the feedback control process which governs the generation, transmission, and the effect on great relevance as the problem of the model (Giorgio et al. 2019).

In Park and Lakes (1986), Yang and Lakes (1982), the micromorphic continua was used for saturated bone. One of the important works which has been done at the micro-scale, is adding a rotational degree of freedom (Park and Lakes 1986).

Computational costs for numerical simulations at micro-scale are immense, so if the characterization of a representative elementary volume (REV) would be used in homogenization procedures, the method would be handy. Moreover, there is no need to propose any specific functions in this method to represent the amount of available surface for bone cells (Della Corte et al. 2019). We also refer to Marmo et al. (2020), Vaiana et al. (2019, 2021b), Serpieri et al. (2018), Sessa et al. (2018b), Greco et al. (2018), and Marmo et al. (2018c) for examples of alternative ways to handle the computational costs. Applications in civil engineering may also be found in Marmo et al. (2018a), Paradiso et al. (2019), Marmo et al. (2019, 2018b), Perricone et al. (2020), Vaiana et al. (2017), Cricri et al. (2015), Sessa et al. (2015), Sessa et al. (2019b, 2018a), Sessa et al. (2017), Sessa et al. (2019a), Vaiana et al. (2021a).

Bone is well known as one of the organs of our body which is responsible for damping and energy absorption. The soft collagen gives bones their elasticity and the ability to dissipate energy under mechanical deformation, and toughening mechanisms are active during crack propagation rather than crack initiation (Ritchie et al. 2009). In An et al. (2014), a bone-like material is studied which is structured by arranging hard platelets embedded in a soft matrix. In order to consider crack growth resistance, a model within the thermodynamic framework was developed taking into account microscopic deformation mechanisms (elastic and plastic deformations as well as damage). Experimental data presented in that work show a very good agreement with the proposed model. Another description was introduced by Elbanna and Carlson (2013) who developed a kinetic model with random properties assigned to fibrils, and that model examined the effect of loading rate using classical Bell's theory (Bell 1978). The results showed that large amounts of energy are lost at the molecular level. In addition, increasing the loading rate, which causes the system to move away from equilibrium, leads to higher strength and failure resistance (Lieou et al. 2013). As it is reported in Lanyon and Rubin (1984), Turner (1998), the energy dissipation may have an important and significant influence on the remodeling process. A poro-elastic analysis was performed on a simplified geometric model that was simulated with ABAQUS by looking into a variation of pressure and fluid velocity in pores with time and location. The evaluation of the dissipation energy stimulus demonstrates that it increases with low frequency range and saturates at the higher

frequencies (Kumar et al. 2011). In Giorgio et al. (2016), the phenomena of resorption and growth of bone tissue are studied by means of a numerical method based on finite elements. It considers stimulus as a linear combination of strain energy density and viscous dissipation. This model also takes into account a dissipation associated with the micromorphic variable controlling the porosity change. In order to have a better description for mechanical behavior of bone tissue at different scales, a constitutive model of bone bio-material is presented by Giorgio et al. (2017a). In this study, the second gradient model used for accounting size effects in visco-elastic material and the model is compared with a simpler one. The second gradient causes a delay for evolution process.

Mechanical properties affect bone healing as well as biological aspects and that's the reason why mathematical models in order to have predicting capabilities should consider both (George et al. 2018). Moreover, it is shown that mechanical contribution is more important at the beginning of bone reconstruction when high strain energy is developed with low bone density (George et al. 2019). There are also models having a bio-resorbable material in the gap part, and it is shown that the final distribution of Young's modulus does not have significant dependence on diffusion rate for small gaps (Lu and Lekszycki 2017). A continuum model is used to reproduce the behavior of bone tissue regeneration and growth inside a defect as a result of LIPUS treatment; both 2D and 3D cases are considered for bone growth simulations (Scala et al. 2017). In Lu and Lekszycki (2016), one can find models that introduce constitutive equation for Young's modulus evolution accounting for its dependence on nutrient concentration and a variable number of active cells. In this study, stimulus and energy dissipation are considered as mechanical parameters, while the three types of bone cells (osteoblast, osteocytes, and osteoclasts) with their specific functions are biological factors of the model. It will be demonstrated that the dissipation term has an important effect on stimulus and bone healing. Moreover, gap size, porosity, and the local density of cells are the other crucial factors of bone healing in this model. It is worth underlining here that for living tissue (or bone tissue in our specific case), the effect of microstructure is non-negligible, and it can be captured by modeling living material as a Cosserat or second-gradient material. Thus, bone tissue even in the absence of grafted materials can be regarded as metamaterial (Del Vescovo and Giorgio 2014) and models appropriate for metamaterials can be fruitfully exploited to describe biological phenomena characterized by the presence of (lattice) microstructure (Giorgio et al. 2017d, b).

Most of the researchers working in the field of bone fractures and toughness are acknowledged energy loss and have proven their results with experimental data. Moreover in this study, the next step will be taken toward advancing the science of mechanical behavior of bone by considering an energy loss while investigating the healing of a crack. Therefore, in order to achieve a more accurate prediction of bone fracture recovery, the energy loss has been introduced in the descriptive differential equations for bone density changes and its effect has been shown in the amount of stimulus. We assert that adding this gap size factor and considering the energy dissipation term both in stimulus and the energy equations made our model more accurate and appropriate to simulate the natural bone healing process.

For some historical information on development of higher-gradient continua, we can refer to dell’Isola et al. (2016), dell’Isola et al. (2014). Patient factors like the nutritional status of a patient (e.g. lack of calcium, phosphorus, and vitamins C and D), abnormal growth on the bone called osteophyte (Bednarczyk and Lekszycki 2016), and pharmacological factors are neglected in this model for the sake of simplicity (Webb and Tricker 2000).

The paper is organized as follows. First, we express the geometry of our model and loading conditions. Then, the ODEs system is proposed describing the time evolution of cells and bone density during the process of healing. The stimulus function is defined in the next part by considering the energy dissipation. After that, the mechanical framework and dissipation terms are discussed. Finally, we demonstrate the value of our work by comparing the results for two cases: in the presence and absence of energy dissipation. Also, it has been shown how important are the critical gap size and the dependence of healing to the fracture width. The results are presented with dynamic loading conditions.

3.2 The Model

3.2.1 The Main Assumptions

In this study, a rectangular 2D specimen of a living bone tissue with initial porosity $\varphi = 0.5$ is considered to undergo a cyclic compression loading. In Fig. 3.1, one can see a schematic for the specimen and boundary conditions. The loading has the following form:

$$f_x(t) = F_0 + F_1 \sin(\omega t). \quad (3.1)$$

The main assumptions accepted by the authors are the following:

- ‘stimulus’ is defined as a scalar field providing a connection between the sensor and actor cells. It is defined at every point of the bone and depends on the overall mechanical load and density of sensor cells;
- an actual state of the system at a given time is described by the macro-mechanical variables just like internal state;
- inertial effects have not been taken into account because of the large time scale.
- elastic properties of the bone tissue are explained by means of an isotropic Cauchy continuum;
- the precursor cells are indefinitely accessible.

Models in Giorgio et al. (2017d), Della Corte et al. (2019) did not consider any information about energy dissipation. Thus, they could not predict what is going to happen if the gap between 2 parts of bone tissue changes. Therefore, the aim of the paper is to take into account the following features (Rapisarda et al. 2019):

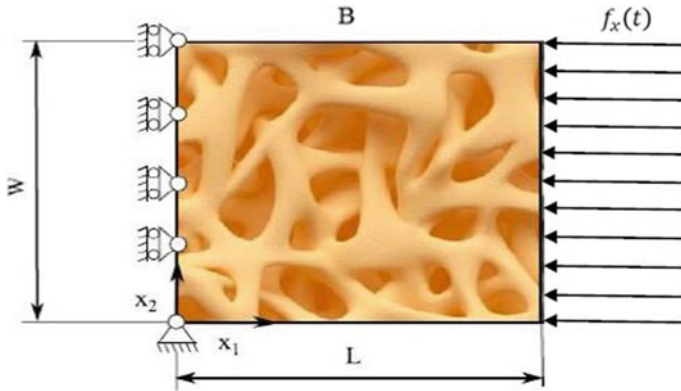


Fig. 3.1 Initial configuration of bone tissue under a cyclic compressing load (Giorgio et al. 2017a). Rollers make the bone able to have different widths under this cyclic load (due to the presence of Poisson ratio)

- energy dissipation;
- a novel parameter to the equation of density evolution to affiliate gap size and bone tissue healing (Giorgio et al. 2017d).

3.2.2 The Governing Equations

The proposed system of ODE describes the evolution of cells and bone density in time:

$$\frac{\partial x_k}{\partial t} = -\beta_k X_k + \gamma_{bk} x_b \kappa(\varphi) \quad (3.2)$$

$$\frac{\partial x_b}{\partial t} = -\beta_b X_b - \gamma_{bk} x_b \kappa(\varphi) + \alpha_b S^+ x_k \quad (3.3)$$

$$\frac{\partial x_c}{\partial t} = -\beta_c X_c - \gamma_c x_c \kappa(\varphi) + \alpha_c S^- x_k \quad (3.4)$$

$$\frac{\partial \rho}{\partial t} = (\alpha x_b - b x_c) H(\varphi) \times p w(\gamma). \quad (3.5)$$

By x_k , x_b , and x_c , densities of osteocytes, osteoblast, and osteoclasts are denoted, respectively. The terms $-\beta_k X_k$, $-\beta_b X_b$, and $-\beta_c X_c$ indicate apoptosis of the cells which is activated when cell densities reach threshold values denoted by \tilde{x}_k , \tilde{x}_b , \tilde{x}_c :

$$X_k = \begin{cases} x_k, & \text{if } x_k > \tilde{x}_k \\ 0, & \text{if } x_k \leq \tilde{x}_k \end{cases} \quad (3.6)$$

$$X_b = \begin{cases} x_b, & \text{if } x_b > \tilde{x}_b \\ 0, & \text{if } x_b \leq \tilde{x}_b \end{cases} \quad (3.7)$$

$$X_c = \begin{cases} x_c, & \text{if } x_c > \tilde{x}_c \\ 0, & \text{if } x_c \leq \tilde{x}_c \end{cases} \quad (3.8)$$

Each of the constant parameters β_k , β_b , and β_c are responsible for a fraction of cells that go into apoptosis. The terms $+\gamma_{bk}x_b\kappa(\varphi)$ and $-\gamma_{bk}x_b\kappa(\varphi)$ are related, and they are responsible for the differentiation from osteoblasts to osteocytes. The γ_{bk} is assumed to be constant instead. Also, α_b and α_c are considered as constant parameters which indicate the fraction of osteoblasts and osteoclasts that are created due to the stimulus. In Eq. (3.5), there are two quantities, a and b , which represent synthesis and resorption rates for osteoblast and osteoclast, respectively.

By γ , we denote the evaluation of the overall density in each part of a bone where a stimulus is defined. The output of a piecewise function $p_w(\gamma)$ could be either zero or one according to the value of γ .

The quantity φ represents porosity and the function H is utilized in order to consider the influence of effective porosity on the biological activity of cells. If the porosity is too big, then there is not enough material for actor cells to stay on. If the porosity is too low, then there is a lack of free space in pores, to allow for cells' mobility and deposit.

The function $H(\varphi)$ is defined as follows:

$$H(\varphi) = H(1 - \rho) = 2(1 - \rho)\rho \quad (3.9)$$

where ρ is the mass density of the bone.

Finally, S^+ denotes the positive part of stimulus while S^- represents the negative part.

3.2.3 The Stimulus

The stimulus combination of strain energy and power dissipation in the actual configuration C_t is defined as

$$S(x, y, t) = \frac{\int_{C_t} (U(x_0, y_0, t) + (D_s \times \beta)\eta_{x_k}(x_0, y_0, t)f(x, y, x_0, y_0))dx_0dy_0}{\int_{C_t} f(x, y, x_0, y_0)dx_0dy_0} - S_0 \quad (3.10)$$

where $f(x, y, x_0, y_0) = e^{-\frac{\|x-x_0\|^2 + \|y-y_0\|^2}{2D^2}}$, $U = U(x, y, t)$ is the volume strain-energy density, S_0 is the reference value of stimulus, x_k is the density of osteocytes, η is a constant that represents the capability of osteocytes to amplify mechanical signals, D measures the range of action of sensor cells, and D_s is the dissipation power.

3.2.4 The Function $\kappa(\varphi)$

The function $\kappa(\varphi)$ deserves special attention. In general, one may suppose that the function $\kappa(\varphi)$ can change between Eqs. (3.2)–(3.5) (Rapisarda et al. 2019). But for the sake of simplicity, we started by considering just one $\kappa(\varphi)$ function for Eqs. (3.2)–(3.5). For this function, we used a parabola (same as for the function H), since if the bone is too dense or too rare the actor cell activity stops.

The constitutive equation for porosity is (Rapisarda et al. 2019):

$$\varphi = 1 - \theta \frac{\rho}{\rho_{max}}, \quad 0 < x \leq 1. \quad (3.11)$$

For the sake of simplicity, bone density ρ is considered to be normalized with respect to the maximal value of bone density, and θ is assumed to be 1. Finally, the relation between density and porosity can be written as (Rapisarda et al. 2019):

$$\varphi = 1 - \rho. \quad (3.12)$$

Unless otherwise indicated, $\kappa(\varphi)$ has the following expression (Rapisarda et al. 2019):

$$\kappa(\varphi) = \kappa(1 - \rho) = 2(1 - \rho)\rho. \quad (3.13)$$

3.2.5 The Mechanical Framework

It has been assumed that the deformation energy density can be expressed as a function of the Green-Saint Venant strain tensor, the apparent volume Lagrangian mass densities, and the position of the considered material particle. The deformation gradient F , its determinant J , and the Green-Saint Venant strain tensor G are defined as follows (Rapisarda et al. 2019):

$$F = \nabla \chi, \quad J = \det F, \quad G = \frac{1}{2} (F^T F - I), \quad (3.14)$$

where $\chi : B \rightarrow \mathbb{R}^3$ is the placement function.

It is remarkable that the assumed deformation energy does not pertain explicitly to time and that the mass of the bone tissue changes very slowly in time. As already said,

the time changing is assumed to be slow enough to avoid considering any inertial effects, thus the behavior can be considered quasi-static. It is assumed that there exists a function U , representing the strain energy having the following expression (Rapisarda et al. 2019):

$$U(G, \rho, x) = \mu \text{tr}(G^2) + \frac{\lambda}{2} (\text{tr}(G))^2. \quad (3.15)$$

Here, μ and λ are the Lamé parameters. Since the material is not homogeneous, and its density changes with time, μ and λ are supposed to depend on t and x . Thus (Rapisarda et al. 2019),

$$\mu = \hat{\mu}(\rho, x), \quad \lambda = \hat{\lambda}(\rho, x). \quad (3.16)$$

For our aims, it will be advantageous to use Young's modulus and Poisson's ratio, related to Lamé parameters by the common relations (Rapisarda et al. 2019):

$$\mu = \frac{Y}{2(1 + \nu)}, \quad \lambda = \frac{Y\nu}{(1 + \nu)(1 - 2\nu)}, \quad (3.17)$$

where Y is the Young modulus and ν is the Poisson ratio. The Young modulus for the bone tissue is assumed (Rapisarda et al. 2019) as

$$Y = Y_m \left(\frac{\rho}{\rho_{max}} \right)^c. \quad (3.18)$$

Here, ρ_{max} is the maximum possible value for ρ and Y_m is the maximum value for the Young modulus, while c is a constant parameter. The mechanical equilibrium of the sample is controlled by the balance equations (Rapisarda et al. 2019):

$$\text{Div } T = \text{Div} \left(F \cdot \frac{\partial U}{\partial G} \right) = -b^{ext} \quad (3.19)$$

$$T[N] = F \cdot \frac{\partial U}{\partial G} \cdot N = f^{ext}, \quad (3.20)$$

where T is the first Piola stress tensor. Equation (3.19) gives the force $-b^{ext}$ acting on a REV of the sample considered, while Eq. (3.20) gives the force acting on the surface f^{ext} (with outward unit normal N). In a nutshell, the proposed model consists of the system of ODE (Eqs. (3.2)–(3.5)) and balance equations (Eqs. (3.19)–(3.20)), reminding that the energy density U depends on ρ through Eq. (3.18), while the stimulus S appearing in Eqs. (3.2)–(3.4) depends on U .

Table 3.1 Numerical data used for simulations

| | | | |
|----------------------|----------------------|------------------|---------------------|
| $a = 1$ | $b = 1$ | $S_0 = 0.6$ | $\rho_0 = 0.5$ |
| $x_{k0} = 1$ | $x_{b0} = 0.5$ | $x_{c0} = 0.1$ | $\eta = 1000$ |
| $\beta_k = 20$ | $\beta_k = 20$ | $\beta_k = 10$ | $\alpha_b = 0.03$ |
| $\gamma_{bk} = 0.1$ | $\gamma_c = 0.1$ | $\alpha_c = 0.1$ | $\tilde{x}_k = 1.1$ |
| $\tilde{x}_c = 0.11$ | $\tilde{x}_b = 0.75$ | $Y_m = 1$ | $\nu = 0.15$ |
| $D = 0.02$ | $L = 1$ | $l = 0.2$ | $c = 2$ |

3.2.6 Numerical Data

The complexity of the phenomena investigated needs a large number of constitutive parameters to be defined in order to model both the mechanical and biological behavior. Values of the parameters exploited in numerical simulations are presented in Table 3.1 (Rapisarda et al. 2019).

By Y_{mb} , the maximum possible value for the Young modulus is denoted, ν is the Poisson ratio, and L and l are the normalized length and the height of the sample of considered bone tissue. All the parameters are dimensionless.

Validation of these parameters is difficult in the absence of experimental data. Therefore, the values given here are chosen in order to obtain a qualitative behavior in the largest possible set of different cases.

3.2.7 Healing of Bone

In order to show that there is a gap in the bone, the following initial values are used:

$$X_i = \begin{cases} x_{i0} & \text{if } 0 \leq x \leq 0.45L \\ \frac{x_{i0}}{10} & \text{if } 0.45L \leq x \leq 0.55L \\ x_{i0} & \text{if } 0.55L \leq x \leq L \end{cases} \quad (3.21)$$

$$\rho_i = \begin{cases} \rho_{i0} & \text{if } 0 \leq x \leq 0.45L \\ \frac{\rho_{i0}}{10} & \text{if } 0.45L \leq x \leq 0.55L \\ \rho_{i0} & \text{if } 0.55L \leq x \leq L \end{cases} \quad (3.22)$$

In this paper, we utilize the same equations for cell population as the previous model did. But we want to use a specific parameter which leads us to a better and more realistic result. This new quantity, called γ , enables our model to distinguish a healthy region of the bone from the one which is occupied by a fracture. Figure 3.2 shows the idea behind this: contribution of γ helps us to increase sensitivity of the model with respect to different locations of the bone tissue.

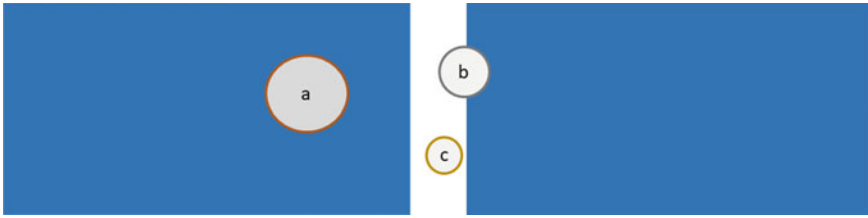


Fig. 3.2 Schematic of operative function γ containing **a** the healthy bone region, **b** the both regions of healthy and fractured part, And **c** the gap size region. Each circle evaluates the density in each point and determines if the bone density should increase

When stimulus is calculated in a healthy zone, osteocytes can receive more signals from adjacent cells since there are a lot of them in an area surrounding the evaluation point. But when overlap reduces and becomes less than a specific threshold, signals become less and healing does not occur. This is a biological feature that pushes us to improve and generalized the previous modeling.

We consider γ as an integral over a ball (or a circle in our 2D case) evaluating mass of osteocytes within the ball in every evaluation point of stimulus:

$$\gamma = \iint \rho \times ((x - x_0)^2 + (y - y_0)^2) dx_0 dy_0. \tag{3.23}$$

When the point considered has a location within the healthy zone $\dot{\rho}$, the equation should remain the same but if the overlap is less than the threshold ($\bar{\gamma}$) then $\dot{\rho}$ turns to zero.

We denote the density of osteocytes within the ball as x_k , and x and y are coordinates of the point where the stimulus is assessed in. The integral measures mass of osteocytes then a piecewise function compares the value estimated with a threshold to see if this point is located in the healthy zone or not. If the point is within the healthy zone, $\dot{\rho}$ should be the same as the equation of previous models, otherwise it should be zero. The step function is defined as follows:

$$f = \begin{cases} 0 & \text{if } \rho < \bar{\gamma} \\ 1 & \text{if } \rho > \bar{\gamma} \end{cases} \tag{3.24}$$

and

$$\bar{\gamma} = \xi \times C \times A_R, \tag{3.25}$$

where $C(kg/m)$ is the largest value of γ when f function is not used in Eq. (3.5), and A_R is the area of the circle having radius r . The quantity ξ is used to show how much the gap should be less than the radius to have healing on boundaries. We consider ξ as a constant value of $\frac{2}{3}$. Adding γ to the $\dot{\rho}$ equation should change the previous model for which if the radius is greater than the gap, healing takes place and when it is less than the gap, healing does not take place. Also, this function should cause the

bone to start healing from the boundaries, since bone density there is higher than in the fractured zone.

3.2.8 Dissipation

The basic kinematic field is the displacement $u(X, t)$ —designated by the components u_i where t is time and X stands for the selected space parametrization, i.e. three material coordinates for Lagrangian formulation. Then, to include the notion of deformation, the strain tensor E is employed, and its components are expressed as (Giorgio et al. 2016)

$$E_{ij}(X, t) = \frac{1}{2}(u_{i,j} + u_{j,i}). \quad (3.26)$$

Since bone is a hierarchical composite characterized by multiple structures at different length scales, dissipation can arise from a variety of mechanisms. In this work, dissipative phenomena occurring in bones are assumed to belong only to bulk viscosity (Giorgio et al. 2016).

Bulk viscosity: a damping increase with frequency in both saturated and dry bone was observed; as a result, it is reasonable to attribute the damping not only to the fluid flow but also to other sources. Thus, due to its composition, trabecular bone presents dissipation related to phenomena similar to those which have been already observed to occur in polymers, and to an interstitial fluid flow in bone canaliculi. The viscous stress can be expressed as (Giorgio et al. 2017a)

$$T_{ij}^v(\dot{E}) = 2\mu^v(\dot{E}_{ij} - \frac{1}{3}\dot{E}_{kk}\delta_{ij}) + \kappa^v(\dot{E}_{kk}\delta_{ij}), \quad (3.27)$$

where μ^v is the shear viscosity and κ^v is bulk viscosity evaluated for trabecular bone. Consequently, the Rayleigh dissipation function in the solid matrix is (Giorgio et al. 2017a)

$$2D_s = T_{ij}^v\dot{E}_{ij}. \quad (3.28)$$

3.2.8.1 Dimensionless Form

A dimensionless form of the considered problem is obtained in order to be utilized for numerical simulations. It has been done by normalization of the variables involved in the analysis by reference quantities. In this regard, dimensionless quantities are denoted with a superimposed tilde. In particular, the stored energy density E is normalized with respect to the maximum bone stiffness $Y_b^{Max} = 18 \text{ GPa}$ and therefore takes the following form (Giorgio et al. 2016):

$$\tilde{\varepsilon} = \varepsilon / Y_b^{Max} \quad (3.29)$$

As a consequence of this normalization, the material parameters related to Young modulus become (Giorgio et al. 2016)

$$\tilde{Y} = (\zeta^*)^{\beta_b} \quad (3.30)$$

being

$$\begin{aligned} \tilde{Y} &= Y/Y_b^{Max}, \quad \tilde{\lambda} = \lambda/Y_b^{Max} \\ \tilde{K}_f &= K_f/Y_b^{Max}, \quad \tilde{K}_2 = K_2/(Y_b^{Max} L_0^2), \end{aligned}$$

where L_0 is a characteristic length, which is assumed to be equal to the length of the sample. Dimensionless time is introduced as follows:

$$\tilde{t} = t/t_{ref}, \quad (3.31)$$

where a reference time t_{ref} is defined as the time interval in which the physiological processes, leading to fulfillment of the phenomenon bone synthesis, are accomplished. In this work, the reference time is assumed as $t_{ref} = 6.048 \times 10^5$ (s) which is the specific number of seconds constituting a week. Similarly, by defining the dimensionless form of the dissipation energy D as follows (Giorgio et al. 2016):

$$\tilde{D} = (t_{ref}/Y_b^{Max})D, \quad (3.32)$$

one gets

$$\begin{aligned} \tilde{K}_D &= K_D L_0^2 / (t_{ref} Y_b^{Max}), \quad \tilde{K}_B = K_B / (t_{ref} Y_b^{Max}), \\ \tilde{K}_\zeta &= K_\zeta / (t_{ref} Y_b^{Max}), \quad \tilde{\mu}^v = \mu^v / (t_{ref} Y_b^{Max}), \\ \tilde{\kappa}^v &= \kappa^v / (t_{ref} Y_b^{Max}). \end{aligned}$$

The external applied force τ_i is normalized following the same criterion with respect to the stiffness Y_b^{Max} . The dimensionless mass densities of bone and material are normalized with respect to $\hat{\rho} = 1800 \text{ kg/m}^3$ (Giorgio et al. 2016):

$$\tilde{\rho} = \rho / \hat{\rho} = \zeta_b. \quad (3.33)$$

The dimensionless stimulus can be defined as (Giorgio et al. 2016)

$$\tilde{S} = \tilde{S}_x - \tilde{S}_0, \quad (3.34)$$

where $\tilde{S}_0 = S_0/Y_b^{Max}$ and \tilde{S}_x comes from the assumptions $\tilde{\epsilon}_s = \epsilon_s/Y_b^{Max}$, $\tilde{D}_s = (t_{ref}/Y_b^{Max})D_s$, and $\tilde{b} = \beta/t_{ref}$.

3.3 Results and Discussion

In this study, we have developed a mechanobiological model of bone remodeling in order to achieve an accurate prediction for bone fracture recovery. Moreover, the effect of gap size, representing a scale of fracture on the bone surface, and energy dissipation terms have been studied in the healing process.

It can be noticed from Fig. 3.3 that the influence range of osteocytes r can have a significant effect on an outcome of calculations and it is shown clinically that the large gap size, showing complete fracture of bone, causes the unsuccessful formation of callus and failure of fracture healing (Lu and Lekszycski 2015). If we use a small radius, the healing does not occur (the small blue region shown in the last time step in Fig. 3.3a represents a very low density), since the circle of influence is totally inside the gap that has low density. Increasing the radius, we increase the bone density within the influence region and when the density threshold is reached, the healing must take place. Additionally, when there is no healing, the mass density in the gap and Young's modulus are constants and equal to their initial values. Therefore, the cyclic loading will cause the bone to be compressed only in the gap part.

Experimental studies are challenging at the level of fracture healing by considering the performance factor of all cells (dell'Isola et al. 2016). Thus, in this study, simulation of bone healing in different crack dimensions has been investigated taking into account energy loss in order to obtain a better prognosis for the healing process. The energy loss in an organ such as bone has been proven, and many researchers

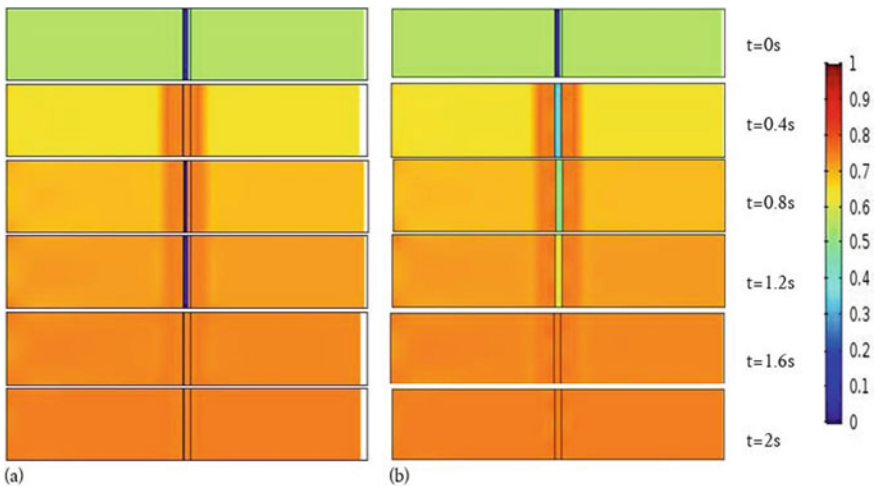


Fig. 3.3 Mass density in the process of bone remodeling for different time steps with **a** $r = 0.005$, **b** $r = 0.03$; r represents non-dimensional radius of the influence range of osteocytes. The range having a small value (shown in **a**) causes to a long healing time frame (blue region at $t=2$ in **a** which illustrates a very low density). On the other hand, an appropriate radius (shown in **b**) makes the bone healing time frame closer to the experimental observation

have shown this issue experimentally (Bednarczyk and Lekszycki 2016; George et al. 2018, 2019; An et al. 2014; Ridha and Thurner 2013; Hosseini et al. 2012). The remarkable point of this research and remodeling is to show the effects of energy dissipation using the numerical solution on the process of bone recovery during cyclic loading as well as its effect on the mechanism of cells affecting bone density changes. The effect of the dissipation term on the total energy is presented in Fig. 3.4. It is shown that taking into account the dissipation term, we obtain significantly reduced total energy of the system. Since the healing process is obviously related to the energy of our system, the energy has a key role in our modeling and cannot be neglected. Figure 3.4a shows a sudden increase in the energy at first with respect to what we see in Fig. 3.4b. In short, the dissipation term changes our model in such a way that the damping becomes more evident and does not let the energy of our system increase dramatically.

In this section, the radius of the circle equals 0.005 what is less than the critical radius. According to Fig. 3.5, the bone tissue density in the middle of the gap in the presence of γ is always zero, because the density of osteocyte, which is evaluated over the small circle, is less than the piecewise threshold function. As data suggested in Fig. 3.5, the density of osteoblasts increases sharply in the first period of 0.2s following an abrupt decrease from 0.2s to 0.5s; then a slight decline was experienced by osteoblasts until 2s. It was also observed in Maes et al. (2006) that during experimental investigations of fracture healing of knocked out mice, the osteoblast differentiation was reduced. The same phenomenon was observed also in Mayr-Wohlfart et al (2001). In Fig. 3.5a and Fig. 3.5b, the bone density of osteoblasts is higher than for other kinds of cells, but in the presence of γ osteoblasts are not activated owing to loss of osteocytes in that region. In other words, there are no cells to produce incited signals to activate bone tissue generation. However, there exist osteoblasts. So, the healing does not take place. On the other hand, due to Fig. 3.5b, in the absence of γ , the density of osteocytes increases activating osteoblasts. This leads to the increasing of bone tissue density which, in turn, means that healing always takes place without considering the gap size.

3.4 Conclusion

As previously discussed, experimental studies are challenging at the level of fracture healing by considering the performance factor of all cells. Thus, in this study, simulations of bone healing in different crack dimensions has been investigated taking into account energy loss in order to obtain a better prognosis for the healing process.

There is proposed a model which describes the healing process by considering dissipation terms in energy equation which is capable of detecting different gap size values by a quantity called γ . This novel quantity γ in the equation for density evaluation helps us to avoid the healing process to occur for large fracture sizes. It means that the existing gap size of the fracture should be less than the critical value in order to activate bone fracture healing. On the other hand, ignoring γ causes to

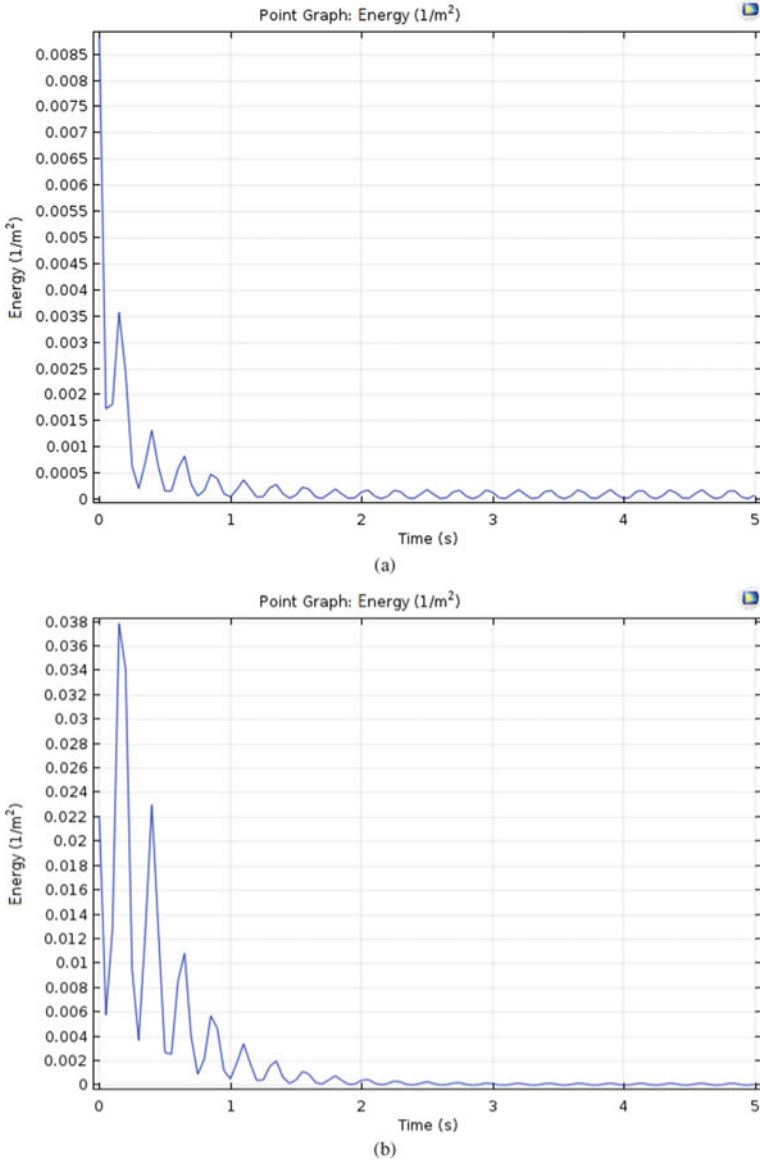


Fig. 3.4 Energy distribution: **a** without dissipation and **b** with dissipation. From the plots, one can see that dissipation terms make a significant change in total energy of the bone and make the energy damping much better, so it cannot be neglected in simulations

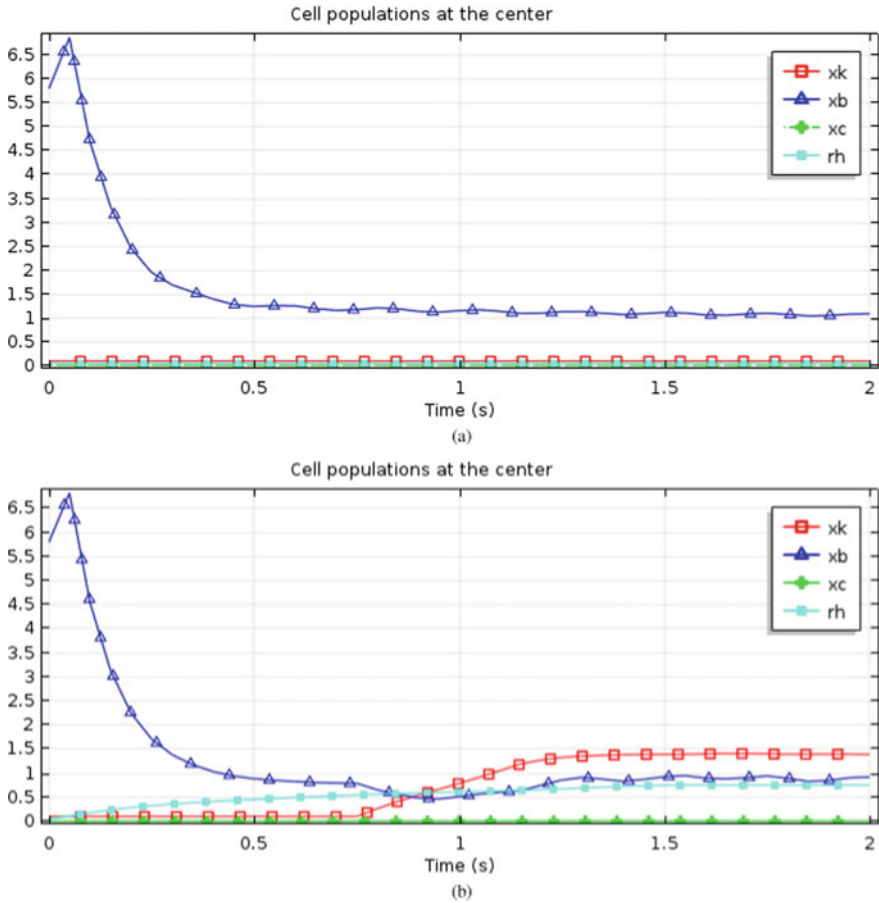


Fig. 3.5 **a** Cell population at the center point in the presence of γ . **b** cell population at the center in the absence of γ . In the presence of γ (shown in **a**), there are not any cells to produce signals to activate osteoblast so the density remains constant, but in the absence of γ healing takes place even from the middle of the fractured zone

have healing for every gap size which is unrealistic. So γ increases the accuracy of the model for mimicking the natural healing in one's body. The energy loss in an organ such as bone has been proven, and many researchers have shown this issue experimentally. The remarkable point of this research and remodeling is to show the effects of energy dissipation using the numerical solution on the process of bone recovery during cyclic loading as well as its effect on the mechanism of cells affecting bone density changes.

Acknowledgements We thank Dr. Ivan Giorgio for his hints and advise in this research. We are also grateful to Dr. Alessandro Della Corte for his comments on an earlier version of the manuscript.

We would like to thank the “International Research Center for the Mathematics and Mechanics of Complex Systems” (M&MoCS), Universit’a dell’Aquila, Italy, for all the support, and also Prof. Mahmoud Kadhodaei, Mechanical Engineering Department of Isfahan University of Technology, Iran.

References

- An B, Zhao X, Arola D, Zhang D (2014) Fracture analysis for biological materials with an expanded cohesive zone model. *J Biomech* 47(10):2244–2248
- Andreas U, Giorgio I, Madeo A (2015) Modeling of the interaction between bone tissue and resorbable biomaterial as linear elastic materials with voids. *Z Angew Math Phys* 66(1):209–237
- Baiotto S, Zidi M (2004) Theoretical and numerical study of a bone remodeling model: the effect of osteocyte cells distribution. *Biomech Model Mechanobiol* 3(1):6–16
- Bednarczyk E, Lekszycki T (2016) A novel mathematical model for growth of capillaries and nutrient supply with application to prediction of osteophyte onset. *Z Angew Math Phys* 67(4):94
- Bell GI (1978) Models for the specific adhesion of cells to cells. *Science* 200(4342):618–627
- Cricri G, Perrella M, Sessa S, Valoroso N (2015) A novel fixture for measuring mode iii toughness of bonded assemblies. *Eng Fract Mech* 138:1–18
- Del Vescovo D, Giorgio I (2014) Dynamic problems for metamaterials: Review of existing models and ideas for further research. *Int J Eng Sci* 80. <https://doi.org/10.1016/j.ijengsci.2014.02.022>
- Della Corte A, Giorgio I, Scerrato D (2019) A review of recent developments in mathematical modeling of bone remodeling. *Proc Inst Mech Eng, Part H: J Eng Med*, 0954411919857599
- dell’Isola F, Andreas U, Placidi L (2014) At the origins and in the vanguard of peri-dynamics, non-local and higher gradient continuum mechanics. an underestimated and still topical contribution of gabrio piola. *Math Mech Solids* 20:887–928. <https://doi.org/10.1177/1081286513509811>
- dell’Isola F, Corte A, Giorgio I (2016) Higher-gradient continua: The legacy of piola, mindlin, sedov and toupin and some future research perspectives. *Math Mech Solids* 22. <https://doi.org/10.1177/1081286515616034>
- Elbanna AE, Carlson JM (2013) Dynamics of polymer molecules with sacrificial bond and hidden length systems: towards a physically-based mesoscopic constitutive law. *PLoS one* 8(4)
- George D, Allena R, Rémond Y (2018) A multiphysics stimulus for continuum mechanics bone remodeling. *Math Mech Complex Syst* 6(4):307–319
- George D, Allena R, Rémond Y (2019) Integrating molecular and cellular kinetics into a coupled continuum mechanobiological stimulus for bone reconstruction. *Continuum Mech Thermodyn* 31(3):725–740
- Giorgio I, Andreas U, Scerrato D, Dell’Isola F (2016) A visco-poroelastic model of functional adaptation in bones reconstructed with bio-resorbable materials. *Biomech Model Mechanobiol* 15(5):1325–1343
- Giorgio I, Andreas U, Dell’Isola F, Lekszycki T (2017a) Viscous second gradient porous materials for bones reconstructed with bio-resorbable grafts. *Extreme Mech Lett* 13:141–147
- Giorgio I, Andreas U, Lekszycki T, Corte AD (2017b) The influence of different geometries of matrix/scaffold on the remodeling process of a bone and bioresorbable material mixture with voids. *Math Mech Solids* 22(5):969–987
- Giorgio I, Andreas U, Scerrato D, Braidotti P (2017c) Modeling of a non-local stimulus for bone remodeling process under cyclic load: application to a dental implant using a bioresorbable porous material. *Math Mech Solids* 22(9):1790–1805
- Giorgio I, Rizzi N, Turco E (2017d) Continuum modelling of pantographic sheets for out-of-plane bifurcation and vibrational analysis. *Proc R Soc A: Math, Phys Eng Sci* 473(2207):20170,636

- Giorgio I, Dell'Isola F, Andreaus U, Alzahrani F, Hayat T, Lekszycki T (2019) On mechanically driven biological stimulus for bone remodeling as a diffusive phenomenon. *Biomech Model Mechanobiol*, 1–25
- Greco F, Luciano R, Serino G, Vaiana N (2018) A mixed explicit-implicit time integration approach for nonlinear analysis of base-isolated structures. *Ann Solid Struct Mech* 10(1):17–29
- Hosseini HS, Pahr DH, Zysset PK (2012) Modeling and experimental validation of trabecular bone damage, softening and densification under large compressive strains. *J Mech Behav Biomed Mater* 15:93–102
- Klein-Nulend J, Bacabac R, Bakker A (2012) Mechanical loading and how it affects bone cells: the role of the osteocyte cytoskeleton in maintaining our skeleton. *Eur Cells Mater* 24:278–291
- Kumar C, Jasiuk I, Dantzig J (2011) Dissipation energy as a stimulus for cortical bone adaptation. *J Mech Mater Struct* 6(1):303–319
- Lanyon LE, Rubin C (1984) Static vs dynamic loads as an influence on bone remodelling. *J Biomech* 17(12):897–905
- Lekszycki T, dell'Isola F (2012) A mixture model with evolving mass densities for describing synthesis and resorption phenomena in bones reconstructed with bio-resorbable materials. *ZAMM-J Appl Math Mech/Zeitschrift für Angewandte Mathematik und Mechanik* 92(6):426–444
- Lieou CK, Elbanna AE, Carlson JM (2013) Sacrificial bonds and hidden length in biomaterials: a kinetic constitutive description of strength and toughness in bone. *Phys Rev E* 88(1):012,703
- Lu Y, Lekszycki T (2015) Modeling of an initial stage of bone fracture healing. *Continuum Mech Thermodyn* 27(4–5):851–859
- Lu Y, Lekszycki T (2016) A novel coupled system of non-local integro-differential equations modelling young's modulus evolution, nutrients' supply and consumption during bone fracture healing. *Z Angew Math Phys* 67(5):111
- Lu Y, Lekszycki T (2017) Modelling of bone fracture healing: influence of gap size and angiogenesis into bioresorbable bone substitute. *Math Mech Solids* 22(10):1997–2010
- Madeo A, George D, Lekszycki T, Nierenberger M, Rémond Y (2012) A second gradient continuum model accounting for some effects of micro-structure on reconstructed bone remodelling. *Comptes Rendus Mécanique* 340(8):575–589
- Maes C, Coenegrachts L, Stockmans I, Daci E, Luttun A, Petryk A, Gopalakrishnan R, Moermans K, Smets N, Verfaillie CM et al (2006) Placental growth factor mediates mesenchymal cell development, cartilage turnover, and bone remodeling during fracture repair. *J Clin Investig* 116(5):1230–1242
- Marmo F, Masi D, Rosati L (2018a) Thrust network analysis of masonry helical staircases. *Int J Architect Herit* 12(5):828–848
- Marmo F, Ruggieri N, Toraldo F, Rosati L (2018b) Historical study and static assessment of an innovative vaulting technique of the 19th century. *Int J Architect Herit*
- Marmo F, Toraldo F, Rosati A, Rosati L (2018c) Numerical solution of smooth and rough contact problems. *Meccanica* 53(6):1415–1440
- Marmo F, Demartino C, Candela G, Sulpizio C, Briseghella B, Spagnuolo R, Xiao Y, Vanzi I, Rosati L (2019) On the form of the musmeci's bridge over the basento river. *Eng Struct* 191:658–673
- Marmo F, Sessa S, Vaiana N, De Gregorio D, Rosati L (2020) Complete solutions of three-dimensional problems in transversely isotropic media. *Continuum Mech Thermodyn* 32(3):775–802
- Mayr-Wohlfart U, Kessler S, Puhl W, Günther K, Knöchel W (2001) Bmp-4 of xenopus Laevis stimulates differentiation of human primary osteoblast-like cells. *J Bone Joint Surgery British* 83(1):144–147
- Paradiso M, Marmo F, Rosati L (2019) Consistent derivation of a beam model from the saint Venant's solid model. *Int J Solids Struct* 159:90–110
- Park H, Lakes R (1986) Cosserat micromechanics of human bone: strain redistribution by a hydration sensitive constituent. *J Biomech* 19(5):385–397

- Perricone V, Grun T, Marmo F, Langella C, Carnevali MDC (2020) Constructional design of echinoid endoskeleton: main structural components and their potential for biomimetic applications. *Bioinspirat Biomimet*
- Rapisarda AC, Della Corte A, Drobnicki R, Di Cosmo F, Rosa L (2019) A model for bone mechanics and remodeling including cell populations dynamics. *Z Angew Math Phys* 70(1):9
- Ridha H, Thurner PJ (2013) Finite element prediction with experimental validation of damage distribution in single trabeculae during three-point bending tests. *J Mech Behav Biomed Mater* 27:94–106
- Ritchie RO, Buehler MJ, Hansma P (2009) Plasticity and toughness in bone. *Phys Today*
- Scala I, Spingarn C, Rémond Y, Madeo A, George D (2017) Mechanically-driven bone remodeling simulation: Application to lipus treated rat calvarial defects. *Math Mech Solids* 22(10):1976–1988
- Serpieri R, Sessa S, Rosati L (2018) A mitc-based procedure for the numerical integration of a continuum elastic-plastic theory of through-the-thickness-jacketed shell structures. *Compos Struct* 191:209–220
- Sessa S, Marmo F, Rosati L (2015) Effective use of seismic response envelopes for reinforced concrete structures. *Earthquake Eng Struct Dyn* 44(14):2401–2423
- Sessa S, Serpieri R, Rosati L (2017) A continuum theory of through-the-thickness jacketed shells for the elasto-plastic analysis of confined composite structures: Theory and numerical assessment. *Compos B Eng* 113:225–242
- Sessa S, Marmo F, Rosati L, Leonetti L, Garcea G, Casciaro R (2018a) Evaluation of the capacity surfaces of reinforced concrete sections: Eurocode versus a plasticity-based approach. *Meccanica* 53(6):1493–1512
- Sessa S, Marmo F, Vaiana N, Rosati L (2018b) A computational strategy for eurocode 8-compliant analyses of reinforced concrete structures by seismic envelopes. *J Earthquake Eng*, 1–34
- Sessa S, Marmo F, Vaiana N, De Gregorio D, Rosati L (2019a) Strength hierarchy provisions for transverse confinement systems of shell structural elements. *Compos B Eng* 163:413–423
- Sessa S, Marmo F, Vaiana N, Rosati L (2019b) Probabilistic assessment of axial force-biaxial bending capacity domains of reinforced concrete sections. *Meccanica* 54(9):1451–1469
- Sheidaei A, Kazempour M, Hasanabadi A, Nosouhi F, Pithioux M, Baniassadi M, Rémond Y, George D (2019) Influence of bone microstructure distribution on developed mechanical energy for bone remodeling using a statistical reconstruction method. *Math Mech Solids*, 1081286519828418
- Turner CH (1998) Three rules for bone adaptation to mechanical stimuli. *Bone* 23(5):399–407
- Vaiana N, Spizzuoco M, Serino G (2017) Wire rope isolators for seismically base-isolated lightweight structures: experimental characterization and mathematical modeling. *Eng Struct* 140:498–514
- Vaiana N, Sessa S, Marmo F, Rosati L (2019) Nonlinear dynamic analysis of hysteretic mechanical systems by combining a novel rate-independent model and an explicit time integration method. *Nonlinear Dyn* 98(4):2879–2901
- Vaiana N, Capuano R, Sessa S, Marmo F, Rosati L (2021a) Nonlinear dynamic analysis of seismically base-isolated structures by a novel opensees hysteretic material model. *Appl Sci* 11(3):900
- Vaiana N, Sessa S, Rosati L (2021b) A generalized class of uniaxial rate-independent models for simulating asymmetric mechanical hysteresis phenomena. *Mech Syst Signal Process* 146(106):984
- Webb J, Tricker J (2000) A review of fracture healing. *Curr Orthop* 14(6):457–463
- Wolff J (1892) *Das Gesetz der Transformation der Knochen* (The Law of Bone Remodeling, translated by P. Maquet and R. Furlong, 1986). Springer, Berlin
- Yang J, Lakes RS (1982) Experimental study of micropolar and couple stress elasticity in compact bone in bending. *J Biomech* 15(2):91–98

Chapter 4

Second Gradient Linear and Nonlinear Constitutive Models of Architected Materials: Static and Dynamic Behaviors



Yosra Rahali, Hilal Reda, Benoit Vieille, Hassan Lakiss,
and Jean-François Ganghoffer

Abstract We provide in this chapter a synthetic overview of homogenization methods for the setting up of second gradient linear and nonlinear anisotropic continuum media representative of periodic network materials made of beam-type structural elements, considering successively static and dynamic aspects in the context and linear and nonlinear theories. Generalized continuum models accounting for either nodal rotations or strain gradient contributions emerge from the extended asymptotic homogenization schemes taking into account either additional nodal degrees of freedom or long-range interactions between neighboring representative unit cells. The strain energy density of the effective continuum is derived relying either on analytic methods or based on dedicated asymptotic homogenization methods specific to discrete network materials. Strain gradient theories lead to dispersive wave propagation features that are overlooked by classical elasticity and that reflect measurements. Based on these models, we study the dispersion of elastic waves propagating in periodic beam networks, considering the pantographic structures, the re-entrant hexagonal lattice, the diamond chiral lattice, plain weave fabric, and the 3D hexagonal unit cell representative of trabecular bone. In the framework of nonlinear strain gradient theories, different types of waves propagate depending on the degree of nonlinearity; a supersonic mode occurs for a weak nonlinearity, whereas wave propagation changes from a supersonic to an evanescent subsonic mode for a higher degree of nonlinearity.

Y. Rahali (✉) · B. Vieille

GPM, INSA Rouen, Université de Rouen, Avenue de l'université, Saint-Étienne-du-Rouvray,
France

e-mail: rahali.yosra@gmail.com

B. Vieille

e-mail: benoit.vieille@insa-rouen.fr

H. Reda · H. Lakiss

Faculty of Engineering, Section III, Lebanese University, Campus Rafic Hariri, Beirut, Lebanon

e-mail: hassanlakiss@yahoo.com

J.-F. Ganghoffer

LEM3, Université de Lorraine, CNRS. 7, rue Félix Savart., 57073 Metz Cedex, France

e-mail: jean-francois.Ganghoffer@univ-lorraine.fr

© Springer Nature Switzerland AG 2021

F. Marmo et al. (eds.), *Mathematical Applications in Continuum and Structural Mechanics*, Advanced Structured Materials 127,
https://doi.org/10.1007/978-3-030-42707-8_4

Keywords Periodic networks · Homogenization · Effective continuum · Second gradient models · Dispersive waves

4.1 Introduction

The homogenization of network materials with a discrete topology toward an effective Cauchy continuum has deserved lots of research activities in the last two decades, following different types of methods (Hubert and Palencia 1992; Bornert et al. 2001; Jarroudi and Brillard 2001; Bouchitté and Bellieud 2002; Sili 2005; Dos Reis and Ganghoffer 2010, 2012). Homogenization faces limitations when the wavelength of the loading or of the strain field becomes comparable to the typical microstructure size. One shall especially underline that size effects cannot be adequately captured by the standard first gradient-based elasticity theory (Askes and Aifantis 2011). The main motivation for scientists in 1960–1970s to develop non-classical continuum mechanics theories like generalized continua is to extend their validity range from a mathematical viewpoint beyond the strict assumption of scale separation (Trinh et al. 2012). As mentioned in Forest (2006), criteria of choice of the homogenization method include the ability to account for impact of the morphology and distribution of phases on the material response and to capture scale effects.

Microstructured models or higher order/grade continuum models recourse to additional kinematic variables or additional intrinsic parameters like internal length scales to account for the microstructure kinematics at the macrolevel via suitably introduced macro-fields (Auffray et al. 2015; dell’Isola et al. 2015b). Higher order continuum theories introducing additional degrees of freedom find their origin in the seminal contribution of the Cosserat brothers (1909), Toupin (1962) and Mindlin (1964; 1965) and have been properly formulated in a generalized sense in Germain (1973) using the virtual power method (Jouan et al. 2014).

Higher order micro-continuum theories have been developed to account for microstructure effects by introducing additional degrees of freedom like the Cosserat medium (Cosserat and Cosserat 1896) and the micromorphic medium (Eringen and Suhubi 1964) or additional higher gradients like the second gradient continuum (Toupin 1962; Mindlin and Eshel 1968) and associated material constants (Chen et al. 2004; Edelen 1969; Eringen 2012, 1966; Hadjesfandiari and Dargush 2011; Lam et al. 2003; Polyzos and Fotiadis 2012; Yang et al. 2002; Forest 1998, 2002; Kouznetsova et al. 2002; Mindlin 1964, 1965). Strain localization zones observed in experimental tests (Desrues and Viggiani 2004) cannot be modeled with classical continuum mechanics models. Several authors developed novel homogenization procedures to account for the heterogeneous nature of the material at the microlevel involving a second gradient macroscopic constitutive law (Pideri and Seppecher 1997; Camar-Eddine and Seppecher 2003). In both the linear and nonlinear regimes, higher order homogenization schemes have been built for architected materials in the work of Trinh et al. (2012). The homogenization of nonlinear elastic material in contact with a set of more rigid nonlinear elastic fibers disposed periodically has

been treated in El Jarroudi (2013). In Jouan et al. (2014), the second gradient model developed by Chambon and co-workers is a specific higher order medium (Chambon et al. 1996, 1998, 2001), aiming to regularize ill-posed strain localization problems in soils and for geomaterials.

In Rahali et al. (2015b, 2017), second gradient continuum models of beam networks have been developed, considering two alternative formulations originating in the heuristic homogenization methodology developed by Piola (see Mindlin 1965; dell'Isola et al. 2015b, a; Alibert et al. 2003; Turco et al. 2017): (i) an analytical method based on an evaluation of the strain energy density at the microscopic level and (ii) the extension of the asymptotic expansion method up to the second gradient of the mesoscopic kinematic variables. Both identification procedures lead to the same second gradient linear continuum. Three discrete homogenization models have been developed in Rahali et al. (2017): the so-called simplified Euler–Bernoulli model considering the local displacement as the sole kinematic variable, the complete Euler–Bernoulli model incorporating both displacement and a local rotation as kinematic descriptors, and a third model accounting for the lattice curvature and another microstructural level. The first model ignores nodal rotations and proves more adequate for tension dominated lattices. The consideration of the nodal rotations in the second model leads to a more accurate model, since it can be used for both bending dominated lattices (requiring a local microrotation) and tension dominated lattices. The network curvature is incorporated in a third step, considering a general parameterization of the material points with curvilinear coordinates. This more general model may consider both lattice curvature and microstructure, or only the microstructure (without curvature).

The aforementioned homogenization methods and their associated numerical schemes are versatile enough to handle any lattice, periodical, or not. They lead to the full set of first and second gradient effective moduli accounting for the full anisotropy of the effective continuum. Applications have been made to both two-dimensional (2D) (like pantograph and hexagonal lattice) and three-dimensional (3D) network materials, including 3D prototype geometries of trabecular bone in the field of biomechanics (Giorgio et al. 2017; Madeo et al. 2012). The linearized homogenized model of pantographic lattices represents an exact second gradient medium (Rahali et al. 2015b), as per the definition given by Germain (1973). Numerical simulations illustrate some peculiarities of the obtained continuum models, for instance, localization of energy due to the strain gradient contributions.

Network materials are most often much more flexible in bending than in traction, thus they are prone to geometrical nonlinearities. The homogenization methods to identify first and higher gradient moduli have therefore been extended to account for large deformations due to geometrical nonlinearities (Reda et al. 2016b, a).

Nonlinear wave propagation in periodic nonlinear lattice materials has been studied based on the derived homogenized continuum in Reda et al. (2016b). The nonlinear wave propagation analysis is done relying on the identified effective strain energy density including nonlinear kinematic variables. The ensuing analysis show that subsonic or supersonic modes may propagate within the effective continuum. Subsonic

waves become evanescent beyond a certain wavenumber, while the supersonic waves are characterized by frequency increasing with the wavenumber.

Periodic lattice materials exhibit a strong contrast of their microscopic properties and they constitute a special class of metamaterials, as explained in Del Vescovo and Giorgio (2014), Hans and Boutin (2008), Boutin and Soubestre (2011), dell’Isola et al. (2012), Kamotski and Smyshlyaev (2019). They witness heterogeneous deformations and are likely to develop high strain gradients due to the voided matrix (Forest and Trinh 2011; Hütter 2017). Pantographic sheets are exact strain gradient materials under conditions of inextensible fibers; since then, most of the energy goes into the bending mode; this entails that periodic pantographs deserve second gradient continuum models at the continuum level (after homogenization) due to the dominant flexural response of their fibers. The resistance in torsion at the junction between both fibers of the pantograph is an essential parameter governing the transition from a Cauchy-type effective continuum to a second gradient effective medium description (Coutris et al. 2019). The extension of linear models of metamaterials toward the large deformation regime preserves the higher gradient effects, see the recent contributions on the topic (Rahali et al. 2015a; Rokoš et al. 2019). The possible forms of the strain energy density for generalized pantographic sheets with non orthogonal or inequivalent fibers has been done recently in Rahali et al. (2015a).

The chapter consists of four main sections: Sect. 4.2 provides a summary of the developed anisotropic linear continuum higher order models accounting for the rotations at the lattices nodes. An analytical method based on the derivation of the strain energy density at microlevel is first exposed, followed by an extension of the asymptotic expansion method up to the second gradient. Based on these models, the dispersion of elastic waves in periodic beam networks is next analyzed. The propagation of nonlinear waves in homogenized periodic nonlinear beam networks based on second gradient nonlinear constitutive models deserves Sect. 4.3. The chapter concludes with a summary of the work in Sect. 4.4.

4.2 First- and Second-Order Effective Moduli of Periodic Networks

Different methods have been recently developed in Rahali et al. (2015b, 2017), Giorgio et al. (2018), Abdoul-Anziz and Seppecher (2018) for periodic 2D and 3D network materials, in order to construct second gradient continua (accounting for the lattices nodes rotations, surface effects and the network curvature). The implementation of the discrete homogenization method uses a dedicated code written in symbolic language.

We summarize, in the following, the main steps for the determination of the first- and second-order effective moduli of periodic lattices considering the simplified Euler–Bernoulli scheme.

Homogenization steps

1. Forces applied to a beam b to the end node E .

$$N_E^{eb} = \frac{E^b S^{eb}}{L^{eb}} (e^b \cdot (\mathbf{u}_E^\epsilon - \mathbf{u}_O^\epsilon)) \quad (4.1)$$

$$T_E^{eb} = \frac{12E^b I^{eb}}{(L^{eb})^3} (e^{b\perp} \cdot (\mathbf{u}_E^\epsilon - \mathbf{u}_O^\epsilon)) \quad (4.2)$$

$$M_E^{eb} e_3 = \left(\frac{2E^b I^{eb}}{(L^{eb})^2} (-3e^{b\perp} \cdot (\mathbf{u}_E^\epsilon - \mathbf{u}_O^\epsilon)) \right) e_3 \quad (4.3)$$

The subscripts O and E refer to the origin and extremity nodes of the beam, N , T , E^b , I^{eb} , S^{eb} and L^{eb} are, respectively, the normal and transverse forces, Young modulus, the beam length, the beam section, and the quadratic moment, \mathbf{e}^b the unit director along each beam, $\mathbf{e}^{b\perp}$ the normal unit vector, \mathbf{e}_3 is normal to the planar lattice, u_O^ϵ , and u_E^ϵ the displacements of the two extremity nodes of the beam. As to notations, vectors and second-order tensors are here and in the sequel denoted using boldface symbols.

2. Asymptotic expansion of the variables in curvilinear coordinates

- The beam width and length $t^{eb} = \varepsilon t^b$, $l_b^\epsilon = \varepsilon L^b$
- The relative nodal displacement reads

$$\begin{aligned} (\mathbf{u}_E^\epsilon - \mathbf{u}_O^\epsilon) &= \varepsilon \left(\mathbf{u}_1^E - \mathbf{u}_1^O - L_i \delta_{ib} \frac{\partial \mathbf{u}_0(\lambda^\epsilon)}{\partial \lambda_i} \right) \\ &+ \varepsilon^2 \left(\mathbf{u}_2^E - \mathbf{u}_2^O - L_i \delta_{ib} \frac{\partial \mathbf{u}_1^E(\lambda^\epsilon)}{\partial \lambda_i} - \frac{L_i^2 \delta_{ib}^2}{2} \frac{\partial^2 \mathbf{u}_0(\lambda^\epsilon)}{\partial \lambda_i^2} \right) \end{aligned} \quad (4.4)$$

with λ the curvilinear coordinates, $\delta_i \in \{-1, 0, 1\}$. The index $i \in \{-1, 0, 1\}$ indicating the considered axis \mathbf{e}_1 or \mathbf{e}_2 .

3. Insert Eq. (4.4) into Eqs. (4.1)–(4.3).

4. The equilibrium of forces and moments in virtual power form

$$\sum_{v^i \in \mathbb{Z}^2} \sum_{b \in B_R} (T^b \dot{V} + N^b \dot{U}) = 0 \quad (4.5)$$

$$\sum_{v^i \in \mathbb{Z}^2} \sum_{b \in B_R} \left(M_O^b \cdot w_O^b + M_E^b \cdot w_E^b + \frac{l^b}{2} (e^b \wedge F_E^b) \cdot w_C^b - \frac{l^b}{2} (e^b \wedge F_O^b) \cdot w_C^b \right) = 0 \quad (4.6)$$

B_R refer to the set of beams within the reference unit cell, \mathbf{w} the virtual rotation velocity and $F^b = N^b e^b + T^b e^{b\perp}$ the force exerted on the beam b .

5. The virtual power of internal forces over an elementary cell

$$P_e = \sum_b (T_E (\dot{V}_E - \dot{V}_O) + N_E (\dot{U}_E - \dot{U}_O)) \quad (4.7)$$

with \dot{V}_i and \dot{U}_i therein the two components of the virtual velocity field

6. Continualization process

$$\begin{aligned} \lim_{\varepsilon \rightarrow 0} P &= \lim_{\varepsilon \rightarrow 0} \varepsilon^2 \sum_{c \in \mathcal{Z}} P_e = \int_{\Omega} P_e d\lambda \\ &= \int_{\Omega} \left[\frac{1}{g} \sum_b \left(T_E^1 L_i \delta_{ib} \frac{\partial \dot{V}_o(\lambda^\varepsilon)}{\partial \lambda_i} + N_E^1 L_i \delta_{ib} \frac{\partial \dot{U}_o(\lambda^\varepsilon)}{\partial \lambda_i} \right. \right. \\ &\quad + \varepsilon \left(T_E^1 \frac{L_i^2 \delta_{ib}^2}{2} \frac{\partial^2 \dot{V}_o(\lambda^\varepsilon)}{\partial \lambda_i^2} + T_E^2 L_i \delta_{ib} \frac{\partial \dot{V}_o(\lambda^\varepsilon)}{\partial \lambda_i} \right. \\ &\quad + N_E^1 \frac{L_i^2 \delta_{ib}^2}{2} \frac{\partial^2 \dot{U}_o(\lambda^\varepsilon)}{\partial \lambda_i^2} + N_E^2 L_i \delta_{ib} \frac{\partial \dot{U}_o(\lambda^\varepsilon)}{\partial \lambda_i} \left. \right) \\ &\quad \left. \left. + \varepsilon^2 \left(T_E^2 \frac{L_i^2 \delta_{ib}^2}{2} \frac{\partial^2 \dot{V}_o(\lambda^\varepsilon)}{\partial \lambda_i^2} + N_E^2 \frac{L_i^2 \delta_{ib}^2}{2} \frac{\partial^2 \dot{U}_o(\lambda^\varepsilon)}{\partial \lambda_i^2} \right) \right] dV \end{aligned} \quad (4.8)$$

with $N_E = (\varepsilon N_E^1 + \varepsilon^2 N_E^2)$, $T_E = (\varepsilon T_E^1 + \varepsilon^2 T_E^2)$ and g is the Jacobian of the transformation (Cartesian to curvilinear). One has to rewrite previous expression in Cartesian coordinates. In the following, we do not study the couplings terms, restricting to centrosymmetric networks.

7. Equivalence with a second-order gradient continuum in order to express the stress and hyperstress tensors

$$\begin{aligned} P^i &= \int_{\Omega} ((\boldsymbol{\sigma} - \mathbf{S} \cdot \nabla) \cdot \nabla) \cdot \dot{\mathbf{D}} dV \\ &= \int_{\Omega} \left(\mathbf{F}^q \cdot \left(\frac{\partial \dot{\mathbf{D}}}{\partial x_q} \right) - \mathbf{H}^{pq} \cdot \left(\frac{\partial^2 \dot{\mathbf{D}}}{\partial x_p \partial x_q} \right) \right) dV \end{aligned} \quad (4.9)$$

With $\dot{\mathbf{D}}$ the virtual rate of deformation, $\boldsymbol{\sigma}$ the Cauchy stress and \mathbf{S} the third-order hyperstress tensor with index symmetry $S_{ijk} = S_{ikj}$.

8. Calculation of the stress and hyperstress tensors

$$\boldsymbol{\sigma} = (\sigma_{iq} \mathbf{e}_i) \otimes \mathbf{e}_q = F^q \otimes \mathbf{e}_q \quad (4.10)$$

$$\mathbf{S} = (S_{kqp} \mathbf{e}_k) \otimes \mathbf{e}_q \otimes \mathbf{e}_p = H^{pq} \otimes \mathbf{e}_q \otimes \mathbf{e}_p \quad (4.11)$$

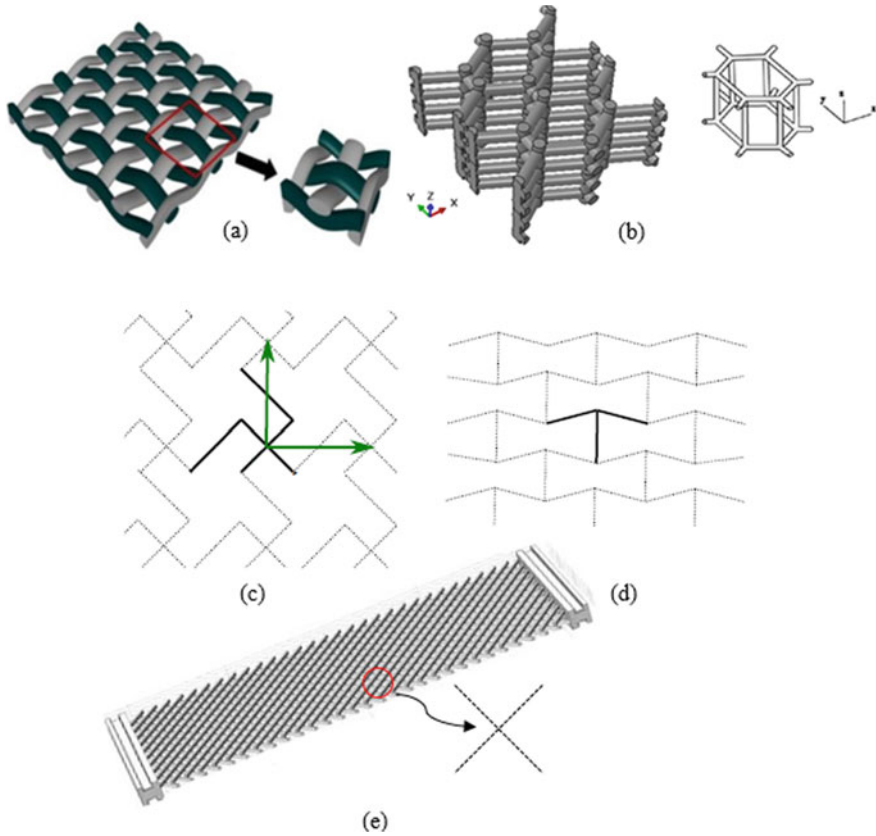


Fig. 4.1 Representative unit cell of some studied structures: **a** plain weave fabric, **b** 3D hexagonal lattice, **c** Diamond chiral lattice, **d** re-entrant lattice ($\theta < 0$), **e** pantograph

2D and 3D examples have been treated in Rahali et al. (2015b, 2017); Reda et al. (2016c), some of them shown in Fig. 4.1. The method allows to treat any periodic structure.

In Rahali et al. (2015b), relying on the complete Bernoulli schema (the rotation is limited to the zero order), it has been shown that the linearized homogenized model for the pantographic lattice must necessarily be a second gradient continuum. Some numerical simulations are represented in Fig. 4.2 to illustrate some peculiarities of the obtained continuum models, especially the ability of strain gradient models to capture localization of energy in narrow bands.

FE computations performed over an elementary unit cell assess the validity of the computed homogenized moduli and a satisfactory agreement is obtained with 13% as a maximum percentage of differences for the second-order shear moduli. The effective properties evaluated by the asymptotic expansion have been verified from an analytical evaluation of the strain energy density for the lattice, using the Euler–Bernoulli model.

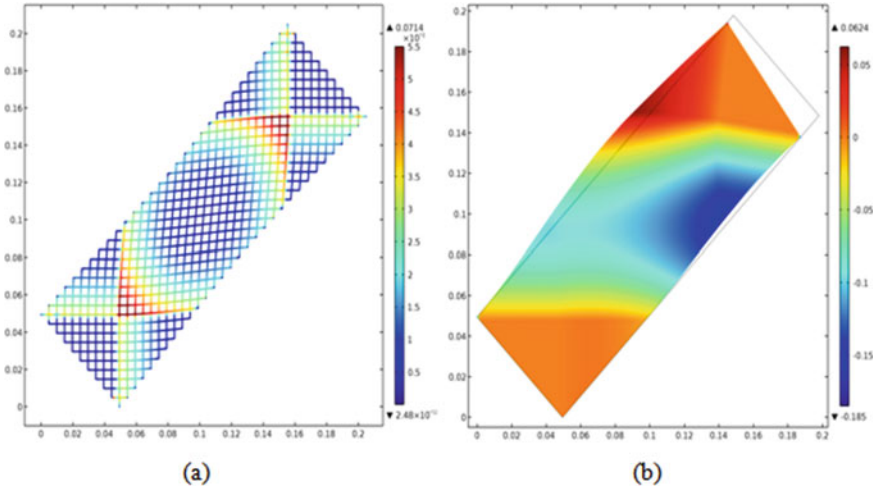


Fig. 4.2 **a** Deformed shape in extension: the scale of colors measures bending energy, **b** shear deformation field showing regions of constant shear and transition zones (plotted surface energy densities are in $J.m^{-2}$)

4.2.1 Analytical Method

An analytical method has been developed in Reda et al. (2016a,b, 2017, 2018), based on an evaluation of the lattice strain energy density in both the linear and non-linear regimes, to evaluate the effective mechanical properties of a periodic network materials. This section is focused on the linear regime. One considers a unit cell made of 2D beam elements. $\mathbf{U}=(u,v)$ is the displacement field and θ the rotation, see in Fig. 4.3.

M , F , and T are the moment, the normal, and transverse forces, respectively, applied to the extremity nodes. The strain energy W_S is expressed as follows (Rahali et al. 2015b; Reda et al. 2018):

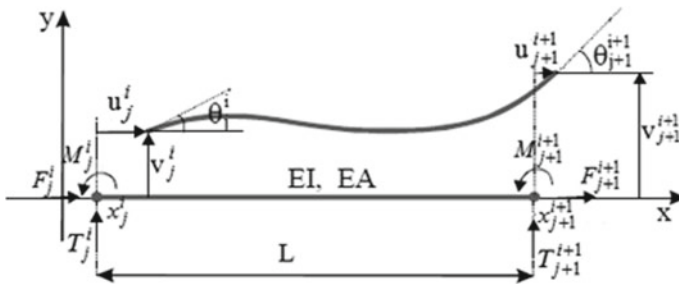


Fig. 4.3 Kinematics of a beam element

$$\begin{aligned}
W_S = & \underbrace{\frac{1}{2} \frac{EA}{L} (u_{j+1}^i - u_j^i)^2}_{\text{Extension Energy}} + \underbrace{\frac{1}{2} \frac{EI}{L} (\theta_{j+1}^i - \theta_j^i)^2}_{\text{Flexion Energy}} \\
& + \underbrace{\frac{1}{2} \frac{12EI}{L^3} \left((v_{j+1}^i - v_j^i) - \frac{L}{2} (\theta_{j+1}^i + \theta_j^i) \right)^2}_{\text{Shear Energy}}
\end{aligned} \tag{4.12}$$

In Eq.(4.12), A , E , I and L stand for the beam section, the Young modulus, the quadratic moment, and the beam's length, respectively.

After development (Taylor expansion of the kinematic variables) the beam's strain energy contributions are written as follow, s is the curvilinear coordinate:

$$\begin{aligned}
W_{\text{extension}} &= \frac{1}{2} k_l \left[L \left. \frac{\partial u}{\partial s} \right|_j^i + \frac{L^2}{2} \left. \frac{\partial^2 u}{\partial s^2} \right|_j^i \right]^2 \\
&= \frac{1}{2} k_l \left(\underbrace{\left(L \left. \frac{\partial u}{\partial s} \right|_j^i \right)^2}_{\text{Linear Energy}} + 2 \underbrace{\left(L \left. \frac{\partial u}{\partial s} \right|_j^i \right) \left(\frac{L^2}{2} \left. \frac{\partial^2 u}{\partial s^2} \right|_j^i \right)}_{\text{Coupling Energy}} + \underbrace{\left(\frac{L^2}{2} \left. \frac{\partial^2 u}{\partial s^2} \right|_j^i \right)^2}_{\text{SG Energy}} \right) \\
W_{\text{flexion}} &= 0 \\
W_{\text{shear}} &= \frac{1}{2} k_c \left[\left(L \left. \frac{\partial v}{\partial s} \right|_j^i + \frac{L^2}{2} \left. \frac{\partial^2 v}{\partial s^2} \right|_j^i \right) - \frac{L}{2} \left(2 \left. \frac{\partial v}{\partial s} \right|_j^i \right) \right]^2 \\
&= \frac{1}{2} k_c \underbrace{\left[\left(\frac{L^2}{2} \left. \frac{\partial^2 v}{\partial s^2} \right|_j^i \right) \right]^2}_{\text{SG Energy}}
\end{aligned} \tag{4.13}$$

Using expressions Eq.(4.13), we distinguish between energy contribution terms associated with the first-order gradient denoted as W_{S_L} , coupling terms W_{S_C} , and second gradient terms W_{S_2} . The total strain energy takes the form:

$$W_S = W_{S_L} + W_{S_2} + W_{S_C} \tag{4.14}$$

One restricts the analysis to periodic structures thus the coupling term vanishes.

One then obtains the Cauchy stress tensor σ_{ij} and the hyperstress tensor S_{ijk}

$$\sigma_{ij} = \frac{\partial (W_{S_L})}{\partial (\partial u_i / \partial x_j)} \quad S_{ijk} = \frac{\partial (W_{S_2})}{\partial (\partial^2 u_{ij} / \partial x_k^2)} \tag{4.15}$$

Both identification procedures (asymptotic or analytic method) lead to the construction of the same second gradient linear continuum. The second gradient models

obtained by the discrete homogenization method, see Sect. 4.1, are the basis for the analysis (Reda et al. 2016c).

4.2.2 Homogenized Viscoelastic Behavior

Viscoelastic 2D beam elements obeying a Kelvin–Voigt rheological behavior have been considered in Reda et al. (2016c). The difference with the exposed model in subsection 1, lies in the expressions of the forces and moments, summarized below:

$$\begin{aligned}
 N_E^{\varepsilon b} &= \frac{E^b S^{\varepsilon b}}{L^{\varepsilon b}} (\mathbf{e}^b \cdot (\mathbf{u}_E^\varepsilon - \mathbf{u}_O^\varepsilon)) + \frac{\mu_e S^{\varepsilon b}}{L^{\varepsilon b}} (\mathbf{e}^b \cdot (\dot{\mathbf{u}}_E^\varepsilon - \dot{\mathbf{u}}_O^\varepsilon)) \\
 T_E^{\varepsilon b} &= \frac{12E^b I^{\varepsilon b}}{(L^{\varepsilon b})^3} (\mathbf{e}^{b\perp} \cdot (\mathbf{u}_E^\varepsilon - \mathbf{u}_O^\varepsilon)) + \frac{12\mu_e I^{\varepsilon b}}{(L^{\varepsilon b})^3} (\mathbf{e}^{b\perp} \cdot (\dot{\mathbf{u}}_E^\varepsilon - \dot{\mathbf{u}}_O^\varepsilon)) \\
 M_E^{\varepsilon b} \mathbf{e}_3 &= \left(\frac{2E^b I^{\varepsilon b}}{(L^{\varepsilon b})^2} (-3\mathbf{e}^{b\perp} \cdot (\mathbf{u}_E^\varepsilon - \mathbf{u}_O^\varepsilon)) + \frac{2\mu_e I^{\varepsilon b}}{(L^{\varepsilon b})^2} (-3\mathbf{e}^{b\perp} \cdot (\dot{\mathbf{u}}_E^\varepsilon - \dot{\mathbf{u}}_O^\varepsilon)) \right) \cdot \mathbf{e}_3
 \end{aligned} \tag{4.16}$$

$\dot{\mathbf{u}}^\varepsilon$ and μ_e are the velocity vector and the extensional viscosity, respectively. After straightforward developments, the constitutive law (centrosymmetric lattices) []receives the following form:

$$\begin{aligned}
 \{\sigma\} &= \underbrace{[A^e]}_{\text{elastic part}} \{\epsilon\} + \underbrace{[A^v]}_{\text{viscous part}} \{\dot{\epsilon}\} \\
 \{S\} &= \underbrace{[D^e]}_{\text{elastic part}} \{\kappa\} + \underbrace{[D^v]}_{\text{viscous part}} \{\dot{\kappa}\}
 \end{aligned} \tag{4.17}$$

with σ_{ij} , S_{ijk} , ϵ_{pq} , κ_{pqr} , $\dot{\epsilon}_{pq}$, $\dot{\kappa}_{pqr}$, respectively, the stress and hyperstress tensors, and their conjugated kinematic quantities, namely, the first and second deformation gradients and their time derivatives, the first and second deformation velocity gradients. A^e_{ijpq} , D^e_{ijkpqr} , A^v_{ijpq} , D^v_{ijkpqr} are, respectively, the first and second gradient elasticity and viscosity coefficients.

The main steps to compute the dynamical equilibrium and the characteristic equation are summarized below:

1. The motion equations in the x_j directions

$$\left(\frac{\partial \sigma_{ij}}{\partial x_j} \right) - \frac{\partial^2 S_{ijk}}{\partial x_j \partial x_k} = \alpha^* \ddot{u}_j, \quad j = 1, 2 \tag{4.18}$$

ρ^* is the effective density.

2. Write the generalized displacement field, for harmonic planar waves \mathbf{r}

$$U = \widehat{U} e^{(\lambda t - i k \cdot r)}, \quad V = \widehat{V} e^{(\lambda t - i k \cdot r)} \quad (4.19)$$

\widehat{U} , \widehat{V} are the wave amplitude and λ the complex frequency function, respectively, and $k = (k_1, k_2)$ the wave vector.

3. Substitute Eq. (4.19) into Eq. (4.18), delivering

$$[D(k_1, k_2, \cdot)] \left\{ \begin{array}{c} \widehat{U} \\ \widehat{V} \end{array} \right\} = 0 \quad (4.20)$$

4. The characteristic equation is written as

$$\lambda^4 + a \lambda^3 + b \lambda^2 + c \lambda + d = 0 \quad (4.21)$$

5. The roots of Eq. (4.21) are

$$\lambda_s(k) = -\zeta_s(k) \cdot \omega_{ns}(k) \pm i \cdot \omega_{ns}(k) \sqrt{1 - \zeta_s^2} \quad (4.22)$$

where s represents the branch type, $\omega_{ns}(k)$, $\omega_{ds}(k)$ the natural and damped frequency and ζ_s the damping factor

$$\omega_{ns}(k) = \sqrt{\text{real}(\lambda_s)^2 + \text{imag}(\lambda_s)^2}; \quad \omega_{ds}(k) = \omega_{ns}(k) \sqrt{1 - \zeta_s^2};$$

$$\zeta_s = -\frac{\text{real}(\lambda_s)}{\omega_{ns}}$$

Relying on these expressions, one can represent the dispersion curve, Fig. 4.4. The results show shifts in the frequency band diagrams due to damping.

Figure 4.6 shows a considerable difference between second gradient media description with and without the coupling energy term contributions. We analyze in the next section the acoustic properties of periodic network material undergoing configuration changes associated to geometrical nonlinearities.

4.2.3 Incremental Scheme

We summarize below the main steps of the discrete homogenization method leading to the nonlinear response of the homogenized continuum (Elnady et al. 2016).

For each iteration k :

1. Computation of the effective mechanical properties in the linear regime.
2. Computation of the incremental Second Piola–Kirchhoff stress tensor

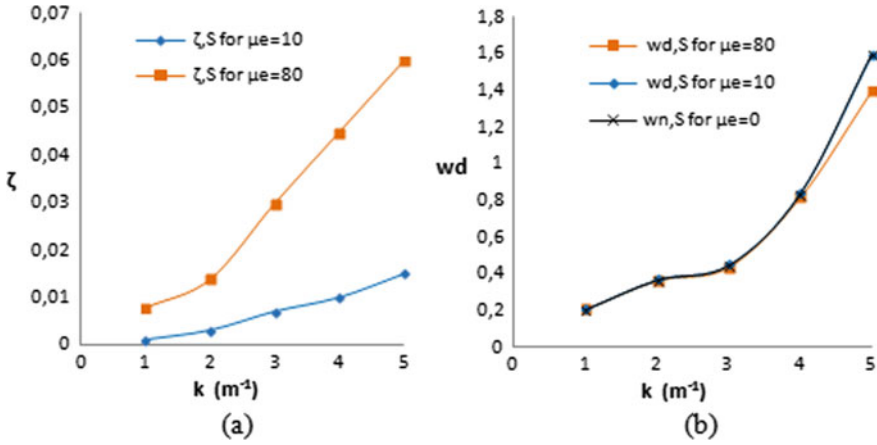
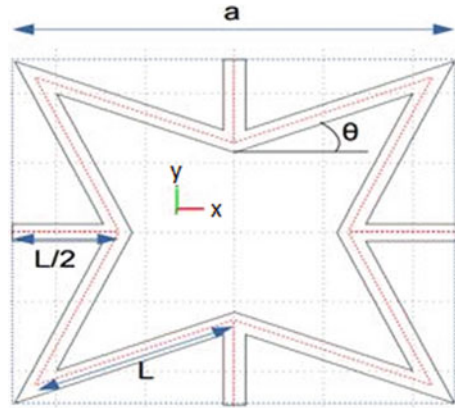


Fig. 4.4 a Damping ratio and b Dispersion relation with a direction of propagation $\theta = \pi/6$ for re-entrant lattice, Fig. 4.5, μ_e is given in MPa.sec and ω_d in rad/sec

Fig. 4.5 Representative unit cell of the re-entrant lattice



$$\Delta S_n^{(k)} = \mathbf{K}_{T,n}^S : \Delta \mathbf{E}_{Gn}^{(k)}$$

$\Delta \mathbf{E}_{Gn}^{(k)}$ is the strain tensor

3. Go to next step if convergence is reached
4. Update Cauchy stress

$$\begin{aligned} \sigma_{n+1}^{(k)} &= \mathbf{J}_n^{-1} \mathbf{F}_n \cdot \{ \mathbf{S}_n^{(k)} + \Delta \mathbf{S}_n^{(k)} \} \cdot \mathbf{F}_n^T \\ &= \underbrace{(\mathbf{J}_n^{-1} \mathbf{F}_n \cdot \mathbf{S}_n^{(k)} \cdot \mathbf{F}_n^T)}_{\sigma_n^{(k)}} + \underbrace{(\mathbf{J}_n^{-1} \mathbf{F}_n \cdot (\Delta \mathbf{S}_n^{(k)}) \cdot \mathbf{F}_n^T)}_{\Delta \sigma_n^{(k)}} \end{aligned} \quad (4.23)$$

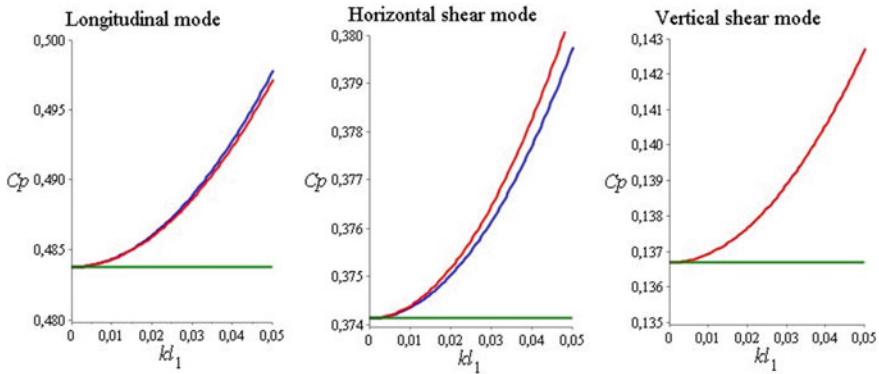


Fig. 4.6 Phase velocity for the three modes of propagation for the pyramid shaped unit cell (Reda et al. 2018). Blue curve: second gradient medium with coupling energy terms. Red curve: second gradient medium without coupling energy. Green curve: Cauchy medium

5. Repeat steps 1–4 up to the maximum applied strain and curvature over the unit cell.

The strain energy of the second gradient medium undergoing large deformations can be expressed in the one-dimensional (1D) context as follows:

$$W = Au_{,x} + B \frac{(u_{,x})^2}{2} + C \frac{(u_{,x})^3}{3} + D \frac{(u_{,x})^4}{4} + \beta \frac{(u_{,xx})^2}{2} \quad (4.24)$$

where β is the factor of the linear second gradient term. The Cauchy stress σ and the hyperstress tensor S are defined by

$$\sigma = \frac{\partial W}{\partial \frac{\partial u}{\partial x}}, \quad S = \frac{\partial W}{\partial \frac{\partial^2 u}{\partial x^2}} \quad (4.25)$$

The wave propagation equation along the x direction

$$\left(\frac{\partial \sigma}{\partial x} \right) - \underbrace{\frac{\partial^2 S}{\partial x^2}}_{SG} = a^* \ddot{u} \quad (4.26)$$

Inserting the constitutive law obtained combining Eqs.(4.24) and (4.25) into the previous Eq.(4.26) leads to

$$\left(B \frac{\partial^2 u}{\partial x^2} \right) + \left(2C \frac{\partial^2 u}{\partial x^2} \left(\frac{\partial u}{\partial x} \right) + 3D \frac{\partial^2 u}{\partial x^2} \left(\frac{\partial u}{\partial x} \right)^2 \right) - \left(\beta \frac{\partial^4 u}{\partial x^4} \right) = \rho^* \frac{\partial^2 u}{\partial t^2} \quad (4.27)$$

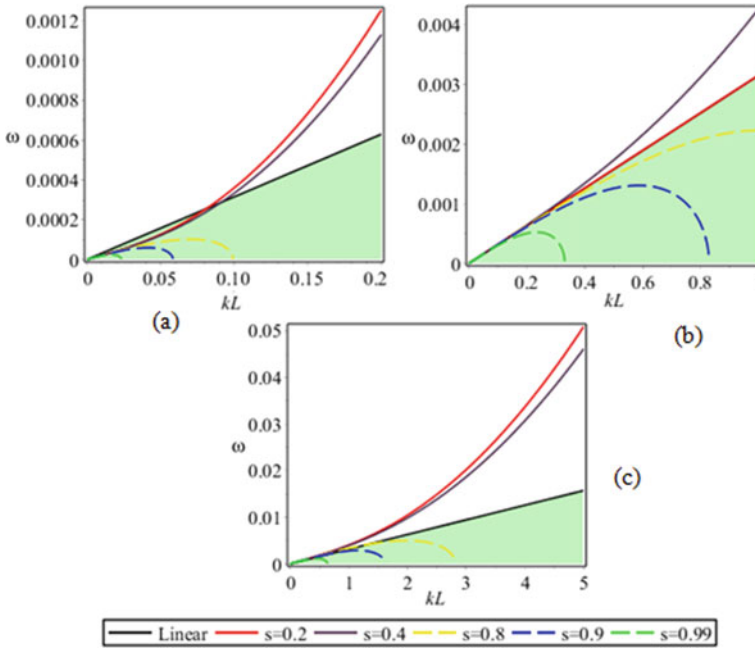


Fig. 4.7 Dispersion relation with different values of s with second gradient terms equation for the **a** Hexagonal lattice, **b** Re-entrant lattice, and **c** Textile Plane weave lattice

A similar problem was investigated in detail in Reda et al. (2016a), when neglecting the C coefficient in the nonlinear form of the strain energy Eq. (4.24).

Doing the change of variable $z = x - (w/k)t$, in which w is the frequency and k the wavenumber, following a simple transformation, PDE Eq. (4.27) is transformed into an ordinary differential equation (ODE in short) for the new non-dimensional strain of the wave function; its solution is of the solitary wave type:

$$N(z) = -\frac{A}{2} + \frac{A s^2}{2 \left(1 - \frac{E(s)}{K(s)}\right)} sn^2\left(\frac{k_0}{2}z, s\right) \tag{4.28}$$

Second gradient terms in the nonlinear motion equation lead to two different modes: an evanescent subsonic mode (high values of s) and a supersonic mode (low values of s). The dispersion relations are pictured in Fig.4.7 for different values of the nonlinear parameter s . In the sequel, parameters v and v_0 refer to the phase velocities in the nonlinear and linear effective medium, respectively

The propagation of nonlinear waves in homogenized periodic nonlinear beam networks based on second gradient nonlinear constitutive models will be analyzed in the sequel. The essential difference with the previous approach lies in the fact that the geometrical nonlinearity is incorporated into the beam model.

4.3 Wave Propagation Analysis Based on Nonlinear Models

The study of nonlinear elastic waves restrict most of the time in the literature to the Cauchy-type elasticity theory, involving only the first displacement gradient. Models based on Cauchy-type theory do not give realistic predictions of dynamical behaviors such as the dispersion relation, since the Cauchy effective medium lacks internal length parameters.

The Cauchy medium is by essence non dispersive, and waves propagate independently of the wavenumber (Reda et al. 2016b). Experiments show to the contrary that most waves are dispersive so that each wavenumber travels with a different phase velocity (Vladimir et al. 2003; Jakata and Every 2008). This explains the success of gradient-enriched theories in capturing dynamic behaviors overlooked by classical elasticity. In order to circumvent this drawback, different methods have been developed (Reda et al. 2016b, a, 2017) to link the dispersive aspects of wave propagation to gradient elasticity theories in a nonlinear effective medium in both 1D, 2D, and 3D situations.

4.3.1 Strain Energy Density

An analytical method based on the strain energy has been developed in Reda et al. (2016b) to predict the effective properties of the nonlinear effective medium in the context of a second gradient theory. The developments exposed in subsection 2 for the linear case remain valid for the nonlinear regime, only the expressions of the forces and moments are changed to incorporate nonlinear terms:

$$F = EA \left(\frac{\Delta \mathbf{U} \cdot \mathbf{e}^b}{L} + \frac{1}{2} \left(\frac{(\Delta \mathbf{U} \cdot \mathbf{e}^b)^2}{L^2} + \frac{(\Delta \mathbf{U} \cdot \mathbf{e}^{b\perp})^2}{L^2} \right) + \frac{\psi_c}{2} \right) + EI_z \left(\frac{\Delta \psi_c}{2} \right)^2 \quad (4.29)$$

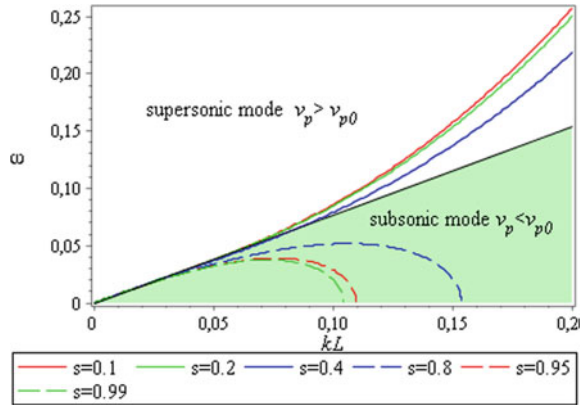
$$T = GA \left(-\psi_c \left(\frac{\Delta \mathbf{U} \cdot \mathbf{e}^b}{L} + 1 \right) + \frac{\Delta \mathbf{U} \cdot \mathbf{e}^{b\perp}}{L} \right) \quad (4.30)$$

$$M = EI_z \left(\frac{\Delta \psi_c}{L} \left(1 + \frac{\Delta \mathbf{U} \cdot \mathbf{e}^b}{L} \right) + \psi_c \frac{\Delta \mathbf{U} \cdot \mathbf{e}^{b\perp}}{L} \right) \quad (4.31)$$

In previous expressions, I_z is the beam quadratic moment, $GA = \frac{12EI_z}{L^2}$ the shear rigidity, ψ_c the central node rotation of the beam and \mathbf{U} the 2D displacement vector. The symbol $\Delta(\cdot)$ denoted the variation of any quantity (\cdot) between both beam extremities. The expression of the internal deformation energy of a single beam element is obtained relying on previous expressions as

$$W_S = W_{S_1} + W_{S_2} + W_{S_3} \quad (4.32)$$

Fig. 4.8 Dispersion relation for different values of s for the hexagonal re-entrant lattice $\theta = \frac{\pi}{6}$



where W_{s_1} and W_{s_2} are the first and second gradient terms of the strain energy density for small strains, and W_{s_3} is the nonlinear contribution of the strain energy density.

The strain energy density leads to

$$\sigma_{ij} = \frac{\partial (W_{s_1} + W_{s_3})}{\partial (\partial u_i / \partial x_j)} ; S_{ijk} = \frac{\partial (W_{s_2})}{\partial (\partial^2 u_{ij} / \partial x_k^2)} \quad (4.33)$$

The equations of motion for a second gradient homogenized medium are then written. The methodology for determining the acoustic characteristics is exposed into more details in Reda et al. (2016b).

The obtained second gradient nonlinear continuum is characterized by an evanescent subsonic mode and a supersonic mode, both represented in Fig. 4.8.

Parameter s describes the degree of nonlinearity it accounts for the shape, the period, and the velocity of waves.

4.4 Conclusion

A synthetic overview of homogenization methods employed to compute the static and dynamic responses of periodic network materials is exposed in this contribution. These effective homogenized models can account for additional degrees of freedom (like the Cosserat medium) or higher strain gradients, thereby reflecting the discrete network kinematics. Strain gradient theories lead to dispersive wave propagation reflecting the experimental observations. Since these networks have a low bending rigidity of the inherent beams, they are prone to geometrical nonlinearities, the impact of which on wave propagation is assessed, leading to different wave propagation regimes. The powerfulness and versatility of homogenization schemes

of network materials shall be exploited in future contributions to exhibit topologies giving rise to band gaps (Misra and Poorsolhjoui 2016; NejadSadeghi et al. 2019) and other interesting phenomena in both the static and dynamic range that metamaterials exhibit.

References

- Abdoul-Anziz H, Seppecher P (2018) Strain gradient and generalized continua obtained by homogenizing frame lattices. *Math Mech Complex Syst* 6(3):213–250
- Alibert JJ, Seppecher P, dell’Isola F (2003) Truss modular beams with deformation energy depending on higher displacement gradients. *Math Mech Solids* 8(1):51–73
- Askes H, Aifantis EC (2011) Gradient elasticity in statics and dynamics: an overview of formulations, length scale identification procedures, finite element implementations and new results. *Int J Solids Struct* 48(13):1962–1990
- Auffray N, dell’Isola F, Eremeyev VA, Madeo A, Rosi G (2015) Analytical continuum mechanics à la hamilton-piola least action principle for second gradient continua and capillary fluids. *Math Mech Solids* 20(4):375–417
- Bornert M, Bretheau T, Gilormini P (2001) Homogénéisation en mécanique des matériaux, Tome 1: Matériaux aléatoires élastiques et milieux périodiques
- Bouchitté G, Bellieud M (2002) Homogenization of a soft elastic material reinforced by fibers. *Asymptot Anal* 32(2):153–183
- Boutin C, Soubestre J (2011) Generalized inner bending continua for linear fiber reinforced materials. *Int J Solids Struct* 48(3–4):517–534
- Camar-Eddine M, Seppecher P (2003) Determination of the closure of the set of elasticity functionals. *Arch Ration Mech Anal* 170(3):211–245
- Chambon R, Caillerie D, El Hassan N (1996) Etude de la localisation unidimensionnelle à l’aide d’un modèle de second gradient. *Comptes rendus de l’Académie des sciences Série II, Mécanique, physique, chimie, astronomie* 323(4):231–238
- Chambon R, Caillerie D, El Hassan N (1998) One-dimensional localisation studied with a second grade model. *Eur J Mech-A/Solids* 17(4):637–656
- Chambon R, Caillerie D, Matsushima T (2001) Plastic continuum with microstructure, local second gradient theories for geomaterials: localization studies. *Int J Solids Struct* 38(46–47):8503–8527
- Chen Y, Lee JD, Eskandarian A (2004) Atomistic viewpoint of the applicability of microcontinuum theories. *Int J Solids Struct* 41(8):2085–2097
- Cosserat E, Cosserat F (1896) Sur la théorie de l’élasticité. premier mémoire. In: *Annales de la Faculté des sciences de Toulouse: Mathématiques* 10(3–4):I1–I116
- Cosserat E, Cosserat F (1909) Théorie des corps déformables. A. Hermann et fils
- Coutris N, Thompson LL, Kosaraju S (2019) Asymptotic homogenization models for pantographic lattices with variable order rotational resistance at pivots. *J Mech Phys Solids*, 103718
- Del Vescovo D, Giorgio I (2014) Dynamic problems for metamaterials: review of existing models and ideas for further research. *Int J Eng Sci* 80:153–172
- dell’Isola F, Seppecher P, Madeo A (2012) How contact interactions may depend on the shape of Cauchy cuts in nth gradient continua: approach “à la d’Alembert”. *Z Angew Math Phys* 63(6):1119–1141
- dell’Isola F, Andreaus U, Placidi L (2015a) At the origins and in the vanguard of peridynamics, non-local and higher-gradient continuum mechanics: An underestimated and still topical contribution of gabrio piola. *Math Mech Solids* 20(8):887–928
- dell’Isola F, Giorgio I, Andreaus U (2015b) Elastic pantographic 2d lattices: a numerical analysis on the static response and wave propagation. *Proc Est Acad Sci* 64(3):219

- Desrues J, Viggiani G (2004) Strain localization in sand: an overview of the experimental results obtained in grenoble using stereophotogrammetry. *Int J Numer Anal Meth Geomech* 28(4):279–321
- Dos Reis F, Ganghoffer J (2010) Discrete homogenization of architected materials: Implementation of the method in a simulation tool for the systematic prediction of their effective elastic properties. *Tech Mech* 30(1–3):85–109
- Dos Reis F, Ganghoffer J (2012) Construction of micropolar continua from the asymptotic homogenization of beam lattices. *Comput Struct* 112:354–363
- Edelen DG (1969) Protoelastic bodies with large deformation. *Arch Ration Mech Anal* 34(4):283–300
- El Jarroudi M (2013) Homogenization of a nonlinear elastic fibre-reinforced composite: a second gradient nonlinear elastic material. *J Math Anal Appl* 403(2):487–505
- Elnady K, Goda I, Ganghoffer JF (2016) Computation of the effective nonlinear mechanical response of lattice materials considering geometrical nonlinearities. *Comput Mech* 58(6):957–979
- Eringen AC (1966) A unified theory of thermomechanical materials. *Int J Eng Sci* 4(2):179–202
- Eringen AC (2012) *Microcontinuum field theories: I Foundations and solids*. Springer Science & Business Media, Berlin
- Eringen AC, Suhubi E (1964) Nonlinear theory of simple micro-elastic solids–i. *Int J Eng Sci* 2(2):189–203
- Forest S (1998) Mechanics of generalized continua: construction by homogenization. *Le Journal de Physique IV* 8(PR4):Pr4–39
- Forest S (2002) Homogenization methods and the mechanics of generalized continua-part 2. *Theoret Appl Mech* 28(29):113–144
- Forest S (2006) *Milieux continus généralisés et matériaux hétérogènes*. Presses des MINES
- Forest S, Trinh DK (2011) Generalized continua and non-homogeneous boundary conditions in homogenisation methods. *ZAMM-J Appl Math Mech/Zeitschrift für Angewandte Mathematik und Mechanik* 91(2):90–109
- Germain P (1973) The method of virtual power in continuum mechanics. part 2: Microstructure. *SIAM J Appl Math* 25(3):556–575
- Giorgio I, Andraus U, dell’Isola F, Lekszycki T (2017) Viscous second gradient porous materials for bones reconstructed with bio-resorbable grafts. *Extreme Mech Lett* 13:141–147
- Giorgio I, Harrison P, dell’Isola F, Alsayednoor J, Turco E (2018) Wrinkling in engineering fabrics: a comparison between two different comprehensive modelling approaches. *Proc R Soc A: Math, Phys Eng Sci* 474(2216):20180,063
- Hadjesfandiari AR, Dargush GF (2011) Couple stress theory for solids. *Int J Solids Struct* 48(18):2496–2510
- Hans S, Boutin C (2008) Dynamics of discrete framed structures: a unified homogenized description. *J Mech Mater Struct* 3(9):1709–1739
- Hubert JS, Palencia ES (1992) *Introduction aux méthodes asymptotiques et à l’homogénéisation: application à la mécanique des milieux continus*. Masson
- Hütter G (2017) Homogenization of a Cauchy continuum towards a micromorphic continuum. *J Mech Phys Solids* 99:394–408
- Jakata K, Every A (2008) Determination of the dispersive elastic constants of the cubic crystals GE, SI, GAAS, and INSB. *Phys Rev B* 77(17):174,301
- Jarroudi ME, Brillard A (2001) Asymptotic behaviour of a cylindrical elastic structure periodically reinforced along identical fibres. *IMA J Appl Math* 66(6):567–590
- Jouan G, Kotronis P, Collin F (2014) Using a second gradient model to simulate the behaviour of concrete structural elements. *Finite Elem Anal Des* 90:50–60
- Kamotski IV, Smyshlyaev VP (2019) Bandgaps in two-dimensional high-contrast periodic elastic beam lattice materials. *J Mech Phys Solids* 123:292–304
- Kouznetsova V, Geers MG, Brekelmans WM (2002) Multi-scale constitutive modelling of heterogeneous materials with a gradient-enhanced computational homogenization scheme. *Int J Numer Meth Eng* 54(8):1235–1260

- Lam DC, Yang F, Chong A, Wang J, Tong P (2003) Experiments and theory in strain gradient elasticity. *J Mech Phys Solids* 51(8):1477–1508
- Madeo A, George D, Lekszycki T, Nierenberger M, Rémond Y (2012) A second gradient continuum model accounting for some effects of micro-structure on reconstructed bone remodelling. *Comptes Rendus Mécanique* 340(8):575–589
- Mindlin RD (1964) Micro-structure in linear elasticity. *Arch Ration Mech Anal* 16(1):51–78
- Mindlin RD (1965) Second gradient of strain and surface-tension in linear elasticity. *Int J Solids Struct* 1(4):417–438
- Mindlin RD, Eshel N (1968) On first strain-gradient theories in linear elasticity. *Int J Solids Struct* 4(1):109–124
- Misra A, Poursolhjouy P (2016) Granular micromechanics based micromorphic model predicts frequency band gaps. *Continuum Mech Thermodyn* 28(1–2):215–234
- Nejadsadeghi N, Placidi L, Romeo M, Misra A (2019) Frequency band gaps in dielectric granular metamaterials modulated by electric field. *Mech Res Commun* 95:96–103
- Pideri C, Seppacher P (1997) A second gradient material resulting from the homogenization of an heterogeneous linear elastic medium. *Continuum Mech Thermodyn* 9(5):241–257
- Polyzos D, Fotiadis D (2012) Derivation of Mindlin’s first and second strain gradient elastic theory via simple lattice and continuum models. *Int J Solids Struct* 49(3–4):470–480
- Rahali Y, Ganghoffer JF, Chaouachi F, Zghal A et al (2015a) Strain gradient continuum models for linear pantographic structures: a classification based on material symmetries. *J Geometry Symm Phys* 40:35–52
- Rahali Y, Giorgio I, Ganghoffer J, dell’Isola F (2015b) Homogenization à la piola produces second gradient continuum models for linear pantographic lattices. *Int J Eng Sci* 97:148–172
- Rahali Y, Dos Reis F, Ganghoffer JF (2017) Multiscale homogenization schemes for the construction of second-order grade anisotropic continuum media of architected materials. *Int J Multiscale Comput Eng* 15(1)
- Reda H, Rahali Y, Ganghoffer J, Lakiss H (2016a) Nonlinear dynamical analysis of 3d textiles based on second order gradient homogenized media. *Compos Struct* 154:538–555
- Reda H, Rahali Y, Ganghoffer J, Lakiss H (2016b) Wave propagation analysis in 2d nonlinear hexagonal periodic networks based on second order gradient nonlinear constitutive models. *Int J Non-Linear Mech* 87:85–96
- Reda H, Rahali Y, Ganghoffer JF, Lakiss H (2016c) Analysis of dispersive waves in repetitive lattices based on homogenized second-gradient continuum models. *Compos Struct* 152:712–728
- Reda H, Rahali Y, Ganghoffer JF, Lakiss H (2017) Wave propagation analysis in 2d nonlinear periodic structures prone to mechanical instabilities. In: *Bridging the gap, from microstructure investigations to multiscale modeling*, pp 67–97
- Reda H, Karathanasopoulos N, Rahali Y, Ganghoffer JF, Lakiss H (2018) Influence of first to second gradient coupling energy terms on the wave propagation of three-dimensional non-centrosymmetric architected materials. *Int J Eng Sci* 128:151–164
- Rokoš O, Ameen MM, Peerlings R, Geers M (2019) Micromorphic computational homogenization for mechanical metamaterials with patterning fluctuation fields. *J Mech Phys Solids* 123:119–137
- Sili A (2005) Homogenization of an elastic medium reinforced by anisotropic fibers. *Asympt Anal* 42(1, 2):133–171
- Toupin RA (1962) Elastic materials with couple-stresses. *Arch Ration Mech Anal* 11(1):385–414
- Trinh DK, Janicke R, Auffray N, Diebels S, Forest S (2012) Evaluation of generalized continuum substitution models for heterogeneous materials. *Int J Multiscale Comput Eng* 10(6)
- Turco E, Giorgio I, Misra A, dell’Isola F (2017) King post truss as a motif for internal structure of (meta) material with controlled elastic properties. *R Soc Open Sci* 4(10):171.153
- Vladimir E et al (2003) *Wave processes in solids with microstructure*, vol 8. World Scientific, Singapore
- Yang F, Chong A, Lam DCC, Tong P (2002) Couple stress based strain gradient theory for elasticity. *Int J Solids Struct* 39(10):2731–2743

Chapter 5

An Application of Coulomb-Friction Model to Predict Internal Dissipation in Concrete



Giuliano Aretusi and Alessandro Ciallella

Abstract To explore the possibility of proper modeling, the dissipation in specimens made of concrete, a reduced two-degrees-of-freedom model, obtained from a nonlinear micromorphic model is employed in the case of cyclic mono-axial compressive tests. This model assumes that the nonlinear nature of the mechanical response arises from the microstructure and specifically from the micro-cracks regularly present in the cement matrix. The dissipation, therefore, is introduced as Coulomb-type friction associated with the relative motion of the faces of the micro-cracks. Numerical simulations showing that the proposed model is fitting to describe some of the known responses of the concrete are performed.

Keywords Continua with microstructure · Frictional sliding · Concrete-based material · Energy dissipation under cyclic load

5.1 Introduction

It is astonishing that one of the most used materials in civil engineering, namely the concrete, is still not utterly understood. Depending on how the term “concrete” is interpreted, one can say that human constructions are made of concrete for more than thousands of years. A long way has been covered since the dawn of civil engineering, and the concrete that at the beginning was crude cement made by crushing and burning gypsum or limestone nowadays is a more advanced and complex composite material. As a matter of fact, it is the internal microstructure of the concrete that bestows to the material its peculiar behavior. The various components that are used

G. Aretusi (✉)

MeMoCS - University of L'Aquila, 18 Via Giovanni Gronchi, 67100 L'Aquila, Italy

A. Ciallella

DICEAA - University of L'Aquila, 18 Via Giovanni Gronchi, 67100 L'Aquila, Italy
e-mail: alessandro.ciallella@univaq.it

© Springer Nature Switzerland AG 2021

F. Marmo et al. (eds.), *Mathematical Applications in Continuum and Structural Mechanics*, Advanced Structured Materials 127,
https://doi.org/10.1007/978-3-030-42707-8_5

in its recipe, i.e., Portland cement, sand, gravel with different sizes and shapes, produce a very heterogeneous material whose strength is particularly influenced by the water/cement ratio and the possibility of using additives that alter the properties of the final concrete chemically (Misra 1998) and/or mechanically (Scerrato et al. 2016). From a modeling viewpoint, many challenging aspects must be addressed to properly describe the behavior of such material, foremost among them there are the nonlinear behavior even in small deformation regime, the dissipation effects due to the microstructure both for the elastic and plastic regime, the evolution of the cracks inside it.

The microstructure of the concrete as the first level of conceptualization can be thought of as a matrix made by the solid phase of the cement paste that collects within it, distributed in a more or less uniform way, pieces of inert which comprise a quite large variety of sizes (Contrafatto et al. 2017; Bilotta et al. 2021). Moreover, the microstructure is still more complex because during the curing for the effect of the quantity and location of the chemical species and thermal cycles of heating and cooling (day and night), naturally inside the material originate a certain quantity of micro-cracks. These micro-cracks, generally speaking, affect the macroscopic behavior of the concrete. Still, unless the external loads, both mechanical and thermal, are not sufficiently large, they do not evolve, reducing, in turn, the strength of the material. To predict the behavior of the concrete, different models in the literature are exploited. Apart from the standard Cauchy model that decisively does not fit the purpose, other possibilities have been explored in the past in the framework of generalized continua. For instance, if one thinks of the stiffer aggregates inside the cement paste, one of the most straightforward ways to model the concrete is a Cosserat-type model (see, e.g., Giorgio et al. 2020a; Turco et al. 2019; De Borst and Sluys 1991; Eremeyev and Pietraszkiewicz 2016; Altenbach and Eremeyev 2014). On the other hand, the strong heterogeneity can suggest that some long-range interactions may play a decisive role (Pideri and Seppecher 1997; dell'Isola et al. 2015a, b; Javili et al. 2019), thus one can use a second gradient continuum (dell'Isola et al. 2017; Germain 2020; Epstein and Smelser 2020; Jouan et al. 2014; Matsushima et al. 2002) or rather a higher gradient continuum (Reiher et al. 2017; Alibert et al. 2003; Abali et al. 2017, 2015). Besides, there is room to treat the concrete as a porous material for the space left by the air in the curing process and for the micro-cracks (see, e.g., Coussy and Monteiro 2008; dell'Isola et al. 2009; Madeo et al. 2013; Gagneux and Millet 2016; Giorgio et al. 2020b).

On top of that the micro-cracks have a twofold effect on the macroscopic behavior of the concrete: the interaction between the opposite faces of them in compression—when they are in contact—and tension—when they are separated, namely open cracks—produces a lack of symmetry in the mechanical response of bulk material; in a cyclic mechanical compressive load these faces can slide each over the other and produce friction responsible of an internal dissipation (Pensée et al. 2002; Scerrato et al. 2014; Giorgio and Scerrato 2017). This last point is one of the most delicate because modeling the dissipation in mechanics of continuous solids is exceedingly tough (Bersani and Caressa 2020; Altenbach and Eremeyev 2008; Vaiana et al.

2019). Typically, a viscous action is used to deal with dissipation before any damage or plastic deformation occurs. However, albeit this model fits the description of a creep phenomenon in many cases, it is a rough linearization of the dissipative actions around a specific functioning point characterized by a fixed frequency of the external load. In a common transient excitation, many frequencies are involved, so this approximation is rather poor. On the other hand, the mechanism behind the dissipation seems to be related to a different cause. In the case of the concrete, it is most likely originated from the friction that the opposite faces of each micro-crack experience. Therefore, this kind of dissipation, being of Coulomb-type, is almost frequency-independent differently from viscous actions. Alternatively, rheological models are adopted to tackle the problem of dissipation in solid material (Banks et al. 2011; Lekszycki et al. 2017). This aspect sometimes bring to generalizations that conceive fractional derivatives (Smit and De Vries 1970; Rossikhin and Shitikova 2010; Carcaterra et al. 2015). An approach completely different instead makes use of a thermodynamical setup by introducing a diffusive internal variable that is meant to describe the dissipation (see for more details Maugin 2006; Ziegler and Wehrli 1987).

Finally, it is worth mentioning, even though it is beyond the purview of this paper, the efforts spent by many researchers to face the aspects of the problem related to plasticity and damage evolution. Herein, we recall some of these conceptual results, especially selecting from the literature those works based on a variational formulation. We believe indeed that this approach is always to be preferred because of its logical consistency and because it allows us to dispense with a needless increase of hypotheses (see, e.g., Contrafatto and Cuomo 2006; Contrafatto et al. 2012; Cuomo et al. 2014; Placidi et al. 2018a, b, 2019; Placidi and Barchiesi 2018; Alam and Loukili 2017; Timofeev et al. 2020). Recently, some studies on continuum mechanics were conducted using material particles acting in a sense like a swarm of robots. Some algorithms involving these ideas also deal with multi-crack damage showing an impressive computational efficiency (see, e.g., Della Corte et al. 2017; dell’Erba 2019a, b, 2018; Wiech et al. 2018).

In this context, a small notice of the issues of reinforced concrete also deserves to be made for the sake of completeness (Kezmane et al. 2017; dell’Isola et al. 2019; Franciosi et al. 2019; Spagnuolo et al. 2020).

In this work, we focus our attention on the dissipative effects occurring in the concrete in a small deformation regime to underline the Coulomb nature of this particular phenomenon. Specifically, we investigate a dissipative generalized model of the concrete proposed in Scerrato et al. (2014) through numerical simulations in order to illustrate the rate-independent behavior of the friction.

5.2 A Brief Synopsis of the Employed Model

5.2.1 3D Formulation of a Micromorphic Concrete-Based Material

In this section, we briefly recall the model used to describe the behavior of a concrete-based material (see Scerrato et al. 2014). This particular model considers the concrete as a generalized material, namely a continuum endowed with a microstructure. Two kinematical descriptors are introduced, a bulk displacement \mathbf{u} , which is a vector, and a scalar quantity representing the effect of the micro-cracks at a macroscopic level of observations, namely φ . The phenomenology that this last variable is aiming to capture takes into account the contact interaction between the opposite faces of the typical micro-cracks within the concrete that may slip each over the other, originating a friction interaction responsible for a loss of energy. In other words, the scalar quantity φ can be interpreted as the magnitude of the total amount of relative displacement of the micro-cracks lips in a given representative elementary volume (REV). Naturally, the scalar nature of the variable implies an isotropic hypothesis. A more general model can be conceived if one wants to consider the orientations of the micro-cracks, but for achieving this, a tensorial quantity should be employed instead (Adelaide et al. 2010).

In this framework, the considered energy density per unit of volume Ψ is assumed as follows:

$$\Psi(\nabla\mathbf{u}, \varphi) = \frac{1}{2} [\lambda (\text{tr } \mathbf{E})^2 + 2\mu \mathbf{E} \cdot \mathbf{E}] + \frac{1}{2}k_1\varphi^2 + \frac{1}{3}k_2\varphi^3 + \frac{1}{4}k_3\varphi^4 - \alpha\varphi\sqrt{I_2^{(d)}} \quad (5.1)$$

where it is possible to notice a standard dependence on the classical linearized strain tensor $\mathbf{E} = \text{Sym}(\nabla\mathbf{u})$, i.e., the symmetric part of $\nabla\mathbf{u}$, the nonlinear dependence on φ that can induce nonlinear behavior also for the displacement \mathbf{u} , which is similar to a Duffing oscillator, and finally the coupling terms between φ and the second invariant of the deviatoric strain tensor $\text{dev } \mathbf{E} = \mathbf{E} - \frac{1}{3}\text{tr } \mathbf{E} \mathbf{1}$, i.e.,

$$I_2^{(d)} = \frac{1}{2} \text{tr} (\text{dev } \mathbf{E} \text{ dev } \mathbf{E}). \quad (5.2)$$

Here, the rationale behind the coupling term is that an exchange of energy between the motion described by the two kinematic descriptors occurs when a shear bulk deformation induces a relative movement of the micro-cracks faces or vice versa. Therefore, the material parameters involved are the Lamé ones for linearly elastic isotropic materials, i.e., λ and μ , to which k_1 , k_2 , and k_3 are added to consider the tendency of the micro-cracks faces to prevent the slip each over the other, and α is the coupling coefficient between the micro-macro scales of the deformation. All these material parameters can be evaluated with specific techniques as done in

Scerrato et al. (2016), Giorgio et al. (2018), De Angelo et al. (2019), Abali et al. (2016), Misra and Poorsolhjoui (2015), Bolzon et al. (2002), Rosi et al. (2018).

To introduce the dissipation, a Rayleigh functional \mathcal{R} depending on the time rate of the micro-slip φ is considered. Specifically, we use the expression:

$$\mathcal{R} = \zeta \operatorname{tr} \mathbf{E} \left[\frac{\operatorname{Log}(\operatorname{Cosh}(\eta \dot{\varphi}))}{\eta} \right]. \quad (5.3)$$

This particular functional is conceived to obtain a dissipative internal force which resembles as close as possible a signum function and, therefore, a Coulomb-type friction force. Indeed, the derivative of \mathcal{R} with respect of the velocity $\dot{\varphi}$, i.e., the friction force is a hyperbolic tangent, η being the slope of this function near zero, or a coefficient of smoothness. This means that the dissipation is almost entirely viscous for low micro-velocities while increasing the micro-velocities, the Coulomb law becomes more significant. Besides, ζ is a material coefficient that takes into account the bulk stiffness of the material and the friction. Indeed, the bulk stiffness multiplied by the $\operatorname{tr} \mathbf{E}$ is nothing but the normal stress that close the micro-cracks and allows an internal dissipation by friction.

The inertial effects are introduced by postulating a kinetic energy density as follows:

$$\mathcal{K} = \frac{1}{2} \rho \dot{\mathbf{u}}^2 + \frac{1}{2} \rho_\varphi \dot{\varphi}^2 \quad (5.4)$$

where ρ is the apparent mass density at the macro-level and the ρ_φ is an effective mass density related to the microstructure of the micro-cracks. It is worth noting that for reasons of coherency among units of measure, the parameter ρ_φ is also a mass density.

By applying the generalized principle of virtual work, the equation of motion of the considered material can be written as

$$\delta W^{(Elast)} + \delta W^{(Iner)} + \delta W^{(Diss)} = \delta W^{(Ext)} \quad (5.5)$$

where the elastic and inertial virtual work are

$$\delta W^{(Elast)} = \int_V \delta \Psi \, dV, \quad \delta W^{(Iner)} = \int_V \rho \ddot{\mathbf{u}} \delta \mathbf{u} + \rho_\varphi \ddot{\varphi} \delta \varphi \, dV, \quad (5.6)$$

the virtual work done by the friction forces is obtained by

$$\delta W^{(Diss)}(\mathbf{E}, \varphi, \dot{\varphi}) = \int_V \left(\frac{\partial \mathcal{R}}{\partial \dot{\varphi}} \delta \varphi \right) dV = \int_V \zeta \operatorname{tr} \mathbf{E} \tanh(\eta \dot{\varphi}) \delta \varphi \, dV, \quad (5.7)$$

and, finally, the virtual work done by the external force is

$$\delta W^{(Ext)} = \int_V \mathbf{b}^{ext} \cdot \delta \mathbf{u} \, dV, \quad (5.8)$$

where the integrations are performed on the volume of the considered sample.

5.2.2 Simplified Formulation for the Case of a Pure Compression

To study a representative case, namely a pure compressive test, the Eq. (5.5) can be reduced to a set of two ODEs because we partially know the solution. Thus, we can employ this information to simplify the starting general PDE. As a matter of fact, the strain tensor and consequently the displacement vector in a pure compression can be represented in the form

$$\mathbf{E} = \begin{pmatrix} -\nu\varepsilon & 0 & 0 \\ 0 & -\nu\varepsilon & 0 \\ 0 & 0 & \varepsilon \end{pmatrix}, \quad \mathbf{u} = \begin{pmatrix} -\nu\varepsilon x_1 \\ -\nu\varepsilon x_2 \\ \varepsilon x_3 \end{pmatrix}, \quad (5.9)$$

for a cylindrical specimen whose longitudinal axis coincides with x_3 -axis of a reference coordinate frame. For the hypothesis of isotropy, the deformation is independent from the space along all the sample and can be made explicit as $\varepsilon = E_{33} = du_3/dx_3$. In this formulation, also the Poisson effect is considered as highlighted by the relative coefficient ν . The same isotropy allow us to assume uniform with the space also the micro-displacement field φ . By substituting the Eq. (5.9) in the principle of virtual work (5.5), one obtains the set of two ODEs in the variables $\varepsilon(t)$ and $\varphi(t)$ that are here only time dependent as follows:

$$\begin{cases} M\ddot{\varepsilon}(t) + K\varepsilon(t) + \tilde{\alpha}\varphi(t) = F(t) \\ m_\varphi\ddot{\varphi}(t) + \tilde{k}_1\varphi(t) + \tilde{k}_2\varphi^2(t) + \tilde{k}_3\varphi^3(t) + \tilde{\alpha}\varepsilon(t) - \tilde{\zeta}\tanh[\eta\dot{\varphi}(t)]\varepsilon(t) = 0 \end{cases} \quad (5.10)$$

where all the material parameters can be computed by

$$K = \int_V [\lambda + 2\mu + 4(\lambda + \mu)\nu^2 - 4\lambda\nu] dV, \quad \tilde{\alpha} = \int_V [\sqrt{3}/3(1 + \nu)\alpha] dV,$$

$$\tilde{k}_1 = \int_V k_1 dV, \quad \tilde{k}_2 = \int_V k_2 dV, \quad \tilde{k}_3 = \int_V k_3 dV, \quad \tilde{\zeta} = \int_V \zeta(1 - 2\nu) dV,$$

$$M = \int_V \rho [v^2(x_1^2 + x_2^2) + x_3^2] dV, \quad m_\varphi = \int_V \rho_\varphi dV,$$

in terms of the previously defined ones. Eventually, the external applied force has been chosen as a compression, hence $\mathbf{b}^{ext} = [0, 0, -b(t)]^T$. Therefore, the generalized load $F(t) = k b(t)$ being $k = \int_V x_3 dV$.

Table 5.1 Material coefficients used in numerical simulations

| K (Nm) | $\tilde{\alpha}$ (N) | \tilde{k}_1 (N/m) | \tilde{k}_2 (N/m ²) | \tilde{k}_3 (N/m ³) | η (s/m) | $\tilde{\zeta}$ (N) |
|-----------------------|----------------------|-----------------------|-----------------------------------|-----------------------------------|-------------------|---------------------|
| 5.81×10^{10} | 1.5×10^{11} | 9.65×10^{11} | 1.2×10^8 | 7.78×10^{18} | 2.0×10^4 | 7.29×10^9 |

Finally, we mention that a similar model reduction for the case of bending and compression has been made in Scerrato et al. (2015), but the complexity added with the bending deformation seems not to be very significative as the pure compression.

5.3 Numerical Simulations and Discussions

To illustrate the behavior of the investigated model, we solve the Eq. (5.10) deploying a Matlab code which makes use of the routine ode23s that evaluates the unknown variables at the next time step using a modified Rosenbrock formula of order 2, particularly fit to solve stiff problems. The external load is a cyclic sinusoidal load at a fixed frequency and with a mean value different from zero to assure that the micro-cracks responsible for the internal dissipation are closed, namely, the opposite faces are in contact (see Fig. 5.1). Naturally, this is a quite common example of a structural element when an earthquake occurs. Therefore, this kind of problem is of the utmost importance in understanding the behavior of the concrete in the presence of cyclic external loads. As a note, we consider a small initial transient which lasts one period of the sinus evaluated as a spline (3rd order polynomial) that starts with zero value and velocity and ends with the same value and derivative of the biased sinus. In other words, we have a G_1^1 connection between the two pieces of the loading curve. The reason for this choice lies in the fact that we want to avoid a sudden increase in force and therefore reducing possibly negative inertial effects. The mass parameters are roughly estimated as $M = 0.4616$ kg m², $m_\varphi = 0.5057$ kg. The other material parameters used in the numerical simulations are recorded in Table 5.1.

Specifically, we test the specimen under compression with an external load as plotted in Fig. 5.1, with different frequencies, namely 0.1, 0.5, 1, 2 Hz. Figure 5.2 shows clearly that all the frequencies but the one at 0.1 Hz are characterized by an almost coincident cycle and, therefore, by the same dissipation. Indeed, the figure exhibits the stress-strain curves for the loading and unloading of the sample, and the area of the cycle represents the dissipated energy at the specific frequency. Thus, as expected, the investigated model has a threshold behavior that, once exceeded, results in a dissipation that becomes almost rate-independent as predicted by the Coulomb-friction model. Before reaching the threshold, the primary behavior of the system is viscous and is governed by the parameter η , which represents the slope of the hyperbolic tangent near zero in Eqs. (5.10).

¹ Geometric continuity G_1 stands for the continuity of two curves together with their tangents in the contact point.

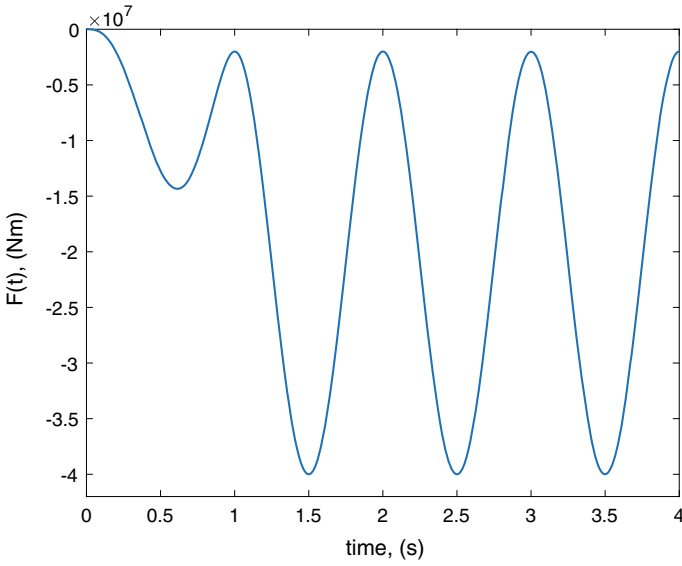


Fig. 5.1 External mechanical load applied to the sample, $F(t)$

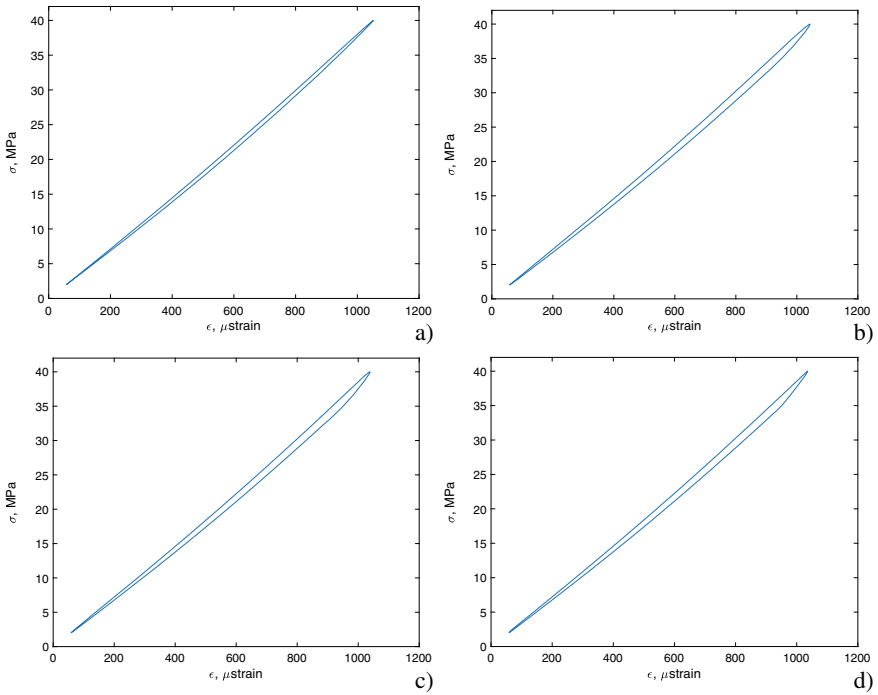


Fig. 5.2 Dissipative cycles for different frequencies: **a** 0.1 Hz; **b** 0.5 Hz; **c** 1 Hz; **d** 2 Hz

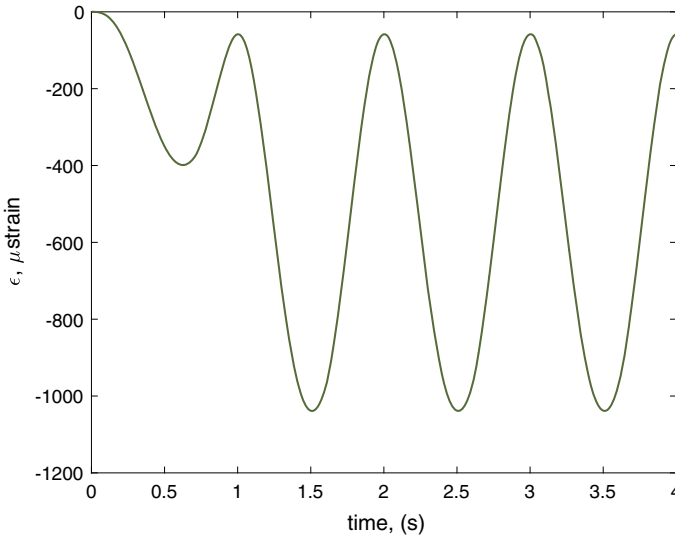


Fig. 5.3 Uniform compression $\varepsilon(t)$ for an applied cyclic load at a frequency 1 Hz

From a model viewpoint, this is very useful because by varying the parameter η , it is possible to increase or decrease the range of frequencies where the Coulomb behavior is prevalent. In Figs. 5.3 and 5.4, the kinematical descriptors are plotted in the case 1 Hz. They both show a nonlinear path, even though this more evident in the case of the micro-crack sliding variable φ .

Finally, Fig. 5.5 plot the dissipative internal generalized force $\tilde{\zeta} \tanh[\eta \dot{\varphi}(t)] \varepsilon(t)$ also in this case for a cyclic external load 1 Hz. In this plot, we remark that the characteristic trend of the generalized force is not as one can erroneously imagine almost a square wave ‘signal’ governed by the smooth version of the function *sign* (i.e., hyperbolic tangent), but rather a sawtooth wave. The reason behind this behavior is the presence of $\varepsilon(t)$ that modulates the amplitude of the signal. As a matter of fact, the friction force depends on the normal stress, in turns proportional to the compression $\varepsilon(t)$, that pushes in contact the opposite faces of the micro-cracks. Therefore, when the compression is low also the friction force is small in magnitude.

5.4 Conclusion

In this paper, we examine the predictive capabilities of a model conceived to describe the complex behavior of concrete-based materials as proposed in Scerrato et al. (2014). The model is quite useful because, regardless of its simplicity is able to take into account the nonlinear behavior of the material, even in the small regime of deformation, and its internal dissipation. This last effect is modeled with a Coulomb-

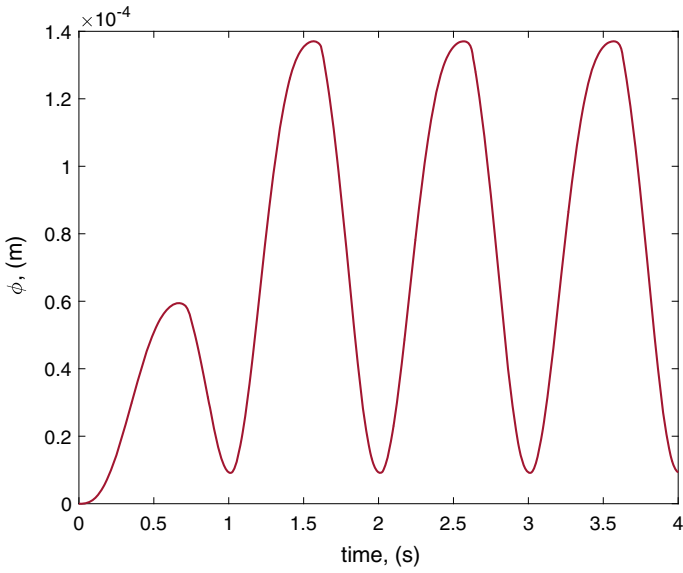


Fig. 5.4 Uniform micro-crack sliding variable φ for an applied cyclic load at a frequency 1 Hz

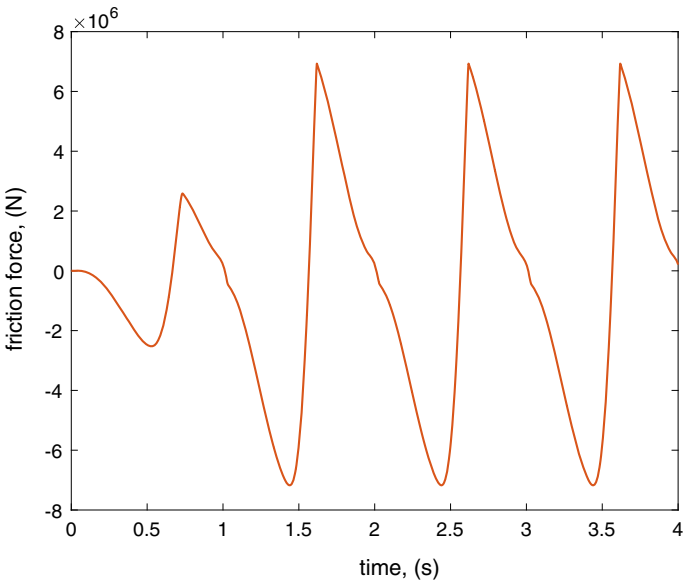


Fig. 5.5 Dissipative internal generalized force $\tilde{\zeta} \tanh[\eta \dot{\varphi}(t)] \varepsilon(t)$ for an applied cyclic load at a frequency 1 Hz

type model of friction and therefore turns to be rate-independent at least when a certain tunable threshold is exceeded. The presented study is complementary to other works on concrete (Sessa et al. 2018a, b, 2019b, 2015), with possible applications to civil engineering (Raeder et al. 2008; Sessa et al. 2019a, 2017; Li et al. 2018; Cricri et al. 2015).

References

- Abali BE, Müller WH, Eremeyev VA (2015) Strain gradient elasticity with geometric nonlinearities and its computational evaluation. *Mech Adv Mater Modern Process* 1(1):1–11
- Abali BE, Wu CC, Müller WH (2016) An energy-based method to determine material constants in nonlinear rheology with applications. *Continuum Mech Thermodyn* 28(5):1221–1246
- Abali BE, Müller WH, dell’Isola F (2017) Theory and computation of higher gradient elasticity theories based on action principles. *Arch Appl Mech* 87(9):1495–1510
- Adelaide L, Richard B, Ragueneau F, Cremona C (2010) Thermodynamical admissibility of a set of constitutive equations coupling elasticity, isotropic damage and internal sliding. *Comptes rendus mécanique* 338(3):158–163
- Alam SY, Loukili A (2017) Transition from energy dissipation to crack openings during continuum-discontinuum fracture of concrete. *Int J Fract* 206(1):49–66
- Alibert JJ, Seppecher P, Dell’Isola F (2003) Truss modular beams with deformation energy depending on higher displacement gradients. *Math Mech Solids* 8(1):51–73
- Altenbach H, Eremeyev V (2014) Strain rate tensors and constitutive equations of inelastic micropolar materials. *Int J Plast* 63:3–17
- Altenbach H, Eremeyev VA (2008) Analysis of the viscoelastic behavior of plates made of functionally graded materials. *ZAMM-Zeitschrift für Angewandte Mathematik und Mechanik: Applied Mathematics and Mechanics* 88(5):332–341
- Banks HT, Hu S, Kenz ZR (2011) A brief review of elasticity and viscoelasticity for solids. *Adv Appl Math Mech* 3(1):1–51
- Bersani AM, Caressa P (2020) Lagrangian descriptions of dissipative systems: a review. *Math Mech Solids*. <https://doi.org/10.1177/1081286520971834>
- Bilotta A, Causin A, Solci M, Turco E (2021) Representative volume elements for the analysis of concrete like materials by computational homogenization. In: *Mathematical modeling in cultural heritage*. Springer, Berlin, pp 13–35
- Bolzoni G, Fedele R, Maier G (2002) Parameter identification of a cohesive crack model by Kalman filter. *Comput Methods Appl Mech Eng* 191(25–26):2847–2871
- Carcattera A, Roveri N, Pepe G (2015) Fractional dissipation generated by hidden wave-fields. *Math Mech Solids* 20(10):1251–1262
- Contrafatto L, Cuomo M (2006) A framework of elastic-plastic damaging model for concrete under multiaxial stress states. *Int J Plast* 22(12):2272–2300
- Contrafatto L, Cuomo M, Fazio F (2012) An enriched finite element for crack opening and rebar slip in reinforced concrete members. *Int J Fract* 178(1–2):33–50
- Contrafatto L, Cuomo M, Greco L (2017) Meso-scale simulation of concrete multiaxial behaviour. *Eur J Environ Civ Eng* 21(7–8):896–911
- Coussy O, Monteiro PJ (2008) Poroelastic model for concrete exposed to freezing temperatures. *Cem Concr Res* 38(1):40–48
- Cricri G, Perrella M, Sessa S, Valoroso N (2015) A novel fixture for measuring mode iii toughness of bonded assemblies. *Eng Fract Mech* 138:1–18
- Cuomo M, Contrafatto L, Greco L (2014) A variational model based on isogeometric interpolation for the analysis of cracked bodies. *Int J Eng Sci* 80:173–188

- De Angelo M, Barchiesi E, Giorgio I, Abali BE (2019) Numerical identification of constitutive parameters in reduced-order bi-dimensional models for pantographic structures: application to out-of-plane buckling. *Arch Appl Mech* 89(7):1333–1358
- De Borst R, Sluys L (1991) Localisation in a Cosserat continuum under static and dynamic loading conditions. *Comput Methods Appl Mech Eng* 90(1–3):805–827
- Della Corte A, Battista A, dell’Isola F, Giorgio I (2017) Modeling deformable bodies using discrete systems with centroid-based propagating interaction: fracture and crack evolution. In: *Mathematical modelling in solid mechanics*. Springer, Berlin, pp 59–88
- dell’Erba R (2018) Position-based dynamic of a particle system: a configurable algorithm to describe complex behaviour of continuum material starting from swarm robotics. *Continuum Mech Thermodyn* 30(5):1069–1090
- dell’Erba R (2019a) On how swarm robotics can be used to describe particle system’s deformation. *Continuum Mech Thermodyn*, 1–21
- dell’Erba R (2019b) Swarm robotics and complex behaviour of continuum material. *Continuum Mech Thermodyn* 31(4):989–1014
- dell’Isola F, Madeo A, Sepecher P (2009) Boundary conditions at fluid-permeable interfaces in porous media: a variational approach. *Int J Solids Struct* 46(17):3150–3164
- dell’Isola F, Andreaus U, Placidi L (2015a) At the origins and in the vanguard of peridynamics, non-local and higher-gradient continuum mechanics: an underestimated and still topical contribution of Gabrio Piola. *Math Mech Solids* 20(8):887–928
- dell’Isola F, Sepecher P, Della Corte A (2015b) The postulations à la D’Alembert and à la Cauchy for higher gradient continuum theories are equivalent: a review of existing results. *Proc R Soc A: Math, Phys Eng Sci* 471(2183):20150415
- dell’Isola F, Della Corte A, Giorgio I (2017) Higher-gradient continua: the legacy of Piola, Mindlin, Sedov and Toupin and some future research perspectives. *Math Mech Solids* 22(4):852–872
- dell’Isola F, Bragov AM, Igunnov LA, Abali BE, Lomunov AK, Lamzin DA, Konstantinov AY (2019) Mechanical response change in fine grain concrete under high strain and stress rates. In: Altenbach H, dell’Isola F, Eremeyev V, Öchsner A (eds) *Abali B. New achievements in continuum mechanics and thermodynamics*. Springer, Berlin, pp 71–80
- Epstein M, Smelser R (2020) An appreciation and discussion of Paul Germain’s “The method of virtual power in the mechanics of continuous media, I: second-gradient theory”. *Math Mech Complex Syst* 8(2):191–199
- Eremeyev VA, Pietraszkiewicz W (2016) Material symmetry group and constitutive equations of micropolar anisotropic elastic solids. *Math Mech Solids* 21(2):210–221
- Franciosi P, Spagnuolo M, Salman OU (2019) Mean green operators of deformable fiber networks embedded in a compliant matrix and property estimates. *Continuum Mech Thermodyn* 31(1):101–132
- Gagneux G, Millet O (2016) Modeling capillary hysteresis in unsaturated porous media. *Math Mech Complex Syst* 4(1):67–77
- Germain P (2020) The method of virtual power in the mechanics of continuous media, I: second-gradient theory. *Math Mech Complex Syst* 8(2):153–190
- Giorgio I, Scerrato D (2017) Multi-scale concrete model with rate-dependent internal friction. *Eur J Environ Civ Eng* 21(7–8):821–839
- Giorgio I, Harrison P, dell’Isola F, Alsayednoor J, Turco E (2018) Wrinkling in engineering fabrics: a comparison between two different comprehensive modelling approaches. *Proc R Soc A: Math, Phys Eng Sci* 474(2216):20180063
- Giorgio I, De Angelo M, Turco E, Misra A (2020a) A Biot-Cosserat two-dimensional elastic non-linear model for a micromorphic medium. *Continuum Mech Thermodyn* 32:1357–1369
- Giorgio I, Spagnuolo M, Andreaus U, Scerrato D, Bersani AM (2020b) In-depth gaze at the astonishing mechanical behavior of bone: a review for designing bio-inspired hierarchical metamaterials. *Math Mech Solids*. <https://doi.org/10.1177/1081286520978516>
- Javili A, Morasata R, Oterkus E, Oterkus S (2019) Peridynamics review. *Math Mech Solids* 24(11):3714–3739

- Jouan G, Kotronis P, Collin F (2014) Using a second gradient model to simulate the behaviour of concrete structural elements. *Finite Elem Anal Des* 90:50–60
- Kezmane A, Chiaia B, Kumpyak O, Maksimov V, Placidi L (2017) 3D modelling of reinforced concrete slab with yielding supports subject to impact load. *Eur J Environ Civ Eng* 21(7–8):988–1025
- Lekszycki T, Bucci S, Del Vescovo D, Turco E, Rizzi NL (2017) A comparison between different approaches for modelling media with viscoelastic properties via optimization analyses. *ZAMM-Zeitschrift für Angewandte Mathematik und Mechanik* 97(5):515–531
- Li Y, Chen Y, Li T, Cao S, Wang L (2018) Hoberman-sphere-inspired lattice metamaterials with tunable negative thermal expansion. *Compos Struct* 189:586–597
- Madeo A, dell’Isola F, Darve F (2013) A continuum model for deformable, second gradient porous media partially saturated with compressible fluids. *J Mech Phys Solids* 61(11):2196–2211
- Matsushima T, Chambon R, Caillerie D (2002) Large strain finite element analysis of a local second gradient model: application to localization. *Int J Numer Meth Eng* 54(4):499–521
- Maugin GA (2006) On canonical equations of continuum thermomechanics. *Mech Res Commun* 33(5):705–710
- Misra A (1998) Stabilization characteristics of clays using class C fly ash. *Transp Res Rec* 1611(1):46–54
- Misra A, Poolsolhjouy P (2015) Identification of higher-order elastic constants for grain assemblies based upon granular micromechanics. *Math Mech Complex Syst* 3(3):285–308
- Pensée V, Kondo D, Dormieux L (2002) Micromechanical analysis of anisotropic damage in brittle materials. *J Eng Mech* 128(8):889–897
- Pideri C, Seppecher P (1997) A second gradient material resulting from the homogenization of an heterogeneous linear elastic medium. *Continuum Mech Thermodyn* 9(5):241–257
- Placidi L, Barchiesi E (2018) Energy approach to brittle fracture in strain-gradient modelling. *Proc R Soc A: Math, Phys Eng Sci* 474(2210):20170,878
- Placidi L, Barchiesi E, Misra A (2018a) A strain gradient variational approach to damage: a comparison with damage gradient models and numerical results. *Mathematics and Mechanics of Complex Systems* 6(2):77–100
- Placidi L, Misra A, Barchiesi E (2018b) Two-dimensional strain gradient damage modeling: a variational approach. *Z Angew Math Phys* 69(3):1–19
- Placidi L, Misra A, Barchiesi E (2019) Simulation results for damage with evolving microstructure and growing strain gradient moduli. *Continuum Mech Thermodyn* 31(4):1143–1163
- Raeder J, Larson D, Li W, Kepko EL, Fuller-Rowell T (2008) Openpgcm simulations for the themis mission. *Space Sci Rev* 141(1):535–555
- Reiher JC, Giorgio I, Bertram A (2017) Finite-element analysis of polyhedra under point and line forces in second-strain gradient elasticity. *J Eng Mech* 143(2):04016,112
- Rosi G, Placidi L, Auffray N (2018) On the validity range of strain-gradient elasticity: a mixed static-dynamic identification procedure. *Eur J Mech-A/Solids* 69:179–191
- Rossikhin YA, Shitikova MV (2010) Application of fractional calculus for dynamic problems of solid mechanics: novel trends and recent results. *Appl Mech Rev* 63(1)
- Scerrato D, Giorgio I, Madeo A, Limam A, Darve F (2014) A simple non-linear model for internal friction in modified concrete. *Int J Eng Sci* 80:136–152
- Scerrato D, Giorgio I, Della Corte A, Madeo A, Limam A (2015) A micro-structural model for dissipation phenomena in the concrete. *Int J Numer Anal Meth Geomech* 39(18):2037–2052
- Scerrato D, Giorgio I, Della Corte A, Madeo A, Dowling N, Darve F (2016) Towards the design of an enriched concrete with enhanced dissipation performances. *Cem Concr Res* 84:48–61
- Sessa S, Marmo F, Rosati L (2015) Effective use of seismic response envelopes for reinforced concrete structures. *Earthquake Eng Struct Dyn* 44(14):2401–2423
- Sessa S, Serpieri R, Rosati L (2017) A continuum theory of through-the-thickness jacketed shells for the elasto-plastic analysis of confined composite structures: Theory and numerical assessment. *Compos B Eng* 113:225–242

- Sessa S, Marmo F, Rosati L, Leonetti L, Garcea G, Casciaro R (2018a) Evaluation of the capacity surfaces of reinforced concrete sections: Eurocode versus a plasticity-based approach. *Meccanica* 53(6):1493–1512
- Sessa S, Marmo F, Vaiana N, Rosati L (2018b) A computational strategy for eurocode 8-compliant analyses of reinforced concrete structures by seismic envelopes. *J Earthquake Eng*, 1–34
- Sessa S, Marmo F, Vaiana N, De Gregorio D, Rosati L (2019a) Strength hierarchy provisions for transverse confinement systems of shell structural elements. *Compos B Eng* 163:413–423
- Sessa S, Marmo F, Vaiana N, Rosati L (2019b) Probabilistic assessment of axial force-biaxial bending capacity domains of reinforced concrete sections. *Meccanica* 54(9):1451–1469
- Smit W, De Vries H (1970) Rheological models containing fractional derivatives. *Rheol Acta* 9(4):525–534
- Spagnuolo M, Franciosi P, dell’Isola F (2020) A green operator-based elastic modeling for two-phase pantographic-inspired bi-continuous materials. *Int J Solids Struct* 188:282–308
- Timofeev D, Barchiesi E, Misra A, Placidi L (2020) Hemivariational continuum approach for granular solids with damage-induced anisotropy evolution. *Math Mech Solids*. <https://doi.org/10.1177/1081286520968149>
- Turco E, dell’Isola F, Misra A (2019) A nonlinear Lagrangian particle model for grains assemblies including grain relative rotations. *Int J Numer Anal Meth Geomech* 43(5):1051–1079
- Vaiana N, Sessa S, Marmo F, Rosati L (2019) Nonlinear dynamic analysis of hysteretic mechanical systems by combining a novel rate-independent model and an explicit time integration method. *Nonlinear Dyn* 98(4):2879–2901
- Wiech J, Eremeyev VA, Giorgio I (2018) Virtual spring damper method for nonholonomic robotic swarm self-organization and leader following. *Continuum Mech Thermodyn* 30(5):1091–1102
- Ziegler H, Wehrli C (1987) The derivation of constitutive relations from the free energy and the dissipation function. *Adv Appl Mech* 25:183–238

Chapter 6

From the Swarm Robotics to Material Deformations



Paolo D'Avanzo, Alessio Ciro Rapisarda, and Salvatore Samuele Sirletti

Abstract In this chapter a discrete 2D kinematic system model is presented. Its aim is to reproduce the behavior of several 2D continuum systems. We started from studies on swarm robotics; in these papers, simple interaction laws among the elements of the swarm are used to manage its behavior. We have employed them to simulate materials deformation. This model seems to be promising because it is able to qualitatively reproduce standard deformations and a lot of exotic phenomena that other methods in literature can't reproduce. Furthermore, it has a low computational cost and it is parallelizable, allowing us to take profit of CUDA[®] architecture. Some numerical simulations are provided and discussed using two different kinds of lattices and changing some model's parameters.

Keywords Discrete mechanical system · Second gradient continua · Elastic law · Swarm robotics · Numerical simulations · Exotic phenomena

6.1 Introduction

Simulation of non-standard continua behavior is gaining interest nowadays. This happens because standard deformation models, like Cauchy, are unable to describe the behavior of modern composite Casale et al. (1998) and structured materials Dell'Erba (2001). Therefore, there is the need to find new numerical approaches allowing us to obtain these exotic behaviors. In the literature, it is possible to find some models with this purpose, for example, the Position-Based Dynamics (PBD) (Müller et al. (2005, 2007)) and the swarm robotic model (dell'Erba 2015; Dell'Erba 2020a, 2021a; Şahin 2005; Battista et al. 2018): they are briefly described in this chapter; our own model is inspired by these models and can obtain the researched results with lower computational cost. An important aspect that must be considered is that our model is purely kinematic, i.e., there are not forces or masses; there are only laws that rule the motion of points. The algorithm developed is parallelizable and

P. D'Avanzo (✉) · A. C. Rapisarda · S. S. Sirletti
University of Naples Federico II, Naples, Italy

runs with CUDA® programming language, so we can obtain numerical simulations in few seconds, also if they are very complex and using a modest desktop PC. Another important aspect of our model to be considered is the possibility to correlate it to the theory of generalized continua.

We are aware of the fact that a lot of mathematical results are demanding for proving; we believe that the presented computation scheme is somehow equivalent to those used in continuum mechanics. This hypothesis requires an in-depth investigation in this direction. But it is our opinion that the model can be useful in a large variety of mechanical application. In particular, we believe that the demanding computational problems to be faced in:

1. second gradient continuum theory (Abdoul-Anziz et al. 2019; Barchiesi et al. 2019a; Scerrato et al. 2016; Sciarra et al. 2007; Turco et al. 2016a; Epstein and Smelser 2020; Germain 2020; Yang and Misra 2012);
2. peridynamics (Dell'Isola et al. 2015a; Javili et al. 2019);
3. explicit time integration (Vaiana et al. 2019; Greco et al. 2018a);
4. plasticity (Sessa et al. 2017, 2018a; Serpieri et al. 2018);
5. concrete structures (Sessa et al. 2019b; Marmo et al. 2019);
6. masonry structures (Marmo et al. 2018a, b);
7. bone growth phenomena and biomimetics (George et al. 2018, 2020; Giorgio et al. 2016, 2017a, 2019b, 2020b; Rapisarda et al. 2018, 2020; Perricone et al. 2020);
8. generalized shell theories (Altenbach et al. 2010; Altenbach and Eremeyev 2011, 2015; Giorgio 2020b; Steigmann 2018; Spagnuolo et al. 2020; Giorgio et al. 2021; Altenbach and Eremeyev 2008a, b; Andreaus et al. 2018; Bilotta et al. 2019; Desmorat et al. 2020; Steigmann and dell'Isola 2015; Sessa et al. 2017, 2019a; Valoroso et al. 2015) and composite laminates (Cazzani and Ruge 2016; Cazzani et al. 2018b, a; Giorgio et al. 2021; Browning and Askes 2019; Altenbach et al. 2015);
9. beams in large deformations (Baroudi et al. 2019; Giorgio and Del Vescovo 2018, 2019; Barchiesi et al. 2020b, a, 2021a; Spagnuolo and Andreaus 2019; Paradiso et al. 2021, 2019);
10. seismic analysis (Vaiana et al. 2017, 2021; Sessa et al. 2018b, 2015);
11. micro-morphic (Misra and Poorsolhjoui 2016b, a; Misra et al. 2020; Giorgio and Scerrato 2017; Giorgio et al. 2019a; Abali et al. 2012; Gagneux and Millet 2016; Rickert et al. 2019; Franciosi et al. 2019; Scerrato et al. 2014) and micro-polar continuum theories (Altenbach and Eremeyev 2015; Eremeyev and Pietraszkiewicz 2016; Giorgio 2020a; Greco 2020; Eugster et al. 2014; Olive 2019; Turco et al. 2019; Turco 2018b);

maybe dramatically simplified if the algorithm presented here will prove to be an efficient integration scheme for all mentioned continuum models (see, e.g., also Wiech et al. 2018). It has to be remarked that generalized continua already demanded the introduction of complex integration schemes, among which we believe that isogeometric ones are of particular relevance (Cuomo et al. 2014; Greco et al. 2018b; Niiranen et al. 2016; Cazzani et al. 2016a, b, c; Yildizdag et al. 2020b; Schulte et al. 2020; Tran and Niiranen 2020).

Therefore, we believe that the algorithm presented here not only can represent a powerful predictive tool in metamaterial theory (Barchiesi et al. 2019c, 2021b; Dell’Isola et al. 2015b, 2019; Del Vescovo and Giorgio 2014; Eremeyev and Turco 2020; Eugster et al. 2019; Scerrato and Giorgio 2019; Spagnuolo 2020; Vangelatos et al. 2019; Yang et al. 2019; Yildizdag et al. 2019; Alibert et al. 2003; Seppacher et al. 2011; Giorgio et al. 2017b, 2019c, 2020a; Cuomo et al. 2016; Yildizdag et al. 2020a; Spagnuolo and Scerrato 2020), and in general in the theory of deformable bodies, but also can represent a heuristic tool in helping in search of micro-macro identification results (De Angelo et al. 2019a; Rosi et al. 2018; Giorgio et al. 2018; Andreus et al. 2016; Barchiesi et al. 2019b; Boutin et al. 2017; De Angelo et al. 2020; Placidi et al. 2017; Abali et al. 2016; NejadSadeghi et al. 2019; Yang et al. 2018; Bolzon et al. 2002).

It has to be remarked that the presented algorithm can be used for calculating families of equilibrium shapes by using variable load parameters, in a very similar way as done in continuum mechanics (Turco et al. 2020; Turco and Barchiesi 2019; Turco 2018a, 2019; Boutin et al. 2017). When damage phenomena occur in standard continuum mechanics, some Karush–Kuhn–Tucker (KKT) conditions (Placidi 2016; Placidi et al. 2018a, b; Timofeev et al. 2020) need to be used in order to take into account for plastic and damage phenomena or crack onset (Cuomo 2019; De Angelo et al. 2019b; Bilotta et al. 2018). All quoted dissipation phenomena can be more easily modeled in the present algorithm, employing the purely deformation-based criterion already in Spagnuolo et al. (2017), Turco et al. (2016b). We believe that by introducing a similar threshold in our algorithm, it will be possible to predict not only crack onset and damage progression, but also plastic phenomena (Contrafatto and Cuomo 2002; Del Piero 2018; Cuomo 2017; Vaiana et al. 2018).

The chapter is organized as follows: in the second section, we recall the principal and most important other models used in the literature from which our model takes origin; in the third section, we construct step by step our own model. The fourth section is dedicated to show some numerical simulations obtained; we divide them into two groups: the standard ones and the exotic ones. In the last section, conclusions with advantages and disadvantages are discussed.

6.2 Other Models in Literature

In literature there are several other models and methods that can approximate the evolution of material under deformations; many of them share the use of points linked by an interaction or a law that manages the motion of points in space. We started from the study of these to develop a slightly different-mixed approach, so here we briefly recap some important methods that inspired us.

6.2.1 Position-Based Dynamics (PBD)

The Position-Based Dynamics (PBD) method of Matthias Müller was described in his article (Müller et al. 2005, 2007). In this method, the dynamic object is approximated by a set of vertices and the internal forces by constraints (the external forces are used in the definition of the vertices velocities in a classical way). The vertices have a position \mathbf{x}_i , velocity \mathbf{v}_i , and a mass, whose reciprocal is w_i , meanwhile there are different constraint functions C_j that are used to simulate various types of materials and particular behaviors in PBD. The main task of the PBD method is to handle the positions of the vertices, in fact, every time step, as shown in Table 6.1, the velocities are evaluated and slightly dumped only to get the “virtual” new positions $\tilde{\mathbf{x}}$. These are checked and rearranged to satisfy the constraints (for example, the distance between two vertices) typically using a Gauss-Seidel-type iteration. This kind of solving method is fast and allows to obtain good-like simulations in real time (this is the reason why it is used to reproduce the physics in some video games).

This method is able to simulate collisions among objects (generating specific constraints), simulate friction (updating the velocities after their upgrade), avoid autocom penetrations, and simulate the breaking.

6.2.2 Swarm Robotics

Unlike the PBD method, in which the external forces are used, the swarm robotics use a kinematic approach where a forced motion to some elements is imposed. In this method, the material is seen as an ensemble elements that compose a swarm geometric

Table 6.1 The algorithm operation scheme of the PBD method shown in Müller et al. (2007)

| | |
|------|--|
| (1) | loop |
| (2) | for-all the vertices i do $\mathbf{v}_i \leftarrow \mathbf{v}_i + \Delta t w_i \mathbf{f}_{ext}(\mathbf{x}_i)$ |
| (3) | DumpVelocities($\mathbf{v}_1, \dots, \mathbf{v}_N$) |
| (4) | for-all the vertices i do $\tilde{\mathbf{x}}_i \leftarrow \mathbf{x}_i + \Delta t \mathbf{v}_i$ |
| (5) | for-all the vertices i do generate Collision Constraints($\mathbf{x}_i \rightarrow \tilde{\mathbf{x}}_i$) |
| (6) | loop solver Iterations times |
| (7) | project Constraints($C_1; \dots; C_{M+M_{coll}}; \tilde{\mathbf{x}}_1; \dots; \tilde{\mathbf{x}}_N$) |
| (8) | end loop |
| (9) | for-all the vertices i |
| (10) | $\mathbf{v}_i \leftarrow (\tilde{\mathbf{x}}_i - \mathbf{x}_i) / \Delta t$ |
| (11) | $\mathbf{x}_i \leftarrow \tilde{\mathbf{x}}_i$ |
| (12) | end for |
| (13) | velocityUpdate($\mathbf{v}_1; \dots; \mathbf{v}_N$) |
| (14) | end loop |

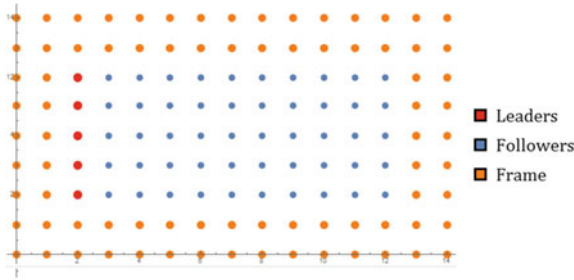


Fig. 6.1 An example of the three types of points for a square lattice, in red the leaders, in blue the followers, and in orange the frame points. We underline the presence of two shells of frame points that means the use of an interaction that includes first and second neighbors of every follower

configuration (dell’Erba 2015); the idea is that these simple-acting elements together can describe more complex behaviors. This approach is defined in Şahin (2005), Moriconi and Dell’Erba (2014), Dell’Erba (2018, 2019a, 2020b, 2021b, c) as

Swarm robotics is the study of how a large number of relatively simple physically embodied agents can be designed such that a desired collective behavior emerges from the local interactions among agents and between the agents and the environment.

The works, which were our start point in this research, Battista et al. (2016; 2018) and Dell’Erba (2019b) are based on this approach: “Can we describe a material under deformations through tiny robots that control every time the relative distances as in Dell’Erba (2020a, 2021a)?”. So inspired by the natural swarms, in which there are leader elements that control the motions of the followers, and so of the entire swarm, in these models, there are three principal categories of point as shown in Fig. 6.1:

- **Leaders** that have a forced movement simulating external interaction of the swarm, for example, like a tensile test machine that brings in opposite direction two sides of a metal bar;
- **Followers**, that are the majority of the swarm, represent tiny pieces of the chosen material and every follower has a movement induced by the positions of its neighbors points of the swarm as a centroid rule;
- **Frame points**, points added with the only purpose to balance the lack of neighbors and make sure that the interaction always takes place among the same number of points for the followers closer the edges of the swarm. Every frame point has one or more linked points (followers and/or leaders) and their movement is defined as follow them.

These models divide the neighbors points of a considered point in shell categorized by the distance¹ from it and the type of lattice used. So it is possible to identify first neighbors, second neighbors, and virtually so on. The use of more shells of neighbors

¹ The kind of method used to evaluate the distance influences the shape of the shells. Usually for swarm based on centered square cells (like in Fig. 6.1) is proposed the Chebyshev distance.

Table 6.2 The algorithm operation scheme of the model proposed in Dell'Erba (2019b) with the use of the Centroid rule

| | | |
|-----|---|------------------------------|
| (1) | for-all “time” step i | |
| (2) | for-all Leader j | |
| (3) | do $\mathbf{x}_j^{(i)} = \mathbf{x}_j^{(i-1)} + \mathbf{v}_j^{(i)}$ | (the Leaders are translated) |
| (4) | for-all Follower k | |
| (5) | do $\mathbf{x}_k^{(i)} = \mathbf{Centroid}[\mathit{neighbors}_k]$ | (the Followers are moved) |
| (6) | for-all Frame point h | |
| (7) | do $\mathbf{x}_h^{(i)} = \mathbf{Average_mov}[\mathit{linked_points}_h]$ | (the Frame is moved) |
| (8) | end for | |

allows to obtain more features of the deformations and it is linked with higher gradient order continua as explained in Battista et al. (2016). Then the algorithm proceeds for every iteration following the instructions shown in Table 6.2. As the algorithm steps proceed, the points are moved every iteration: first the leaders, then one by one the followers, and finally the frame as a whole.

6.3 The Model Here Proposed

The model proposed here starts from an approach very similar to that used in Swarm-based models, in fact, in our model is maintained a division in the role of the points, but it eventually becomes similar to a PBD model in some features. Before we have developed the model here presented, we have studied a quite similar model with spring interactions with dynamical evolution carried out with differential equations; this approach is hardly efficient for its computational costs but it gives us some important hints about how to develop the model here proposed.

First of all, we have to make an important specification: In our model, we have only a set of variables, which are points of a Cartesian plane, which change coordinates with the increase of a certain discrete parameter. Therefore, physical concepts such as “motion”, “time” or “velocity” do not exist in our model. The update calculation of the coordinates of our set of points is done through an algorithm (explained in detail in the next section).

We will explore in further papers in quantitatively way the parallelism among some parameters and characteristics of our model and the physics of deformations, so here we will use some terms only through analogy, such as the discrete parameter that orders the iteration of the algorithm will be called “pseudo-time”, just as a single execution of the algorithm (one run of the iteration) will be called “single pseudo-temporal step” or simply “p-time step”, the “updated-trajectory” of a point will indicate the updating of the coordinates of the point (that we call “updated-position” or simply “coordinates” of a point) with a single execution of the algorithm (therefore

in a p-time step) and the “updated-velocity” of a point is the difference between the actual and the previous updated-position. But, we remark again all the variables and parameters that we use are dimensionless and devoid of any real physical meaning. Therefore, it must not be made the mistake of apply standard concepts of physics to our model. The latter, in fact, is composed only of points and an algorithm that redefines their coordinates at each iteration. We will analyze in detail in the next papers the connection between our model and a continuous model, and therefore, among our parameters and those of the physics of deformations.

6.3.1 A Recall About Graph Theory

Our model is based on some concepts of the graph theory (i.e., the lattice, the neighborhood of a point, and the adjacency matrix). A graph is a mathematical structure used to model pairwise relations between objects. To be more specific, let us indicate a graph $G = (P, L)$ as an ordered couple of a set P of “points”, a set L “links” (a pair of points). We will consider only undirected graphs, meaning that there is no direction associated with links. Considering n points P_i , with $i \in \{1, \dots, n\}$, we define the adjacency matrix that carries all the information on the connected points, as the matrix \mathcal{A} of dimension $n \times n$ defined by:

$$\mathcal{A}_{ij} = 1 \text{ if } V_i \text{ is linked to } P_j, \quad 0 \text{ if } V_i \text{ is not linked to } P_j \quad (6.1)$$

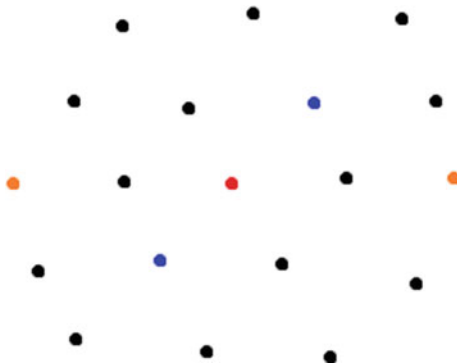
The one given above is the standard definition of adjacency matrix, but as we will see, in order to fulfill some properties in our swarm, we need to modify it to define the neighborhood of a point.

It is possible to define a path on the graph. It is a finite or infinite sequence of links that joins the sequence of points; this will be useful to define the concept of neighborhood order.

6.3.2 Constructing the Model

Let us consider a swarm \mathcal{S} constituted by a finite number of elements, and let us indicate by C_0 the reference configuration of \mathcal{S} . In C_0 , the elements of \mathcal{S} occupy all the points of a generic lattice with step σ . We consider a set of p-time steps, i.e., a set of ordered discrete values for the pseudo-time variable t that we will denote with $\mathcal{T} = \{t_0, t_1, \dots, t_m, \dots\}$. We indicate the elements of \mathcal{S} (at a pseudo-time t_m) by means of an index i like $P_i(t_m) = (r_i^1, r_i^2)(t_m)$ that are the coordinates of the i -th point in C_0 at the pseudo-time t_m in a orthogonal reference system. For each element i in C_0 , we define a chosen number of sets of points representing the k -th neighbors of i .

Fig. 6.2 Here we highlight two different couples of neighbors (one in blue and one in orange), in the set of the first and second neighbors (\mathcal{N}_2) of the considered point, marked in red, on a hexagonal lattice. In particular, we have indicated in blue a couple of first neighbors and in orange a couple of second neighbors of the red point



The first neighbors of a point P_i are all the points of C_0 adjacent to the point P_i in the meaning of the graphs (so it is linked with the coordination number of the lattice). The second neighbors of a point P_i are all the points of C_0 whose minimum path without repetitions is composed of only two links. Therefore, defining $l(i, j)$ as the minimum path without repetitions between points i and j , the k -th neighbors of a point i is the set

$$\mathcal{N}_k(i) = \{j \in C_0 : l(i, j) = k\} \quad (6.2)$$

that we call “shell” of order k .

We will also consider pairs of opposite neighbors compared to a considered point. The pairs collection of opposite k -order neighbors of a point P_i is the set

$$\mathcal{P}_k(i) = \{(h, g) \in \mathcal{N}_k(i) \times \mathcal{N}_k(i) : (P_h - P_i) = -(P_g - P_i)\}, \quad (6.3)$$

so the j -th pair of the point P_i will be indicated with ρ_{ij} , see Fig. 6.2.

Note that $\mathcal{N}_k(i)$ is the i -th row of the adjacency matrix: this means that our adjacency matrix \mathcal{A} is not $n \times n$ but $n \times m$ where m is the number of the total neighbors considered until the k -th order. Let us select a set of Leaders \mathcal{L} , they are a subset of C_0 to which is imposed an updated-trajectory, i.e., a collection of positions in our reference system for each p-time step. Instead, all the remaining elements of C_0 form the set of the followers \mathcal{F} , so $C_0 = \mathcal{L} \cup \mathcal{F}$; the updated-trajectory of each point $P_i \in \mathcal{F}$ is defined by the coordinate of its neighbors until the k -th order considered. For constructing the model, we are interested to have an elastic interaction between the points in order to obtain a swarm that exhibits a behavior qualitatively similar to an elastic continuum. For this reason, we have started from a system of equations that rules the kinematic a point P_i that belongs to a system of points with elastic interaction among them; then, for not burden the model with the researching of ODE’s solutions, we simplify the classic equations in order to obtain an approximation that leads to a faster algorithm for our model. Moreover, we have enriched the model by introducing another interaction aimed to emphasize the response of the swarm to the shear and

flexural simulations. There follow the equations that define the interaction law for our model:

$$\mathbf{r}_i(t_{m+1}) = \mathbf{r}_i(t_m) + \mathbf{Int}_i(t_m) \quad (6.4)$$

$$\mathbf{Int}_i(t_{m+1}) = \sum_{h=1}^k \left(\left[\sum_{j \in \mathcal{N}_h(i)} (\mathbf{A}_{ij}(t_m)) \right] + \left[\sum_{l \in \mathcal{P}_h(i)} (\mathbf{B}_{il}(t_m)) \right] \right) \quad (6.5)$$

$$\mathbf{A}_{ij}(t_m) = -\frac{\alpha_j}{N_i} (R_{ij}(t_m) - R_{ij}(t_0)) \frac{\mathbf{r}_i(t_m) - \mathbf{r}_{ij}(t_m)}{|\mathbf{r}_i(t_m) - \mathbf{r}_{ij}(t_m)|} \quad (6.6)$$

$$\mathbf{B}_{il}(t_m) = -\frac{\beta_l}{N_i} (\mathbf{r}_i(t_m) - \langle \rho_{il}(t_m) \rangle) \quad (6.7)$$

where all the quantities in the equations are in Table 6.3.

Let a point P_i and its j -th neighbor, the term A_{ij} is proportional to the difference between the actual distance $|\mathbf{r}_i(t_m) - \mathbf{r}_{ij}(t_m)|$ and the same distance in the reference configuration C_0 , and directed as $(\mathbf{r}_i(t_m) - \mathbf{r}_{ij}(t_m))$, so its contribute to the total displacement simulates an elastic interaction: repulsive if $(R_{ij}(t_m) - R_{ij}^0 < 0)$, attractive if $(R_{ij}(t_m) - R_{ij}^0 > 0)$. The subscript j in the term α_j is the label of the considered neighbor in the set \mathcal{N}_h . This means that, in general, we are assuming that a point P_i has a different coupling constant for the interaction. In this chapter, we will use always the same α_j for every point of the h -th shell. So we will use a simpler notation: α_1 for the interaction with the first neighbor (i.e., 1-th order shell), α_2 for

Table 6.3 List of quantities in the equations of the model

| | |
|----------------------------------|---|
| $\mathbf{r}_i(t_{m+1})$ | Is the updated-position of the point P_i at p-time step t_{m+1} |
| $\mathbf{Int}_i(t_m)$ | Is the “interaction” among the point P_i and all its neighbors in the h -th order shell until the k -th order |
| N_i | Is the number of all the considered neighbors of the point P_i |
| $\mathbf{r}_{ij}(t_m)$ | Is the updated-position of the j -th neighbor of the point P_i at the p-time step t_m |
| $R_{ij}(t_m)$ | Is the Euclidean distance between point P_i and its j -th neighbor at the p-time step t_m |
| $R_{ij}(t_0)$ | Is the Euclidean distance between point P_i and its j -th neighbor in C_0 |
| $\langle \rho_{il}(t_m) \rangle$ | Is the average point of the pair ρ_{il} considering the position of the points at time t_m |
| α_j | Is a coefficient that modulates the intensity of the “elastic” interaction (A_{ij}) and the convergence velocity. It depends by the j -th neighbor’s shell order |
| β_l | Is a coefficient that modulates the intensity of the “alignment” interaction (B_{il}). It depends by the j -th neighbor’s shell order; the l is the label of the couple ρ_{il} |
| σ | Is the step of the lattice |

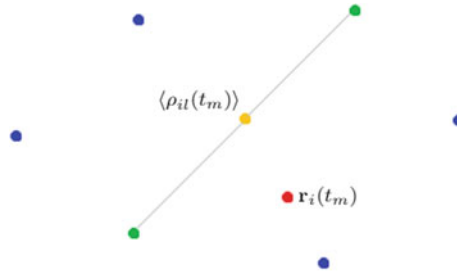


Fig. 6.3 Here is an example of how the interaction \mathbf{B}_{il} works on a hexagonal lattice for the first neighbors. With respect to the red point, the blue and green points are its first neighbors. In green, we have highlighted one of the couples of the set $\mathcal{P}_1(i)$ (i.e., the set of the first neighbors couples of the considered red point) and marked in orange the centroid between the two points of the considered couple. The interaction \mathbf{B}_{il} pushes the considered red point, for the green couple, to be in the orange spot. So this interaction will be proportional to the distance between the current position of the considered point ($\mathbf{r}_i(t_m)$ in red) and the aimed position ($\langle \rho_{il}(t_m) \rangle$ in orange) and the constant β_1 . This interaction is repeated on all the couples in the set $\mathcal{P}_1(i)$

the interaction with the second neighbor (i.e., 2-th order shell), and so on. The same considerations can be done for β_l , but because, in this chapter, we will use the same value for every pair and only for the first neighbors, we will omit the subscript.

The term \mathbf{A}_{ij} and \mathbf{B}_{il} contains also the factor N_i , it dampens the interaction and may be interpreted as if there was a viscous friction. This is because, it reduces the interaction in a way proportional to the number of the neighbors points, therefore, innermost points will see their interaction reduced compared to outermost points. Furthermore, the factor N_i makes the summation on the neighbors an average, so untying it from the number of neighbors. If the point P_i does not have neighbors ($N_i = 0$), the term \mathbf{Int}_i is null because the interaction can’t be defined. The term \mathbf{B}_{il} pushes the point i to place itself into centroid of the couple of neighbors considered ρ_{il} as shown in Fig. 6.3. We have introduced this kind of interaction to have a way to modulate the flexion response of the swarm and help to avoid the overlap of the points as better explained in Sect. 6.4.

The algorithm operation scheme is shown in Table 6.4.

As we can see, for each point i of the lattice, the interaction is evaluated considering only the neighbors up to the k -th order, this allows us to reduce the computational cost, so the complexity of our algorithm is linear.

6.3.3 Relationship with Other Models

It is important to note that in the model, we propose there are only two main roles for the points, unlike the (usually) three used in the swarm models, for example (Battista et al. 2016, 2018; Dell’Erba 2019b). The points are divided into two roles:

Table 6.4 The algorithm operation scheme of the model here proposed (\mathbf{v}_j is the imposed “velocity” of the j -th leader)

| | |
|-----|---|
| (1) | for-all p-time step i |
| (2) | for-all Leader j |
| (3) | do $\mathbf{x}_j^{(i)} = \mathbf{x}_j^{(i-1)} + \mathbf{v}_j^{(i)}$ (the Leaders are translated) |
| (4) | for-all Follower k Interaction phase |
| (5) | do $\mathbf{Int}_k^{(i)} = \mathbf{Function}_k^{(i)}(\mathit{neighbors}_k^{(i-1)})$ (The interactions are evaluated) |
| (6) | for-all Follower k Spread phase |
| (7) | do $\mathbf{x}_k^{(i)} = \mathbf{x}_k^{(i-1)} + \mathbf{Int}_k^{(i)}$ (the Followers are translated) |
| (8) | end |

- *Leader*: points that have an updated motion assigned a priori for every time step. In a physical metaphor, therefore, they represent the interaction between the object modeled by our set of points and the cause of the deformation.
- *Followers*: points that through an algorithmic interaction “follow” the step-movement due to the updated motion of the leaders.

In this model, we do not need the frame points. This is because, unlike (Dell’Erba 2019a, 2020b, 2021b, c), for the interaction used, we do not need that all the shells are complete (i.e., every shell has the maximum number of neighbors expected for the order considered) to balance the interaction on the edges points of the swarm.

Without the frame points, that usually had a proper rules of motion and were moved in a different time respect to the other swarm points, all the non-Leader points are moved simultaneously and they are treated in the same way. This makes the algorithm leaner, more homogeneous, and faster.

In our model, the upgrade of the points coordinates is performed simultaneously (the update takes place based on the coordinates of the previous p-time step without using the updating positions of the current p-time step) this allows us to unbind the result of the simulations with the update order of the points. So we divided the positions upgrade in two steps:

- *Interaction*: in which, based on updated-positions and updated-velocities at the previous p-time step, we calculate the interaction between the points using the algorithm shown below;
- *Spread*: in which the updated-position (and updated-velocity) of the points is updated in proportion to the calculated interaction.

A similar approach is already used in many numerical models such as the PBD.

It is clear that the computational cost of the evolution of the system, in our case, increases approximately linearly with the number of elements of the system (as the number of interactions considered for every element is fixed and the computation is based upon linear operations) while employing a FEM, and the cost is nonlinear in the number of mesh elements.

6.3.4 Meaning of Neighbors

As we can see in the literature, the energy deformation \mathcal{E} of a generalized continuum depends on the high order gradient of the displacement field χ

$$\mathcal{E} = \mathcal{E}(\chi, \nabla\chi, \nabla^2\chi, \dots), \quad (6.8)$$

in particular, in the papers (Della Corte et al. 2015), we can see that there is a link between the energy of first gradient continua and the swarm with first neighbors interaction; however, considering a swarm with second neighbors interaction, the energy deformation is linkable to second gradient continua energy.

As we will see in the next section, our model is able to give results for standard deformation (i.e., deformation of Cauchy continua) that are qualitatively similar to those obtained with FEM, and was also able to simulate typical phenomena of the second gradient continua. The breaking phenomena are not described in this chapter to have a complete description in a future paper, but it can simply be added by introducing a breaking threshold to the distance between the two points.

In the following, we will suppose:

- \mathbf{A}_{ij} evaluated on the first neighbors, is linked to *first* gradient continua;
- \mathbf{A}_{ij} evaluated on the second neighbors, is linked to *second* gradient continua;
- \mathbf{B}_{il} evaluated on the first neighbors, is linked to *second* gradient continua.

In future works, we will try to support such hypothesis.

6.4 Numerical Simulations

We have divided the set of simulations into two sub-sets, as well as this chapter's section: the first set contains the whole *standard simulations* where they are called standard because they contain only the interaction that can be related to the first gradient continua, for this kind of simulations, we have chosen the traction, compression, shear, and flexion deformations. The second set contains the simulation that we will call *exotic* ones, this contains the interactions that can be related to the second gradient continua; in this case, we perform only traction and compression simulations.

In Table 6.5, the dimensions of our swarm and the kind of simulation performed is reported. In Fig. 6.4, it is possible to see the initial configuration for traction and compression, and in Fig. 6.5, for flexion and shear.

Since it is observed that, within some thresholds of the parameters (see Sect. 4.2), stopping the leaders at a chosen pseudo time step and letting the system continue to evolve, this converges to what seems an "equilibrium" in which all the points are practically stationary. So all simulations were performed with the following scheme:

Table 6.5 Table of swarms' dimensions used in our simulations. N_E and N_E^H are clearly the number of elements of the swarm, respectively, without and with hole

| Dimension | Deformation | Lattice | N_E | N_E^H |
|-------------------|--------------------------|-----------|-------|---------|
| 0.7×1.4 | Traction and compression | Hexagonal | 2891 | 2768 |
| 0.7×1.4 | Traction and compression | Squared | 2556 | 2452 |
| 0.56×2.8 | Flexion and shear | Hexagonal | 4637 | 4554 |
| 0.56×2.8 | Flexion and shear | Squared | 4089 | 4020 |

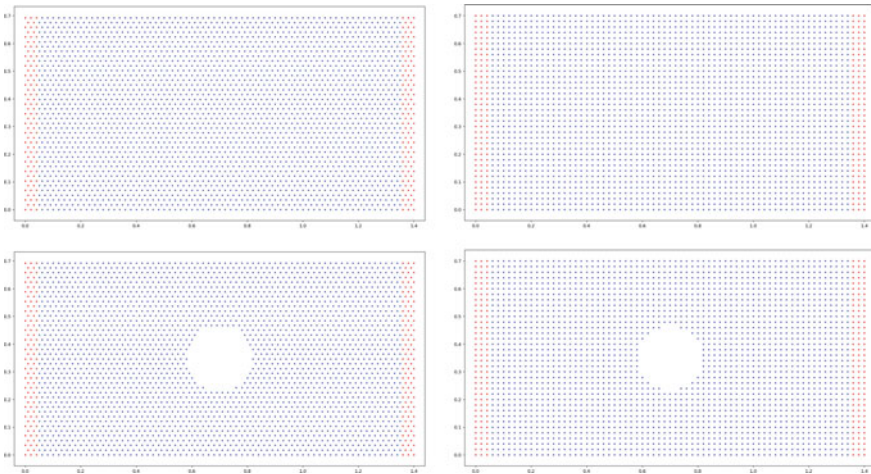


Fig. 6.4 The initial configuration swarm used for traction and compression simulations. The leaders are in red, the followers are in blue. (Left: hexagonal lattice. Right: squared lattice)

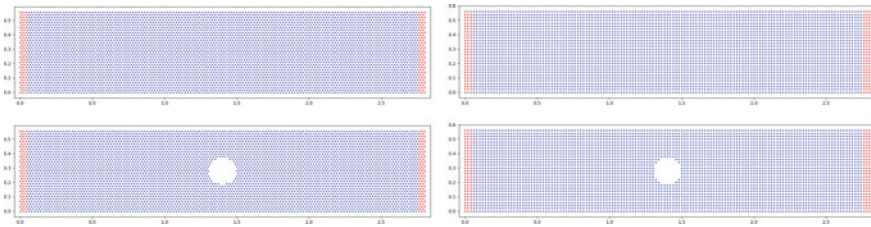


Fig. 6.5 The initial configuration swarm used for shear and flexion simulations. The leaders are in red, the followers are in blue. (Left: hexagonal lattice. Right: squared lattice)

- **Active deformation phase**, in which the leaders are moved up to a certain pseudo time step, at the same time, the followers adapt to this shift.
- **Settling phase**, in which the leaders are kept still and the followers continue to move until they reach an “equilibrium configuration”, i.e., when the difference between the pseudo time step position and the next pseudo time step is less than a chosen tolerance ε value.

Considering only first neighbors interaction, the convergence velocity depends only on α_1 coefficient defined in the previous formula, so the latter increases with the growth of α_1 ; on the other side, the value of α_1 does not influence the equilibrium configuration, but only the dynamics, i.e., the way the system reaches the equilibrium configuration. This happens unless α_1 does not reach a particular value after that exotic phenomena begin and so, growing further α_1 reaches a critical value such that the interaction term $A_{ij} \rightarrow \infty$ and the swarm “explodes”, i.e., the swarm elements leave away to the infinity or move themselves in a chaotic way in a limited domain of space (for more information about this, see the Sect. 6.4, Fig. 6.21). Considering also the second neighbors interactions, the convergence velocity still depends on α_1 as in the latter case, but in this case, we need to distinguish the α_1 related to the first neighbors, and the α_2 related to the second neighbors, moreover, here the equilibrium configuration depends from both α_1 and α_2 values, despite the first case where the final configuration does not changes for α in the normal range, while now there is a different final configuration for every couple (α_1, α_2) , as it is better argued in Sect. 6.4.2.

To show how the swarm deforms itself under the leader’s motion, in addition to its points positions, we have added the *elementary area units* that will be colored by their deformation state.

Here we will define the *elementary area unit* of both hexagonal and squared lattice: let a point i of the hexagonal lattice and its first neighbors, the elementary area is any triangle which vertices are the point i itself and two of its first neighbors that are adjacent to each other; similarly for the squared lattice, let a point i of the squared lattice and its first neighbors, the elementary area is any quadrangle which vertices are the point i itself and three of its first neighbors that are adjacent to each other (see Fig. 6.6).

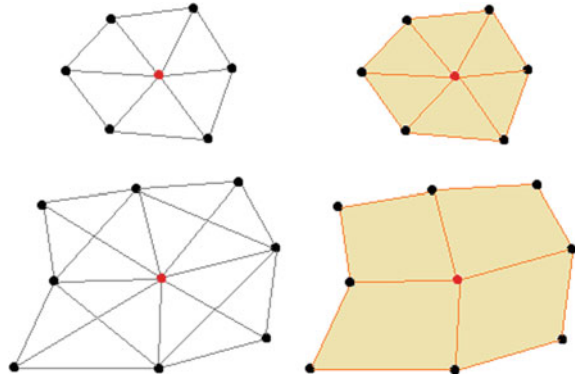
This process is done on the whole elements of lattice, so it is possible to cover it with not superimposed elementary areas.

In the simulations that we will show, the elementary area’s colors represent the absolute value of the percentage variation of the area A , with respect to the initial area A_0

$$\text{Elementary Area Color} = \frac{|A_0 - A|}{A_0}; \quad (6.9)$$

the choice to highlight the elementary areas colors’ spread, in analogy with the continuum mechanics physics, is due to its strong relation with deformation energy distribution.

Fig. 6.6 Example of how elementary area units are considered for an elementary cell of hexagonal and squared lattices



The introduction of the elementary area units has the aim to show where high deformations region occur, where a break is more likely. We will introduce this feature in the next work.

In Fig. 6.7, we have show an example of the two principal phases of the algorithm, the initial configuration and the equilibrium configuration, followed by the colored one. In the rest of the chapter, we will show only the swarms at this latter phase for every simulation because we are interested only in the shape that the system of points assumes at this stage.

As we will see that some simulations will have more pseudo time steps than others; this choice was been done to avoid superpositions of swarm points that would cause undesirable effects (i.e., overlaps and compenetration of the points). These problems can be avoided by lowering the leaders' updated velocity and, in the same time, growing the number of time steps to obtain the same deformation; this allow the followers to better fit to the changing shape of the system. In future, we will modify the interaction law in order to prevent this undesirable phenomenon.

Because we are using a model based on swarm, which does not have a conscience of its own configuration and each of its element does not know as to a priori get the equilibrium configuration, problems can arise due to the overlapping of the points.

An example of these problems is shown for a simple one-dimensional lattice of three points without the implementation of the term \mathbf{B}_{il} in Fig. 6.8. Indeed, the algorithm considers the three configurations as equivalent equilibrium configurations.

Instead with a two-dimensional lattice, the situation is more complicated and, without considering the interaction \mathbf{B}_{il} , we provide an example in Figs. 6.9 and 6.10, in which, we show two compression tests with the same initial configurations and all the same parameters except leaders' velocities.

In Fig. 6.10 is shown the response of the swarm to a low leaders velocities and there is not the overlapping problem, instead in Fig. 6.9 the higher leaders velocities cause an overlapping problem that leads to a new final configuration where the swarm interpenetrates itself.

So the interaction \mathbf{B}_{il} can help to avoid such kinds of situations by giving importance also to the directions and alignments of the link among the points (and not only

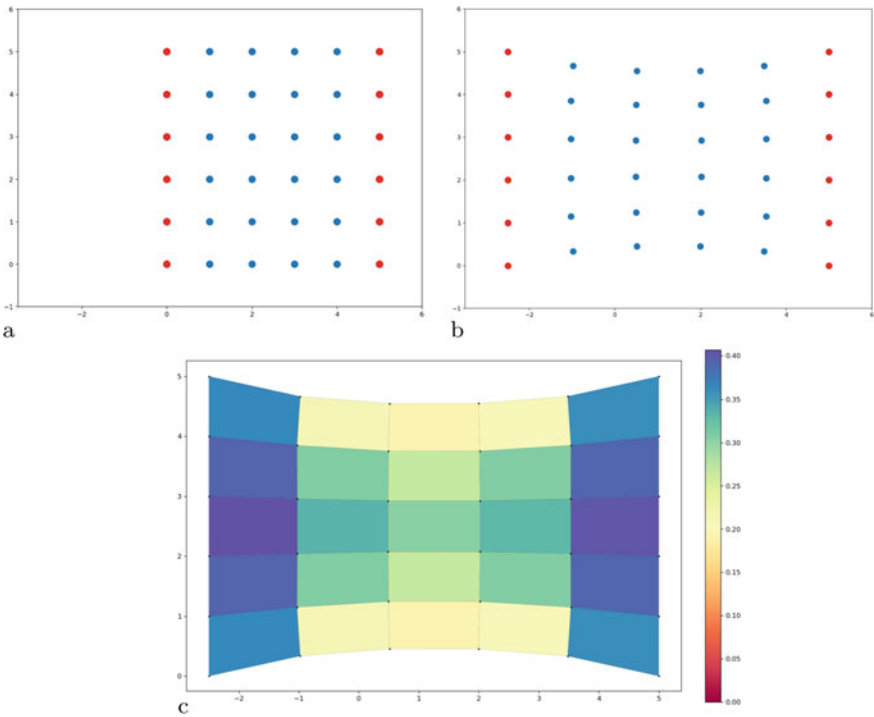
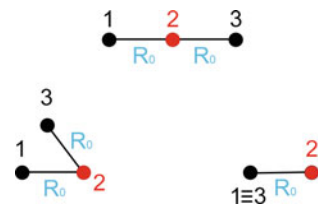


Fig. 6.7 Here we show in (a) and (b) a sample of the true aspect of our model output. In particular, in (a) is shown the initial configuration of a little squared-lattice-swarm subject to a traction test which final equilibrium configuration is shown in (b). But in the follow of the chapter we do not provide this kind of pictures but we provide (c)-like picture. In (c) we shown the same equilibrium configuration of (b) but displaying also the elementary area variations and the associate colorbar. This latter kind of picture is possible to get more information about the swarm deformation

Fig. 6.8 Example of a superposition problem (I)



on the distances between them). It is important to note that the points on the edges of the swarm perceive fewer interactions (because their shells are not complete, all the possible couple ρ_{il} are not available), so we are working also on other interactions of this type to show in future researches, an example is provided in Fig. 6.11 for a one-dimensional lattice.

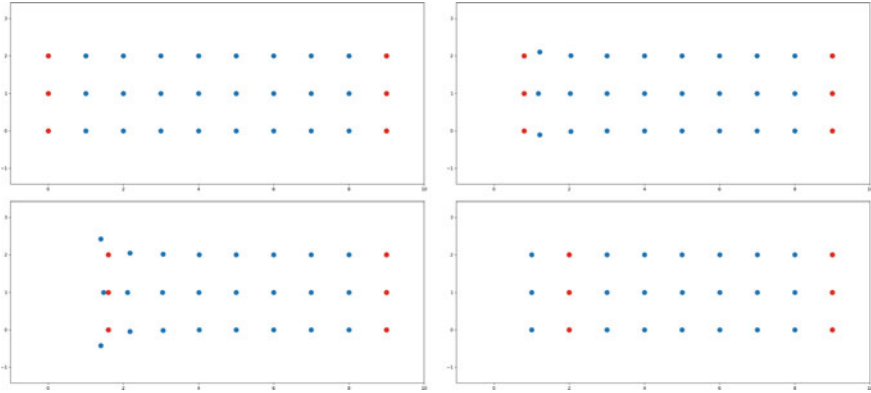


Fig. 6.9 Example of a superposition problem (II). The leaders' high velocities cause an overlapping within the swarm (order of images: top-left, top-right, bottom-left, and bottom-right)

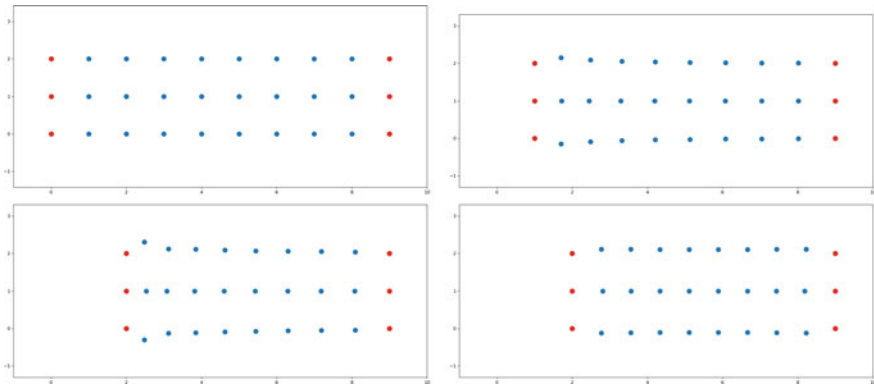


Fig. 6.10 Example of an avoided superposition problem (order of images: top-left, top-right, bottom-left, and bottom-right)

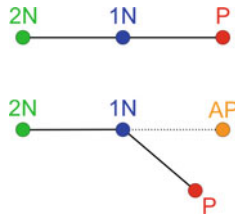


Fig. 6.11 On the top, we show an initial configuration considering the interaction acting on the point P in red. With respect to P , the blue point is its first neighbor ($1N$) and the green one is its second neighbor ($2N$). So an alignment interaction can be introduced by pushing the point P to keep itself in the aimed position (AP), marked in orange, that is on the prolongation of the segment $2N - 1N$ as shown in the bottom. The advantage of this kind of interaction can be its capability to work also with the points on the edges of the swarm

6.4.1 Standard Simulations

As explained, we have used two different systems for the numerical simulations shown in Fig. 6.4, for traction and compression, and in Fig. 6.5, for shear and flexion, both with leaders in red and followers in blue. All these standard simulations have been performed with only the interaction limited to the first neighbors and without considering the alignment term B_{il} ; in other words, in this subsection, our purpose is to show only the deformations attributable to first gradient continua.

In this chapter, we focused on traction and compression tests which are the simplest simulations we can achieve. But in order to show that the model is qualitatively able to simulate also flexion and shear tests, we insert some simulations of this kind only for demonstration purposes.

6.4.1.1 Standard Traction

In these simulations, we hold the leaders of the right side, while pulled those of the left one; we settled this model to obtain an elongation of 50%. It is possible to see the final configuration in Fig. 6.12.² The same simulation with a swarm with a centering hole follows. This kind of simulations have been performed using 30,000 pseudo-time steps, divided into the first 10,000 for active deformation phase, the second 20,000s for the settling phase. From these simulations, we can get the following observations:

- The model is able to reproduce the Poisson effect. The two lattices used seems to show slightly different Poisson effect.
- It is important to note the different behaviors of the lattice around the hole, in particular, on its upper and lower sides. In the first impression, we retained possible that these differences were caused by the discretization around the hole (e.g., observe the different shape of the hole in Fig. 6.4); so we performed the same simulations with a finer discretizations obtaining the two same different behavior around the holes; see Fig. 6.14. Furthermore, the coloration pattern (i.e., lower elementary areas variations) of the hexagonal lattice on the top and bottom of the hole seems compatible with the analog behavior of a isotropic material, meanwhile the same coloration pattern of the squared one seems compatible with the behavior of an orthotropic material (i.e., the stretching). These behaviors seem compatible with our initial conjecture on the kinds of materials that the two lattice should simulate. However, it is premature to do such hypothesis, so we will better argue it in the future paper. Far from the hole, the variations of elementary areas are different, as it may be seen from the differences between the two-color distributions.
- For the traction tests without hole and samples used in Fig. 6.12, the two kind of lattice have approximately a similar response, as it could be seen in the figures

² We want to underline that, in this way, we are out of the region of elasticity because it is not a small deformation.

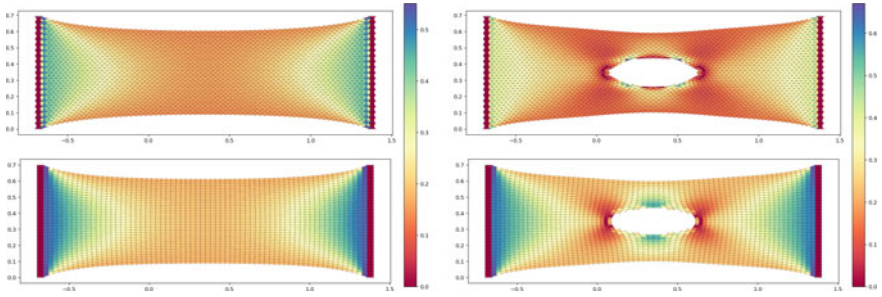


Fig. 6.12 Standard traction simulations, respectively, for the hexagonal (images at the top) and squared (bottom) lattices with $\alpha_1 = 1$, with and without hole

comparing two-color distributions (the areas of greater elementary areas variations are the same in both lattices). It is important to note that, in general, two different lattices can exhibit different behavior. An example is given in Fig. 6.15, where the hexagonal lattice shows a different response if the orientation of discretization is rotated by 90° (an example of such rotation is provided in Fig. 6.16). We want to underline that to get the simulation of Fig. 6.15, we used cells of finite dimensions and that all α s in the cells are the same. We also show how the two lattices can give different results considering finer discretization in Fig. 6.14.

In order to understand if some of the features obtained in the previous simulation are only an effect due to the discretization, we performed another simulation for traction test but by using samples with a finer discretizations. The two initial configurations are shown in Fig. 6.13.

- To get the simulations of the standard traction with a finer discretizations, there were needed 2 million time steps in order to avoid superpositions.
- In Fig. 6.14, a situation similar to that shown in Fig. 6.12 occurs but with a more homogeneous colors distribution in squared lattice.
- As the behaviors of the lattices with the hole in Fig. 6.12, also in Fig. 6.14 the two lattices show a similar patterns around the holes but more homogeneous; this contradicts the previous hypothesis of a mere mesh effect: in fact in this case, as shown in Fig. 6.13, the holes are more round.

As mentioned before, changing the parameter α_1 does not alter the equilibrium configuration, so the magnitude of Poisson effect does not directly depend on α_1 . In order to modulate the Poisson effect, we have to define different values of α_1 for every neighbor in all the shells of the swarm. In particular, by considering a square lattice, we assign a value α_{1vh} for neighbors positioned in vertical and horizontal direction with respect to the central point of the shell, and assign a different value α_{1d} for neighbors positioned in diagonal direction with respect to the central point of the shell. The ratio $(\alpha_{1d}/\alpha_{1vh})$ is linked to the intensity of the Poisson effect. We can also obtain qualitative similarity with auxetic materials setting the two parameters to obtain a negative ratio. We can proceed as the same way for the hexagonal lattice,

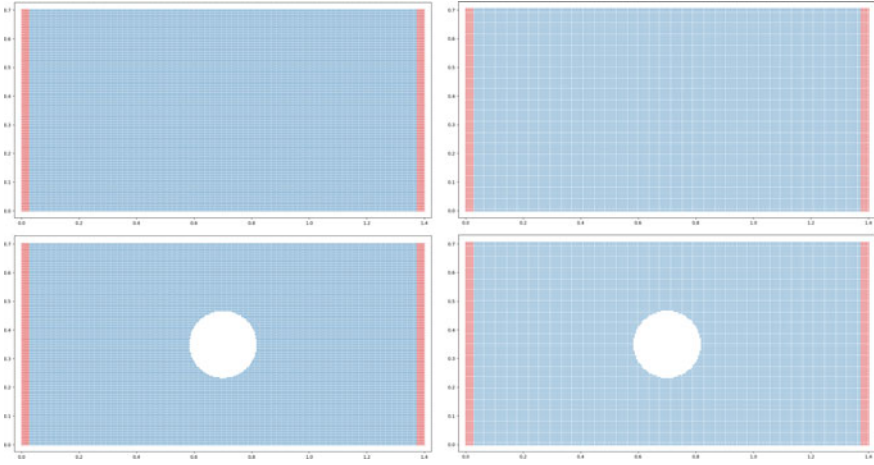


Fig. 6.13 Here we show new initial configurations used to obtain new simulations of traction and compression tests with a finer discretization. We want to underline that with a greater number of elements, the holes are more round

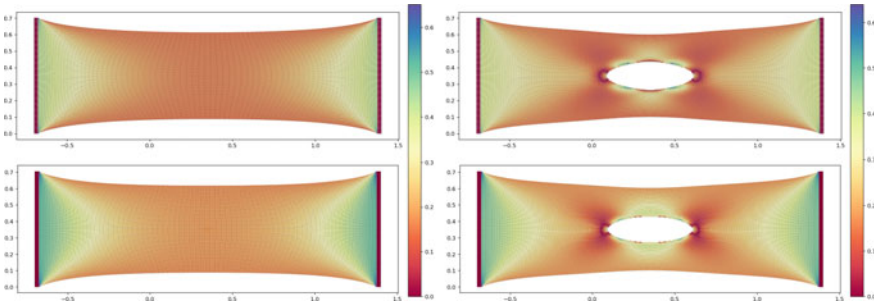


Fig. 6.14 Standard traction simulations with a finer discretizations, respectively, for the hexagonal (top) and squared lattices (bottom) both with $\alpha = 0.5$

but it is more complicated owing to the different cell geometry (Figs. 6.14, 6.15 and 6.16).

6.4.1.2 Standard Compression

In these simulations, we hold the leaders of the right side, while pushing the leaders of the left one towards the right side; we set this model to obtain a compression of about the 18%.³ We performed the same simulations with a swarm with a centering hole. It is possible to see the simulations in Fig. 6.17. The simulations of these kind

³ Also in these simulations we do not have small deformations.

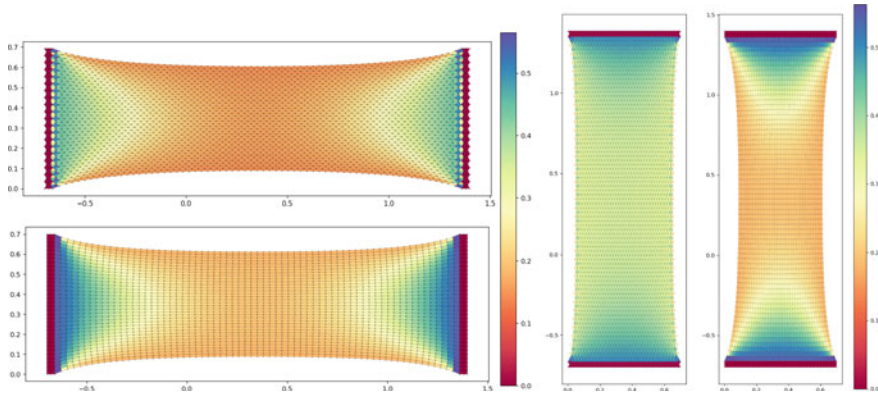


Fig. 6.15 On the left, the standard traction simulations, respectively, for the hexagonal and squared lattices. On the right, we rotated the system keeping the same orientation of discretization of the horizontal samples and all the other parameters of the model

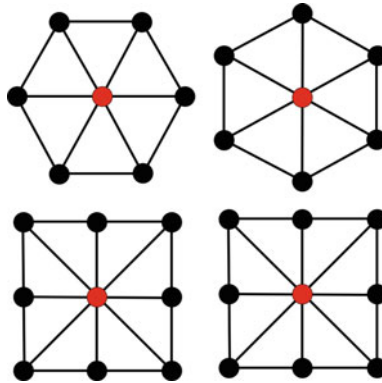


Fig. 6.16 Here is shown what we mean with the rotation of 90° of the orientation of discretization. As it is possible to note in the hexagonal cell such rotation causes an huge change in the structure and in the directions of the interaction between the black and red points. Meanwhile in the square cell, there is no difference. But it is possible to guess that for a rotation of 60° , the situation is reversed

have been performed using 120000 pseudo-time steps, divided into the first 100000 for active deformation phase, the second 20000s for the settling phase. From these simulations, we can get the following observations:

- also in this case there is the Poisson effect, more accentuated in the squared lattice;
- Unlike the traction simulations, here is possible to observe a different color distributions between the two kind of lattices; in particular, the hexagonal one has a more homogeneous color distribution;
- in the simulations with the holes, slight convexity on the top and bottom sides of the swarm appear in both lattices;

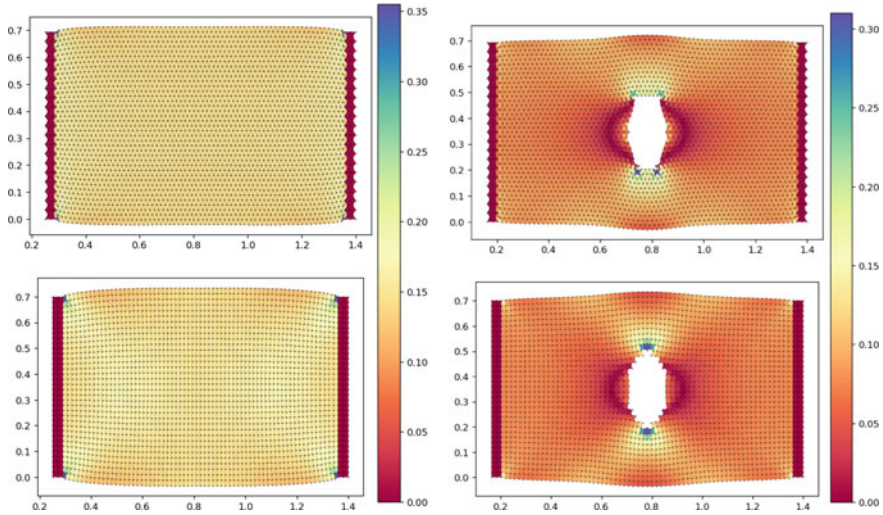


Fig. 6.17 Standard compression tests without hole (left) and with it (right), for the hexagonal lattice (up) and squared one (down). We set $\alpha_1 = 1$ for tests without hole and $\alpha_1 = 0.2$ for tests with hole

- as in the traction test with hole, also Fig. 6.17, in the regions around the holes, two different behaviors can be seen: in the squared lattice the regions of maximum elementary area variation are concentrated in two spots, one on the top and one on the bottom of the hole (orthotropic like materials), meanwhile in hexagonal lattice, the same areas are distributed in four spots, two on the top and two on the bottom of the hole (isotropic like materials). Also, in simulations with a finer discretization, shown in Fig. 6.18, these responses occur.

In order to understand if some of the features obtained in the previous simulation are only an effect due to the discretization, we performed other simulations for compression test but by using samples with a finer discretizations. The two initial configurations are shown in Fig. 6.13.

- in Fig. 6.18 a situation similar to that shown in Fig. 6.17 occurs but with a more homogeneous color distribution in squared lattice;
- as the behaviors of the lattices with the hole in Fig. 6.17, also in Fig. 6.18, the two lattices show a similar pattern around the holes but more homogeneous: also in this case, we can exclude the previous hypothesis of a mere mesh effect.

6.4.1.3 Standard Flexion and Shear

In flexion simulations, shown in Fig. 6.19, we clamped the leaders of the right side, meanwhile the leaders of the left side have been rotated around the lower one on

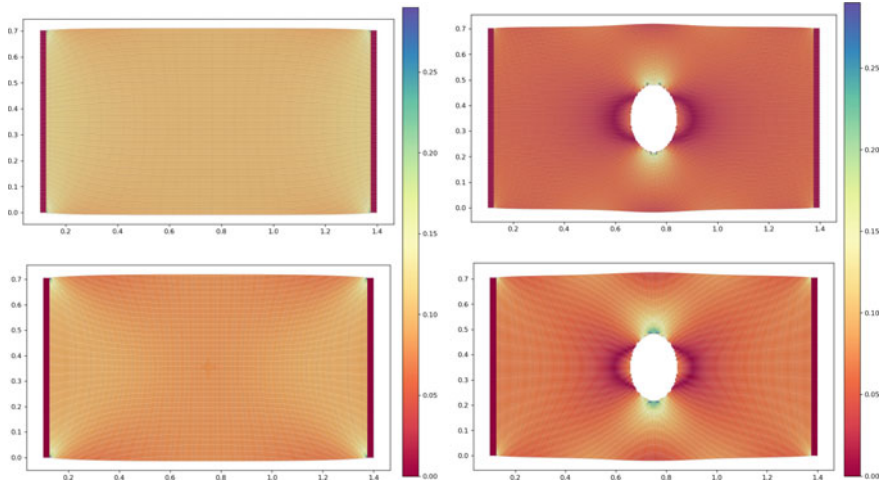


Fig. 6.18 Standard compression simulations with a finer discretizations, respectively, for the hexagonal (top) and squared lattices (bottom) both with $\alpha = 0.05$

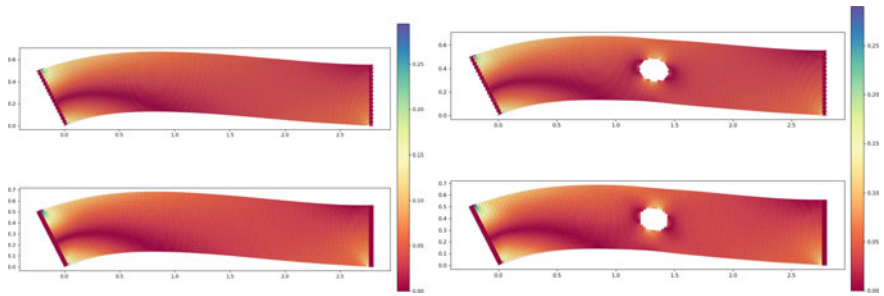


Fig. 6.19 Standard flexion tests without hole (left) and with it (right), for the hexagonal lattice (up) and squared lattice (down). We set $\alpha_1 = 0.2$ for all the tests showed

the side by an angle of about 25° . The simulations of this kind have been performed using more pseudo-time steps (i.e., 2 million from which the firsts 6,00,000 for active deformation phase) in order to avoid the overlap problem as mentioned before. From the color distributions, it seems that the two lattices give qualitatively the same response and shape. In shear simulations, shown in Fig. 6.20, we clamped the leaders of the right side, meanwhile the leaders of the left side have shifted down by a distance equal to the length of the short side. Also, these simulations have been performed using more pseudo-time steps (i.e., 2, 5 million from which the firsts 1 million for active deformation phase) in order to avoid the overlap problem. Also, in this case, from the color distributions, it seems that the two lattices give qualitatively the same response and shape. Note that in both the cases, we performed a huge total deformation.

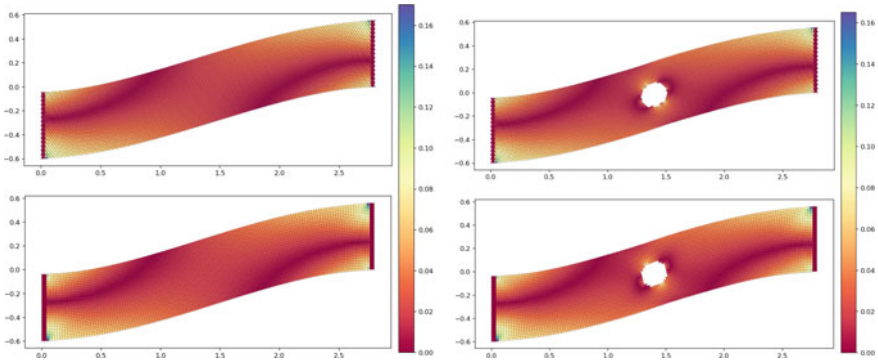


Fig. 6.20 Standard shear tests without hole (left) and with it (right), for the hexagonal lattice (up) and squared lattice (down). We set $\alpha_1 = 0.2$ for all the tests showed

6.4.2 Second Neighborhoods and Exotic Simulations

The simulations shown in the last subsection are made considering only the first neighborhood interaction and a fixed a priori α_1 .

In these type of simulations, changing the value of α_1 does not alter the final “equilibrium configuration” of the swarm if its value is kept between some threshold values, so it is very important to get in which range it can be chosen without compromising the algorithm’s work. It must be investigated in a schematic way, but we do not want to burden this chapter with this kind of complicate and delicate study, and so we reserve it for future investigations. Therefore, here we will show only some heuristic considerations about the working region of the model.

When the parameter α_1 is chosen out of this range, what happens is that, the swarm “explodes” (i.e., the swarm becomes a chaotic swarm), so the interaction among the points becomes huge and consequently they scatter around, far from the leaders, oscillating. Instead, when α_1 is in the range but near to the edges, the swarm assumes exotic behavior, showing patterns and new kinds of “equilibrium configurations”.

We observed that, for traction and compression test, this range seems to be influenced by the leaders motion, the number of points in the swarm, shape, and total deformation of the swarm. But we want to underline that also negative values, very little in module, usually seem to be allowed. This can be important because, especially in combination with the other parameters α_2 and β , it seems promising in order to simulate auxetic material. When we add the interaction with the second neighborhood, the situation becomes even more complicated because the parameters seem to be strictly correlated. In fact, the presence of α_2 , β or both change the range of non-explosion of α_1 and, furthermore, α_2 and β have their own working regions; This overlap of regions makes the swarm gain new exotic behaviors. Furthermore, unlike the case of only first neighbors interaction, varying the combination of the parameters in their working regions causes a change of the equilibrium configuration.

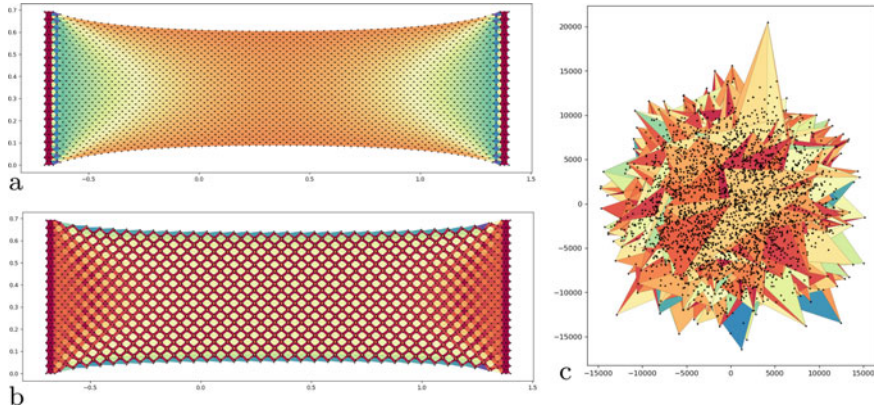


Fig. 6.21 An example of various ranges of behavior: **a** standard range with $\alpha_1 = 1.4$; **b** exotic range with $\alpha_1 = 1.7$; **c** explosion with $\alpha_1 = 2.2$

Our interest in exotic behavior is due to their qualitative similarities with particular kinds of phenomena such as the formation of density patterns like stripes or holes (Fig. 6.21).

In the following simulations, we have implemented the second neighbors and the alignment interaction.⁴ The action of these interactions enriches the phenomenology of the model. The principal observations that we get from these kind of simulations are:

- the swarm is more reactive; the deformation propagates quickly because it is carried through the swarm at the speed of two shells at algorithm iteration, instead when the interaction is limited at the first neighbors, in which the speed is one shell per iteration;
- now the Poisson effect depends from the combination of all the parameters α_1 , α_2 and β .

As said above for the following numerical simulations, we have used the initial configurations shown in Fig. 6.4 and performed only traction and compression tests to show the qualitative response of the model without going into too much detail in commenting about them. We want to underline that changing the kind of lattice changes also the ranges of the parameters α_1 , α_2 , and β , so setting the same parameters doesn't lead to the same result on different lattices (this also happens in standard simulations). Furthermore, we want to remind that in case of only the first neighbors interaction, the equilibrium configuration doesn't depend on the value of α_1 as long as it is maintained in the normal range; instead, this invariance is not maintained with the second neighbors interaction, so any set of α_2 and β value makes changes. For these reasons, we have performed many simulations by varying the parameters

⁴ This because as explained in Sect. 6.3.4 we are interested to get behavior qualitatively related with the second gradient continua, and so we use both α_2 and β .

α_1 , α_2 , and β ; then among these, we have chosen and reported only those which seems more significant for us, but there are still a lot of parameters combinations to be explored.

We have divided the simulations in “normal”, “exotic”, and “pre-explosion”. In the first, we show the reaction of the swarm when all the parameters are in the working regions; in the second, we show some exotic behavior when some parameters are near the upper edge of their working regions; in the third, we show extreme behavior when the parameters are at the upper limit of the working region.

We are interested in exotics and pre-explosions behavior because they are qualitatively similar to particular phenomena (e.g., deformation bands).

For the following simulations, we have ever used only traction and compression tests with the same initial configurations shown in Fig. 6.4.

- Let start talking about Fig. 6.22 where we have done a simulation with a traction tests without hole. Here we have used a low α_1 and an high α_2 to underline the effect of second neighbors. In both the lattices, it's possible to see an hardly fluttering of upper and lower edges carrying on to the center comparing to standard traction Fig. 6.12. Furthermore, we have observed the arise of a concentric framing effect: in the figure, it can be noted on the upper and lower sides of the hexagonal lattice (a), where there is a succession of rows with a low color value (dark red) and high color value (light orange). While in the hexagonal lattice, this effect is clearer, in the squared one it is fewer. This effect will be more evident in the compression tests. Comparing the final configuration of the hexagonal lattice (a) in Fig. 6.22 with the one in Fig. 6.12, it is possible to note how the second neighbors interaction homogenize the elementary areas color, making a softer shade. Furthermore, the elementary areas variation on the left and right edges (in yellow in (a) in Fig. 6.22 and green in Fig. 6.12) are slightly the same instead in the central part (dark orange in both the figures); in the second neighbors case, it seems to have an higher value (i.e., the inner cells undergo to a greater deformation). By comparing the squared lattice (b) in Fig. 6.22 with the one in Fig. 6.12, it seems that with the second neighbors interactions, the Poisson effect becomes slightly more intense and the elementary areas variation in the middle region of the swarm are lower.
- Even in Fig. 6.23, we performed a simulation with a traction tests without hole, but this time with such values of α_2 and β to cause the arise of exotic behaviors. In (a) there is a slight exoticism, in the other this is clearer. We observed that by adding the α_2 and β , it is more likely to obtain non-local structures as bands and deformation localization.
- In Fig. 6.24, we used the swarm with an hole for the traction test. We highlight the presence of a depression on the upper and lower edges by carrying on to the center and comparing the standard traction with an hole; Fig. 6.12. The color distributions are different but actually their numerical values are quite similar. The main difference between them is that in the hexagonal lattice, the color distribution is more homogeneous. Even here, there is an arise of concentric framing effect as in the previous traction test. Furthermore, it seems that this new interactions regularize the deformations around the holes.

- Even in Fig. 6.25, we have used the swarm with an hole for the traction test, but this time, with such values of α_2 and β to cause the arise of exotic behaviors with vertical stripes structure. The presence of the hole here, also, causes depressions on the upper and lower edges, but now there is the appearance of color stripes in different ways in the two different lattices, how can be seen comparing (a) and (b) with (c) and (d). Even more, the deformations around the hole are greater than the same in Fig. 6.24. It's important to highlight that these exotic structures (i.e., deformation bands) emerge spontaneously by only setting the right parameters.
- In Fig. 6.26, we performed a simulation with a compression tests without hole. There are no such differences found between the two lattices. Even here, the colors are different but the numerical value is quite the same, so the main difference is the arise of concentric framing effect, which is more evident in the squared one (and it explains why it is called “concentric”) instead of the hexagonal one, where it is low or totally null.
- in Fig. 6.27, we performed a compression test simulation in exotic range. The swarms exhibit an horizontal layering effect phenomena with different schemes;
- Figure 6.28 shows a compression test simulation with the hole. On comparing the color bars, it is found that the two lattices exhibit the quite same elementary areas variation, but even, in this case, the hexagonal one is more homogeneous (e.g., the low variation areas, in red, at the sides of the hole have a softer shade). The square lattice exhibits a stronger concentric framing effect with respect to the hexagonal one. As in Fig. 6.17, also with the second neighbors interactions, we can observe the arise of two convexities, but in this case, it is more pronounced. Also in this case, it seems that this new interactions regularize the deformations around the holes.
- In Fig. 6.29, we used the swarm with the hole for the compression test, but in this case with such values of α_2 and β to cause the arise of exotic behaviors with horizontal layering effect. We want to highlight that choose of the kind lattice can lead to different exotic behaviors, in particular the (b) exhibits the formation of hexagonal regions of high elementary areas variations near the hole, effect that the squared one does not show. This effect is accentuated in the pre-explosion situation shown in (f) of Fig. 6.30.
- As we written before now we provide in Fig. 6.30 a mix of pre-explosion simulations without explanations. In these, it is possible to observe some kind of effects that there were in the previous simulations at all. In particular, in the (a), (b), and (c) there are quickly colors variations; (b), (c), and (f) are not symmetrical, the (f) one exhibits the formation of hexagonal regions of high elementary areas variations, like the (b) of Fig. 6.29, but extended all over the lattice.

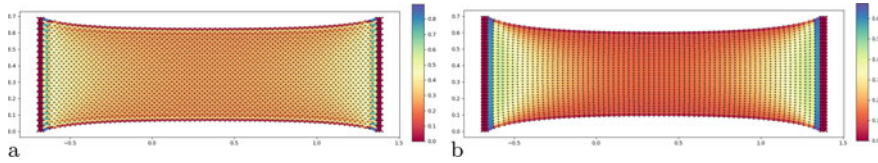


Fig. 6.22 Example of a simulation obtained adding the second neighbors interaction. **a** Hexagonal lattice with $\alpha_1 = 0.2$, $\alpha_2 = 2.2$, and $\beta = 0.04$; **b** Squared lattice with $\alpha_1 = 0.2$, $\alpha_2 = 1.2$, and $\beta = 0.12$

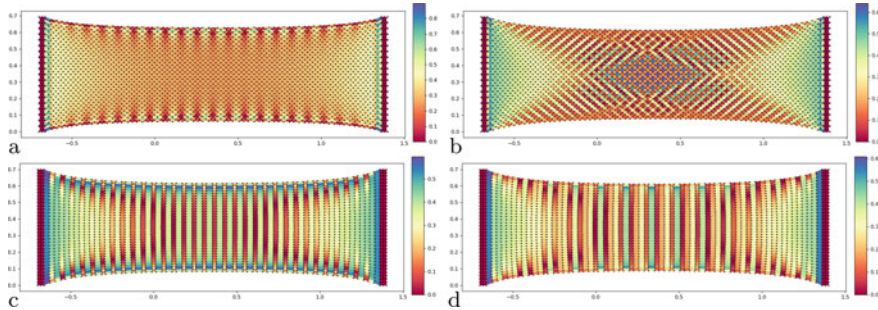


Fig. 6.23 Exotic traction tests. **a** Hexagonal lattice with $\alpha_1 = 0.4$, $\alpha_2 = 2.2$, and $\beta = 0.04$; **b** Hexagonal lattice with $\alpha_1 = 1$, $\alpha_2 = 0$, and $\beta = 0.1$; **c** Squared lattice with $\alpha_1 = 2.2$, $\alpha_2 = 0.4$, and $\beta = 0.08$; **d** Squared lattice with $\alpha_1 = 2.0$, $\alpha_2 = 0.8$, and $\beta = 0.08$

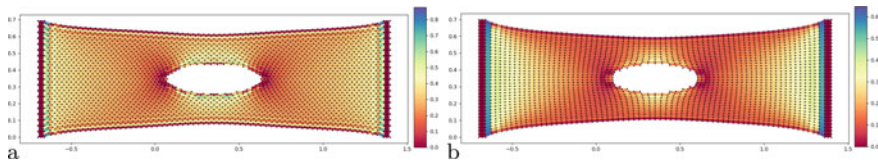


Fig. 6.24 Standard traction tests with hole. **a** Hexagonal lattice with $\alpha_1 = 0.2$, $\alpha_2 = 2.0$, and $\beta = 0$; **b** Squared lattice with $\alpha_1 = 2.0$, $\alpha_2 = 1.4$, and $\beta = 0.08$

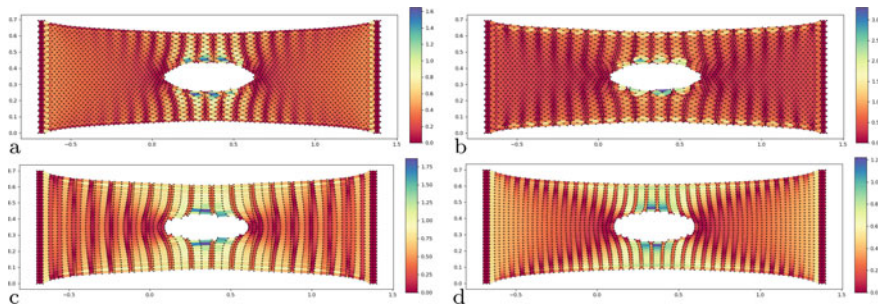


Fig. 6.25 Exotic simulation with holes. **a** Hexagonal lattice with $\alpha_1 = 0.2$, $\alpha_2 = 2.0$, and $\beta = 0.08$; **b** Hexagonal lattice with $\alpha_1 = 0.2$, $\alpha_2 = 2.6$, and $\beta = 0$; **c** Squared lattice with $\alpha_1 = 0.2$, $\alpha_2 = 2.4$, and $\beta = 0$; **d** Squared lattice with $\alpha_1 = 2.2$, $\alpha_2 = 0.4$, and $\beta = 0.08$

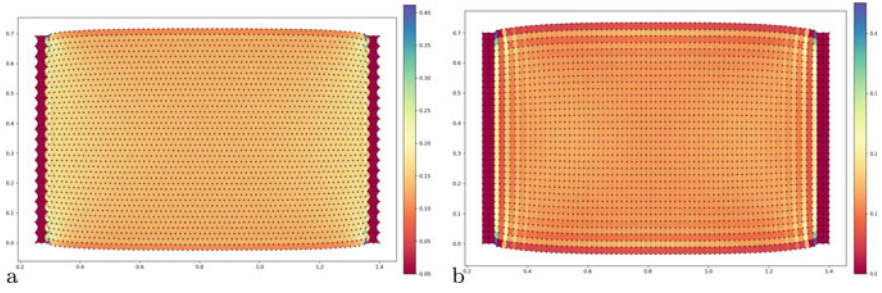


Fig. 6.26 Standard compression tests. **a** Hexagonal lattice with $\alpha_1 = 0.6$, $\alpha_2 = 1.2$, and $\beta = 0.15$; **b** Squared lattice with $\alpha_1 = 0.6$, $\alpha_2 = 2.4$, and $\beta = 0$

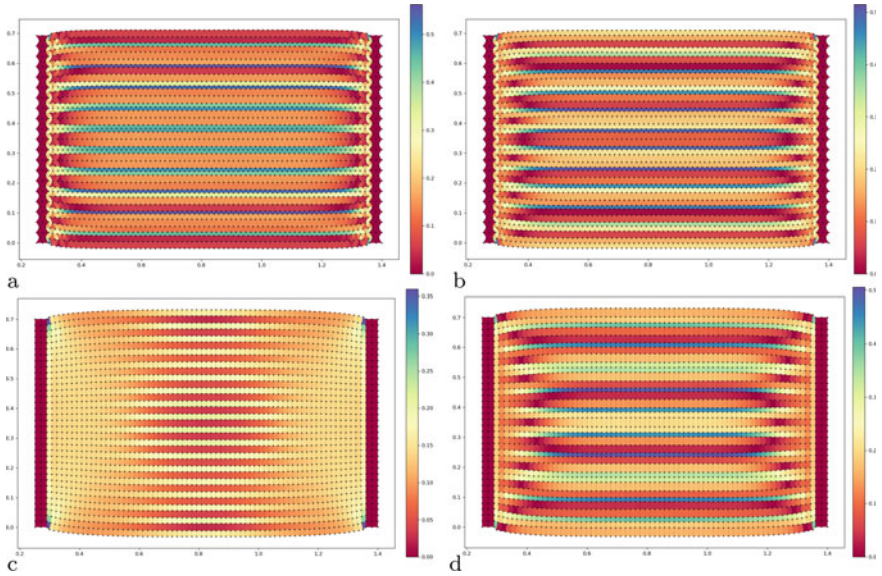


Fig. 6.27 Exotic simulations. **a** Hexagonal lattice with $\alpha_1 = 0.6$, $\alpha_2 = 3.0$, and $\beta = 0$; **b** Hexagonal lattice with $\alpha_1 = 1.2$, $\alpha_2 = 2.4$, and $\beta = 0.05$; **c** Squared lattice with $\alpha_1 = 3.6$, $\alpha_2 = 0.6$, and $\beta = 0.05$; **d** Squared lattice with $\alpha_1 = 3.6$, $\alpha_2 = 1.8$, and $\beta = 0$

6.5 Conclusion

Our model seems to be able to qualitatively simulate the behavior of an elastic continuum, it provide critical pre-failure configurations and work in case of large deformations. It is also possible to implement failure phenomena, new kinds of interaction among the points, and make its computations faster. We can sum up the advantage of our model in:

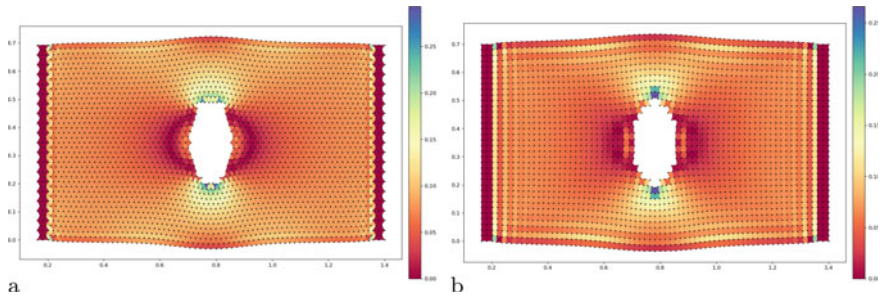


Fig. 6.28 Standard compression tests with hole. **a** Hexagonal lattice with $\alpha_1 = 2.4$, $\alpha_2 = 1.8$, and $\beta = 0$; **b** Squared lattice with $\alpha_1 = 0.6$, $\alpha_2 = 1.8$, and $\beta = 0$

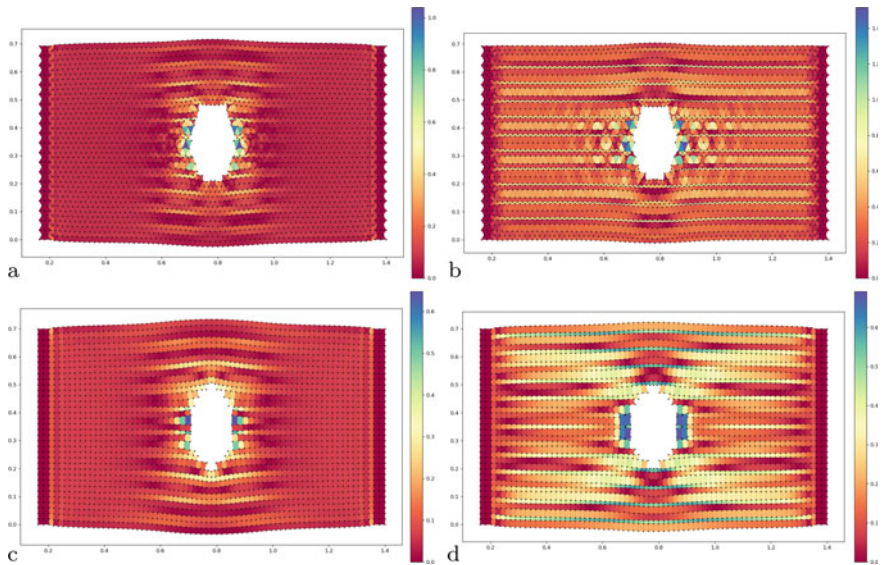


Fig. 6.29 Exotic simulations with holes. **a** Hexagonal lattice with $\alpha_1 = 1.2$, $\alpha_2 = 2.4$, and $\beta = 0.05$; **b** Hexagonal lattice with $\alpha_1 = 0.6$, $\alpha_2 = 2.4$, and $\beta = 0.05$; **c** Squared lattice with $\alpha_1 = 1.8$, $\alpha_2 = 2.4$, and $\beta = 0$; **d** Squared lattice with $\alpha_1 = 3.6$, $\alpha_2 = 1.2$, and $\beta = 0.05$

- it is pretty fast; defining one frame as a pseudo-time step, so the computation of the new position of all the points of the swarm, on our modest computer desktop, it can provide about 14000 frame per seconds with swarm within 10000 elements (e.g., less than 3 s for the simulations of standard traction provided), instead the frame rate decreases to 2000 for swarm within 40000 elements (e.g., about 16 minutes for each simulation shown in Fig. 6.14).
- the algorithm complexity is linear, indeed for every point (for a swarm that contains N points), the interaction is evaluated only with the first (and second in case) neighbors, who's number is fixed once the lattice is chosen. So if the number of

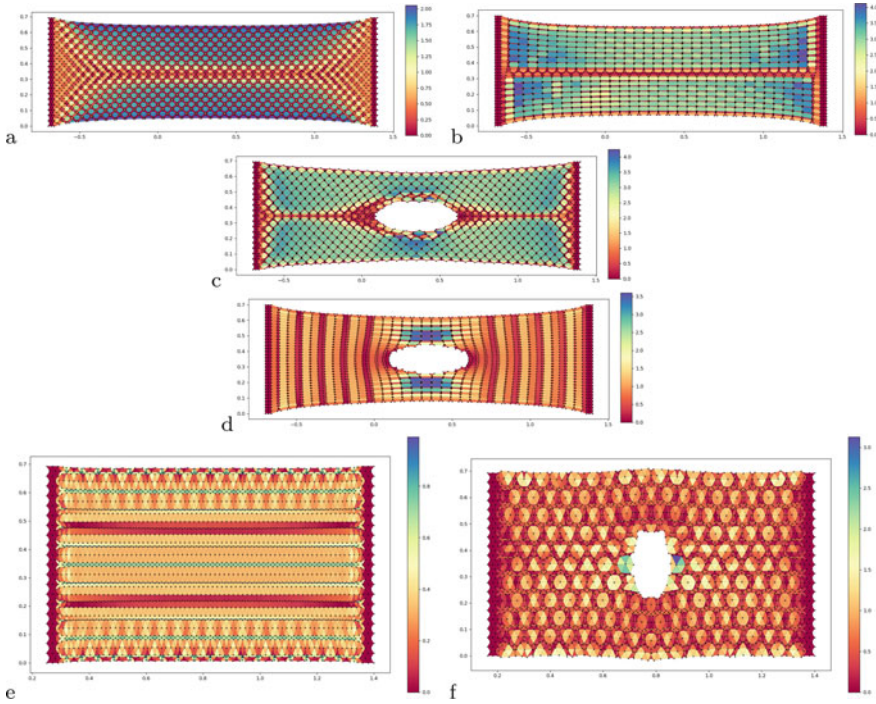


Fig. 6.30 Pre-explosion simulations. **a** Traction of a hexagonal lattice with $\alpha_1 = 1.3$, $\alpha_2 = 0$, and $\beta = 0.06$; **b** Traction of a squared lattice with $\alpha_1 = 2.6$, $\alpha_2 = 0.6$, and $\beta = 0.08$; **c** Traction of a holed hexagonal lattice with $\alpha_1 = 2.6$, $\alpha_2 = 0.4$, and $\beta = 0.12$; **d** Traction of a holed squared lattice with $\alpha_1 = 2.4$, $\alpha_2 = 0.8$, and $\beta = 0.08$; **e** Compression of a hexagonal lattice with $\alpha_1 = 0.6$, $\alpha_2 = 3.0$, and $\beta = 0.05$; **f** Compression of a holed hexagonal lattice with $\alpha_1 = 1.8$, $\alpha_2 = 3.0$, and $\beta = 0$

the mean considered neighbors is N_k , for every pseudo-time step the algorithm evaluate $N \times N_k$ interactions and so its complexity is linear $O(N)$;

- Our model is highly suitable for different kinds of situations: in fact, changing the model’s parameters, like its structure or α and β , it is possible to obtain high variety of responses different among them.
- it can describe complex exotic structure (i.e., deformation bands) by only setting the right parameters and without external modifications.

But our model, as every other model, has also disadvantages that can sum up in:

- now it can only supply qualitative results. There isn’t yet a connection between the constitutive parameters of continua and the parameters of the model. This connection will be investigated in future works;
- the model suffers the superpositions of points; in order to avoid this problem, some precautions have to be taken (e.g., low leader velocities and low α value), which slow down the total computation’s time. These precautions and slow down begin

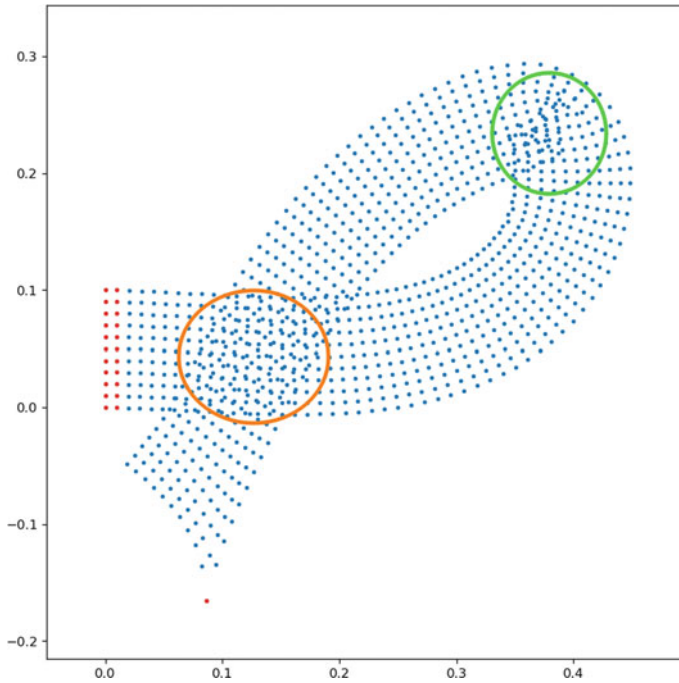


Fig. 6.31 In orange circle, the auto-interpenetration problem occurs, meanwhile in the green circle, we can see the superposition problem

more and more relevant as the number of points increases; another example of superposition is shown in Fig. 6.31;

- in this chapter, there is no attempt to avoid auto-interpenetration of the swarm's pieces far each other, e.g., if in a beam the two opposite edges are stressed in a way that they occupy the same region of the space (see Fig. 6.31).

References

- Abali BE, Völlmecke C, Woodward B, Kashtalyan M, Guz I, Müller WH (2012) Numerical modeling of functionally graded materials using a variational formulation. *Contin Mech Thermodyn* 24(4–6):377–390
- Abali BE, Wu CC, Müller WH (2016) An energy-based method to determine material constants in nonlinear rheology with applications. *Contin Mech Thermodyn* 28(5):1221–1246
- Abdoul-Anziz H, Seppacher P, Bellis C (2019) Homogenization of frame lattices leading to second gradient models coupling classical strain and strain-gradient terms. *Math Mech Solids* 24(12):3976–3999
- Alibert JJ, Seppacher P, dell'Isola F (2003) Truss modular beams with deformation energy depending on higher displacement gradients. *Math Mech Solids* 8(1):51–73

- Altenbach H, Eremeyev V (2015) On the constitutive equations of viscoelastic micropolar plates and shells of differential type. *Mathematics and Mechanics of Complex Systems* 3(3):273–283
- Altenbach H, Eremeyev VA (2008a) Analysis of the viscoelastic behavior of plates made of functionally graded materials. *ZAMM-Zeitschrift für Angewandte Mathematik und Mechanik* 88(5), 332–341
- Altenbach H, Eremeyev VA (2008b) Direct approach-based analysis of plates composed of functionally graded materials. *Archive of Applied Mechanics* 78(10), 775–794
- Altenbach H, Eremeyev VA (2011) On the shell theory on the nanoscale with surface stresses. *Int J Eng Sci* 49(12):1294–1301
- Altenbach H, Eremeyev VA, Naumenko K (2015) On the use of the first order shear deformation plate theory for the analysis of three-layer plates with thin soft core layer. *ZAMM-Zeitschrift für Angewandte Mathematik und Mechanik* 95(10):1004–1011
- Altenbach J, Altenbach H, Eremeyev VA (2010) On generalized Cosserat-type theories of plates and shells: a short review and bibliography. *Arch Appl Mech* 80(1):73–92
- Andreas U, dell’Isola F, Giorgio I, Placidi L, Lekszycki T, Rizzi NL (2016) Numerical simulations of classical problems in two-dimensional (non) linear second gradient elasticity. *Int J Eng Sci* 108:34–50
- Andreas U, Spagnuolo M, Lekszycki T, Eugster SR (2018) A Ritz approach for the static analysis of planar pantographic structures modeled with nonlinear Euler-Bernoulli beams. *Contin Mech Thermodyn* 30(5):1103–1123
- Barchiesi E, Eugster SR, Placidi L, dell’Isola F (2019a) Pantographic beam: A complete second gradient 1D-continuum in plane. *Z Angew Math Phys* 70(5):135
- Barchiesi E, Ganzosch G, Liebold C, Placidi L, Grygoruk R, Müller WH (2019b) Out-of-plane buckling of pantographic fabrics in displacement-controlled shear tests: experimental results and model validation. *Contin Mech Thermodyn* 31(1):33–45
- Barchiesi E, Spagnuolo M, Placidi L (2019c) Mechanical metamaterials: a state of the art. *Math Mech Solids* 24(1):212–234
- Barchiesi E, dell’Isola F, Hild F, Seppecher P (2020a) Two-dimensional continua capable of large elastic extension in two independent directions: asymptotic homogenization, numerical simulations and experimental evidence. *Mech Res Commun* 103(103):466
- Barchiesi E, Eugster SR, dell’Isola F, Hild F (2020b) Large in-plane elastic deformations of bi-pantographic fabrics: asymptotic homogenization and experimental validation. *Math Mech Solids* 25(3):739–767
- Barchiesi E, dell’Isola F, Bersani AM, Turco E (2021a) Equilibria determination of elastic articulated duoskelion beams in 2D via a Riks-type algorithm. *Int J Non-Linear Mech* 128:1–24
- Barchiesi E, dell’Isola F, Hild F (2021b) On the validation of homogenized modeling for bi-pantographic metamaterials via digital image correlation. *Int J Solids Struct* 208:49–62
- Baroudi D, Giorgio I, Battista A, Turco E, Igumnov LA (2019) Nonlinear dynamics of uniformly loaded elastica: experimental and numerical evidence of motion around curled stable equilibrium configurations. *ZAMM-Zeitschrift für Angewandte Mathematik und Mechanik* 99(7):e201800,121
- Battista A, Rosa L, Dell’Erba R, Greco L (2016) Numerical investigation of a particle system compared with first and second gradient continua: deformation and fracture phenomena. *Math Mech Solids* 22. <https://doi.org/10.1177/1081286516657889>
- Battista A, D’Avanzo P, Laudato M (2018) Discrete systems with geometry-driven evolution: application to 1d elasticity and granular media. *Mech Res Commun* 92:107–110
- Bilotta A, Morassi A, Turco E (2018) The use of quasi-isospectral operators for damage detection in rods. *Meccanica* 53(1):319–345
- Bilotta A, Morassi A, Rosset E, Turco E, Vessella S (2019) Numerical size estimates of inclusions in Kirchhoff-Love elastic plates. *Int J Solids Struct* 168:58–72
- Bolzoni G, Fedele R, Maier G (2002) Parameter identification of a cohesive crack model by kalman filter. *Comput Methods Appl Mech Eng* 191(25–26):2847–2871

- Boutin C, Giorgio dell'Isola I F, Placidi L (2017) Linear pantographic sheets: asymptotic micro-macro models identification. *Math Mech Complex Syst* 5(2):127–162
- Browning F, Askes H (2019) Analytical solutions for the natural frequencies of rectangular symmetric angle-ply laminated plates. *Mathematics and Mechanics of Complex Systems* 7(1):51–61
- Casale L, Avella M, Dell'Erba R, Martuscelli E (1998) Broom fibres as reinforcements for thermo-plastic matrices. *Macromol Symposia* 127(1):211–218
- Cazzani A, Ruge P (2016) Stabilization by deflation for sparse dynamical systems without loss of sparsity. *Mechanical Systems and Signal Processing* 70:664–681
- Cazzani A, Malagù M, Turco E (2016a) Isogeometric analysis of plane-curved beams. *Math Mech Solids* 21(5):562–577
- Cazzani A, Malagù M, Turco E, Stochino F (2016b) Constitutive models for strongly curved beams in the frame of isogeometric analysis. *Math Mech Solids* 21(2):182–209
- Cazzani A, Stochino F, Turco E (2016c) An analytical assessment of finite element and isogeometric analyses of the whole spectrum of timoshenko beams. *ZAMM-Zeitschrift für Angewandte Mathematik und Mechanik* 96(10):1220–1244
- Cazzani A, Rizzi NL, Stochino F, Turco E (2018a) Modal analysis of laminates by a mixed assumed-strain finite element model. *Math Mech Solids* 23(1):99–119
- Cazzani A, Serra M, Stochino F, Turco E (2018b) A refined assumed strain finite element model for statics and dynamics of laminated plates. *Continuum Mechanics and Thermodynamics* pp 1–28, <https://doi.org/10.1007/s00161-018-0707-x>
- Contrafatto L, Cuomo M (2002) A new thermodynamically consistent continuum model for hardening plasticity coupled with damage. *International Journal of Solids and Structures* 39(25), 6241–6271
- Cuomo M (2017) Forms of the dissipation function for a class of viscoplastic models. *Mathematics and Mechanics of Complex Systems* 5(3):217–237
- Cuomo M (2019) Continuum damage model for strain gradient materials with applications to 1D examples. *Continuum Mech Thermodyn* 31(4):969–987
- Cuomo M, Contrafatto L, Greco L (2014) A variational model based on isogeometric interpolation for the analysis of cracked bodies. *Int J Eng Sci* 80:173–188
- Cuomo M, dell'Isola F, Greco L (2016) Simplified analysis of a generalized bias test for fabrics with two families of inextensible fibres. *Z Angew Math Phys* 67(3):61
- De Angelo M, Barchiesi E, Giorgio I, Abali BE (2019a) Numerical identification of constitutive parameters in reduced-order bi-dimensional models for pantographic structures: application to out-of-plane buckling. *Arch Appl Mech* 89(7):1333–1358
- De Angelo M, Spagnuolo M, D'Annibale F, Pfaff A, Hoschke K, Misra A, Dupuy C, Peyre P, Dirrenberger J, Pawlikowski M (2019b) The macroscopic behavior of pantographic sheets depends mainly on their microstructure: experimental evidence and qualitative analysis of damage in metallic specimens. *Contin Mech Thermodyn* 31(4):1181–1203
- De Angelo M, Placidi L, NejadSadeghi N, Misra A (2020) Non-standard timoshenko beam model for chiral metamaterial: Identification of stiffness parameters. *Mech Res Commun* 103(103):462
- Del Piero G (2018) The variational structure of classical plasticity. *Mathematics and Mechanics of Complex Systems* 6(3):137–180
- Del Vescovo D, Giorgio I (2014) Dynamic problems for metamaterials: review of existing models and ideas for further research. *International Journal of Engineering Science* 80:153–172
- Della Corte A, Battista A, Dell'Isola F (2015) Referential description of the evolution of a 2D swarm of robots interacting with the closer neighbors: perspectives of continuum modeling via higher gradient continua. *Int J Non-Linear Mech* 12. <https://doi.org/10.1016/j.ijnonlinmec.2015.06.016>, <https://hal.archives-ouvertes.fr/hal-01236021>
- Dell'Erba R (2001) Rheo-mechanical and rheo-optical characterisation of ultra high molecular mass poly(methylmethacrylate) in solution. *Polymer* 42:2655–2663, DOI: 10.1016/S0032-3861(00)00636-4
- Dell'Erba R (2015) Determination of spatial configuration of an underwater swarm with minimum data. *Int J Adv Robot Syst* 12(7):97

- Dell'Erba R (2018) Position-based dynamic of a particle system: a configurable algorithm to describe complex behaviour of continuum material starting from swarm robotics. *Contin Mech Thermodyn* 30. <https://doi.org/10.1007/s00161-018-0663-5>
- Dell'Erba R (2019a) On how swarm robotics can be used to describe particle system's deformation. *Continuum Mech Thermodyn*. <https://doi.org/10.1007/s00161-019-00845-4>
- Dell'Erba R (2019b) Swarm robotics and complex behaviour of continuum material. *Continuum Mech Thermodyn* 31:1–26. <https://doi.org/10.1007/s00161-018-0675-1>
- Dell'Erba R (2020a) The distances measurement problem for an underwater robotic swarm: a semi-experimental trial, using power leds, in unknown sea water conditions. *Contin Mech Thermodyn* 1–9. <https://doi.org/10.1007/s00161-020-00923-y>
- Dell'Erba R (2020b) A tool to describe particle system evolution from swarm robotics behavior. In: *Developments and novel approaches in nonlinear solid body mechanics*. Springer, pp 191–217
- Dell'Erba R (2021a) Distance estimations in unknown sea underwater conditions by power LED for robotics swarms. *Contin Mech Thermodyn*
- Dell'Erba R (2021b) Flocking rules governing swarm robot as tool to describe continuum deformation. In: *Dynamics, strength of materials and durability in multiscale mechanics*. Springer, pp 223–243
- Dell'Erba R (2021c) A plausible description of continuum material behavior derived by swarm robot flocking rules. In: *Dynamics strength of materials and durability in multiscale mechanics*. Springer, pp 329–378
- Dell'Isola F, Andreaus U, Placidi L (2015a) At the origins and in the vanguard of peridynamics, non-local and higher-gradient continuum mechanics: an underestimated and still topical contribution of Gabrio Piola. *Math Mech Solids* 20(8):887–928
- Dell'Isola F, Lekszycki T, Pawlikowski M, Grygoruk R, Greco L (2015b) Designing a light fabric metamaterial being highly macroscopically tough under directional extension: first experimental evidence. *Z Angew Math Phys* 66(6):3473–3498
- Dell'Isola F, Seppecher P, Alibert JJ et al (2019) Pantographic metamaterials: an example of mathematically driven design and of its technological challenges. *Contin Mech Thermodyn* 31(4):851–884
- Desmorat B, Spagnuolo M, Turco E (2020) Stiffness optimization in nonlinear pantographic structures. *Math Mech Solids* 25(12):2252–2262
- Epstein M, Smelser R (2020) An appreciation and discussion of paul germain's "the method of virtual power in the mechanics of continuous media, i: second-gradient theory." *Mathematics and Mechanics of Complex Systems* 8(2):191–199
- Eremeyev VA, Pietraszkiewicz W (2016) Material symmetry group and constitutive equations of micropolar anisotropic elastic solids. *Mathematics and Mechanics of Solids* 21(2), 210–221
- Eremeyev VA, Turco E (2020) Enriched buckling for beam-lattice metamaterials. *Mechanics Research Communications* 103:103,458
- Eugster S, Hesch C, Betsch P, Glocker C (2014) Director-based beam finite elements relying on the geometrically exact beam theory formulated in skew coordinates. *Int J Numer Meth Eng* 97(2):111–129
- Eugster S, dell'Isola F, Steigmann D (2019) Continuum theory for mechanical metamaterials with a cubic lattice substructure. *Math Mech Complex Syst* 7(1):75–98
- Franciosi P, Spagnuolo M, Salman OU (2019) Mean Green operators of deformable fiber networks embedded in a compliant matrix and property estimates. *Contin Mech Thermodyn* 31(1):101–132
- Gagneux G, Millet O (2016) Modeling capillary hysteresis in unsaturated porous media. *Mathematics and Mechanics of Complex Systems* 4(1):67–77
- George D, Allena R, Remond Y (2018) A multiphysics stimulus for continuum mechanics bone remodeling. *Math Mech Complex Syst* 6(4):307–319
- George D, Allena R, Bourzac C, Pallu S, Bensidhoum M, Portier H, Rémond Y (2020) A new comprehensive approach for bone remodeling under medium and high mechanical load based on cellular activity. *Math Mech Complex Syst* 8(4):287–306

- Germain P (2020) The method of virtual power in the mechanics of continuous media, i: Second-gradient theory. *Math Mech Complex Syst* 8(2):153–190
- Giorgio I (2020a) A discrete formulation of Kirchhoff rods in large-motion dynamics. *Mathematics and Mechanics of Solids* 25(5), 1081–1100
- Giorgio I (2020b) Lattice shells composed of two families of curved Kirchhoff rods: An archetypal example, topology optimization of a cycloidal metamaterial. *Contin Mech Thermodyn*. <https://doi.org/10.1007/s00161-020-00955-4>
- Giorgio I, Del Vescovo D (2018) Non-linear lumped-parameter modeling of planar multi-link manipulators with highly flexible arms. *Robotics* 7(4):60
- Giorgio I, Del Vescovo D (2019) Energy-based trajectory tracking and vibration control for multilink highly flexible manipulators. *Mathematics and Mechanics of Complex Systems* 7(2):159–174
- Giorgio I, Scerrato D (2017) Multi-scale concrete model with rate-dependent internal friction. *European Journal of Environmental and Civil Engineering* 21(7–8), 821–839
- Giorgio I, Andreaus U, Scerrato D, dell'Isola F (2016) A visco-poroelastic model of functional adaptation in bones reconstructed with bio-resorbable materials. *Biomech Model Mechanobiol* 15(5):1325–1343
- Giorgio I, Andreaus U, dell'Isola F, Lekszycki T (2017a) Viscous second gradient porous materials for bones reconstructed with bio-resorbable grafts. *Extreme Mech Lett* 13:141–147
- Giorgio I, Rizzi NL, Turco E (2017b) Continuum modelling of pantographic sheets for out-of-plane bifurcation and vibrational analysis. *Proc R Soc A Math Phys Eng Sci* 473(2207):20170,636
- Giorgio I, Harrison P, dell'Isola F, Alsayednoor J, Turco E (2018) Wrinkling in engineering fabrics: a comparison between two different comprehensive modelling approaches. *Proc R Soc A Math Phys Eng Sci* 474(2216):20180,063
- Giorgio I, De Angelo M, Turco E, Misra A (2019a) A Biot–Cossierat two-dimensional elastic nonlinear model for a micromorphic medium. *Contin Mech Thermodyn* 1–13
- Giorgio I, dell'Isola F, Andreaus U, Alzahrani F, Hayat T, Lekszycki T (2019b) On mechanically driven biological stimulus for bone remodeling as a diffusive phenomenon. *Biomech Model Mechanobiol* 18(6):1639–1663
- Giorgio I, Rizzi NL, Andreaus U, Steigmann DJ (2019c) A two-dimensional continuum model of pantographic sheets moving in a 3D space and accounting for the offset and relative rotations of the fibers. *Math Mech Complex Syst* 7(4):311–325
- Giorgio I, Ciallella A, Scerrato D (2020a) A study about the impact of the topological arrangement of fibers on fiber-reinforced composites: some guidelines aiming at the development of new ultra-stiff and ultra-soft metamaterials. *Int J Solids Struct* 203:73–83
- Giorgio I, Spagnuolo M, Andreaus U, Scerrato D, Bersani AM (2020b) In-depth gaze at the astonishing mechanical behavior of bone: A review for designing bio-inspired hierarchical metamaterials. *Math Mech Solids*. <https://doi.org/10.1177/1081286520978516>
- Giorgio I, Varano V, dell'Isola F, Rizzi NL (2021) Two layers pantographs: a 2D continuum model accounting for the beams' offset and relative rotations as averages in $SO(3)$ Lie groups. *Int J Solids Struct* 216:43–58
- Greco F, Luciano R, Serino G, Vaiana N (2018a) A mixed explicit-implicit time integration approach for nonlinear analysis of base-isolated structures. *Ann Solid Struct Mech* 10(1):17–29
- Greco L (2020) An iso-parametric G^1 -conforming finite element for the nonlinear analysis of Kirchhoff rod. Part I: the 2D case. *Contin Mech Thermodyn* 1–24
- Greco L, Cuomo M, Contrafatto L (2018b) A reconstructed local B formulation for isogeometric Kirchhoff–Love shells. *Comput Methods Appl Mech Eng* 332:462–487
- Javili A, Morasata R, Oterkus E, Oterkus S (2019) Peridynamics review. *Math Mech Solids* 24(11):3714–3739
- Marmo F, Masi D, Rosati L (2018a) Thrust network analysis of masonry helical staircases. *Int J Archit Herit* 12(5):828–848
- Marmo F, Ruggieri N, Toraldo F, Rosati L (2018b) Historical study and static assessment of an innovative vaulting technique of the 19th century. *Int J Archit Herit*

- Marmo F, Demartino C, Candela G, Sulpizio C, Briseghella B, Spagnuolo R, Xiao Y, Vanzi I, Rosati L (2019) On the form of the musmeci's bridge over the basento river. *Eng Struct* 191:658–673
- Misra A, Poorsolhjoui P (2016a) Elastic behavior of 2D grain packing modeled as micromorphic media based on granular micromechanics. *J Eng Mech* 143(1):C4016,005
- Misra A, Poorsolhjoui P (2016b) Granular micromechanics based micromorphic model predicts frequency band gaps. *Continuum Mech Thermodyn* 28(1–2):215–234
- Misra A, Nejadi Sadeghi N, De Angelo M, Placidi L (2020) Chiral metamaterial predicted by granular micromechanics: verified with 1d example synthesized using additive manufacturing. *Continuum Mech Thermodyn* 1–17
- Müller M, Heidelberger B, Teschner M, Gross M (2005) Meshless deformations based on shape matching. *ACM Trans Graph* 24:471–478. <https://doi.org/10.1145/1186822.1073216>
- Müller M, Heidelberger B, Hennix M, Ratcliff J (2007) Position based dynamics. *J Vis Commun Image Represent* 18:109–118. <https://doi.org/10.1016/j.jvcir.2007.01.005>
- Moriconi C, Dell'Erba R (2014) Social dependability: a proposed evolution for future robotics. <https://doi.org/10.12910/EAI2014-63>
- Nejadi Sadeghi N, De Angelo M, Drobnicki R, Lekszycki T, dell'Isola F, Misra A (2019) Parametric experimentation on pantographic unit cells reveals local extremum configuration. *Exp Mech* 59(6):927–939
- Niiranen J, Khakalo S, Balobanov V, Niemi AH (2016) Variational formulation and isogeometric analysis for fourth-order boundary value problems of gradient-elastic bar and plane strain/stress problems. *Comput Methods Appl Mech Eng* 308:182–211
- Olive M (2019) Effective computation of SO(3) and O(3) linear representation symmetry classes. *Mathematics and Mechanics of Complex Systems* 7(3):203–237
- Paradiso M, Marmo F, Rosati L (2019) Consistent derivation of a beam model from the saint venant's solid model. *Int J Solids Struct* 159:90–110
- Paradiso M, Sessa S, Vaiana N, Marmo F, Rosati L (2021) Shear properties of isotropic and homogeneous beam-like solids having arbitrary cross sections. *Int J Solids Struct*
- Perricone V, Grun T, Marmo F, Langella C, Carnevali MDC (2020) Constructional design of echinoid endoskeleton: main structural components and their potential for biomimetic applications. *Bioinspiration Biomim*
- Placidi L (2016) A variational approach for a nonlinear one-dimensional damage-elasto-plastic second-gradient continuum model. *Continuum Mech Thermodyn* 28(1–2):119–137
- Placidi L, Andreaus U, Giorgio I (2017) Identification of two-dimensional pantographic structure via a linear d4 orthotropic second gradient elastic model. *J Eng Math* 103(1):1–21
- Placidi L, Barchiesi E, Misra A (2018a) A strain gradient variational approach to damage: a comparison with damage gradient models and numerical results. *Math Mech Complex Syst* 6(2):77–100
- Placidi L, Misra A, Barchiesi E (2018b) Two-dimensional strain gradient damage modeling: a variational approach. *Z Angew Math Phys* 69(3):56
- Rapisarda A, Della Corte A, Drobnicki R, Cosmo F, Rosa L (2018) A model for bone mechanics and remodeling including cell populations dynamics. *Zeitschrift für angewandte Mathematik und Physik* 70. <https://doi.org/10.1007/s00033-018-1055-1>
- Rapisarda A, Almasi M, Almasi N, Barchiesi E, Della Corte A, Scerrato D (2020) Bone mechanics and cell populations: mathematical description and parametric study of the model, pp 107–126. https://doi.org/10.1007/978-3-030-50464-9_7
- Rickert W, Vilchevskaya E, Müller W (2019) A note on Couette flow of micropolar fluids according to Eringen's theory. *Math Mech Complex Syst* 7(1):25–50
- Rosi G, Placidi L, Auffray N (2018) On the validity range of strain-gradient elasticity: a mixed static-dynamic identification procedure. *Eur J Mech A/Solids* 69:179–191
- Şahin E (2005) Swarm robotics: from sources of inspiration to domains of application, pp 10–20
- Scerrato D, Giorgio I (2019) Equilibrium of two-dimensional cycloidal pantographic metamaterials in three-dimensional deformations. *Symmetry* 11(12):1523
- Scerrato D, Giorgio I, Madeo A, Limam A, Darve F (2014) A simple non-linear model for internal friction in modified concrete. *Int J Eng Sci* 80:136–152

- Scerrato D, Zhurba Eremeeva IA, Lekszycki T, Rizzi NL (2016) On the effect of shear stiffness on the plane deformation of linear second gradient pantographic sheets. *ZAMM-Zeitschrift für Angewandte Mathematik und Mechanik* 96(11):1268–1279
- Schulte J, Dittmann M, Eugster S, Hesch S, Reinicke T, Dell'Isola F, Hesch C (2020) Isogeometric analysis of fiber reinforced composites using kirchhoff-love shell elements. *Comput Methods Appl Mech Eng* 362(112):845
- Sciarra G, dell'Isola F, Coussy O (2007) Second gradient poromechanics. *Int J Solids Struct* 44(20):6607–6629
- Sepecher P, Alibert JJ, dell'Isola F (2011) Linear elastic trusses leading to continua with exotic mechanical interactions. *J Phys. Conference Series*, IOP Publishing, vol 319, p 012018
- Serpieri R, Sessa S, Rosati L (2018) A mitc-based procedure for the numerical integration of a continuum elastic-plastic theory of through-the-thickness-jacketed shell structures. *Compos Struct* 191:209–220
- Sessa S, Marmo F, Rosati L (2015) Effective use of seismic response envelopes for reinforced concrete structures. *Earthq Eng Struct Dyn* 44(14):2401–2423
- Sessa S, Serpieri R, Rosati L (2017) A continuum theory of through-the-thickness jacketed shells for the elasto-plastic analysis of confined composite structures: Theory and numerical assessment. *Compos B Eng* 113:225–242
- Sessa S, Marmo F, Rosati L, Leonetti L, Garcea G, Casciaro R (2018a) Evaluation of the capacity surfaces of reinforced concrete sections: Eurocode versus a plasticity-based approach. *Meccanica* 53(6):1493–1512
- Sessa S, Marmo F, Vaiana N, Rosati L (2018b) A computational strategy for eurocode 8-compliant analyses of reinforced concrete structures by seismic envelopes. *J Earthq Eng* 1–34
- Sessa S, Marmo F, Vaiana N, De Gregorio D, Rosati L (2019a) Strength hierarchy provisions for transverse confinement systems of shell structural elements. *Compos B Eng* 163:413–423
- Sessa S, Marmo F, Vaiana N, Rosati L (2019b) Probabilistic assessment of axial force-biaxial bending capacity domains of reinforced concrete sections. *Meccanica* 54(9):1451–1469
- Spagnuolo M (2020) Circuit analogies in the search for new metamaterials: Phenomenology of a mechanical diode. In: *Nonlinear wave dynamics of materials and structures*. Springer, pp 411–422
- Spagnuolo M, Andreaus U (2019) A targeted review on large deformations of planar elastic beams: extensibility, distributed loads, buckling and post-buckling. *Mathematics and Mechanics of Solids* 24(1), 258–280
- Spagnuolo M, Scerrato D (2020) The mechanical diode: on the tracks of James Maxwell employing mechanical–electrical analogies in the design of metamaterials. In: *Developments and novel approaches in biomechanics and metamaterials*. Springer, pp 459–469
- Spagnuolo M, Barcz K, Pfaff A, dell'Isola F, Franciosi P (2017) Qualitative pivot damage analysis in aluminum printed pantographic sheets: numerics and experiments. *Mech Res Commun* 83:47–52
- Spagnuolo M, Yildizdag ME, Andreaus U, Cazzani AM (2020) Are higher-gradient models also capable of predicting mechanical behavior in the case of wide-knit pantographic structures? *Math Mech Solids*. <https://doi.org/10.1177/1081286520937339>
- Steigmann DJ (2018) Equilibrium of elastic lattice shells. *Journal of Engineering Mathematics* 109(1), 47–61
- Steigmann DJ, dell'Isola F (2015) Mechanical response of fabric sheets to three-dimensional bending, twisting, and stretching. *Acta Mechanica Sinica* 31(3), 373–382
- Timofeev D, Barchiesi E, Misra A, Placidi L (2020) Hemivariational continuum approach for granular solids with damage-induced anisotropy evolution. *Math Mech Solids* 1081286520968149
- Tran LV, Niiranen J (2020) A geometrically nonlinear Euler-Bernoulli beam model within strain gradient elasticity with isogeometric analysis and lattice structure applications. *Mathematics and Mechanics of Complex Systems* 8(4):345–371
- Turco E (2018a) Discrete is it enough? The revival of Piola-Hencky keynotes to analyze three-dimensional Elastica. *Continuum Mech Thermodyn* 30(5):1039–1057
- Turco E (2018b) In-plane shear loading of granular membranes modeled as a Lagrangian assembly of rotating elastic particles. *Mechanics Research Communications* 92:61–66

- Turco E (2019) Numerically driven tuning of equilibrium paths for pantographic beams. *Continuum Mech Thermodyn* 31(6):1941–1960
- Turco E, Barchiesi E (2019) Equilibrium paths of Hencky pantographic beams in a three-point bending problem. *Mathematics and Mechanics of Complex Systems* 7(4):287–310
- Turco E, dell’Isola F, Cazzani A, Rizzi NL (2016a) Hencky-type discrete model for pantographic structures: numerical comparison with second gradient continuum models. *Z Angew Math Phys* 67(4):85
- Turco E, dell’Isola F, Rizzi NL, Grygoruk R, Müller WH, Liebold C (2016b) Fiber rupture in sheared planar pantographic sheets: numerical and experimental evidence. *Mech Res Commun* 76:86–90
- Turco E, dell’Isola F, Misra A (2019) A nonlinear Lagrangian particle model for grains assemblies including grain relative rotations. *Int J Numer Anal Meth Geomech* 43(5):1051–1079
- Turco E, Barchiesi E, Giorgio I, dell’Isola F (2020) A Lagrangian Hencky-type non-linear model suitable for metamaterials design of shearable and extensible slender deformable bodies alternative to Timoshenko theory. *Int J Non-Linear Mech* 123(103):481
- Vaiana N, Spizzuoco M, Serino G (2017) Wire rope isolators for seismically base-isolated lightweight structures: experimental characterization and mathematical modeling. *Eng Struct* 140:498–514
- Vaiana N, Sessa S, Marmo F, Rosati L (2018) A class of uniaxial phenomenological models for simulating hysteretic phenomena in rate-independent mechanical systems and materials. *Nonlinear Dyn* 93(3):1647–1669
- Vaiana N, Sessa S, Marmo F, Rosati L (2019) Nonlinear dynamic analysis of hysteretic mechanical systems by combining a novel rate-independent model and an explicit time integration method. *Nonlinear Dyn* 98(4):2879–2901
- Vaiana N, Capuano R, Sessa S, Marmo F, Rosati L (2021) Nonlinear dynamic analysis of seismically base-isolated structures by a novel open-source hysteretic material model. *Appl Sci* 11(3):900
- Valoroso N, Marmo F, Sessa S (2015) A novel shell element for nonlinear pushover analysis of reinforced concrete shear walls. *Bull Earthq Eng* 13(8):2367–2388
- Vangelatos Z, Gu GX, Grigoropoulos CP (2019) Architected metamaterials with tailored 3D buckling mechanisms at the microscale. *Extreme Mech Lett* 33(100):580
- Wiech J, Eremeyev VA, Giorgio I (2018) Virtual spring damper method for nonholonomic robotic swarm self-organization and leader following. *Contin Mech Thermodyn* 30(5):1091–1102
- Yang H, Ganzosch G, Giorgio I, Abali BE (2018) Material characterization and computations of a polymeric metamaterial with a pantographic substructure. *Z Angew Math Phys* 69(4):1–16
- Yang H, Abali BE, Timofeev D, Müller WH (2019) Determination of metamaterial parameters by means of a homogenization approach based on asymptotic analysis. *Contin Mech Thermodyn* 1–20
- Yang Y, Misra A (2012) Micromechanics based second gradient continuum theory for shear band modeling in cohesive granular materials following damage elasticity. *International Journal of Solids and Structures* 49(18), 2500–2514
- Yildizdag ME, Tran CA, Barchiesi E, Spagnuolo M, dell’Isola F, Hild F (2019) A multi-disciplinary approach for mechanical metamaterial synthesis: A hierarchical modular multiscale cellular structure paradigm. In: *State of the art and future trends in material modeling*. Springer, pp 485–505
- Yildizdag ME, Barchiesi E, dell’Isola F (2020a) Three-point bending test of pantographic blocks: numerical and experimental investigation. *Math Mech Solids* 25(10):1965–1978
- Yildizdag ME, Demirtas M, Ergin A (2020b) Multipatch discontinuous galerkin isogeometric analysis of composite laminates. *Contin Mech Thermodyn* 32(3):607–620

Chapter 7

A Review of the Class of Bouc-Wen Differential Models for Simulating Mechanical Hysteresis Phenomena



Daive Pellecchia and Massimo Paradiso

Abstract One of the most popular hysteretic models used in many areas of engineering, especially the civil one, is the Bouc-Wen model. Although this model is able to simulate several types of hysteretic phenomena, it cannot describe some typical phenomena, such as cyclic degradation of strength and stiffness, pinching effect, and so on. For this reason, many researchers have proposed several variants of the original Bouc-Wen model. We present a review of the Bouc-Wen model and its most significant enhanced versions, utilizing the same technical terminology for all models in order to clarify and to shed some light on the number and physical significance of the parameters that the models require as input. Sensitivity analyses are also illustrated with respect to the input parameters.

Keywords Civil engineering · Hysteresis · Bouc-Wen model · Cyclic degradation · Sensitivity analysis

7.1 Introduction

Hysteresis is a complex phenomenon that can be experienced in many fields of science and technology; undoubtedly it represents the predominant typology of nonlinear constitutive behavior. The importance of properly reproducing hysteretic responses in engineering has been highlighted by several contributions available in the literature (Visintin 2013). The main research fields include civil applications (Bahn and Hsu 1998; Lima et al. 2018; Zuccaro et al. 2017), magnetism (Bai et al. 2019), as well as higher-gradient materials (Alibert et al. 2003; Pideri and Seppecher 1997; Barchiesi et al. 2018), and mechanics of thermal and porous media (Altenbach et al.

D. Pellecchia (✉) · M. Paradiso
Department of Structures for Engineering and Architecture, University
of Naples Federico II, via Claudio 21, 80125 Naples, Italy
e-mail: davide.pellecchia@unina.it

M. Paradiso
e-mail: massimo.paradiso@unina.it

© Springer Nature Switzerland AG 2021
F. Marmo et al. (eds.), *Mathematical Applications in Continuum
and Structural Mechanics*, Advanced Structured Materials 127,
https://doi.org/10.1007/978-3-030-42707-8_7

2012; Eremeyev and Morozov 2010). Beyond basic applications such as the modeling of seismic devices (Kikuchi and Aiken 1997), dampers (Nuzzo et al. 2019), and concrete (Sessa et al. 2018, 2019b), hysteresis plays a significant role also for the analysis of more complex mechanical systems (Badoni and Makris 1996; Song et al. 2007; Greco and Cuomo 2013) including applications concerning framed (Marmo et al. 2011; Marmo and Rosati 2012a,b, 2013) and shell structures (Caggegi et al. 2018; Serpieri et al. 2018; Ascione et al. 2017; Sessa et al. 2017, 2019a; Valoroso et al. 2014, 2015), structural identification (Noël and Kerschen 2017), and random vibrations (Baber and Noori 1985; Sessa 2010; Wen 1976). More recent developments concerns meta-materials (Turco et al. 2017, 2018; De Angelo et al. 2019; di Cosmo et al. 2018; Andreaus et al. 2018) based on pantographic microstructures (Barchiesi et al. 2020; dell'Isola et al. 2019a, 2019b; NejadSadeghi et al. 2019) as well as the modeling of damage (Contrafatto and Cuomo 2002; Contrafatto et al. 2012; Placidi et al. 2018, 2019).

The output of hysteretic systems and materials typically depends on present and past histories of the input variable and can exhibit different peculiar features: in particular, when the first time derivative of the input variable does not influence the output, this hysteresis phenomenon is denominated *rate-independent*.

The development of mathematical models able to describe such nonlinear phenomena is very complicated. In particular, in the last few years, many researchers have proposed different models whose common objective was not to explain the physical origin of the hysteresis but to try to reproduce the overall experimental behavior (Mayergoyz 2003). These models are called *phenomenological* models.

It is possible to classify the phenomenological models according to the nature of the equation to solve for the evaluation of the output variable, namely the generalized force or the generalized displacement. In particular one has:

- algebraic models, such as the ones developed by Ramberg and Osgood Ramberg and Osgood (1943), Menegotto and Pinto Menegotto (1973), and Vaiana et al. (2019a, b, c, 2020, 2021b, a, c);
- transcendental models, such as the ones introduced by Kikuchi and Aiken Kikuchi and Aiken (1997) and Sessa et al. (2020); Vaiana et al. (2018);
- differential models, such as those formulated by Bouc (1967, 1971), Özdemiir Özdemiir (1976), and Wen (1976, 1980);
- damage-based models, such as the one proposed by Fedele et al. (2012), Sessa and Valoroso (2017), Valoroso and Fedele (2010), Valoroso et al. (2013).

Among existing models, the differential ones are currently the most used models to reproduce the behavior of mechanical systems and materials. These models are typically based on the Duhem hysteresis operator (Duhem 1897) whose formulation is defined by a Cauchy problem of the form:

$$\begin{cases} \dot{z}(t) = g_1(x, z) \dot{x}(t)^+ + g_2(x, z) \dot{x}(t)^-, \\ z(0) = z_0, \end{cases} \quad (7.1)$$

in which $z(t)$ and $x(t)$ denote the hysteretic functions and the generalized displacement, respectively, and the superimposed dot denotes the derivative with respect to time t ; g_1 and g_2 are continuous functions whereas $\dot{x}(t)^+ = \max(0, \dot{x}(t))$ and $\dot{x}(t)^- = \min(0, \dot{x}(t))$; finally z_0 represents the value of the function $z(t)$ at the time $t = 0$. All models based on Duhem's class are characterized by a peculiar property: the output value can be evaluated if the current values of the input and output variables (x, z) as well as the sign of the first derivative with respect to time of the input variable ($\text{sign}(\dot{x})$) are known Dimian and Andrei (2014). Examples of differential models based on the Duhem hysteresis operator are the ones proposed by Jiles and Atherton (1983, 1984), Hodgdon (1988), Bouc (1971), Wen (1976, 1980), and Özdemir (1976).

The present work aims to illustrate the evolution of the Bouc-Wen model in the area of mechanics. In particular, such an evolution is described with reference to the modeling of symmetric and asymmetric hysteresis loops, hysteresis loops with pinching, and hysteresis loops with strength and/or stiffness degradation typically displayed by *rate-independent* mechanical systems and materials. The influence of the input parameters on the dimension and/or shape of the hysteresis loops is shown and discussed for each hysteretic model.

This paper is organized into four parts. In Sect. 7.2, we review some models able to describe symmetric hysteresis behaviors, namely the Bouc model (Bouc 1967, 1971) and the Wen model (Wen 1976), the latter currently known as the Bouc-Wen model. In Sect. 7.3, we review some modified Bouc-Wen models able to describe asymmetric hysteresis behaviors. In Sect. 7.4, the modified versions of the Bouc-Wen model, proposed by some researchers in order to account for the pinching effect, are illustrated. Finally, in Sect. 7.5, some models able to simulate both the strength and stiffness degradation are described.

7.2 Modeling of Symmetric Hysteresis Loops

From a mathematical point of view, symmetric hysteresis loops are characterized by odd functions with respect to the origin of the reference frame, i.e. hysteretic functions z fulfilling the condition

$$z(x) = -z(-x). \quad (7.2)$$

Among several mechanical systems and materials that exhibit a nonlinear behavior characterized by symmetric hysteresis loops, we recall, as an example, the typical cross section of steel and concrete filled steel elements (Colombo and Negro 2005; Shih and Sung 2005), metal devices, such as wire rope isolators deforming along their transverse directions (Vaiana et al. 2017), and seismic protection devices, such as isolators (Greco et al. 2018; Hadad et al. 2017; Losanno et al. 2019a,b, 2021; Sierra et al. 2019; Vaiana et al. 2019d; Pellicchia et al. 2020) and dampers (Nuzzo et al. 2018, 2019). In Fig. 7.1, some examples of symmetric hysteresis loops obtained in experimental tests are shown.

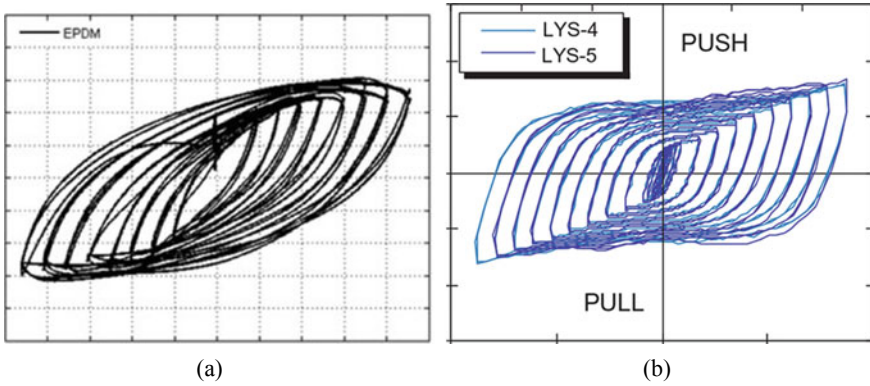


Fig. 7.1 Some symmetric hysteresis loops obtained in experimental tests. **a** The hysteresis behavior of a bearing—Hadad et al. (2017). **b** The hysteresis behavior of a rhombic steel plate Shih and Sung (2005)

The restoring force of the above-described mechanical systems and materials is typically computed as follows:

$$f(x) = f_e(x) + f_h(x), \quad (7.3)$$

where $f_e(x)$ is the elastic component whereas $f_h(x)$ is the hysteretic one. In turn, the restoring force can be described in the following way:

$$f(x) = \alpha k x + (1 - \alpha) k z(x), \quad (7.4)$$

in which α is ratio between the post-yield and pre-yield stiffness whereas k is defined as the stiffness at yield, i.e. the ratio between the yield force and the generalized yield displacement.

7.2.1 Bouc Model and Its Modified Versions

The full class of Bouc models is described by the following general nonlinear first-order ordinary differential equation:

$$\dot{z} = B \dot{x}, \quad (7.5)$$

in which \dot{z} denotes the time derivative of the hysteretic variable, required to evaluate the rate-independent hysteretic component $f_h(x) = (1 - \alpha) k z(x)$, whereas \dot{x} is the generalized velocity. The hysteretic function z basically depends on the system behavior, material properties, and response amplitude.

The nonlinear function B has been assumed of different forms over the years Bouc (1967, 1971):

$$\text{Bouc model 1 (1967): } B = A - z \beta \operatorname{sign}(\dot{x}), \quad (7.6a)$$

$$\text{Bouc model 2 (1967): } B = A - |z| \left(\gamma + \beta \operatorname{sign}(\dot{x} z) \right), \quad (7.6b)$$

$$\text{Wen model (1976): } B = A - |z|^n \left(\gamma + \beta \operatorname{sign}(\dot{x} z) \right) \quad (7.6c)$$

where A , n , and γ are material parameters that tune the size and/or the shape of the hysteresis loops.

Equation (7.6a), that defines the original Bouc model, is characterized by two model parameters, namely A and β . Subsequently, Bouc has modified such an equation by adding a new parameter, that is γ , as shown in Eq. (7.6b). Finally, Wen has extended the class of the Bouc differential models by adding the parameter n in order to smooth the hysteretic curve predicted by the original Bouc model. Note that equation $f(x) = \alpha k x + (1 - \alpha) k z$ and Eq. (7.6c) define the so-called Bouc-Wen model.

The smooth nature of the Bouc model modified by Wen makes it particularly convenient for addressing several engineering problems especially when several dynamic analyses are required. This includes the case of flutter analysis (Carboni et al. 2018) and Random Vibration analysis of structures (Broccardo et al. 2017; Fujimura and Der Kiureghian 2007; Sessa 2010).

The Bouc-Wen model is capable of reproducing several behaviors depending on the parameters A , β , γ , and n , whose influence on the hysteretic variable z is illustrated in Sect. 7.2.2.

7.2.2 Sensitivity Analysis

A parameter sensitivity analysis was carried out to evaluate the effect of each parameter on the hysteretic variable $z(x)$ obtained by adopting Eqs. (7.5) and (7.6c).

The relationship between the hysteretic variable z and the generalized displacement x is shown in Fig. 7.2 for different combinations of the constitutive parameters. All hysteretic loops are obtained by applying a generalized displacement described by the following sine wave:

$$x(t) = 2 \sin(t) \quad (7.7)$$

and integrating differential Eq. (7.5) by MATLAB® using the solver ode45.

The top left plot shows that the tangent stiffness at the origin of the hysteresis loop increases when the parameter A is increased and its sign is the same as that of A ; for negative values of parameter A , the tangent stiffness at the origin becomes negative.

The top right plot shows that the hysteretic energy dissipation increases as β increases. In particular, an elastic nonlinear constitutive law can be obtained by setting $\beta = 0$.

The bottom left plot shows that the hysteresis loop is bounded between two parallel straight lines and it rotates clockwise when the parameter γ is increased. On the other

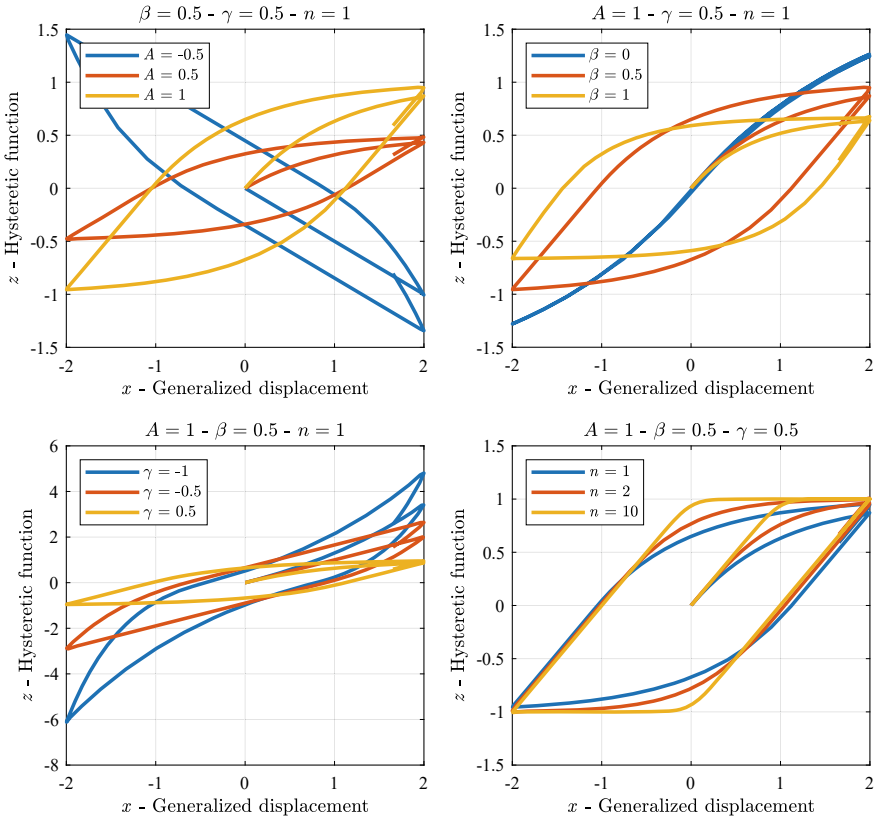


Fig. 7.2 Sensitivity analysis of the Bouc-Wen model with respect to the material parameters

hand, by decreasing the value of γ , the hysteresis loop is bounded by two parallel curves such that, for high values of the displacement x , the hysteresis loop exhibits a work hardening behavior.

Finally, the bottom right plot shows that the hysteresis loop gets smoother with decreasing n so that such a parameter can be related to the smoothness of the hysteresis loop. In the limit case $n \rightarrow \infty$, the constitutive law becomes elastic-perfectly plastic.

7.3 Modeling of Asymmetric Hysteresis Loops

There exist several mechanical systems and materials displaying a nonlinear response characterized by asymmetric hysteresis loops; typical examples are some materials, such as metals (Dobson et al. 1997), polymers (Hossain et al. 2012), and shape memory alloys (Graesser and Cozzarelli 1991), as well as some devices, such as

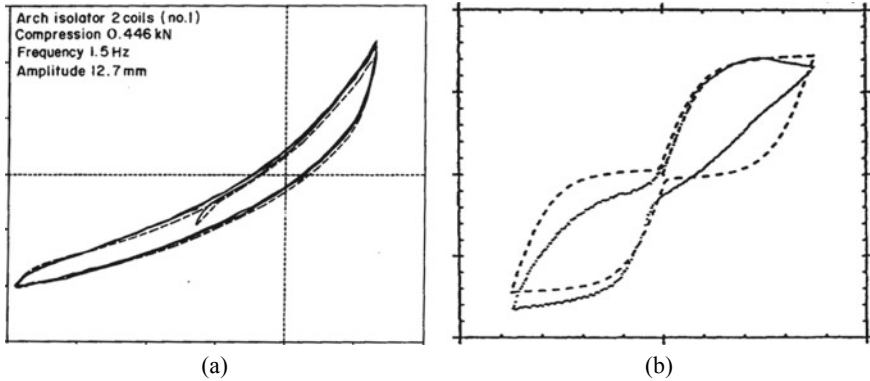


Fig. 7.3 Some asymmetric hysteresis loops obtained in experimental tests. **a** The asymmetric hysteresis behavior of a wire rope isolator along their axial direction—Demetriades et al. (1993). **b** The asymmetric hysteresis behavior of a Nitinol—Dobson et al. (1997)

wire rope isolators deforming along their axial direction (Demetriades et al. 1993) and dampers (Kwok et al. 2006, 2007). Asymmetric hysteresis loops obtained in experimental tests and retrieved from the literature are shown in Fig. 7.3.

7.3.1 Asymmetric Bouc-Wen Models

The differential models described in Sect. 7.2 are not able to reproduce rate-independent asymmetric hysteresis phenomena. Hence, to simulate the typical asymmetric hysteresis loops, some researchers (Sireteanu et al. 2012; Song and Der Kiureghian 2006; Wang and Wen 1998) have proposed the following generalized expression for the function:

$$B = A - |z^n| \Psi, \tag{7.8}$$

where Ψ assumes different forms according to the specific improved model that is adopted. In particular, one has

$$\text{Wang and Wen (1998)} : \Psi = \gamma + \beta \operatorname{sign}(\dot{x} z) + \phi \operatorname{sign}(\dot{x} + \dot{z}) \quad (7.9a)$$

$$\text{Song and Der Kiureghian (2006)} : \left\{ \begin{array}{l} \Psi = \beta_1 \operatorname{sign}(\dot{x} z) + \beta_2 \operatorname{sign}(x \dot{x}) \\ + \beta_3 \operatorname{sign}(x z) + \beta_4 \operatorname{sign}(\dot{x}) \\ + \beta_5 \operatorname{sign}(z) + \beta_6 \operatorname{sign}(x) \end{array} \right. \quad (7.9b)$$

$$\text{Sireteanu et al. (2012)} : \left\{ \begin{array}{l} \Psi = \beta_1 \operatorname{sign}(\dot{x} z) + \beta_2 \operatorname{sign}(x \dot{x}) \\ - \beta_2 \operatorname{sign}(x z) + \beta_4 \operatorname{sign}(\dot{x}) \\ + \beta_5 \operatorname{sign}(z) \end{array} \right. \quad (7.9c)$$

where β_1, \dots, β_6 and ϕ are material parameters.

Equation (7.9a), introduced by Wang and Wen, includes an additional parameter ϕ that takes into account the asymmetric behavior; being independent of the sign of the generalized displacement x , Eq. (7.9a) cannot describe the asymmetric hysteresis due to cyclic phenomena since, during them, the sign of the generalized displacement x changes.

For this reason, Song and Der Kiureghian have developed Eq. (7.9b); basically, the function Ψ defined by this equation can assume different values in six phases depending on the signs of x , \dot{x} , and z and on the values of six fixed parameters, namely β_1, \dots, β_6 . Consequently, this model has six degrees of freedom that affect the complexity of the parameter identification.

Subsequently, Sireteanu et al. have modified the Song and Der Kiureghian model by imposing the following conditions:

$$\beta_3 = -\beta_2 \quad \text{and} \quad \beta_6 = 0, \quad (7.10)$$

that represent a continuity condition of the hysteresis loop at the points of intersections with the axis of ordinates. Equation (7.9c) describes four different behaviors depending on the signs of x , \dot{x} , and z and on the values of only four fixed parameters, namely $\beta_1, \beta_2, \beta_4$, and β_5 .

Figure 7.4 shows the four different curves of the Ψ function defined by Sireteanu et al. The continuity condition (7.10) involves that the hysteretic loop is characterized by the conditions:

$$\Psi_3 = \Psi_4 \quad \text{and} \quad \Psi_6 = \Psi_1. \quad (7.11)$$

Table 7.1 lists the sign combinations of x , \dot{x} , and z for the different curves showed in Fig. 7.4.

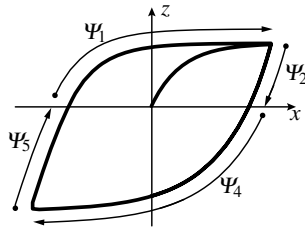


Fig. 7.4 Values of the Ψ function in the model by Sireteanu et al.

Table 7.1 Sign combinations of the Ψ function in the model by Sireteanu et al.

| Phase | x | \dot{x} | z | $\psi(x, \dot{x}, z)$ |
|-------|-------|-----------|-----|--|
| 1 | $[-]$ | $+$ | $+$ | $\psi_1 = \beta_1 + \beta_4 + \beta_5$ |
| 2 | $+$ | $-$ | $+$ | $\psi_2 = -\beta_1 - 2\beta_2 - \beta_4 + \beta_5$ |
| 3 | $[-]$ | $-$ | $-$ | $\psi_4 = \beta_1 - \beta_4 - \beta_5$ |
| 4 | $-$ | $+$ | $-$ | $\psi_5 = -\beta_1 - 2\beta_2 + \beta_4 - \beta_5$ |

7.3.2 Sensitivity Analysis

A parameter sensitivity analysis was carried out to evaluate the effect of each parameter of the Ψ function on the hysteretic variable $z(x)$ evaluated by adopting Eqs. (7.5), (7.8), and (7.9c).

Figure 7.5 shows the relationship between the hysteretic variable z and the generalized displacement x . All hysteretic loops have been obtained by applying a generalized displacement described by the sine wave (7.7).

The top left plot shows the influence of the first value of the Ψ function, namely Ψ_1 , on the hysteretic loop. Such a value modifies the shape of the hysteretic loop in the first and second quadrant when $\dot{x} > 0$ and $z > 0$: the hysteretic variable z is prone to decrease with an increasing value of Ψ_1 ; the hysteretic loop exhibits work hardening(softening) when the Ψ_1 value is negative (positive).

The influence of the Ψ_2 value on the hysteretic loop is shown in the top right plot. The value Ψ_2 modifies the trend of the hysteretic loop in the second quadrant when $x > 0$, $\dot{x} < 0$, and $z > 0$: the hysteretic variable z is prone to decrease with an increasing value of Ψ_2 ; the hysteretic loop is concave (convex) when the Ψ_2 value is negative (positive).

The Ψ_4 value modifies the shape of the hysteretic loop in the third and fourth quadrants when $\dot{x} < 0$ and $z < 0$; the influence of such a value is shown in the bottom left plot: the hysteretic variable z is prone to increase with an increasing value of Ψ_4 ; the hysteretic loop shows work hardening (softening) when the Ψ_4 value is negative (positive).

Finally, the bottom right plot shows the influence of the Ψ_5 value on the hysteretic loop. This value modifies the shape of the hysteretic loop in the third quadrant

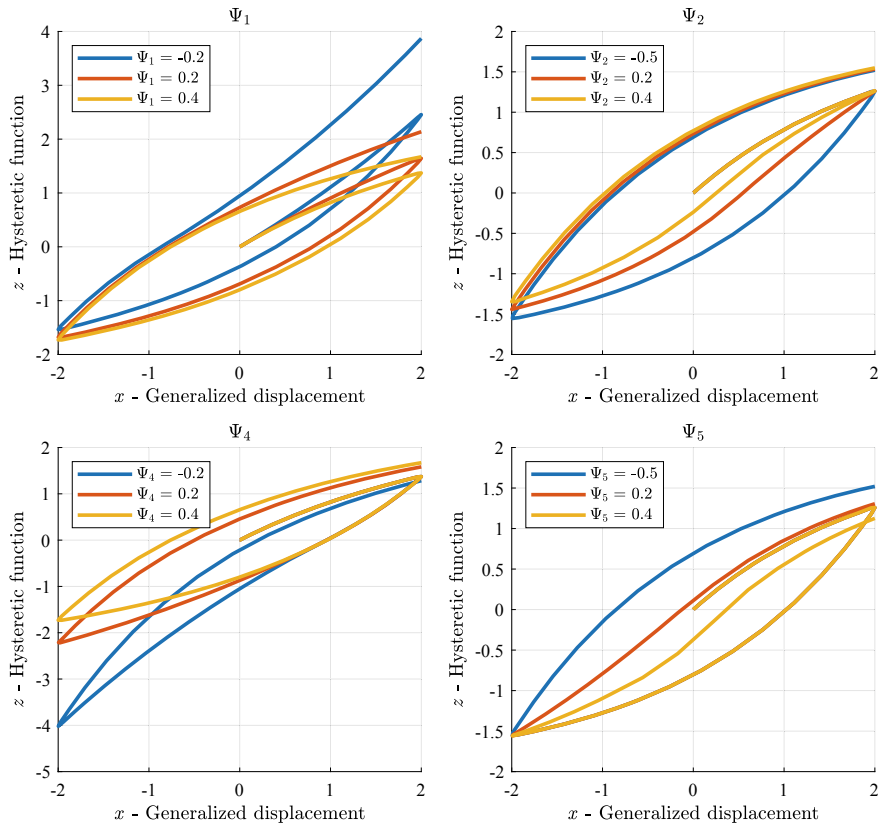


Fig. 7.5 Sensitivity analysis of the model by Sireteanu et al. with respect to the material parameters

when $x < 0$, $\dot{x} > 0$, and $z < 0$: the hysteretic function z is prone to increase with an increasing value of Ψ_5 ; namely, the hysteretic loop is concave (convex) when the Ψ_5 value is positive (negative).

7.4 Modeling of Pinched Hysteresis Loops

The pinching effect is a physical phenomenon, observed in many experimental results (Kreger and Abrams 1978), in which a very low incremental stiffness near the origin is followed by a stiffening under greater generalized displacements. In particular, we can observe the pinching effect in reinforced concrete structures due to the high shear loads, the slippage of longitudinal reinforcement (Banon and Veneziano 1982), the opening and closing of cracks in the compression zones (Park and Paulay 1975), Y-braced steel frames (Zamani et al. 2012), and confined walls of masonry

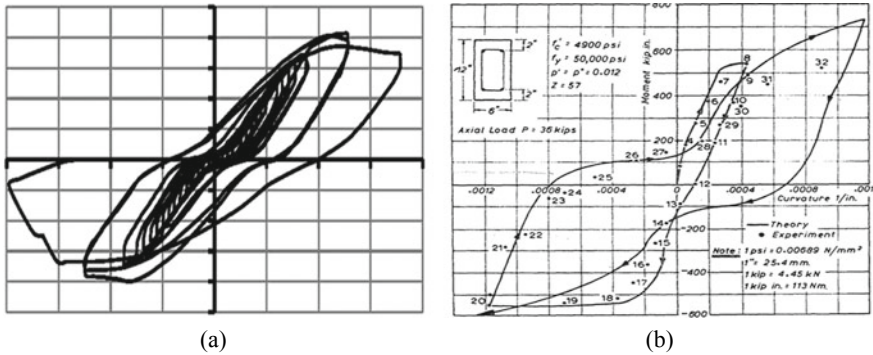


Fig. 7.6 Some hysteresis loops, having the pinching effect, obtained in experimental tests. **a** The hysteresis behavior of a steel frame having single bays with symmetrical y-shaped concentric bracings—Zamani et al. (2012). **b** The hysteresis behavior of a concrete column section—Park and Paulay (1975)

structures (Ahmad et al. 2012). Some hysteresis loops with the pinching effect, obtained in experimental tests, are shown in Fig. 7.6.

7.4.1 Pinching Bouc-Wen Models

To account for the above-described pinching effects, some researchers (Baber and Noori 1985, 1986; Foliente 1995; Sivaselvan and Reinhorn 2000) have modified the expression of the function employed by the symmetric differential models, described in Sect. 7.2, to evaluate the hysteretic variable z . In particular, some modified expressions of such a function are

$$\text{Baber and Noori (1985): } \begin{cases} B &= \frac{B_h B_p}{B_h + B_p} \\ B_h &= A - |z^n| (\gamma + \beta \text{sign}(\dot{x} z)) \\ B_p &= \left(\frac{1}{\sqrt{2\pi} Z_\sigma} \Delta x \exp\left(-\frac{z^2}{2 Z_\sigma^2}\right) \right) \end{cases} \quad (7.12a)$$

$$\text{Baber and Noori (1986): } \begin{cases} B &= A h - |z^n| (\gamma + \beta \text{sign}(\dot{x} z)) \\ h &= 1 - \zeta_1 \exp\left(-\frac{z^2}{2 \zeta_2^2}\right) \end{cases} \quad (7.12b)$$

$$\text{Foliente (1995): } \begin{cases} B = A h - |z^n| \left(\gamma + \beta \operatorname{sign}(\dot{x} z) \right) \\ h = 1 - \zeta_1 \exp\left(-\frac{(z - \bar{z} \operatorname{sign}(\dot{x}))^2}{\zeta_2^2}\right) \end{cases} \quad (7.12c)$$

$$\text{Sivaselvan and Reinhorn (2000): } \begin{cases} B = \frac{B_h B_p}{B_h + B_p} \\ B_h = A - \left| \frac{z}{z_y} \right|^n \left(\gamma + \beta \operatorname{sign}(\dot{x} z) \right) \\ B_p = \left(\frac{1}{\sqrt{2\pi} Z_\sigma} \Delta x \exp\left(-\frac{(z - \bar{z} \operatorname{sign}(\dot{x}))^2}{2 Z_\sigma^2}\right) \right)^{-1} \\ \Delta x = R_s (x_{\max}^+ - x_{\max}^-) \\ Z_\sigma = \sigma z_y \\ \bar{z} = \lambda z_y \end{cases} \quad (7.12d)$$

where B_h , B_p , γ , β , etc. are material parameters.

Baber and Noori (1985) take into account the pinching effect in their model through a pinching spring with stiffness B_p in series with the hysteretic element associated with z , see Eq. (7.12a). The parameter Δx represents the length at which the variable z of the pinching spring tends to $+\infty(-\infty)$, namely:

$$\lim_{x \rightarrow +\Delta x^-} z(x) = +\infty, \quad \lim_{x \rightarrow -\Delta x^+} z(x) = -\infty, \quad (7.13)$$

and is associated with the energy dissipation ε . Z_σ is related to the sharpness of pinching; in particular, a higher Z_σ implies a more uniform pinching effect.

In 1986, Baber and Noori proposed a different strategy to account for the pinching effect (see Eq. (7.12b)); in particular, it amounts to multiply the A parameter by a pinching function h that depends on the energy dissipation ε , the hysteretic function z , and two parameters, namely ζ_1 and ζ_2 : the first one controls the severity of pinching, whereas the second controls the spread of the pinching region.

Foliente followed the same strategy proposed by Baber and Noori (1986) but proposed a pinching function h that depends on ε , z , ζ_1 , and ζ_2 , as well as the pinching function h in Eq. (7.12b); in addition, the function h also depends on the parameter \bar{z} that corresponds to a fraction of z at $dz/dx = 0$.

Finally, Sivaselvan and Reinhorn proposed a model similar to the one by Baber and Noori (1985), the main difference lying in the fact that in the former model the pinching parameter Δx depends on the maximum generalized displacement reached on the positive and negative sides during the response, weighed through the parameter of the model R_s , and no longer on the energy dissipation ε . Z_σ and \bar{z} are two variables that depend on the yield value of the hysteretic variable, i.e. z_y through two parameters of the model, namely σ and λ (see Eq. (7.12d)).

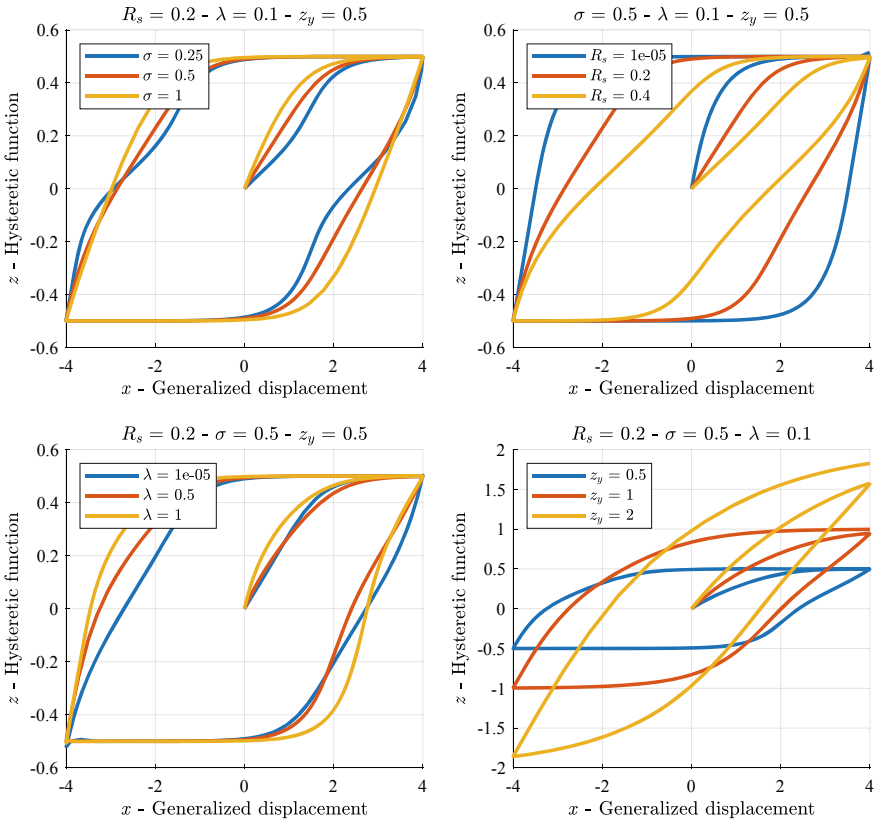


Fig. 7.7 Sensitivity analysis of Sivaselvan and Reinhorn model parameters

7.4.2 Sensitivity Analysis

A sensitivity analysis was carried out to evaluate the effect of each parameter on the hysteretic variable $z(t)$ evaluated by adopting Eqs. (7.5) and (7.12d). The effects of the parameters R_s , σ , λ , and z_y on the hysteretic function z are shown in Fig. 7.7. All hysteretic loops have been obtained by applying a generalized displacement described by the sine wave (7.7).

The top left plot shows the variation of the σ parameter: this parameter controls the pinching region and increasing σ causes the pinching region to spread. The top right plot shows the variation of the R_s parameter: the intensity of the pinching effect is prone to decrease with a decreasing R_s ; specifically, when R_s approaches 0, the pinching effect is null. The bottom left plot shows the variations of the λ parameter: the hysteresis loop tends to become more asymmetric when λ increases. Finally, the bottom right plot shows the variation of the z_y parameter: the tangent stiffness at the origin of the hysteresis loop increases with an increasing value of z_y .

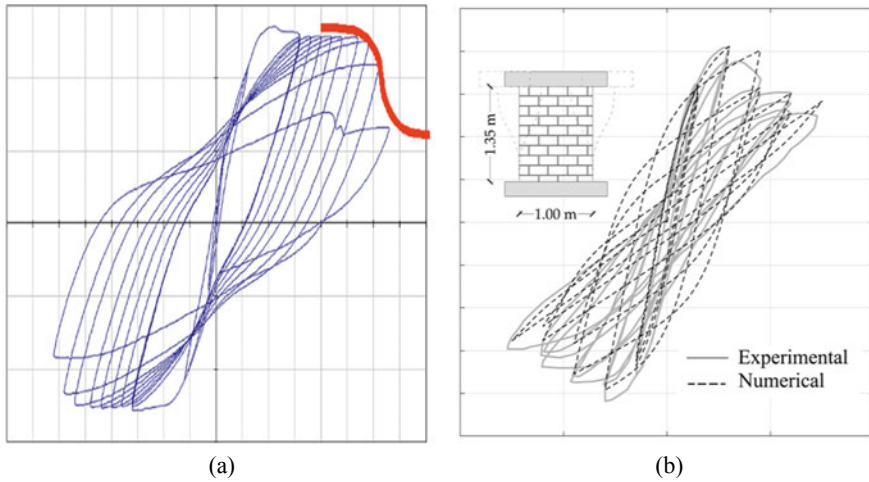


Fig. 7.8 Hysteresis loops with the pinching effect obtained from experimental tests. **a** The hysteresis behaviour of a well confined reinforced concrete column—Colombo and Negro (2005). **b** The hysteresis behavior of a unreinforced masonry panels—Liberatore et al. (2019)

7.5 Modeling of Degrading Hysteresis Loops

It is well known from the scientific literature that many mechanical systems can exhibit strength and stiffness degradation. In general, we can see a hysteretic degrading behavior when the systems are subjected to cyclic loads like earthquakes, winds, and so on. For instance, in concrete (Loh et al. 2011; Sengupta and Li 2013, 2014) and masonry (Liberatore et al. 2019; Tomaževič and Lutman 1996) structures, it is possible to observe a progressive loss of stiffness due to the opening and closing of cracks when the applied loads change direction. Wooden structures also exhibit hysteretic degrading behavior (Xu and Dolan 2009; Zhang et al. 2002). In Fig. 7.8, hysteresis loops exhibiting strength and stiffness degradation are shown.

7.5.1 Degrading Bouc-Wen Models

Similar to the asymmetric and pinched hysteresis phenomena, several researchers (Baber and Wen 1981; Baber and Noori 1985; Foliente 1995) have modified the differential models described in Sect. 7.2 to allow for the simulation of the stiffness and strength degradation effects. Specifically, they have modified the expression employed for evaluating the hysteresis function, required to compute the model output, as follows:

$$\text{Baber and Wen (1981): } \begin{cases} B = \frac{A}{\eta} - \nu |z^n| \left(\gamma + \beta \operatorname{sign}(\dot{x} z) \right) \\ A = A[\varepsilon(t)] = A_0 - \delta_A \varepsilon(t) \\ \eta = \eta[\varepsilon(t)] = \eta_0 + \delta_\eta \varepsilon(t) \\ \nu = \nu[\varepsilon(t)] = \nu_0 + \delta_\nu \varepsilon(t) \end{cases} \quad (7.14a)$$

$$\text{Baber and Noori (1985): } \begin{cases} B = \frac{A}{\eta} - \nu |z^n| \left(\gamma + \beta \operatorname{sign}(\dot{x} z) \right) \\ A = A[\varepsilon(t)] = A_0 - \delta_A \varepsilon(t) \\ \eta = \eta[\varepsilon(t)] = 1 + \delta_\eta \varepsilon(t) \\ \nu = \nu[\varepsilon(t)] = 1 + \delta_\nu \varepsilon(t) \end{cases} \quad (7.14b)$$

$$\text{Foliente (1995): } \begin{cases} B = \frac{A}{\eta} - \nu |z^n| \left(\gamma + \beta \operatorname{sign}(\dot{x} z) \right) \\ \eta = \eta[\varepsilon(t)] = 1 + \delta_\eta \varepsilon(t) \\ \nu = \nu[\varepsilon(t)] = 1 + \delta_\nu \varepsilon(t) \end{cases} \quad (7.14c)$$

where A , η , ν , etc. are material parameters.

All models consider strength, stiffness, or combined degradation, from the initial time $t = 0$ to the present one, as a function of the dissipated energy associated with the hysteretic displacement z ; its expression is given by

$$\varepsilon(t) = \int_0^t z \dot{x} dt. \quad (7.15)$$

In particular, a convenient measure of degradation is the cumulative hysteretic dissipated energy $\varepsilon(t)$ since degradation depends on the intensity and duration of the phenomenon under investigation.

Baber and Wen defined two new parameters: η and ν controlling in turn the stiffness and the strength degradation. Moreover, the amplitude of the hysteresis loop, controlled by the A parameter, can change. In the Baber and Noori 1985 model, the η_0 and ν_0 parameters, which represent the initial values of the degradation functions, are set to 1. Finally, in the Foliente model, the degradation law related to the A parameter is null. All models assume that both parameters η and ν depend linearly on the hysteretic energy $\varepsilon(t)$.

It is worth being emphasized that the energy dissipated by the material coincides with $\varepsilon(t)$ in Eq. (7.15) only for peculiar values of the parameters. In general, $\varepsilon(t)$ does not necessarily fulfill the thermodynamic compatibility (Drucker 1957). For this reason, the use of degrading Bouc-Wen formulations should carefully account for such an issue.

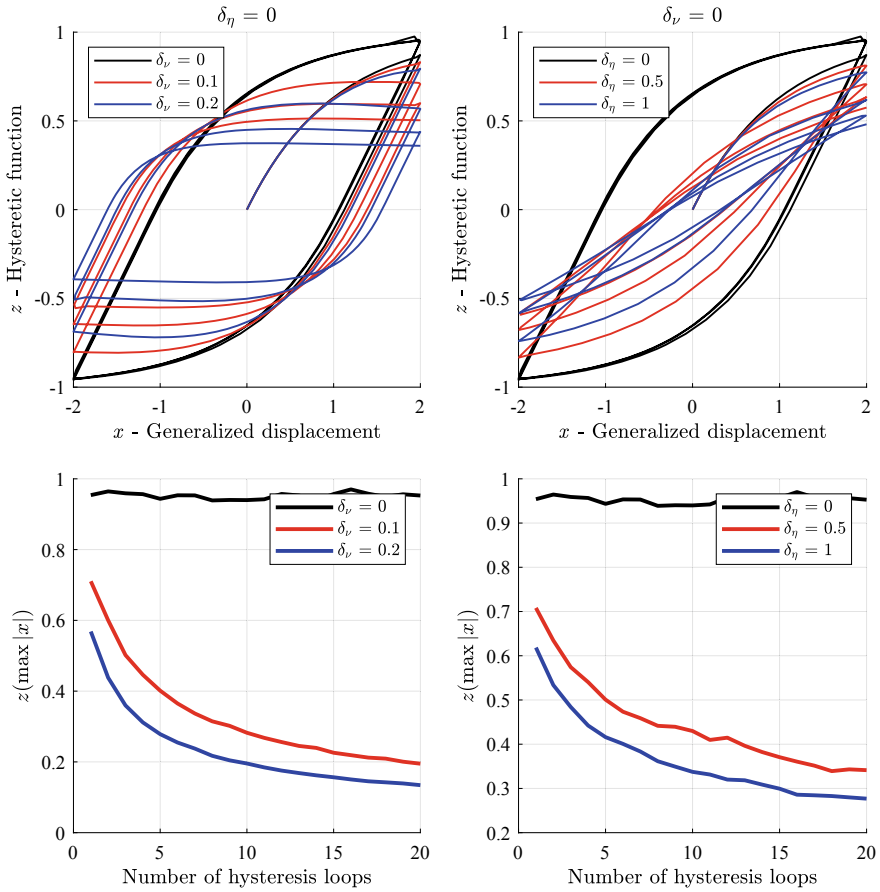


Fig. 7.9 Sensitivity analysis of Foliente model parameters

7.5.2 Sensitivity Analysis

Sensitivity analysis has been carried out on the Foliente model (Foliente 1995) and the results are shown in Fig. 7.9. The top left and the top right plots show the hysteresis loops that exhibit a strength and stiffness degradation, respectively. For both top plots, there are two black colored hysteresis loops without any kind of degradation, obtained by setting to zero the values of δ_η and δ_ν . Conversely, when the latter parameters are greater than zero, a degrading hysteretic behavior is obtained; in particular, the rate of the strength and stiffness degradation gets stronger when the δ_η and δ_ν parameters, respectively, increase. All hysteretic loops have been obtained by applying a generalized displacement described by the sine wave (7.7).

The two bottom plots show the relationship between the number of hysteresis loops and the value of the hysteretic function z associated with the maximum positive

displacement x . In these plots, the effect of δ_η and δ_ν parameters on the hysteresis behavior is more evident.

7.6 Conclusion

Over the years, the Bouc-Wen model has evolved to describe some physical phenomena observed in experimental tests. In this paper, the evolution of the Bouc-Wen model in the field of *rate-independent* mechanical hysteresis phenomena has been presented. In particular, we have reviewed some models based on the Bouc-Wen model able to take into account some mechanical phenomena such as asymmetric hysteresis, the pinching effect, and the strength and stiffness degradation of hysteresis. In all sections, we have used the same technical terminology to help the reader to get acquainted with the physical meaning of the proposed models, to compare each model, and to shed light on their differences, such as the number of parameters that the models require as input.

Finally, for all models, some sensitivity analyses have been carried out to evaluate the effect on the model's result when the input parameters are modified.

References

- Ahmad N, Ali Q, Ashraf M, Khan AN, Alam B (2012) Performance assessment of low-rise confined masonry structures for earthquake induced ground motions. *Int J Civil Struct Eng* 2(3):842–859
- Alibert JJ, Seppecher P, dell'Isola F (2003) Truss modular beams with deformation energy depending on higher displacement gradients. *Math Mech Solids* 8(1):51–73
- Altenbach H, Bîrsan M, Eremeyev VA (2012) On a thermodynamic theory of rods with two temperature fields. *Acta Mech* 223(8):1583–1596
- Andreas U, Spagnuolo M, Lekszycki T, Eugster SR (2018) A Ritz approach for the static analysis of planar pantographic structures modeled with nonlinear Euler-Bernoulli beams. *Contin Mech Thermodyn* 30(5):1103–1123
- Ascione L, Berardi V, Feo L, Fraternali F, Tralli AM (2017) Probabilistic assessment of historical masonry walls retrofitted with through-the-thickness confinement devices. *Proc AIMETA*
- Baber TT, Noori MN (1985) Random vibration of degrading, pinching systems. *J Eng Mech* 111(8):1010–1026
- Baber TT, Noori MN (1986) Modeling general hysteresis behavior and random vibration application. *J Vibr Acoust Stress Rel Des*
- Baber TT, Wen YK (1981) Random vibration of hysteretic, degrading systems. *J Eng Mech Div* 107(6):1069–1087
- Badoni D, Makris N (1996) Nonlinear response of single piles under lateral inertial and seismic loads. *Soil Dyn Earthq Eng* 15(1):29–43
- Bahn BY, Hsu CTT (1998) Stress-strain behavior of concrete under cyclic loading. *ACI Mater J* 95:178–193
- Bai XX, Cai FL, Chen P (2019) Resistor-capacitor (RC) operator-based hysteresis model for magnetorheological (MR) dampers. *Mech Syst Signal Process* 117:157–169
- Banon H, Veneziano D (1982) Seismic safety of reinforced concrete members and structures. *Earthq Eng Struct Dyn* 10(2):179–193

- Barchiesi E, dell'Isola F, Laudato M, Placidi L, Seppecher P (2018) A 1d continuum model for beams with pantographic microstructure: asymptotic micro-macro identification and numerical results. In: *Advances in mechanics of microstructured media and structures*. Springer, pp 43–74
- Barchiesi E, Eugster SR, dell'Isola F, Hild F (2020) Large in-plane elastic deformations of bi-pantographic fabrics: asymptotic homogenization and experimental validation. *Math Mech Solids* 25(3):739–767
- Bouc R (1967) Forced vibrations of mechanical systems with hysteresis. In: *Proceedings of the fourth conference on nonlinear oscillations*, Prague
- Bouc R (1971) Modèle mathématique d'hystérésis. *Acustica* 21:16–25
- Broccardo M, Alibrandi U, Wang Z, Garrè L (2017) The tail equivalent linearization method for nonlinear stochastic processes, genesis and developments. In: *Risk and reliability analysis: theory and applications*. Springer, pp 109–142
- Caggegi C, Sciuto D, Cuomo M (2018) Experimental study on effective bond length of basalt textile reinforced mortar strengthening system: contributions of digital image correlation. *Measurement* 129:119–127
- Carboni B, Lacarbonara W, Brewick PT, Masri SF (2018) Dynamical response identification of a class of nonlinear hysteretic systems. *J Intell Mater Syst Struct* 29(13):2795–2810
- Colombo A, Negro P (2005) A damage index of generalised applicability. *Eng Struct* 27(8):1164–1174
- Contrafatto L, Cuomo M (2002) A new thermodynamically consistent continuum model for hardening plasticity coupled with damage. *Int J Solids Struct* 39(25):6241–6271
- Contrafatto L, Cuomo M, Fazio F (2012) An enriched finite element for crack opening and rebar slip in reinforced concrete members. *Int J Fract* 178(1–2):33–50
- di Cosmo F, Laudato M, Spagnuolo M (2018) Acoustic metamaterials based on local resonances: homogenization, optimization and applications. In: *Generalized models and non-classical approaches in complex materials 1*. Springer, pp 247–274
- De Angelo M, Spagnuolo M, D'annibale F, Pfaff A, Hoschke K, Misra A, Dupuy C, Peyre P, Dirrenberger J, Pawlikowski M (2019) The macroscopic behavior of pantographic sheets depends mainly on their microstructure: experimental evidence and qualitative analysis of damage in metallic specimens. *Contin Mech Thermodyn* 31(4):1181–1203
- dell'Isola F, Seppecher P, Alibert JJ, Lekszycki T, Grygoruk R, Pawlikowski M, Steigmann D, Giorgio I, Andraus U, Turco E et al (2019a) Pantographic metamaterials: an example of mathematically driven design and of its technological challenges. *Contin Mech Thermodyn* 31(4):851–884
- dell'Isola F, Turco E, Misra A, Vangelatos Z, Grigoropoulos C, Melissinaki V, Farsari M (2019b) Force-displacement relationship in micro-metric pantographs: experiments and numerical simulations. *Comptes Rendus Mécanique* 347(5):397–405
- Demetriades GF, Constantinou MC, Reinhorn AM (1993) Study of wire rope systems for seismic protection of equipment in buildings. *Eng Struct* 15(5):321–334
- Dimian M, Andrei P (2014) *Noise-driven phenomena in hysteretic systems*. Springer
- Dobson S, Noori M, Hou Z, Dimentberg M, Baber T (1997) Modeling and random vibration analysis of SDOF systems with asymmetric hysteresis. *Int J Non-Linear Mech* 32(4):669–680
- Drucker DC (1957) A definition of stable inelastic material. BROWN UNIV PROVIDENCE RI, Tech. rep
- Duhem P (1897) Die dauernden aenderungen und die thermodynamik. i. *Zeitschrift für Physikalische Chemie* 22(1):545–589
- Eremeyev V, Morozov N (2010) The effective stiffness of a nanoporous rod. *Dokl Phys* 55:279–282
- Fedele R, Sessa S, Valoroso N (2012) Image correlation-based identification of fracture parameters for structural adhesives. *Technische Mechanik-Europ J Eng Mech* 32(2–5):195–204
- Foliente GC (1995) Hysteresis modeling of wood joints and structural systems. *J Struct Eng* 121(6):1013–1022
- Fujimura K, Der Kiureghian A (2007) Tail-equivalent linearization method for nonlinear random vibration. *Probab Eng Mech* 22(1):63–76

- Graesser E, Cozzarelli F (1991) Shape-memory alloys as new materials for aseismic isolation. *J Eng Mech* 117(11):2590–2608
- Greco F, Luciano R, Serino G, Vaiana N (2018) A mixed explicit-implicit time integration approach for nonlinear analysis of base-isolated structures. *Annals Solid Struct Mech* 10(1):17–29
- Greco L, Cuomo M (2013) B-Spline interpolation of Kirchhoff-love space rods. *Comput Methods Appl Mech Eng* 256:251–269
- Hadad HA, Calabrese A, Strano S, Serino G (2017) A base isolation system for developing countries using discarded tyres filled with elastomeric recycled materials. *J Earthq Eng* 21(2):246–266
- Hodgdon ML (1988) Mathematical theory and calculations of magnetic hysteresis curves. *IEEE Trans Magn* 24(6):3120–3122
- Hossain MM, Browning R, Minkwitz R, Sue HJ (2012) Effect of asymmetric constitutive behavior on scratch-induced deformation of polymers. *Tribol Lett* 47(1):113–122
- Jiles D, Atherton D (1983) Ferromagnetic hysteresis. *IEEE Trans Magn* 19(5):2183–2185
- Jiles DC, Atherton DL (1984) Theory of ferromagnetic hysteresis. *J Appl Phys* 55(6):2115–2120
- Kikuchi M, Aiken ID (1997) An analytical hysteresis model for elastomeric seismic isolation bearings. *Earthq Eng Struct Dyn* 26(2):215–231
- Kreger ME, Abrams DP (1978) Measured hysteresis relationships for small-scale beam-column joints. Tech. rep., University of Illinois Engineering Experiment Station. College of
- Kwok N, Ha Q, Nguyen T, Li J, Samali B (2006) A novel hysteretic model for magnetorheological fluid dampers and parameter identification using particle swarm optimization. *Sens Actuators, A* 132(2):441–451
- Kwok N, Ha Q, Nguyen M, Li J, Samali B (2007) Bouc-wen model parameter identification for a MR fluid damper using computationally efficient GA. *ISA Trans* 46(2):167–179
- Liberatore D, Addessi D, Sangirardi M (2019) An enriched Bouc-Wen model with damage. *Europ J Mech-A/Solids* 77(103):771
- Lima C, Angiolilli M, Barbagallo F, Belletti B, Bergami A, Camata G, Cantagallo C, Di Domenico M, Fiorentino G, Ghersi A, et al (2018) Nonlinear modeling approaches for existing reinforced concrete buildings: The case study of de gasperi-battaglia school building in norcia. In: *Conference on Italian concrete days*. Springer, pp 82–95
- Loh CH, Mao CH, Huang JR, Pan TC (2011) System identification and damage evaluation of degrading hysteresis of reinforced concrete frames. *Earthq Eng Struct Dyn* 40(6):623–640
- Losanno D, Sierra IEM, Spizzuoco M, Marulanda J, Thomson P (2019a) Experimental assessment and analytical modeling of novel fiber-reinforced isolators in unbounded configuration. *Compos Struct* 212:66–82
- Losanno D, Spizzuoco M, Calabrese A (2019b) Bidirectional shaking-table tests of unbonded recycled-rubber fiber-reinforced bearings (rr-frbs). *Struct Control Health Monit* 26(9)
- Losanno D, Palumbo F, Calabrese A, Barrasso T, Vaiana N (2021) Preliminary investigation of aging effects on recycled rubber fiber reinforced bearings (RR-FRBs). *J Earthq Eng*, 1–18
- Marmo F, Rosati L (2012a) Analytical integration of elasto-plastic uniaxial constitutive laws over arbitrary sections. *Int J Numer Meth Eng* 91(9):990–1022
- Marmo F, Rosati L (2012b) An improved flexibility-based nonlinear frame element endowed with the fiber-free formulation. *European congress on computational methods in applied sciences and engineering (ECCOMAS 2012)*. Vienna, Austria, pp 1–17
- Marmo F, Rosati L (2013) The fiber-free approach in the evaluation of the tangent stiffness matrix for elastoplastic uniaxial constitutive laws. *Int J Numer Meth Eng* 94(9):868–894
- Marmo F, Serpieri R, Rosati L (2011) Ultimate strength analysis of prestressed reinforced concrete sections under axial force and biaxial bending. *Comput Struct* 89(1–2):91–108
- Mayergoyz ID (2003) *Mathematical models of hysteresis and their applications*. Academic Press
- Menegotto M (1973) Method of analysis for cyclically loaded RC plane frames including changes in geometry and non-elastic behavior of elements under combined normal force and bending. In: *Proc. of IABSE symposium on resistance and ultimate deformability of structures acted on by well defined repeated loads*, pp 15–22

- Nejadsadeghi N, De Angelo M, Drobnicki R, Lekszycki T, dell'Isola F, Misra A (2019) Parametric experimentation on pantographic unit cells reveals local extremum configuration. *Exp Mech* 59(6):927–939
- Noël JP, Kerschen G (2017) Nonlinear system identification in structural dynamics: 10 more years of progress. *Mech Syst Signal Process* 83:2–35
- Nuzzo I, Losanno D, Caterino N, Serino G, Rotondo LMB (2018) Experimental and analytical characterization of steel shear links for seismic energy dissipation. *Eng Struct* 172:405–418
- Nuzzo I, Losanno D, Caterino N (2019) Seismic design and retrofit of frame structures with hysteretic dampers: a simplified displacement-based procedure. *Bull Earthq Eng* 17(5):2787–2819
- Özdemir H (1976) Nonlinear transient dynamic analysis of yielding structures [ph. d. thesis]. PhD thesis, University of California
- Park R, Paulay T (1975) Reinforced concrete structures. John Wiley & Sons
- Pellecchia D, Sessa S, Vaiana N, Rosati L (2020) Comparative assessment on the rocking response of seismically base-isolated rigid blocks. *Proc Struct Integrity* 29:95–102
- Pideri C, Seppecher P (1997) A second gradient material resulting from the homogenization of an heterogeneous linear elastic medium. *Continuum Mech Thermodyn* 9(5):241–257
- Placidi L, Barchiesi E, Misra A (2018) A strain gradient variational approach to damage: a comparison with damage gradient models and numerical results. *Math Mech Complex Syst* 6(2):77–100
- Placidi L, Misra A, Barchiesi E (2019) Simulation results for damage with evolving microstructure and growing strain gradient moduli. *Continuum Mech Thermodyn* 31(4):1143–1163
- Ramberg W, Osgood WR (1943) Description of stress-strain curves by three parameters. *Nat Adv Committ Aeron*
- Sengupta P, Li B (2013) Modified Bouc-wen model for hysteresis behavior of RC beam-column joints with limited transverse reinforcement. *Eng Struct* 46:392–406
- Sengupta P, Li B (2014) Hysteresis behavior of reinforced concrete walls. *J Struct Eng* 140(7):04014,030
- Serpieri R, Sessa S, Rosati L (2018) A MITC-based procedure for the numerical integration of a continuum elastic-plastic theory of through-the-thickness-jacketed shell structures. *Compos Struct* 191:209–220
- Sessa S (2010) Multiobjective non-linear random vibration analysis for performance-based earthquake engineering. Reliability and optimization of structural systems-proceedings of reliability and optimization of structural systems pp 185–192
- Sessa S, Valoroso N (2017) Kriging interpolation strategy for finite-element-based surrogate responses of DCB delamination tests. In: Risk and reliability analysis: theory and applications. Springer, pp 453–461
- Sessa S, Serpieri R, Rosati L (2017) A continuum theory of through-the-thickness jacketed shells for the elasto-plastic analysis of confined composite structures: theory and numerical assessment. *Compos B Eng* 113:225–242
- Sessa S, Marmo F, Rosati L, Leonetti L, Garcea G, Casciaro R (2018) Evaluation of the capacity surfaces of reinforced concrete sections: eurocode versus a plasticity-based approach. *Meccanica* 53(6):1493–1512
- Sessa S, Marmo F, Vaiana N, De Gregorio D, Rosati L (2019a) Strength hierarchy provisions for transverse confinement systems of shell structural elements. *Compos B Eng* 163:413–423
- Sessa S, Marmo F, Vaiana N, Rosati L (2019b) Probabilistic assessment of axial force-biaxial bending capacity domains of reinforced concrete sections. *Meccanica* 54(9):1451–1469
- Sessa S, Vaiana N, Paradiso M, Rosati L (2020) An inverse identification strategy for the mechanical parameters of a phenomenological hysteretic constitutive model. *Mech Syst Signal Process* 139(106):622
- Shih MH, Sung WP (2005) A model for hysteretic behavior of rhombic low yield strength steel added damping and stiffness. *Comput Struct* 83(12–13):895–908
- Sierra IEM, Losanno D, Strano S, Marulanda J, Thomson P (2019) Development and experimental behavior of HDR seismic isolators for low-rise residential buildings. *Eng Struct* 183:894–906

- Sireteanu T, Giuclea M, Mitu AM, Ghita G (2012) A genetic algorithms method for fitting the generalized bouc-wen model to experimental asymmetric hysteretic loops. *J Vib Acoust* 134(4)
- Sivaselvan MV, Reinhorn AM (2000) Hysteretic models for deteriorating inelastic structures. *J Eng Mech* 126(6):633–640
- Song J, Der Kiureghian A (2006) Generalized Bouc-wen model for highly asymmetric hysteresis. *J Eng Mech* 132(6):610–618
- Song J, Kiureghian AD, Sackman JL (2007) Seismic interaction in electrical substation equipment connected by non-linear rigid bus conductors. *Earthq Eng Struct Dyn* 36(2):167–190
- Tomažević M, Lutman M (1996) Seismic behavior of masonry walls: modeling of hysteretic rules. *J Struct Eng* 122(9):1048–1054
- Turco E, Giorgio I, Misra A, dell'Isola F (2017) King post truss as a motif for internal structure of (meta) material with controlled elastic properties. *Royal Soc Open Sci* 4(10):171,153
- Turco E, Misra A, Pawlikowski M, dell'Isola F, Hild F (2018) Enhanced Piola-Hencky discrete models for pantographic sheets with pivots without deformation energy: numerics and experiments. *Int J Solids Struct* 147:94–109
- Vaiana N, Spizzuoco M, Serino G (2017) Wire rope isolators for seismically base-isolated lightweight structures: experimental characterization and mathematical modeling. *Eng Struct* 140:498–514
- Vaiana N, Sessa S, Marmo F, Rosati L (2018) A class of uniaxial phenomenological models for simulating hysteretic phenomena in rate-independent mechanical systems and materials. *Nonlinear Dyn* 93(3):1647–1669
- Vaiana N, Sessa S, Marmo F, Rosati L (2019a) An accurate and computationally efficient uniaxial phenomenological model for steel and fiber reinforced elastomeric bearings. *Compos Struct* 211:196–212
- Vaiana N, Sessa S, Marmo F, Rosati L (2019b) Nonlinear dynamic analysis of hysteretic mechanical systems by combining a novel rate-independent model and an explicit time integration method. *Nonlinear Dyn* 98(4):2879–2901
- Vaiana N, Sessa S, Paradiso M, Marmo F, Rosati L (2019c) An efficient computational strategy for nonlinear time history analysis of seismically base-isolated structures. In: *Conference of the Italian association of theoretical and applied mechanics*. Springer, pp 1340–1353
- Vaiana N, Sessa S, Paradiso M, Rosati L (2019d) Accurate and efficient modeling of the hysteretic behavior of sliding bearings. In: *7th international conference on computational methods in structural dynamics and earthquake engineering (COMPdyn 2019)*. Crete, Greece, pp 24–26
- Vaiana N, Marmo F, Sessa S, Rosati L (2020) Modeling of the hysteretic behavior of wire rope isolators using a novel rate-independent model. *Nonlinear Dynamics of Structures*. Springer, Systems and Devices, pp 309–317
- Vaiana N, Capuano R, Sessa S, Marmo F, Rosati L (2021a) Nonlinear dynamic analysis of seismically base-isolated structures by a novel open-source hysteretic material model. *Appl Sci* 11(3):900
- Vaiana N, Losanno D, Ravichandran N (2021b) A novel family of multiple springs models suitable for biaxial rate-independent hysteretic behavior. *Comput Struct* 244(106):403
- Vaiana N, Sessa S, Rosati L (2021c) A generalized class of uniaxial rate-independent models for simulating asymmetric mechanical hysteresis phenomena. *Mech Syst Signal Process* 146(106):984
- Valoroso N, Fedele R (2010) Characterization of a cohesive-zone model describing damage and de-cohesion at bonded interfaces. sensitivity analysis and mode-I parameter identification. *International Journal of Solids and Structures* 47(13):1666–1677
- Valoroso N, Sessa S, Lepore M, Cricri G (2013) Identification of mode-I cohesive parameters for bonded interfaces based on DCB test. *Eng Fract Mech* 104:56–79
- Valoroso N, Marmo F, Sessa S (2014) Limit state analysis of reinforced shear walls. *Eng Struct* 61:127–139
- Valoroso N, Marmo F, Sessa S (2015) A novel shell element for nonlinear pushover analysis of reinforced concrete shear walls. *Bull Earthq Eng* 13(8):2367–2388
- Visintin A (2013) Differential models of hysteresis, vol 111. Springer Science & Business Media

- Wang CH, Wen Yk (1998) Reliability and redundancy of pre-Northridge low-rise steel buildings under seismic excitation. na
- Wen Y (1980) Equivalent linearization for hysteretic systems under random excitation. *ASME J Appl Mech*
- Wen YK (1976) Method for random vibration of hysteretic systems. *J Eng Mech Div* 102(2):249–263
- Xu J, Dolan JD (2009) Development of a wood-frame shear wall model in abaqus. *J Struct Eng* 135(8):977–984
- Zamani SM, Vafai A, Aghakouchak A, Kazemi M (2012) Experimental investigation of steel frames with single bays of symmetrical y-shaped concentric bracings. *Scientia Iranica* 19(2):195–210
- Zhang H, Foliente GC, Yang Y, Ma F (2002) Parameter identification of inelastic structures under dynamic loads. *Earthq Eng Struct Dyn* 31(5):1113–1130
- Zuccaro G, Dato F, Cacace F, De Gregorio D, Sessa S (2017) Seismic collapse mechanisms analyses and masonry structures typologies: a possible correlation. *Ingegneria Sismica* 34(4):121–150

Chapter 8

A Generalized Formulation of Time Integration Methods for Nonlinear Dynamic Analysis of Hysteretic Mechanical Systems



Davide Pellecchia and Pasquale Cesarano

Abstract The chapter presents a generalized formulation of time integration methods that allow for the numerical solution of the nonlinear equilibrium equations characterizing mechanical systems having hysteretic behavior. Two families of time integration methods are derived from such a generalized formulation: the celebrated Newmark's family of methods and Chang's family of explicit methods. The former is presented since it represents one of the most employed families of conventional time integration methods available in the literature. On the contrary, the latter is illustrated since it is one of the most efficient families of recently developed structure-dependent time integration methods. For each family, the formulation, the expression for the evaluation of the unknown generalized displacement, velocity, and acceleration vectors, as well as the main numerical properties are first presented. Then, some instances as well as the implementation scheme of each family are illustrated. Finally, nonlinear time history analyses are performed on a rate-independent hysteretic mechanical system, characterized by a stiffening behavior and subjected to an external generalized random force, to illustrate the numerical performance, in terms of accuracy and computational efficiency, of some methods selected within the above-described families.

Keywords Time integration method · Hysteresis · Nonlinear equilibrium equations · Newmark's time integration methods · Chang's integration methods

D. Pellecchia

Department of Structures for Engineering and Architecture, University of Naples Federico II,
via Claudio, 21, 80124 Naples, Italy
e-mail: davide.pellecchia@unina.it

P. Cesarano (✉)

CAE Technologies s.r.l. – Simulia, Centro Direzionale isola F12, 80143 Naples, Italy
e-mail: pasquale.cesarano@caetech.it

© Springer Nature Switzerland AG 2021

F. Marmo et al. (eds.), *Mathematical Applications in Continuum and Structural Mechanics*, Advanced Structured Materials 127,
https://doi.org/10.1007/978-3-030-42707-8_8

8.1 Introduction

Hysteretic mechanical systems typically display a complex behavior characterized by a generalized force that is a function of the generalized displacement (velocity). In the former (latter) case, the hysteretic behavior is referred to as *rate-independent* (*rate-dependent*) (Dimian and Andrei 2014). There exist several hysteretic mechanical systems that display both types of hysteretic behavior at the same time (Tsai et al. 2003; Vaiana et al. 2017; Losanno et al. 2021).

Moreover, hysteretic models can be used in order to reproduce the behavior of more complex systems for which nonlinear analysis represents the sole reliable strategy to estimate structural responses (Lima et al. 2018; De Angelo et al. 2019; di Cosmo et al. 2018; Andreaus et al. 2018; Castellano et al. 2019) and their collapse mechanisms (Zuccaro et al. 2017).

To accurately evaluate the nonlinear response of such systems, appropriate time integration methods, having specific stability, accuracy, and computational efficiency properties, need to be employed to numerically solve the nonlinear equilibrium equations characterizing the discrete structural model of such systems (Wilson 2002).

In the literature, a comprehensive classification of these algorithms is usually performed depending on the kind of coefficients that appear in the expressions employed for the evaluation of the unknown generalized displacement and velocity vectors at the generic time of the analysis (Kolay and Ricles 2016).

Specifically, it is possible to distinguish between *conventional time integration methods*, such as Newmark's family of methods (Newmark 1959), and *structure-dependent time integration methods*, such as Chang's families of methods (Chang 2010, 2014). In the former, the coefficients that characterize the expressions of the generalized displacement and velocity vectors are scalar parameters, whereas, in the latter, the above-mentioned coefficients can be scalar parameters or matrices that may depend on the time step Δt and on the initial properties of the mechanical system.

The formulation of such methods is typically developed in the context of linear or nonlinear elastic systems, thus losing important numerical and implementation details that need to be taken into consideration when hysteretic mechanical systems are analyzed. As an example, conventional explicit methods, such as the Newmark explicit methods (Chang 2009), as well as semi-explicit structure-dependent time integration methods, such as the ones belonging to the family formulated by Chang (2010), do not require iterations when elastic systems are analyzed; on the contrary, they need to be used in conjunction with an iterative procedure when adopted for the nonlinear dynamic analysis of hysteretic mechanical systems (Vaiana et al. 2019b; Abd-alla et al. 2017).

In this chapter, we generalize a formulation of families of integration methods to allow for the solution of the nonlinear equilibrium equations of hysteretic mechanical systems displaying both rate-dependent and rate-independent hysteretic behaviors.

Specifically, using the proposed generalized formulation, that is introduced after presenting the nonlinear equilibrium equations of a typical hysteretic mechanical system, we derive the celebrated Newmark's family of methods (Newmark 1959) and

the recently developed Chang's family of explicit method (Chang 2014). The former is presented because is the most employed family of conventional time integration methods available in the literature, whereas the latter is illustrated since its stability, accuracy and computational efficiency properties make it one of the most suitable families of structure-dependent time integration methods to be employed for the nonlinear time history analysis of hysteretic mechanical systems.

Subsequently, for each family, we present the formulation, the expressions for evaluating the unknown generalized displacement, velocity, and acceleration vectors, and the principal numerical properties. In addition, we also illustrate some instances and an useful implementation scheme to help the reader with the computer implementation.

Finally, we present the results of some numerical experiments conducted on a hysteretic mechanical system subjected to a generalized external random force to show the accuracy and computational efficiency properties of some methods belonging to the above-described families.

8.2 Families of Time Integration Methods

In this section, we first formulate the nonlinear equilibrium equations of a hysteretic mechanical system that display both rate-dependent and rate-independent hysteretic behaviors (Dimian and Andrei 2014). Subsequently, we illustrate a formulation of families of time integration methods that we have generalized to allow for the nonlinear time history analysis of such complex mechanical systems.

8.2.1 *Nonlinear Equilibrium Equations*

An accurate simulation of the dynamic behavior displayed by hysteretic mechanical systems requires the selection of an appropriate discrete structural model, consisting of nodes connected by elements.

The response of a discrete structural model, subjected to external forces depending on time t , is completely described by variables associated with each node, namely, the nodal generalized displacements, velocities, and accelerations, as well as the nodal generalized forces.

In the discrete structural model of a typical hysteretic mechanical system, the nodal generalized forces may be classified into three different categories: elastic forces, rate-dependent hysteretic forces, and rate-independent hysteretic forces.

The nodal generalized external forces are collected in the generalized external force vector $\mathbf{p}(t)$, whereas the nodal generalized displacements, velocities, accelerations, and the nodal generalized forces are collected, respectively, in the generalized displacement $\mathbf{u}(t)$, velocity $\dot{\mathbf{u}}(t)$, acceleration $\ddot{\mathbf{u}}(t)$, and force $\mathbf{f}(t)$ vectors.

The nonlinear equilibrium equations of a discrete structural model may be obtained by adopting d'Alembert's principle that allows one to impose the equilibrium between the generalized force vector and the generalized external force vector, as follows:

$$\mathbf{f}(t) = \mathbf{f}_i(t) + \mathbf{f}_{rd}(t) + \mathbf{f}_{ri}(t) + \mathbf{f}_e(t) = \mathbf{p}(t), \quad (8.1)$$

where $\mathbf{f}_i(t)$ is the generalized inertia force, $\mathbf{f}_{rd}(t)$ the generalized rate-dependent hysteretic force, $\mathbf{f}_{ri}(t)$ the generalized rate-independent hysteretic force, whereas $\mathbf{f}_e(t)$ represents the generalized elastic force.

The generalized inertia force $\mathbf{f}_i(t)$, rate-dependent hysteretic force $\mathbf{f}_{rd}(t)$, and elastic force $\mathbf{f}_e(t)$ vectors can be written as

$$\mathbf{f}_i(t) = \mathbf{M}\ddot{\mathbf{u}}(t), \quad (8.2a)$$

$$\mathbf{f}_{rd}(t) = \mathbf{C}\dot{\mathbf{u}}(t) + \mathbf{f}_{rdn}(t), \quad (8.2b)$$

$$\mathbf{f}_e(t) = \mathbf{K}\mathbf{u}(t) + \mathbf{f}_{en}(t), \quad (8.2c)$$

where \mathbf{M} , \mathbf{C} , and \mathbf{K} are the generalized constant mass, damping, and elastic stiffness matrices, whereas $\mathbf{f}_{rdn}(t)$ and $\mathbf{f}_{en}(t)$ are the nonlinear components of the generalized rate-dependent hysteretic force $\mathbf{f}_{rd}(t)$ and elastic force $\mathbf{f}_e(t)$ vectors, respectively.

By using Eq. (8.2), we can rewrite Eq. (8.1) as follows:

$$\mathbf{M}\ddot{\mathbf{u}}(t) + \mathbf{C}\dot{\mathbf{u}}(t) + \mathbf{K}\mathbf{u}(t) + \mathbf{f}_{rdn}(t) + \mathbf{f}_{ri}(t) + \mathbf{f}_{en}(t) = \mathbf{p}(t). \quad (8.3)$$

The numerical integration of Eq. (8.3), performed by employing a suitable time integration method, requires the following two initial conditions:

$$\mathbf{u}(0) = \mathbf{d}_0, \quad (8.4a)$$

$$\dot{\mathbf{u}}(0) = \mathbf{v}_0, \quad (8.4b)$$

where \mathbf{d}_0 and \mathbf{v}_0 are, respectively, the generalized displacement and velocity vectors of the discrete structural model defined at the beginning of the analysis.

8.2.2 Generalized Formulation of Time Integration Methods

To introduce the proposed generalized formulation of families of time integration methods, suitable for the nonlinear time history analyses of mechanical systems with rate-dependent and/or rate-independent hysteretic behavior, it is useful to express the system of coupled nonlinear Ordinary Differential Equations (ODEs) of the second order in time, given by Eq. (8.3), at the generic time $t + \Delta t$ as follows:

$$\begin{aligned} &\mathbf{M}\ddot{\mathbf{u}}(t + \Delta t) + \mathbf{C}\dot{\mathbf{u}}(t + \Delta t) + \mathbf{K}\mathbf{u}(t + \Delta t) \\ &+ \mathbf{f}_{rdn}(t + \Delta t) + \mathbf{f}_{ri}(t + \Delta t) + \mathbf{f}_{en}(t + \Delta t) = \mathbf{p}(t + \Delta t), \end{aligned} \quad (8.5)$$

where Δt represents the time step of a nonlinear time history analysis.

The above-mentioned generalized formulation of families of time integration methods, required to numerically solve Eq. (8.5), is characterized by the following set of three equations:

$$\mathbf{d}_{i+1} = \mathbf{d}_i + \mathbf{A}_1 \Delta t \mathbf{v}_i + \mathbf{A}_2 (\Delta t)^2 \mathbf{a}_i + \mathbf{A}_3 (\Delta t)^2 \mathbf{a}_{i+1} + \mathbf{q}_{i+1}, \quad (8.6a)$$

$$\mathbf{v}_{i+1} = \mathbf{v}_i + \mathbf{B}_1 \Delta t \mathbf{a}_i + \mathbf{B}_2 \Delta t \mathbf{a}_{i+1} + \mathbf{r}_{i+1}, \quad (8.6b)$$

$$\mathbf{a}_{i+1} = \mathbf{M}^{-1} \left[\mathbf{p}_{i+1} - \mathbf{C} \mathbf{v}_{i+1} - \mathbf{K} \mathbf{d}_{i+1} - (\tilde{\mathbf{f}}_{rdn})_{i+1} - (\tilde{\mathbf{f}}_{ri})_{i+1} - (\tilde{\mathbf{f}}_{en})_{i+1} \right], \quad (8.6c)$$

where \mathbf{d}_{i+1} (\mathbf{d}_i), \mathbf{v}_{i+1} (\mathbf{v}_i), and \mathbf{a}_{i+1} (\mathbf{a}_i) are approximate estimates of the generalized displacement $\mathbf{u}(t + \Delta t)$ ($\mathbf{u}(t)$), velocity $\dot{\mathbf{u}}(t + \Delta t)$ ($\dot{\mathbf{u}}(t)$), and acceleration $\ddot{\mathbf{u}}(t + \Delta t)$ ($\ddot{\mathbf{u}}(t)$) vectors at the $(i + 1)$ -th (i -th) time step, respectively; $(\tilde{\mathbf{f}}_{rdn})_{i+1} = \mathbf{f}_{rdn}(\mathbf{v}_{i+1})$, $(\tilde{\mathbf{f}}_{ri})_{i+1} = \mathbf{f}_{ri}(\mathbf{d}_{i+1})$, $(\tilde{\mathbf{f}}_{en})_{i+1} = \mathbf{f}_{en}(\mathbf{d}_{i+1})$, and \mathbf{p}_{i+1} are approximate estimates of the generalized nonlinear rate-dependent hysteretic force $\mathbf{f}_{rdn}(t + \Delta t)$, rate-independent hysteretic force $\mathbf{f}_{ri}(t + \Delta t)$, nonlinear elastic force $\mathbf{f}_{en}(t + \Delta t)$, and external force $\mathbf{p}(t + \Delta t)$ vectors at the $(i + 1)$ -th time step, respectively.

The matrices \mathbf{A}_1 , \mathbf{A}_2 , \mathbf{A}_3 , as well as \mathbf{B}_1 , \mathbf{B}_2 are coefficient matrices that define a specific family of time integration methods, whereas \mathbf{q}_{i+1} and \mathbf{r}_{i+1} are load-dependent vectors, namely, vectors that are functions of the external force vector.

According to the nature of the coefficient matrices and load-dependent vectors, we can distinguish between (Kolay and Ricles 2016):

- families of *conventional time integration methods*;
- families of *structure-dependent time integration methods*.

In families of conventional time integration methods (Newmark 1959; Bathe 1996), all the coefficient matrices become scalar quantities, that is, A_1 , A_2 , A_3 , B_1 , and B_2 , and both the load-dependent vectors become zero vectors, that is, $\mathbf{q}_{i+1} = \mathbf{r}_{i+1} = \mathbf{0}$.

On the contrary, in families of structure-dependent time integration methods (Chen and Ricles 2008; Chang 2010, 2014; Gui et al. 2014), only some of the coefficient matrices become scalars; moreover, some of them are functions of the time step Δt and of the initial properties of the discrete structural model, namely, the mass matrix \mathbf{M} , and the initial generalized tangent damping \mathbf{C}_0 and stiffness \mathbf{K}_0 matrices.

8.3 Conventional Time Integration Methods

Conventional time integration methods have been classified by Bathe (1996) into two categories: *explicit* and *implicit* methods.

In explicit methods, such as the Newmark explicit method, belonging to Newmark's Family of Methods (NFM) (Newmark 1959), the unknown generalized displacement vector at time $t + \Delta t$ can be determined adopting quantities evalu-

ated at time steps preceding time $t + \Delta t$. Such methods, that are conditionally stable (Dahlquist 1956, 1963), do (do not) require iterations when hysteretic (elastic) mechanical systems are analyzed.

In implicit methods, such as the Newmark average acceleration method and the Newmark linear acceleration method, both belonging to Newmark's family of methods (Newmark 1959), the expression of the unknown generalized displacement vector at time $t + \Delta t$ also depends on unknown quantities evaluated at time $t + \Delta t$. Such methods, that can be conditionally or unconditionally stable (Bathe and Wilson 1972; HUGHES 1987), always require the use of iterative procedures.

In this section, we present Newmark's family of methods since it represents one of the widely used families of conventional time integration methods available in the literature (Nagarajaiah et al. 1991; Wilson 2002; Greco et al. 2018).

8.3.1 Newmark's Family of Methods

8.3.1.1 Formulation

The family of methods developed by Newmark (1959) can be derived from Eq. (8.6) by setting:

$$\mathbf{A}_1 = \mathbf{1}, \quad (8.7)$$

and by substituting the coefficient matrices \mathbf{A}_2 , \mathbf{A}_3 , \mathbf{B}_1 , and \mathbf{B}_2 with corresponding scalar quantities, that is, A_2 , A_3 , B_1 , and B_2 . Hence, the formulation of such a family is

$$\mathbf{d}_{i+1} = \mathbf{d}_i + \Delta t \mathbf{v}_i + A_2 (\Delta t)^2 \mathbf{a}_i + A_3 (\Delta t)^2 \mathbf{a}_{i+1} + \mathbf{q}_{i+1}, \quad (8.8a)$$

$$\mathbf{v}_{i+1} = \mathbf{v}_i + B_1 \Delta t \mathbf{a}_i + B_2 \Delta t \mathbf{a}_{i+1} + \mathbf{r}_{i+1}, \quad (8.8b)$$

$$\mathbf{a}_{i+1} = \mathbf{M}^{-1} \left[\mathbf{p}_{i+1} - \mathbf{C} \mathbf{v}_{i+1} - \mathbf{K} \mathbf{d}_{i+1} - (\tilde{\mathbf{f}}_{rdn})_{i+1} - (\tilde{\mathbf{f}}_{ri})_{i+1} - (\tilde{\mathbf{f}}_{en})_{i+1} \right], \quad (8.8c)$$

where the scalar quantities, assumed to be constant during the complete numerical integration procedure, are computed as follows:

$$A_2 = (0.5 - \alpha), \quad (8.9)$$

$$A_3 = \alpha, \quad (8.10)$$

$$B_1 = (1 - \beta), \quad (8.11)$$

$$B_2 = \beta, \quad (8.12)$$

in which the scalar parameters α and β define the numerical properties, namely, stability and accuracy, of the time integration method selected within such a family.

The load-dependent vectors \mathbf{q} and \mathbf{r} at the $(i + 1)$ -th time step are evaluated as

$$\mathbf{q}_{i+1} = \mathbf{0}, \quad (8.13)$$

$$\mathbf{r}_{i+1} = \mathbf{0}. \quad (8.14)$$

It is important to note that an iterative procedure needs to be implemented since the expressions for evaluating the unknown generalized displacement \mathbf{d}_{i+1} and velocity \mathbf{v}_{i+1} vectors, namely, Eqs. (8.8a) and (8.8b), respectively, are both functions of the unknown generalized acceleration vector \mathbf{a}_{i+1} .

8.3.1.2 Expressions for \mathbf{d}_{i+1} , \mathbf{v}_{i+1} , and \mathbf{a}_{i+1}

Adopting the above-described formulation of Newmark's family of methods, we derive the expressions for the evaluation of the generalized displacement \mathbf{d}_{i+1} , velocity \mathbf{v}_{i+1} , and acceleration \mathbf{a}_{i+1} vectors at the generic time step $i + 1$ of the analysis.

To this end, we consider a generic time interval $t_i \leq t \leq t_{i+1}$ and we assume that the generalized external force vector \mathbf{p}_i (\mathbf{p}_{i+1}) is assigned at the beginning (end) of such an interval. Furthermore, we also assume that the generalized displacement \mathbf{d}_i , velocity \mathbf{v}_i , and acceleration \mathbf{a}_i vectors at time step i are known.

At this point, we first subtract the equilibrium equations at time i to the ones at time $i + 1$ thus obtaining the following nonlinear equilibrium equations in incremental form:

$$\mathbf{M}\Delta\mathbf{a}_{i+1} + \mathbf{C}\Delta\mathbf{v}_{i+1} + \mathbf{K}\Delta\mathbf{d}_{i+1} + (\Delta\tilde{\mathbf{f}}_n)_{i+1} = \mathbf{p}_{i+1} - \mathbf{M}\mathbf{a}_i - \mathbf{C}\mathbf{v}_i - \mathbf{K}\mathbf{d}_i - (\tilde{\mathbf{f}}_n)_i, \quad (8.15)$$

in which the generalized nonlinear force vector $(\tilde{\mathbf{f}}_n)_i$ and the incremental generalized nonlinear force vector $(\Delta\tilde{\mathbf{f}}_n)_{i+1}$ are computed, respectively, as

$$(\tilde{\mathbf{f}}_n)_i = (\tilde{\mathbf{f}}_{rdn})_i + (\tilde{\mathbf{f}}_{ri})_i + (\tilde{\mathbf{f}}_{en})_i, \quad (8.16a)$$

$$(\Delta\tilde{\mathbf{f}}_n)_{i+1} = (\Delta\tilde{\mathbf{f}}_{rdn})_{i+1} + (\Delta\tilde{\mathbf{f}}_{ri})_{i+1} + (\Delta\tilde{\mathbf{f}}_{en})_{i+1}, \quad (8.16b)$$

whereas the generic incremental vector $\Delta(\bullet)_{i+1}$ is given by

$$\Delta(\bullet)_{i+1} = (\bullet)_{i+1} - (\bullet)_i. \quad (8.17)$$

Then, combining Eqs. (8.8a) and (8.8b), we obtain the incremental generalized velocity vector:

$$\Delta\mathbf{v}_{i+1} = \frac{\beta}{\alpha\Delta t}\Delta\mathbf{d}_{i+1} - \frac{\beta}{\alpha}\mathbf{v}_i + \left(1 - \frac{\beta}{2\alpha}\right)\Delta t\mathbf{a}_i, \quad (8.18)$$

whereas, from Eq. (8.8a), we derive the incremental generalized acceleration vector:

$$\Delta\mathbf{a}_{i+1} = \frac{1}{\alpha(\Delta t)^2}\Delta\mathbf{d}_{i+1} - \frac{1}{\alpha\Delta t}\mathbf{v}_i - \frac{1}{2\alpha}\mathbf{a}_i. \quad (8.19)$$

Substituting Eqs. (8.18) and (8.19) in Eq. (8.15), we get the incremental generalized displacement vector:

$$\Delta \mathbf{d}_{i+1} = \hat{\mathbf{K}}^{-1} \hat{\mathbf{p}}_{i+1}, \quad (8.20)$$

where the matrix $\hat{\mathbf{K}}$, referred to as the effective generalized constant stiffness matrix, is given by

$$\hat{\mathbf{K}} = \frac{1}{\alpha (\Delta t)^2} \mathbf{M} + \frac{\beta}{\alpha \Delta t} \mathbf{C} + \mathbf{K}, \quad (8.21)$$

whereas the vector $\hat{\mathbf{p}}_{i+1}$, denominated effective generalized external force vector, is evaluated as

$$\begin{aligned} \hat{\mathbf{p}}_{i+1} = & \mathbf{p}_{i+1} - (\Delta \tilde{\mathbf{f}})_{i+1} + \mathbf{M} \left[\frac{1}{\alpha \Delta t} \mathbf{v}_i - \left(1 - \frac{1}{2\alpha} \right) \mathbf{a}_i \right] + \\ & - \mathbf{C} \left[\left(1 - \frac{\beta}{\alpha} \right) \mathbf{v}_i + \left(1 - \frac{\beta}{2\alpha} \right) \Delta t \mathbf{a}_i \right] - \mathbf{K} \mathbf{d}_i - (\tilde{\mathbf{f}})_i. \end{aligned} \quad (8.22)$$

Hence, on account of Eq. (8.17), we can obtain the following expression for the unknown generalized displacement vector \mathbf{d}_{i+1} :

$$\mathbf{d}_{i+1} = \mathbf{d}_i + \Delta \mathbf{d}_{i+1}, \quad (8.23)$$

where $\Delta \mathbf{d}_{i+1}$ is given by Eq. (8.20). Furthermore, using Eq. (8.18), we get the following expression for the unknown generalized velocity vector \mathbf{v}_{i+1} :

$$\mathbf{v}_{i+1} = \frac{\beta}{\alpha \Delta t} \Delta \mathbf{d}_{i+1} + \left(1 - \frac{\beta}{\alpha} \right) \mathbf{v}_i + \left(1 - \frac{\beta}{2\alpha} \right) \Delta t \mathbf{a}_i, \quad (8.24)$$

whereas, adopting Eq. (8.19), we derive the following expression for the unknown generalized acceleration vector \mathbf{a}_{i+1} :

$$\mathbf{a}_{i+1} = \frac{1}{\alpha (\Delta t)^2} \Delta \mathbf{d}_{i+1} - \frac{1}{\alpha \Delta t} \mathbf{v}_i + \left(1 - \frac{1}{2\alpha} \right) \mathbf{a}_i. \quad (8.25)$$

It is very important to note that an iterative procedure, such as the pseudo-force method (Clough and Penzien 2003), is required to compute $\Delta \mathbf{d}_{i+1}$ from Eq. (8.20). Indeed, the incremental generalized nonlinear force vector $(\Delta \tilde{\mathbf{f}}_n)_{i+1}$, defined by Eq. (8.16) and appearing in the right side of Eq. (8.20), is a function of two unknown quantities, namely, \mathbf{d}_{i+1} and \mathbf{v}_{i+1} . Such a vector can be evaluated by employing suitable phenomenological models available in the literature (Bouc 1971; Seleemah and Constantinou 1997; Sessa et al. 2020; Vaiana et al. 2018, 2019a, b, d, 2021c, 2020, 2021a, b; Wen 1976, 1980).

A significant and appealing property of Newmark's family of integration methods consists in the fact that such algorithms can be used regardless of the properties of the structural model, as long as it is statically determined. Thus, Newmark's strategy

has become one of the most popular time step procedure in several engineering applications and, contrarily to structure-dependent procedures, it has been often used to analyze nonlinear shell structures subject to both monothonic loads (Valoroso et al. 2014, 2015) and cyclic excitations (Sessa et al. 2017; Serpieri et al. 2018; Sessa et al. 2019a).

8.3.1.3 Numerical Properties

The stability and the accuracy of Newmark's family of methods depend on the values assumed by the scalar parameters α and β .

As far as the stability is concerned, the critical time step Δt_{cr} , that is, the maximum value of the time step that can be adopted to avoid stability problems is different for each natural mode of the discrete structural model evaluated at the $(i + 1)$ -th time step of a nonlinear time history analysis. Specifically, assuming a zero viscous damping ratio, the value of the critical time step of the j -th mode at the $(i + 1)$ -th time step, that is, $(\Delta t_{cr})_{i+1}^{(j)}$, can be evaluated as follows (Bathe 1996):

$$(\Delta t_{cr})_{i+1}^{(j)} = \frac{T_{i+1}^{(j)}}{\pi \sqrt{2} \sqrt{\beta - 2\alpha}}, \quad (8.26)$$

where $T_{i+1}^{(j)}$ is the natural period of the j -th mode evaluated by using the generalized tangent stiffness matrix \mathbf{K}_{i+1} at the $(i + 1)$ -th time step.

As regards the accuracy, the subfamily of methods for which $\beta = 1/2$ has a second-order accuracy, does not suffer from numerical damping, and displays a small relative period error for $\Delta t \leq 0.05 T_{i+1}^{(j)}$.

Generally speaking, for a fixed value of β , increasing the value of α , the critical time step of the j -th mode at the $(i + 1)$ -th time step increases whereas the accuracy decreases.

8.3.2 Some Instances of the NFM's

Some celebrated instances of Newmark's family of methods that exhibit different stability and accuracy properties are

- Newmark explicit method, obtained for $\alpha = 0$ and $\beta = 1/2$;
- Newmark linear acceleration method, obtained for $\alpha = 1/6$ and $\beta = 1/2$;
- Newmark average acceleration method, obtained for $\alpha = 1/4$ and $\beta = 1/2$.

Specifically, the Newmark explicit method and the Newmark linear acceleration method are conditionally stable, whereas the Newmark average acceleration method is unconditionally stable, as it can be easily shown by computing the critical time step Δt_{cr} with Eq. (8.26).

8.3.3 Implementation Scheme of the NFM's

Table 8.1 summarizes the implementation scheme of Newmark's family of methods. Such an algorithm that adopts the Pseudo-Force Method (PFM) (Clough and Penzien 2003) as iterative procedure, is composed of two parts. In the first one, called *Initial settings*, the generalized constant mass \mathbf{M} , damping \mathbf{C} , and stiffness \mathbf{K} matrices are first assembled. Then, the initial generalized displacement \mathbf{d}_0 and velocity \mathbf{v}_0 vectors are initialized and the initial generalized acceleration vector \mathbf{a}_0 is evaluated using the following equation:

Table 8.1 NFM's algorithm

1. Initial settings.

- 1.1 Assemble the following matrices: \mathbf{M} , \mathbf{C} , and \mathbf{K} .
 - 1.2 Initialize \mathbf{d}_0 and \mathbf{v}_0 ; then evaluate the initial generalized acceleration vector:

$$\mathbf{a}_0 = \mathbf{M}^{-1} [\mathbf{p}_0 - \mathbf{C}\mathbf{v}_0 - \mathbf{K}\mathbf{d}_0 - (\tilde{\mathbf{f}}_{rdn})_0 - (\tilde{\mathbf{f}}_{ri})_0 - (\tilde{\mathbf{f}}_{en})_0].$$
 - 1.3 Select time step Δt , set α and β , and compute the following integration constants:

$$a_1 = \frac{\beta}{\alpha\Delta t}, a_2 = 1 - \frac{\beta}{\alpha}, a_3 = \left(1 - \frac{\beta}{2\alpha}\right)\Delta t, a_4 = \frac{1}{\alpha(\Delta t)^2}, a_5 = \frac{1}{\alpha\Delta t}, a_6 = 1 - \frac{1}{2\alpha}.$$
 - 1.4 Evaluate the effective generalized constant stiffness matrix and its inverse:

$$\hat{\mathbf{K}} = a_4\mathbf{M} + a_1\mathbf{C} + \mathbf{K},$$

$$\bar{\mathbf{K}} = \hat{\mathbf{K}}^{-1}.$$
-

2. Calculations at each time step.

- 2.1 Set $i = 0$.
 - 2.2 Assume $(\Delta\tilde{\mathbf{f}}_n)_{i+1}^{(j)} = \mathbf{0}$ at iteration $j = 1$.
 - 2.3 Compute the effective generalized external force vector:

$$\hat{\mathbf{p}}_{i+1}^{(j)} = \mathbf{p}_{i+1} - (\Delta\tilde{\mathbf{f}}_n)_{i+1}^{(j)} + \mathbf{M}[a_5\mathbf{v}_i - a_6\mathbf{a}_i] - \mathbf{C}[a_2\mathbf{v}_i + a_3\mathbf{a}_i] - \mathbf{K}\mathbf{d}_i - (\tilde{\mathbf{f}}_n)_i.$$
 - 2.4 Evaluate the incremental generalized displacement vector:

$$\Delta\mathbf{d}_{i+1}^{(j)} = \bar{\mathbf{K}}\hat{\mathbf{p}}_{i+1}^{(j)}.$$
 - 2.5 Compute the generalized displacement, velocity, and acceleration vectors:

$$\mathbf{d}_{i+1}^{(j)} = \mathbf{d}_i + \Delta\mathbf{d}_{i+1}^{(j)}, \mathbf{v}_{i+1}^{(j)} = a_1\Delta\mathbf{d}_{i+1}^{(j)} + a_2\mathbf{v}_i + a_3\mathbf{a}_i, \text{ and } \mathbf{a}_{i+1}^{(j)} = a_4\Delta\mathbf{d}_{i+1}^{(j)} - a_5\mathbf{v}_i + a_6\mathbf{a}_i.$$
 - 2.6 Evaluate the generalized nonlinear force vector:

$$(\tilde{\mathbf{f}}_n)_{i+1}^{(j)} = \mathbf{f}_{rdn}(\mathbf{v}_{i+1}^{(j)}) + \mathbf{f}_{ri}(\mathbf{d}_{i+1}^{(j)}) + \mathbf{f}_{en}(\mathbf{d}_{i+1}^{(j)}).$$
 - 2.7 Compute the incremental generalized nonlinear force vector:

$$(\Delta\tilde{\mathbf{f}}_n)_{i+1}^{(j+1)} = (\tilde{\mathbf{f}}_n)_{i+1}^{(j)} - (\tilde{\mathbf{f}}_n)_i.$$
 - 2.8 Evaluate the error:

$$\varepsilon = \left\| (\Delta\tilde{\mathbf{f}}_n)_{i+1}^{(j+1)} - (\Delta\tilde{\mathbf{f}}_n)_{i+1}^{(j)} \right\|_2.$$
 - 2.9 If $\varepsilon \geq \textit{toll}$, a further iteration is needed. Replace j by $j + 1$, and go to point (2.3).
 If $\varepsilon < \textit{toll}$, no further iteration is needed. Update:

$$\mathbf{d}_{i+1} = \mathbf{d}_{i+1}^{(j)}, \mathbf{v}_{i+1} = \mathbf{v}_{i+1}^{(j)}, \mathbf{a}_{i+1} = \mathbf{a}_{i+1}^{(j)}, (\tilde{\mathbf{f}}_n)_{i+1} = (\tilde{\mathbf{f}}_n)_{i+1}^{(j)},$$
 replace i by $i + 1$, and go to point (2.2).
-

$$\mathbf{a}_0 = \mathbf{M}^{-1} \left[\mathbf{p}_0 - \mathbf{C}\mathbf{v}_0 - \mathbf{K}\mathbf{d}_0 - (\tilde{\mathbf{f}}_{rdn})_0 - (\tilde{\mathbf{f}}_{ri})_0 - (\tilde{\mathbf{f}}_{en})_0 \right] \quad (8.27)$$

that has been formally obtained by setting $i = -1$ in Eq. (8.8c).

Subsequently, after the selection of the time step Δt and the definition of the two scalar parameters α and β , the following six integration constants, introduced to simply the implementation procedure, are evaluated:

$$\begin{aligned} a_1 &= \frac{\beta}{\alpha \Delta t}, & a_2 &= 1 - \frac{\beta}{\alpha}, & a_3 &= \left(1 - \frac{\beta}{2\alpha}\right) \Delta t, \\ a_4 &= \frac{1}{\alpha (\Delta t)^2}, & a_5 &= \frac{1}{\alpha \Delta t}, & a_6 &= 1 - \frac{1}{2\alpha}. \end{aligned} \quad (8.28)$$

Finally, the effective generalized constant stiffness matrix $\hat{\mathbf{K}} = a_4 \mathbf{M} + a_1 \mathbf{C} + \mathbf{K}$ is computed and its inverse $\bar{\mathbf{K}}$, that is, $\bar{\mathbf{K}} = \hat{\mathbf{K}}^{-1}$, appearing in Eq. (8.20), is evaluated. It is important to note that $\bar{\mathbf{K}}$ needs to be inverted only once during the nonlinear time history analysis and has to be saved for the subsequent computations.

In the second part of the algorithm, called *Calculations at each time step*, the generalized displacement, velocity, and acceleration vectors are computed, at each time step of the analysis, by performing iterations.

In particular, at the first iteration of the generic time step i , namely, for $j = 1$, the incremental generalized nonlinear force vector $(\Delta \tilde{\mathbf{f}}_n)_{i+1}^{(j)}$ is set equal to a zero vector. Then, after the evaluation of the effective generalized external force vector $\hat{\mathbf{p}}_{i+1}^{(j)}$ and of the incremental generalized displacement vector $\Delta \mathbf{d}_{i+1}^{(j)}$, by using Eqs. (8.22) and (8.20), respectively, the generalized displacement $\mathbf{d}_{i+1}^{(j)}$, velocity $\mathbf{v}_{i+1}^{(j)}$, and acceleration $\mathbf{a}_{i+1}^{(j)}$ vectors, as well as the generalized nonlinear force $(\tilde{\mathbf{f}}_n)_{i+1}^{(j)}$ and incremental generalized nonlinear force $(\Delta \tilde{\mathbf{f}}_n)_{i+1}^{(j+1)}$ vectors are computed by adopting Eqs. (8.23), (8.24), (8.25), (8.16a), and (8.16b), respectively.

At this point, if the error ϵ , evaluated as the Euclidean norm of the vector $(\Delta \tilde{\mathbf{f}}_n)_{i+1}^{(j+1)} - (\Delta \tilde{\mathbf{f}}_n)_{i+1}^{(j)}$, is bigger than a fixed convergence tolerance value $toll$, typically assumed equal to 10^{-8} , a further iteration is needed. In such a case, it is required to replace j by $j + 1$ and to go to point (2.3).

On the contrary, if the error ϵ is smaller than the convergence tolerance value $toll$, no further iteration is needed. Thus, after updating \mathbf{d}_{i+1} , \mathbf{v}_{i+1} , \mathbf{a}_{i+1} , $(\tilde{\mathbf{f}}_n)_{i+1}$, and replacing i by $i + 1$, it is possible going to point (2.2).

8.4 Structure-Dependent Time Integration Methods

Structure-dependent time integration methods have been classified by Kolay and Ricles (2016) into two categories: *explicit* and *semi-explicit* methods.

In explicit methods, such as the ones belonging to Chang's Family of Explicit Methods (CFEMs) (Chang 2014), the expressions for evaluating the unknown gen-

eralized displacement and velocity vectors at time $t + \Delta t$ both require known quantities evaluated at the current time t of the analysis. Thus, such methods, that can be conditionally or unconditionally stable, do not require iterations.

On the contrary, in semi-explicit methods, such as the ones belonging to Chang's Family of Semi-Explicit Methods (CFSEMs) (Chang 2010), the expression for the evaluation of the unknown generalized velocity vector at time $t + \Delta t$ also depends on unknown quantities evaluated at time $t + \Delta t$. Therefore, such methods, that can be conditionally or unconditionally stable, do (do not) require iterations when hysteretic (elastic) mechanical systems are analyzed.

In this section, we present Chang's family of explicit methods since it represents one of the most suitable families of structure-dependent time integration methods for performing nonlinear time history analyses of hysteretic mechanical systems (Vaiana et al. 2019b).

8.4.1 Chang's Family of Explicit Methods

8.4.1.1 Formulation

The family of explicit methods developed by Chang (2014) can be derived from Eq. (8.6) by setting:

$$\mathbf{A}_1 = \mathbf{1}, \quad \mathbf{A}_3 = \mathbf{0}, \quad \text{and} \quad \mathbf{B}_2 = \mathbf{0}. \quad (8.29)$$

Hence, the formulation of such a family is

$$\mathbf{d}_{i+1} = \mathbf{d}_i + \Delta t \mathbf{v}_i + \mathbf{A}_2 (\Delta t)^2 \mathbf{a}_i + \mathbf{q}_{i+1}, \quad (8.30a)$$

$$\mathbf{v}_{i+1} = \mathbf{v}_i + \mathbf{B}_1 \Delta t \mathbf{a}_i + \mathbf{r}_{i+1}, \quad (8.30b)$$

$$\mathbf{a}_{i+1} = \mathbf{M}^{-1} \left[\mathbf{p}_{i+1} - \mathbf{C} \mathbf{v}_{i+1} - \mathbf{K} \mathbf{d}_{i+1} - (\tilde{\mathbf{f}}_{rdn})_{i+1} - (\tilde{\mathbf{f}}_{ri})_{i+1} - (\tilde{\mathbf{f}}_{en})_{i+1} \right], \quad (8.30c)$$

where the coefficient matrices \mathbf{A}_2 and \mathbf{B}_1 , assumed to be constant during the complete numerical integration procedure, depend on the time step Δt and on the initial properties of the analyzed discrete structural model, that is, \mathbf{M} , \mathbf{C}_0 , and \mathbf{K}_0 . Specifically, \mathbf{A}_2 and \mathbf{B}_1 are computed as follows:

$$\mathbf{A}_2 = [\mathbf{M} + \beta \Delta t \mathbf{C}_0 + \alpha (\Delta t)^2 \mathbf{K}_0]^{-1} \mathbf{M} = \mathbf{S}_0^{-1} \mathbf{M}, \quad (8.31)$$

$$\mathbf{B}_1 = \mathbf{A}_2, \quad (8.32)$$

in which the scalar parameters α and β define the numerical properties, namely, stability and accuracy, of the time integration method selected within such a family.

The load-dependent vectors \mathbf{q} and \mathbf{r} at the $(i + 1)$ -th time step are evaluated as

$$\mathbf{q}_{i+1} = \mathbf{S}_0^{-1} [\alpha(\Delta t)^2 (\mathbf{p}_{i+1} - \mathbf{p}_i)], \quad (8.33)$$

$$\mathbf{r}_{i+1} = \mathbf{0}. \quad (8.34)$$

Such vectors allow one to eliminate the unusual amplitude growth that occurs in the steady-state response of a high frequency mode when structure-dependent methods are employed in forced vibration problems (Chang 2018a, b).

Considering Eqs. (8.2b) and (8.2c), the initial generalized tangent damping \mathbf{C}_0 and stiffness \mathbf{K}_0 matrices of the discrete structural model can be computed as follows:

$$\mathbf{C}_0 = \left. \frac{\partial \mathbf{f}_{rd}}{\partial \dot{\mathbf{u}}} \right|_{\mathbf{v}_0} = \mathbf{C} + \left. \frac{\partial \mathbf{f}_{rdn}}{\partial \dot{\mathbf{u}}} \right|_{\mathbf{v}_0}, \quad (8.35)$$

$$\mathbf{K}_0 = \left. \frac{\partial \mathbf{f}_{ri}}{\partial \mathbf{u}} \right|_{\mathbf{d}_0} + \left. \frac{\partial \mathbf{f}_e}{\partial \mathbf{u}} \right|_{\mathbf{d}_0} = \left. \frac{\partial \mathbf{f}_{ri}}{\partial \mathbf{u}} \right|_{\mathbf{d}_0} + \mathbf{K} + \left. \frac{\partial \mathbf{f}_{en}}{\partial \mathbf{u}} \right|_{\mathbf{d}_0}. \quad (8.36)$$

It is important to note that no iterative procedures need to be implemented since the expressions for evaluating the unknown generalized displacement and velocity vectors, namely, Eqs. (8.30a) and (8.30b) both require known quantities evaluated at the current time of the analysis.

8.4.1.2 Expressions for \mathbf{d}_{i+1} , \mathbf{v}_{i+1} , and \mathbf{a}_{i+1}

Using the above-described formulation of Chang's family of explicit methods, we derive the expressions for the evaluation of the generalized displacement \mathbf{d}_{i+1} , velocity \mathbf{v}_{i+1} , and acceleration \mathbf{a}_{i+1} vectors at the generic time step $i + 1$ of the analysis.

To this end, we consider a generic time interval $t_i \leq t \leq t_{i+1}$ and we assume that the generalized external force vector \mathbf{p}_i (\mathbf{p}_{i+1}) is assigned at the beginning (end) of such an interval. Furthermore, we also assume that the generalized displacement \mathbf{d}_i , velocity \mathbf{v}_i , and acceleration \mathbf{a}_i vectors at time step i are known.

At this point, the expression for the evaluation of the unknown generalized displacement vector \mathbf{d}_{i+1} can be obtained by substituting Eqs. (8.31) and (8.33) into Eq. (8.30a), so that we get

$$\mathbf{d}_{i+1} = \mathbf{d}_i + \Delta t \mathbf{v}_i + \mathbf{S}_0^{-1} [\mathbf{M}(\Delta t)^2 \mathbf{a}_i + \alpha(\Delta t)^2 (\mathbf{p}_{i+1} - \mathbf{p}_i)]. \quad (8.37)$$

Similarly, the expression for the evaluation of the unknown generalized velocity vector \mathbf{v}_{i+1} can be derived by substituting Eqs. (8.32) and (8.34) into Eq. (8.30b), thus obtaining:

$$\mathbf{v}_{i+1} = \mathbf{v}_i + \mathbf{S}_0^{-1} \mathbf{M} \Delta t \mathbf{a}_i. \quad (8.38)$$

Finally, the expression for the evaluation of the unknown generalized acceleration vector \mathbf{a}_{i+1} is given by Eq. (8.30c):

$$\mathbf{a}_{i+1} = \mathbf{M}^{-1} \left[\mathbf{p}_{i+1} - \mathbf{C}\mathbf{v}_{i+1} - \mathbf{K}\mathbf{d}_{i+1} - (\tilde{\mathbf{f}}_{rdn})_{i+1} - (\tilde{\mathbf{f}}_{ri})_{i+1} - (\tilde{\mathbf{f}}_{en})_{i+1} \right]. \quad (8.39)$$

Such an equation can be adopted after evaluating the generalized force vectors $(\tilde{\mathbf{f}}_{rdn})_{i+1} = \mathbf{f}_{rdn}(\mathbf{v}_{i+1})$, $(\tilde{\mathbf{f}}_{ri})_{i+1} = \mathbf{f}_{ri}(\mathbf{d}_{i+1})$, and $(\tilde{\mathbf{f}}_{en})_{i+1} = \mathbf{f}_{en}(\mathbf{d}_{i+1})$ by employing suitable phenomenological models available in the literature (Bouc 1971; Wen 1976, 1980; Seleemah and Constantinou 1997; Vaiana et al. 2018, 2019a,b,c).

8.4.1.3 Numerical Properties

The stability and the accuracy of Chang's family of explicit methods depend on the values assumed by the scalar parameters α and β .

As far as the stability is concerned, the critical time step Δt_{cr} is different for each natural mode of the discrete structural model evaluated at the $(i + 1)$ -th time step of a nonlinear time history analysis. Specifically, assuming a zero viscous damping ratio and imposing $\beta \geq \frac{1}{2}$, the value of the critical time step of the j -th mode at the $(i + 1)$ -th time step, that is, $(\Delta t_{cr})_{i+1}^{(j)}$, can be evaluated as follows (Chang 2014):

$$(\Delta t_{cr})_{i+1}^{(j)} = \begin{cases} \infty & \text{if } \alpha \geq \frac{1}{4} \left(\beta + \frac{1}{2} \right)^2 \kappa_{i+1}^{(j)} \\ \frac{T_0^{(j)}}{2\pi \sqrt{\frac{1}{4} \left(\beta + \frac{1}{2} \right)^2 \kappa_{i+1}^{(j)} - \alpha}} & \text{if } \alpha < \frac{1}{4} \left(\beta + \frac{1}{2} \right)^2 \kappa_{i+1}^{(j)}, \end{cases} \quad (8.40a)$$

$$(8.40b)$$

where $T_0^{(j)}$ is the initial natural period of the j -th mode, whereas $\kappa_{i+1}^{(j)}$ is the current degree of nonlinearity of the j -th mode at the $(i + 1)$ -th time step:

$$\kappa_{i+1}^{(j)} = \left[\frac{T_0^{(j)}}{T_{i+1}^{(j)}} \right]^2, \quad (8.41)$$

in which $T_{i+1}^{(j)}$ is the natural period of the j -th mode evaluated by using the generalized tangent stiffness matrix \mathbf{K}_{i+1} at the $(i + 1)$ -th time step. It is worth being emphasized that $\kappa_{i+1}^{(j)}$ turns out to be greater (smaller) than 1 in presence of (non-) stiffening behavior.

As regards the accuracy, the subfamily of methods for which $\beta = 1/2$ has a second-order accuracy, does not suffer from numerical damping, and displays a small relative period error for $\Delta t \leq 0.05 T_{i+1}^{(j)}$.

Generally speaking, for a fixed value of β , increasing the value of α , the critical time step of the j -th mode at the $(i + 1)$ -th time step increases whereas the accuracy decreases.

8.4.2 Some Instances of the CFEMs

Some instances of Chang's family of explicit methods that exhibit good stability and accuracy properties are

- Chang explicit method 1, obtained for $\alpha = 1/4$ and $\beta = 1/2$;
- Chang explicit method 2, obtained for $\alpha = 1/3$ and $\beta = 1/2$;
- Chang explicit method 3, obtained for $\alpha = 1/2$ and $\beta = 1/2$.

Specifically, the Chang explicit method 1 is (un)conditionally stable for all (non-)stiffening hysteretic mechanical systems, whereas the Chang explicit method 2 and the Chang explicit method 3 are unconditionally stable also for some stiffening hysteretic mechanical systems, as it can be easily shown by computing the critical time step Δt_{cr} with Eq. (8.40).

8.4.3 Implementation Scheme of the CFEMs

Table 8.2 summarizes the implementation scheme of Chang's family of explicit methods that is composed of two parts. In the first one, called *Initial settings*, the generalized constant mass \mathbf{M} , damping \mathbf{C} , and stiffness \mathbf{K} matrices as well as the initial generalized tangent damping \mathbf{C}_0 and stiffness \mathbf{K}_0 matrices, obtained from Eqs. (8.35) and (8.36), respectively, are first assembled. Then, the initial generalized displacement \mathbf{d}_0 and velocity \mathbf{v}_0 vectors are initialized and the initial generalized acceleration vector \mathbf{a}_0 is evaluated using the following equation:

$$\mathbf{a}_0 = \mathbf{M}^{-1} \left[\mathbf{p}_0 - \mathbf{C}\mathbf{v}_0 - \mathbf{K}\mathbf{d}_0 - (\tilde{\mathbf{f}}_{rdn})_0 - (\tilde{\mathbf{f}}_{ri})_0 - (\tilde{\mathbf{f}}_{en})_0 \right] \quad (8.42)$$

that has been formally obtained by setting $i = -1$ in Eq. (8.39).

Finally, after the selection of the time step Δt and the definition of the two scalar parameters α and β , matrix $\mathbf{S}_0 = \mathbf{M} + \beta\Delta t\mathbf{C}_0 + \alpha(\Delta t)^2\mathbf{K}_0$, appearing in Eqs. (8.37) and (8.38), is computed and the inverse of matrices \mathbf{M} and \mathbf{S}_0 , that is, $\bar{\mathbf{M}} = \mathbf{M}^{-1}$ and $\bar{\mathbf{S}}_0 = \mathbf{S}_0^{-1}$, are evaluated. It is important to note that \mathbf{M} and \mathbf{S}_0 need to be inverted only once during the nonlinear time history analysis and have to be saved for the subsequent computations.

In the second part of the algorithm, called *Calculations at each time step*, the generalized displacement \mathbf{d}_{i+1} , velocity \mathbf{v}_{i+1} , and acceleration \mathbf{a}_{i+1} vectors are computed, at each time step of the analysis, by using Eqs. (8.37), (8.38), and (8.39), respectively.

8.5 Numerical Experiments

In this section, the nonlinear dynamic response of a mechanical system, having stiffening rate-independent hysteretic behavior, is simulated by solving the nonlinear equilibrium equation by means of time integration methods introduced in the previous sections.

Specifically, in order to numerically investigate the accuracy properties of the recently developed structure-dependent Chang Explicit Method 3 (CEM3) and its capability to decrease the computational burden of nonlinear time history analyses, the numerical results and the computational times are compared with those obtained by solving the nonlinear equilibrium equation by employing the conventional Newmark Average Acceleration Method (NAAM).

The Chang Explicit Method 3 is selected since it has the best numerical properties among methods belonging to the CFEMs, presented in Sect. 8.4, whereas the Newmark Average Acceleration Method is adopted since it is one of the most used methods belonging to the NFMs, presented in Sect. 8.3.

The solution algorithms of the NFMs and of the CFEMs, summarized in Tables 8.1 and 8.2, respectively, have been programmed in MATLAB and run on a computer having an Intel®Core™i7-4700MQ processor and a CPU at 2.40GHz with 16 GB of RAM.

Table 8.2 CFEMs algorithm

1. Initial settings.

- 1.1 Assemble the following matrices: \mathbf{M} , \mathbf{C} , \mathbf{K} , \mathbf{C}_0 , and \mathbf{K}_0 .
 - 1.2 Initialize \mathbf{d}_0 and \mathbf{v}_0 ; then evaluate the initial generalized acceleration vector:

$$\mathbf{a}_0 = \mathbf{M}^{-1} [\mathbf{p}_0 - \mathbf{C}\mathbf{v}_0 - \mathbf{K}\mathbf{d}_0 - (\tilde{\mathbf{f}}_{rdn})_0 - (\tilde{\mathbf{f}}_{ri})_0 - (\tilde{\mathbf{f}}_{en})_0].$$
 - 1.3 Select time step Δt , set α and β , and compute \mathbf{S}_0 :

$$\mathbf{S}_0 = \mathbf{M} + \beta\Delta t\mathbf{C}_0 + \alpha(\Delta t)^2\mathbf{K}_0.$$
 - 1.4 Evaluate the following inverted matrices:

$$\bar{\mathbf{M}} = \mathbf{M}^{-1},$$

$$\bar{\mathbf{S}}_0 = \mathbf{S}_0^{-1}.$$
-

2. Calculations at each time step.

- 2.1 Set $i = 0$.
 - 2.2 Compute the generalized displacement vector:

$$\mathbf{d}_{i+1} = \mathbf{d}_i + \Delta t\mathbf{v}_i + \bar{\mathbf{S}}_0 [\mathbf{M}(\Delta t)^2\mathbf{a}_i + \alpha(\Delta t)^2(\mathbf{p}_{i+1} - \mathbf{p}_i)].$$
 - 2.3 Evaluate the generalized velocity vector:

$$\mathbf{v}_{i+1} = \mathbf{v}_i + \bar{\mathbf{S}}_0\mathbf{M}\Delta t\mathbf{a}_i.$$
 - 2.4 Compute the generalized force vectors:

$$(\tilde{\mathbf{f}}_{rdn})_{i+1} = \mathbf{f}_{rdn}(\mathbf{v}_{i+1}), (\tilde{\mathbf{f}}_{ri})_{i+1} = \mathbf{f}_{ri}(\mathbf{d}_{i+1}), \text{ and } (\tilde{\mathbf{f}}_{en})_{i+1} = \mathbf{f}_{en}(\mathbf{d}_{i+1}).$$
 - 2.5 Evaluate the generalized acceleration vector:

$$\mathbf{a}_{i+1} = \bar{\mathbf{M}} [\mathbf{p}_{i+1} - \mathbf{C}\mathbf{v}_{i+1} - \mathbf{K}\mathbf{d}_{i+1} - (\tilde{\mathbf{f}}_{rdn})_{i+1} - (\tilde{\mathbf{f}}_{ri})_{i+1} - (\tilde{\mathbf{f}}_{en})_{i+1}].$$
 - 2.6 Replace i by $i + 1$ and repeat points (2.2)-(2.5).
-

8.5.1 Mechanical System Properties

The discrete structural model of the analyzed hysteretic mechanical system is made up of two nodes, namely, Node 1 and Node 2, connected by one straight element, as shown in Fig. 8.1. Such an element can be decomposed into three subelements, namely a Linear Elastic Subelement (LESe), with generalized force f_{el} and generalized stiffness K , a Linear Rate-Dependent Hysteretic Subelement (LRDSe), having generalized force f_{rdl} and generalized viscous damping coefficient C , and a Rate-Independent Hysteretic Subelement (RISe), with generalized force f_{ri} and initial generalized tangent stiffness k .

Assuming that Node 1 is attached to a fixed support and that the element is flexurally rigid, the only free Degree Of Freedom (DOF) of the above-described discrete structural model is the axial displacement u of Node 2, the latter having a lumped mass M applied along such a direction.

Specifically, the initial properties of the structural model are $M = 1 \text{ Ns}^2/\text{m}$, $C = 1 \text{ Ns}/\text{m}$, $K = 1 \text{ N}/\text{m}$, and $k = 40 \text{ N}/\text{m}$. Thus, the initial natural period along the axial direction, evaluated as $T = 2\pi \sqrt{M / (K + k)}$, is 0.981 s.

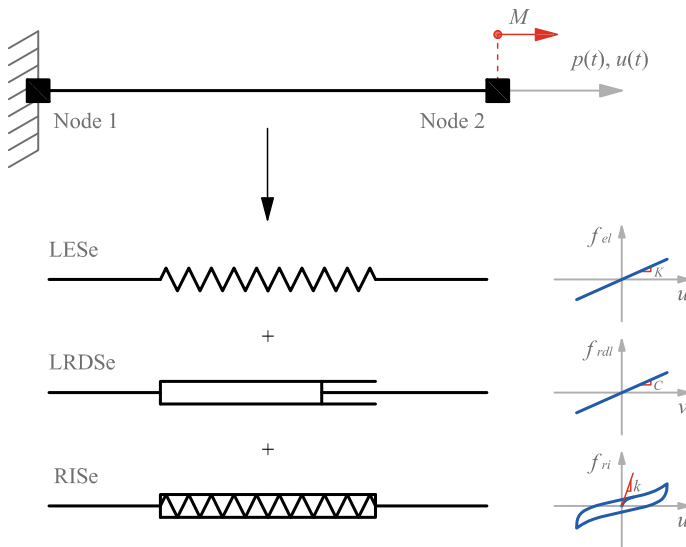


Fig. 8.1 Discrete structural model of the analyzed hysteretic mechanical system

8.5.2 Applied Generalized External Force

The analyses are performed for a generalized external random force $p(t)$, that is, a Gaussian white noise with an intensity $wn = 9\text{ N}$ and a time duration $t_d = 10\text{ s}$. Such a force is applied at Node 2 along the axial direction of the element, as shown in Fig. 8.1.

8.5.3 Hysteretic Model Parameters

The dynamic behavior of the Rate-Independent Hysteretic Subelement is simulated adopting a novel rate-independent model; such an uniaxial model, representing a specific instance of the general class formulated by Vaiana et al. (2018), requires a set of only four parameters, namely, k_a , k_b , γ_1 , and γ_2 , and two internal model parameters, namely, u_0 and f_0 , expressed as a function of k_a , k_b , and γ_1 . Specifically, $k_a > k_b$, $k_a > 0$, $\gamma_1 > 0$, $u_0 > 0$, $f_0 > 0$, whereas γ_2 is real.

In particular, the generalized rate-independent hysteretic force f_{ri} is evaluated by solving the following transcendental equation, when $us < u_j s$:

$$f_{ri} = -2\gamma_2 u + e^{\gamma_2 u} - e^{-\gamma_2 u} - s \frac{k_a - k_b}{\gamma_1} \left[e^{-\gamma_1 (us - u_j s + 2u_0)} - e^{-2\gamma_1 u_0} \right] + k_b u + f_0 s, \quad (8.43)$$

whereas, if $us > u_j s$, it is computed as follows:

$$f_{ri} = -2\gamma_2 u + e^{\gamma_2 u} - e^{-\gamma_2 u} + k_b u + f_0 s, \quad (8.44)$$

in which u is the generalized displacement, s is the sign of the generalized velocity, namely, $s = \text{sign}(v)$, and u_j is the model history variable.

Specifically, the parameters adopted to perform the nonlinear analyses are $k_a = 40\text{ Nm}^{-1}$, $k_b = 1\text{ Nm}^{-1}$, $\gamma_1 = 30\text{ m}^{-1}$, and $\gamma_2 = 10\text{ Nm}^{-1}$.

8.5.4 Results of the Nonlinear Time History Analyses

The selection of an appropriate time step Δt is a crucial aspect to accurately analyze the above-described discrete structural model. As suggested in the literature (Clough and Penzien 2003; Bathe 1996), time history analyses of linear elastic systems can be performed adopting $\Delta t = T/10$ or $T/20$. Since for nonlinear systems a smaller time step is required to limit the detrimental effects due to factors that affect the accuracy of the adopted time integration method, such as the period distortion, the analyses are performed adopting a time step $\Delta t = 0.001\text{ s}$, that is smaller than $T/100$.

Table 8.3 NLTHAs results—random force

| | tct [s] | $tctp$ [%] | d [m] | | v [ms ⁻¹] | | a [ms ⁻²] | |
|------|-----------|------------|---------|---------|-------------------------|---------|-------------------------|----------|
| | | | max | min | max | min | max | min |
| NAAM | 1.221 | – | 0.1839 | –0.1474 | 0.6458 | –0.6933 | 34.7285 | –29.3396 |
| CEM3 | 0.600 | 49.14 | 0.1839 | –0.1476 | 0.6526 | –0.6950 | 34.7456 | –29.3541 |

The results of the Nonlinear Time History Analyses (NLTHAs) carried out on the selected hysteretic mechanical system are shown in Table 8.3. The accuracy of the CEM3 is very satisfactory since the maximum and minimum values of the approximate estimates of the axial displacement d , velocity v , and acceleration a of the analyzed model are numerically quite close to those predicted by using the conventional NAAM.

The response of the analyzed model, simulated by applying the random force along the axial direction, is illustrated in terms of time histories of the axial displacement, velocity, and acceleration, shown, respectively, in Figs. 8.2a–c, and in terms of axial rate-independent force-displacement hysteresis loops, illustrated in Fig. 8.2d. Generally speaking, the comparison between the responses obtained with the CEM3 and the NAAM shows a very good agreement.

Finally, as regards the computational efficiency, Table 8.3 also shows the total computational time tct required by the two methods as well as the total computational time percentage $tctp$ required by the CEM3 with respect to the NAAM, evaluated as

$$CEM3 \ tctp \ [%] = \frac{CEM3 \ tct}{NAAM \ tct} \cdot 100. \quad (8.45)$$

It transpires that the computational burden of the CEM3 is smaller than the one characterizing the NAAM since the former does not require iterations for each time step of the performed nonlinear time history analyses.

8.6 Conclusion

We have presented a generalized formulation of time integration methods that take into account the presence of generalized force vectors, namely the nonlinear rate-dependent and rate-independent hysteretic force vectors, typical of discrete structural models characterizing hysteretic mechanical systems.

Starting from the proposed formulation, we have derived Newmark’s family of methods and Chang’s family of explicit method, both suitable to perform nonlinear dynamic analysis of hysteretic mechanical systems.

To show the accuracy and the computational efficiency of two methods belonging to the above-described families, namely, the Newmark Average Acceleration Method (NAAM) and the Chang Explicit Method 3 (CEM3), presented in Sects. 8.3.2 and

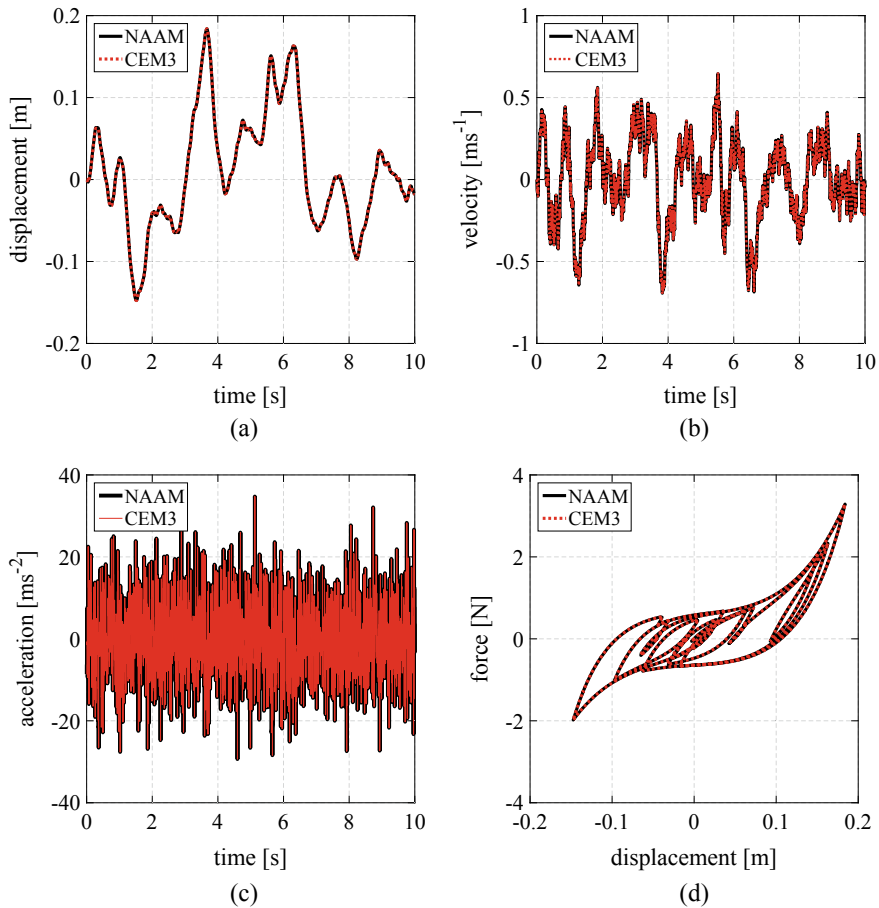


Fig. 8.2 Discrete structural model response in terms of axial displacement (a), velocity (b), acceleration (c), and axial force-displacement hysteresis loops (d)

8.4.2, respectively, some nonlinear time history analyses have been performed on a stiffening hysteretic mechanical system by modeling the rate-independent hysteretic force employing a novel uniaxial model developed by Vaiana et al. (2018). Specifically, the numerical results and the computational times obtained with the recently developed CEM3 have been compared to those obtained by employing the conventional NAAM.

The dynamic responses of the analyzed hysteretic mechanical system, obtained for a generalized external random force, reveal that the accuracy of the CEM3 is very satisfactory since the numerical results closely match those predicted by the NAAM. Furthermore, these results also reveal that the computational burden required by the CEM3 is reduced with respect to that characterizing the NAAM; in particular, the total computational time percentage, $tctp$, of CEM3 is less than 50.00%.

Future enhancements of the presented generalized formulation consist in comparing the computed responses with different strategies of the structural engineering such as seismic envelopes (Sessa et al. 2015, 2018b) and limit-analysis approaches (Sessa et al. 2018a, 2019b). Moreover, Chang's family of integration algorithms is particularly feasible for extensions to soil-structure interaction analyses in which the behavior of the foundations is modeled by means of half-spaces (Marmo et al. 2016, 2018; Franciosi et al. 2019) because of its capability of accounting for the structural behavior. Finally, the proposed formulation will be adopted for the nonlinear analysis of metamaterials (De Angelo et al. 2020; dell'Isola et al. 2019, b; NejadSadeghi et al. 2019b, a; Turco et al. 2017, 2018, 2019; Turco and Barchiesi 2019; Turco et al. 2020).

References

- Abd-alla AenN, Alshaikh F, Del Vescovo D, Spagnuolo M (2017) Plane waves and eigenfrequency study in a transversely isotropic magneto-thermoelastic medium under the effect of a constant angular velocity. *J Thermal Stress* 40(9):1079–1092
- Andreas U, Spagnuolo M, Lekszycki T, Eugster SR (2018) A Rtz approach for the static analysis of planar pantographic structures modeled with nonlinear Euler-Bernoulli beams. *Continuum Mech Thermodyn* 30(5):1103–1123
- Bathe K, Wilson E (1972) Stability and accuracy analysis of direct integration methods. *Earthq Eng Struct Dyn* 1(3):283–291
- Bathe KJ (1996) Finite element procedures. New Jersey
- Bouc R (1971) Modèle mathématique d'hystérésis. *Acustica* 21:16–25
- Castellano A, Fraddosio A, Scacco J, Milani G, Piccioni MD (2019) Dynamic response of FRCM reinforced masonry arches. *Key Eng Mater Trans Tech Publ* 817:285–292
- Chang SY (2009) Accurate integration of nonlinear systems using newmark explicit method. *J Mech* 25(3):289–297
- Chang SY (2010) A new family of explicit methods for linear structural dynamics. *Comput Struct* 88(11–12):755–772
- Chang SY (2014) Family of structure-dependent explicit methods for structural dynamics. *J Eng Mech* 140(6):06014,005
- Chang SY (2018a) Elimination of overshoot in forced vibration responses for chang explicit family methods. *J Eng Mech* 144(2):04017,177
- Chang SY (2018b) An unusual amplitude growth property and its remedy for structure-dependent integration methods. *Comput Methods Appl Mech Eng* 330:498–521
- Chen C, Ricles JM (2008) Development of direct integration algorithms for structural dynamics using discrete control theory. *J Eng Mech* 134(8):676–683
- Clough RW, Penzien J (2003) Dynamics of structures. Computers and Structures, Berkeley, CA
- di Cosmo F, Laudato M, Spagnuolo M (2018) Acoustic metamaterials based on local resonances: homogenization, optimization and applications. In: Generalized models and non-classical approaches in complex materials 1. Springer, pp 247–274
- Dahlquist G (1956) Convergence and stability in the numerical integration of ordinary differential equations. *Mathematica Scandinavica* pp 33–53
- Dahlquist GG (1963) A special stability problem for linear multistep methods. *BIT Numer Math* 3(1):27–43
- De Angelo M, Spagnuolo M, D'annibale F, Pfaff A, Hoschke K, Misra A, Dupuy C, Peyre P, Dirrenberger J, Pawlikowski M, (2019) The macroscopic behavior of pantographic sheets depends

- mainly on their microstructure: experimental evidence and qualitative analysis of damage in metallic specimens. *Contin Mech Thermodyn* 31(4):1181–1203
- De Angelo M, Placidi L, NejadSadeghi N, Misra A (2020) Non-standard Timoshenko beam model for chiral metamaterial: identification of stiffness parameters. *Mechanics Research Communications* 103
- dell'Isola F, Seppecher P, Alibert JJ, Lekszycki T, Grygoruk R, Pawlikowski M, Steigmann D, Giorgio I, Andraus U, Turco E et al (2019) Pantographic metamaterials: an example of mathematically driven design and of its technological challenges. *Contin Mech Thermodyn* 31(4):851–884
- dell'Isola F, Seppecher P, Spagnuolo M, Barchiesi E, Hild F, Lekszycki T, Giorgio I, Placidi L, Andraus U, Cuomo M et al (2019b) Advances in pantographic structures: design, manufacturing, models, experiments and image analyses. *Contin Mech Thermodyn* 31(4):1231–1282
- Dimian M, Andrei P (2014) Noise-driven phenomena in hysteretic systems. Springer
- Franciosi P, Spagnuolo M, Salman OU (2019) Mean green operators of deformable fiber networks embedded in a compliant matrix and property estimates. *Contin Mech Thermodyn* 31(1):101–132
- Greco F, Luciano R, Serino G, Vaiana N (2018) A mixed explicit-implicit time integration approach for nonlinear analysis of base-isolated structures. *Annal Solid Struct Mech* 10(1):17–29
- Gui Y, Wang JT, Jin F, Chen C, Zhou MX (2014) Development of a family of explicit algorithms for structural dynamics with unconditional stability. *Nonlinear Dyn* 77(4):1157–1170
- Hughes T (1987) The finite element method. Linear static and dynamic finite element analysis
- Kolay C, Ricles JM (2016) Assessment of explicit and semi-explicit classes of model-based algorithms for direct integration in structural dynamics. *Int J Numer Meth Eng* 107(1):49–73
- Lima C, Angiolilli M, Barbagallo F, Belletti B, Bergami A, Camata G, Cantagallo C, Di Domenico M, Fiorentino G, Ghersi A, et al (2018) Nonlinear modeling approaches for existing reinforced concrete buildings: The case study of de gasperi-battaglia school building in norcia. In: *Conference on Italian concrete days*. Springer, pp 82–95
- Losanno D, Palumbo F, Calabrese A, Barrasso T, Vaiana N (2021) Preliminary investigation of aging effects on recycled rubber fiber reinforced bearings (RR-FRBs). *J Earthq Eng* 1–18
- Marmo F, Sessa S, Rosati L (2016) Analytical solution of the cerruti problem under linearly distributed horizontal loads over polygonal domains. *J Elast* 124(1):27–56
- Marmo F, Sessa S, Vaiana N, De Gregorio D, Rosati L (2018) Complete solutions of three-dimensional problems in transversely isotropic media. *Contin Mech Thermodyn* 32(3):775–802
- Nagarajiah S, Reinhorn AM, Constantinou MC (1991) Nonlinear dynamic analysis of 3-d-base-isolated structures. *J Struct Eng* 117(7):2035–2054
- NejadSadeghi N, De Angelo M, Drobnicki R, Lekszycki T, Dell'Isola F, Misra A (2019a) Parametric experimentation on pantographic unit cells reveals local extremum configuration. *Exp Mech* 59(6):927–939
- NejadSadeghi N, Placidi L, Romeo M, Misra A (2019b) Frequency band gaps in dielectric granular metamaterials modulated by electric field. *Mech Res Commun* 95:96–103
- Newmark NM (1959) A method of computation for structural dynamics. *J Eng Mech Div* 85(3):67–94
- Seleemah A, Constantinou MC (1997) Investigation of seismic response of buildings with linear and nonlinear fluid viscous dampers. National Center for Earthquake Engineering Research Buffalo
- Serpieri R, Sessa S, Rosati L (2018) A MITC-based procedure for the numerical integration of a continuum elastic-plastic theory of through-the-thickness-jacketed shell structures. *Compos Struct* 191:209–220
- Sessa S, Marmo F, Rosati L (2015) Effective use of seismic response envelopes for reinforced concrete structures. *Earthq Eng Struct Dyn* 44(14):2401–2423
- Sessa S, Serpieri R, Rosati L (2017) A continuum theory of through-the-thickness jacketed shells for the elasto-plastic analysis of confined composite structures: theory and numerical assessment. *Compos B Eng* 113:225–242
- Sessa S, Marmo F, Rosati L, Leonetti L, Garcea G, Casciaro R (2018a) Evaluation of the capacity surfaces of reinforced concrete sections: Eurocode versus a plasticity-based approach. *Meccanica* 53(6):1493–1512

- Sessa S, Marmo F, Vaiana N, Rosati L (2018b) A computational strategy for eurocode 8-compliant analyses of reinforced concrete structures by seismic envelopes. *J Earthq Eng* 1–34
- Sessa S, Marmo F, Vaiana N, De Gregorio D, Rosati L (2019a) Strength hierarchy provisions for transverse confinement systems of shell structural elements. *Compos B Eng* 163:413–423
- Sessa S, Marmo F, Vaiana N, Rosati L (2019b) Probabilistic assessment of axial force-biaxial bending capacity domains of reinforced concrete sections. *Meccanica* 54(9):1451–1469
- Sessa S, Vaiana N, Paradiso M, Rosati L (2020) An inverse identification strategy for the mechanical parameters of a phenomenological hysteretic constitutive model. *Mech Syst Signal Process* 139(106):622
- Tsai C, Chiang TC, Chen BJ, Lin SB (2003) An advanced analytical model for high damping rubber bearings. *Earthq Eng Struct Dyn* 32(9):1373–1387
- Turco E, Barchiesi E (2019) Equilibrium paths of Hencky pantographic beams in a three-point bending problem. *Math Mech Complex Syst* 7(4):287–310
- Turco E, Giorgio I, Misra A, Dell’Isola F (2017) King post truss as a motif for internal structure of (meta) material with controlled elastic properties. *Royal Soc Open Scie* 4(10):171,153
- Turco E, Misra A, Pawlikowski M, Dell’Isola F, Hild F (2018) Enhanced Piola-Hencky discrete models for pantographic sheets with pivots without deformation energy: numerics and experiments. *Int J Solids Struct* 147:94–109
- Turco E, Misra A, Sarikaya R, Lekszycki T (2019) Quantitative analysis of deformation mechanisms in pantographic substructures: experiments and modeling. *Contin Mech Thermodyn* 31(1):209–223
- Turco E, Barchiesi E, Giorgio I, Dell’Isola F (2020) A Lagrangian Hencky-type non-linear model suitable for metamaterials design of shearable and extensible slender deformable bodies alternative to Timoshenko theory. *Int J Non-Linear Mech* 123(103):481
- Vaiana N, Spizzuoco M, Serino G (2017) Wire rope isolators for seismically base-isolated lightweight structures: experimental characterization and mathematical modeling. *Eng Struct* 140:498–514
- Vaiana N, Sessa S, Marmo F, Rosati L (2018) A class of uniaxial phenomenological models for simulating hysteretic phenomena in rate-independent mechanical systems and materials. *Nonlinear Dyn* 93(3):1647–1669
- Vaiana N, Sessa S, Marmo F, Rosati L (2019a) An accurate and computationally efficient uniaxial phenomenological model for steel and fiber reinforced elastomeric bearings. *Compos Struct* 211:196–212
- Vaiana N, Sessa S, Marmo F, Rosati L (2019b) Nonlinear dynamic analysis of hysteretic mechanical systems by combining a novel rate-independent model and an explicit time integration method. *Nonlinear Dyn* 98(4):2879–2901
- Vaiana N, Sessa S, Paradiso M, Marmo F, Rosati L (2019c) An efficient computational strategy for nonlinear time history analysis of seismically base-isolated structures. In: Conference of the Italian Association of theoretical and applied mechanics. Springer, pp 1340–1353
- Vaiana N, Sessa S, Paradiso M, Rosati L (2019d) Accurate and efficient modeling of the hysteretic behavior of sliding bearings. 7th International conference on computational methods in structural dynamics and earthquake engineering (COMPDYN 2019). Crete, Greece, pp 24–26
- Vaiana N, Marmo F, Sessa S, Rosati L (2020) Modeling of the hysteretic behavior of wire rope isolators using a novel rate-independent model. *Nonlinear Dynamics of Structures, Springer, Systems and Devices*, pp 309–317
- Vaiana N, Capuano R, Sessa S, Marmo F, Rosati L (2021a) Nonlinear dynamic analysis of seismically base-isolated structures by a novel opensees hysteretic material model. *Appl Sci* 11(3):900
- Vaiana N, Losanno D, Ravichandran N (2021b) A novel family of multiple springs models suitable for biaxial rate-independent hysteretic behavior. *Comput Struct* 244(106):403
- Vaiana N, Sessa S, Rosati L (2021c) A generalized class of uniaxial rate-independent models for simulating asymmetric mechanical hysteresis phenomena. *Mech Syst Signal Process* 146(106):984
- Valoroso N, Marmo F, Sessa S (2014) Limit state analysis of reinforced shear walls. *Eng Struct* 61:127–139

- Valoroso N, Marmo F, Sessa S (2015) A novel shell element for nonlinear pushover analysis of reinforced concrete shear walls. *Bull Earthq Eng* 13(8):2367–2388
- Wen YK (1976) Method for random vibration of hysteretic systems. *J Eng Mech Div* 102(2):249–263
- Wen Y (1980) Equivalent linearization for hysteretic systems under random excitation. *J Appl Mech-T*
- Wilson EL (2002) Three-dimensional static and dynamic analysis of structures. *Comput Struct*
- Zuccaro G, Dato F, Cacace F, De Gregorio D, Sessa S (2017) Seismic collapse mechanisms analyses and masonry structures typologies: a possible correlation. *Ingegneria Sismica* 34(4):121–150

Chapter 9

Quasi-Harmonic Solutions for Transversely Isotropic Magneto-Electro-Thermo-Elasticity: A Symbolic Mathematics Approach



Francesco Marmo  and Massimo Paradiso

Abstract The behaviour of magneto-electro-thermo-elastic materials is governed by a set of six differential equations in which the piezoelectric, the piezomagnetic, the magnetoelectric and thermal effects are coupled. Under the steady-state condition, this system of equations is homogeneous and can be rewritten as a set of uncoupled modified Laplace equations expressed as a function of the roots of a characteristic polynomial associated with the original set of governing equations. Differently from previous proposals, the presented approach employs the entire kernel of the adjoint differential operator so as to preserve completeness. Finally, due to the large number of constitutive parameters involved in the uncoupling process, two Mathematica scripts that compute the coefficients of the characteristic polynomial and the components of the adjoint differential operator are described in full detail.

Keywords Piezoelectricity · Piezomagnetism · Electromagnetism · Thermoelasticity · Laplace equation · Adjoint differential operator

9.1 Introduction

The distinctive property of magneto-electro-elastic composites is the coupling between strain, electric polarization and magnetization. These materials offer a wide range of applications in nanoscience and nanotechnology and can be successfully employed for the fabrication of electronic devices such as sensors, actuators, trans-

F. Marmo (✉) · M. Paradiso
Department of Structures for Engineering and Architecture, University
of Naples Federic II, via Claudio 21, 80124 Napoli, Italy
e-mail: f.marmo@unina.it

M. Paradiso
e-mail: massimo.paradiso@unina.it

© Springer Nature Switzerland AG 2021
F. Marmo et al. (eds.), *Mathematical Applications in Continuum
and Structural Mechanics*, Advanced Structured Materials 127,
https://doi.org/10.1007/978-3-030-42707-8_9

ducers and memories (Eerenstein et al. 2006; Milton et al. 2009; Wang et al. 2010; NejadSadeghi et al. 2019; di Cosmo et al. 2018).

The equations that govern the behaviour of this class of materials, often characterized by transverse isotropy, describe coupling between the infinitesimal strain, electric and magnetic fields, eventually accounting for the effects of temperature. These formulas constitute a system of coupled differential equations (Bardzokas et al. 2007) whose solution is of particular interest in practical applications.

Since the beginning of the XX century, many researchers have approached the problem of rewriting this system of differential equation as a set of uncoupled modified Laplace equations. Accordingly, the solution can be expressed as the sum of quasi-harmonic functions φ_i that fulfil the condition

$$(\partial_x^2 + \partial_y^2 + s_i^2 \partial_z^2) \varphi_i = 0, \quad (9.1)$$

where $\partial_{(\cdot)}$ represents differentiation with respect to (\cdot) and s_i are scalars evaluated as a function of the material constitutive parameters. Their values are computed as the roots of a characteristic equation associated with the governing system of equations.

Although these potential functions need to be evaluated for specific boundary conditions, their determination is simpler than the direct application of the original differential equation. Actually, many solution techniques, both analytical and numerical, are available for Laplace equations, while a specific solving technique needs to be employed for the more general governing set of coupled equations.

With reference to transversely isotropic elasticity, the first use of quasi-harmonic potential functions dates back to the paper by Michell (1900), later followed by the alternative solutions (Lekhnitskii 1940; Elliott and Mott 1948; Shield 1951; Chen 1966; Green and Zerna 1968; Pan and Chou 1976, 1979; Lekhnitskii 1981; Fabrikant 1989; Lin et al. 1991; Ding et al. 2006; Rosati and Marmo 2014; Marmo and Rosati 2016; Marmo et al. 2016a, 2018).

These solutions employ a variable number of scalar quasi-harmonic potential functions that range between two and eight. Questioning about the problem of completeness of the potential solutions proposed in the literature, Wang and Wang (1995) furnished two separate expressions that employ only three quasi-harmonic functions. However, in a recent contribution, the authors (2017) have shown a fundamental property of the quasi-harmonic potential, which have a vector nature and can be used to express the solution as a linear combination of arbitrary derivatives of all their components. This property can be used to specialize the solutions that employ three quasi-harmonic potentials to all other approaches formulated in the earlier literature, hence showing their substantial equivalence.

More recently, the authors (2016b, 2020) have proposed an alternative approach that exploits the entire kernel of the differential operator associated with the governing equations, what again furnishes the same set of three quasi-harmonic potentials. Actually, the minimum number of potential functions to handle in the solution process is equal to number of unknown scalar fields. In case of transversely isotropic elasticity, these amount to three components of displacement.

Generalizations to the case of piezoelectricity have been proposed in Zikung and Bailin (1995), Haojiang et al. (1996) and employ four quasi-harmonic potentials due to the presence of the additional unknown scalar field represented by the electric potential. A discussion about the completeness of these solutions is reported in Xu et al. (2008). Solutions that account for thermal coupling, either in absence or presence of the piezoelectric effect, are described in Podil'chuk and Sokolovskii (1994), Chen (2000), Ashida et al. (1993).

The case of magneto-electro-elasticity, in which piezoelectric, piezomagnetic and magnetoelectric couplings are present, is considered in Pan (2002), Wang and Shen (2002), Ding and Jiang (2003). These solutions consider five quasi-harmonic potentials, the additional one being generated by the presence of a new unknown scalar field, i.e. the magnetic potential.

Thermal coupling is considered in Chen et al. (2004) and, as expected, includes six quasi-harmonic potentials. However this solution is obtained by considering only one row of the adjoint differential operator associated with the system of governing equations. Hence, similarly to what was done by the authors in the case of transversely isotropic linear elasticity (Marmo et al. 2020), we propose below a solution that employs the entire kernel of the differential operator associated with the governing equations in presence of thermal, electric, and magnetic couplings.

Accordingly, after introducing the field equations that govern the behaviour of magneto-electro-thermo-elastic materials (Sect. 9.2), we uncouple the equations by inverting the associated differential operator (Sect. 9.3). Due to the large number of constitutive parameters involved in this operation, we furnish a Mathematica script that computes the coefficients of the characteristic polynomial associated with the magneto-electro-thermo-elastic coupling and the components of the adjoint differential operator employed to express the final solution (Sect. 9.4)

9.2 Field Equations

For a magneto-electro-thermo-elastic body, the infinitesimal stress tensor \mathbf{T} , the electric displacement (or electric charge density displacement or electric flux density) \mathbf{d} and the magnetic flux \mathbf{b} are expressed as a function of the infinitesimal strain tensor \mathbf{S} , the electric field \mathbf{e} , the magnetic field \mathbf{h} and the temperature increment T , by the following constitutive equations (Bardzokas et al. 2007):

$$\begin{aligned}\mathbf{T} &= \mathbf{C} : \mathbf{S} - \mathbf{E}^{t13} \mathbf{e} - \mathbf{Q}^{t13} \mathbf{h} - \mathbf{B} T \\ \mathbf{d} &= \mathbf{E} : \mathbf{S} + \mathbf{D} \mathbf{e} + \mathbf{A} \mathbf{h} + \mathbf{p} T \\ \mathbf{b} &= \mathbf{Q} : \mathbf{S} + \mathbf{A} \mathbf{e} + \mathbf{M} \mathbf{h} + \mathbf{l} T\end{aligned}\tag{9.2}$$

where \mathbf{C} , \mathbf{E} , \mathbf{Q} and \mathbf{B} are the elastic, piezoelectric, piezomagnetic, thermoelastic tensors, \mathbf{D} , \mathbf{A} , and \mathbf{p} are the dielectric, magnetoelectric, and pyroelectric tensors, \mathbf{M} and \mathbf{l} are the magnetic permeability and pyromagnetic tensors. Although this property

will not be used below, we recall that the thermoelastic tensor \mathbf{B} can be expressed as a function of the tensor of linear thermal expansion Δ as $\mathbf{B} = \mathbf{C} : \Delta$.

The infinitesimal strain tensor \mathbf{S} and the electric and magnetic fields, \mathbf{e} and \mathbf{h} , are evaluated as a function of the displacement field \mathbf{u} and of the electric and magnetic potentials, ϕ and ψ , as

$$\mathbf{S} = \text{sym}(\text{grad } \mathbf{u}) \quad \mathbf{e} = - \text{grad } \phi \quad \mathbf{h} = - \text{grad } \psi \tag{9.3}$$

Finally, the piezo-electro-magneto-thermic fields are governed by the following steady-state equilibrium equations:

$$\text{div} \mathbf{T} = \mathbf{0} \quad \text{div} \mathbf{d} = 0 \quad \text{div} \mathbf{b} = 0 \quad \text{div}(\mathbf{K} \text{ grad } T) = \mathbf{K} : \mathbf{H}(T) = 0 \tag{9.4}$$

where \mathbf{K} is the thermal conductivity tensor and $\mathbf{H}(\cdot)$ is the Hessian of (\cdot) .

We assume that the material is transversely isotropic, with the plane of isotropy parallel to the plane $x - y$ of the reference system and we indicate by h either one of the two direction of isotropy, i.e. x or y , and by v the direction orthogonal to the plane of isotropy, i.e. z . Accordingly, the constitutive tensors are

$$\mathbf{C} = \left[\begin{array}{ccc|ccc|ccc} M_h & 0 & 0 & 0 & G_{hh} & 0 & 0 & 0 & G_{hv} \\ 0 & \lambda_{hh} & 0 & G_{hh} & 0 & 0 & 0 & 0 & 0 \\ 0 & 0 & \lambda_{hv} & 0 & 0 & 0 & G_{hv} & 0 & 0 \\ \hline 0 & G_{hh} & 0 & \lambda_{hh} & 0 & 0 & 0 & 0 & 0 \\ G_{hh} & 0 & 0 & 0 & M_h & 0 & 0 & 0 & G_{hv} \\ 0 & 0 & 0 & 0 & 0 & \lambda_{hv} & 0 & G_{hv} & 0 \\ \hline 0 & 0 & G_{hv} & 0 & 0 & 0 & \lambda_{hv} & 0 & 0 \\ 0 & 0 & 0 & 0 & 0 & G_{hv} & 0 & \lambda_{hv} & 0 \\ G_{hv} & 0 & 0 & 0 & G_{hv} & 0 & 0 & 0 & M_v \end{array} \right] \tag{9.5}$$

$$\mathbb{E} = \left[\begin{array}{ccc} 0 & 0 & N_{hv} \\ 0 & 0 & 0 \\ \hline N_{hv} & 0 & 0 \\ 0 & 0 & 0 \\ 0 & 0 & N_{hv} \\ 0 & N_{hv} & 0 \\ \hline E_{hv} & 0 & 0 \\ 0 & E_{hv} & 0 \\ 0 & 0 & E_v \end{array} \right] \quad \mathbb{Q} = \left[\begin{array}{ccc} 0 & 0 & L_{hv} \\ 0 & 0 & 0 \\ \hline L_{hv} & 0 & 0 \\ 0 & 0 & 0 \\ 0 & 0 & L_{hv} \\ 0 & L_{hv} & 0 \\ \hline Q_{hv} & 0 & 0 \\ 0 & Q_{hv} & 0 \\ 0 & 0 & Q_v \end{array} \right] \tag{9.6}$$

$$\mathbf{B} = \begin{bmatrix} \beta_h & 0 & 0 \\ 0 & \beta_h & 0 \\ 0 & 0 & \beta_v \end{bmatrix} \quad \mathbf{D} = \begin{bmatrix} D_h & 0 & 0 \\ 0 & D_h & 0 \\ 0 & 0 & D_v \end{bmatrix} \quad \mathbf{A} = \begin{bmatrix} \alpha_h & 0 & 0 \\ 0 & \alpha_h & 0 \\ 0 & 0 & \alpha_v \end{bmatrix} \quad \mathbf{M} = \begin{bmatrix} \mu_h & 0 & 0 \\ 0 & \mu_h & 0 \\ 0 & 0 & \mu_v \end{bmatrix} \tag{9.7}$$

$$\mathbf{K} = \begin{bmatrix} k_h & 0 & 0 \\ 0 & k_h & 0 \\ 0 & 0 & k_v \end{bmatrix} \quad \mathbf{p} = \begin{bmatrix} 0 \\ 0 \\ p_v \end{bmatrix} \quad \mathbf{l} = \begin{bmatrix} 0 \\ 0 \\ l_v \end{bmatrix} \quad (9.8)$$

where:

$$G_{hh} = \frac{M_h - \lambda_{hh}}{2} \quad (9.9)$$

Accounting for the symmetry of the constitutive tensors, formulas (9.2) and (9.3) are used into (9.4) to obtain the following homogeneous system of differential equations:

$$\begin{cases} \mathbf{C} : \mathbb{H}(\mathbf{u}) + \mathbb{E}^{t_{13}} : \mathbf{H}(\phi) + \mathbf{Q}^{t_{13}} : \mathbf{H}(\psi) - \mathbf{B} \mathbf{grad} T = \mathbf{0} \\ \mathbb{E} : \mathbb{H}(\mathbf{u}) - \mathbf{D} : \mathbf{H}(\phi) - \mathbf{A} : \mathbf{H}(\psi) + \mathbf{p} \cdot \mathbf{grad} T = 0 \\ \mathbf{Q} : \mathbb{H}(\mathbf{u}) - \mathbf{A} : \mathbf{H}(\phi) - \mathbf{M} : \mathbf{H}(\mathbf{h}) + \mathbf{l} \cdot \mathbf{grad} T = 0 \\ \mathbf{K} : \mathbf{H}(T) = 0 \end{cases} \quad (9.10)$$

where $:$ and 3 respectively denote saturation of the two and three inner indices in the product between tensors. In this respect, notice that $\mathbb{H}(\mathbf{u})$ is a third order tensor representing the Hessian of \mathbf{u} , and is defined as

$$\mathbb{H}(\mathbf{u}) = \begin{bmatrix} \mathbf{H}(u_x) \\ \mathbf{H}(u_y) \\ \mathbf{H}(u_z) \end{bmatrix} \quad (9.11)$$

Introducing the vector $\mathbf{f} = \{u_x, u_y, u_z, \phi, \psi, T\}^t$, the previous system of equations can be rewritten in compact form as

$$\mathcal{L} \mathbf{f} = \mathbf{0} \quad (9.12)$$

where \mathcal{L} is the following differential operator:

$$\mathcal{L} = \begin{Bmatrix} \mathcal{L}_C & \mathcal{L}_E & \mathcal{L}_Q & \mathcal{L}_B \\ \mathcal{L}_E^t & \mathcal{L}_D & \mathcal{L}_A & \mathcal{L}_P \\ \mathcal{L}_Q^t & \mathcal{L}_A & \mathcal{L}_M & \mathcal{L}_L \\ (0 \ 0 \ 0) & 0 & 0 & \mathcal{L}_K \end{Bmatrix} \quad (9.13)$$

with

$$\mathcal{L}_C = \begin{Bmatrix} M_h \partial_x^2 + G_{hh} \partial_y^2 + G_{hv} \partial_z^2 & (\lambda_{hh} + G_{hh}) \partial_x \partial_y & (\lambda_{hv} + G_{hv}) \partial_x \partial_z \\ (\lambda_{hh} + G_{hh}) \partial_x \partial_y & G_{hh} \partial_x^2 + M_h \partial_y^2 + G_{hv} \partial_z^2 & (\lambda_{hv} + G_{hv}) \partial_y \partial_z \\ (\lambda_{hv} + G_{hv}) \partial_x \partial_z & (\lambda_{hv} + G_{hv}) \partial_y \partial_z & G_{hv} \partial_h^2 + M_v \partial_z^2 \end{Bmatrix} \quad (9.14)$$

$$\mathcal{L}_E = \begin{Bmatrix} (N_{hv} + E_{hv})\partial_x\partial_z \\ (N_{hv} + E_{hv})\partial_y\partial_z \\ N_{hv}\partial_h^2 + E_v\partial_z^2 \end{Bmatrix} \quad \mathcal{L}_Q = \begin{Bmatrix} (L_{hv} + Q_{hv})\partial_x\partial_z \\ (L_{hv} + Q_{hv})\partial_y\partial_z \\ L_{hv}\partial_h^2 + Q_v\partial_z^2 \end{Bmatrix} \quad \mathcal{L}_B = \begin{Bmatrix} -\beta_h\partial_x \\ -\beta_h\partial_y \\ -\beta_v\partial_z \end{Bmatrix} \quad (9.15)$$

$$\mathcal{L}_D = -D_h\partial_h^2 - D_v\partial_z^2 \quad \mathcal{L}_A = -\alpha_h\partial_h^2 - \alpha_v\partial_z^2 \quad \mathcal{L}_M = -\mu_h\partial_h^2 - \mu_v\partial_z^2 \quad (9.16)$$

and

$$\mathcal{L}_P = p_v\partial_z \quad \mathcal{L}_L = l_v\partial_z \quad \mathcal{L}_K = k_h\partial_h^2 + k_v\partial_z^2 \quad \partial_h^2 = \partial_x^2 + \partial_y^2 \quad (9.17)$$

Remark 9.1 The elastic parameters in \mathbb{C} , i.e. see Formula (9.5), can be expressed as a function of the Young moduli, Y_h and Y_v , and Poisson's ratios, ν_{hh} and ν_{hv} , in the plane of isotropy and along the perpendicular direction, respectively:

$$M_h = \frac{Y_h(Y_h\nu_{hv}^2 - Y_v)}{(1 + \nu_{hh})[Y_v(\nu_{hh} - 1) + 2Y_h\nu_{hv}^2]} \quad M_v = \frac{Y_v^2(\nu_{hh} - 1)}{Y_v(\nu_{hh} - 1) + 2Y_h\nu_{hv}^2}$$

$$\lambda_{hh} = -\frac{Y_h(Y_v\nu_{hh} + Y_h\nu_{hv}^2)}{(1 + \nu_{hh})[Y_v(\nu_{hh} - 1) + 2Y_h\nu_{hv}^2]} \quad \lambda_{hv} = \frac{Y_h Y_v \nu_{hv}}{Y_v - Y_v\nu_{hh} - 2Y_h\nu_{hv}^2}$$

□

Remark 9.2 The constitutive equations (9.2) can be rewritten in Voigt notation to express the stress and strain tensors as six-component vectors, i.e.

$$\mathbf{T} \rightarrow \mathbf{t} = [\sigma_x, \sigma_y, \sigma_z, \tau_{yz}, \tau_{zx}, \tau_{xy}]^t \quad \mathbf{S} \rightarrow \mathbf{s} = [\varepsilon_x, \varepsilon_y, \varepsilon_z, \gamma_{yz}, \gamma_{zx}, \gamma_{xy}]^t$$

Accordingly, Eq. (9.2) become

$$\mathbf{t} = \mathbf{C}\mathbf{s} - \mathbf{E}^t\mathbf{e} - \mathbf{Q}^t\mathbf{h} - \beta T \quad \mathbf{d} = \mathbf{E}\mathbf{s} + \mathbf{D}\mathbf{e} + \mathbf{A}\mathbf{h} + \mathbf{p}T \quad \mathbf{b} = \mathbf{Q}\mathbf{s} + \mathbf{a}\mathbf{e} + \mathbf{M}\mathbf{h} + \mathbf{1}T$$

where

$$\mathbf{C} = \begin{bmatrix} M_h & \lambda_{hh} & \lambda_{hv} & 0 & 0 & 0 \\ \lambda_{hh} & M_h & \lambda_{hv} & 0 & 0 & 0 \\ \lambda_{hv} & \lambda_{hv} & M_v & 0 & 0 & 0 \\ 0 & 0 & 0 & G_{hv} & 0 & 0 \\ 0 & 0 & 0 & 0 & G_{hv} & 0 \\ 0 & 0 & 0 & 0 & 0 & G_{hh} \end{bmatrix} \quad \mathbf{E} = \begin{bmatrix} 0 & 0 & 0 & 0 & N_{hv} & 0 \\ 0 & 0 & 0 & N_{hv} & 0 & 0 \\ E_{hv} & E_{hv} & E_v & 0 & 0 & 0 \end{bmatrix} \quad \beta = \begin{bmatrix} \beta_h \\ \beta_h \\ \beta_v \\ 0 \\ 0 \\ 0 \end{bmatrix}$$

$$\mathbf{Q} = \begin{bmatrix} 0 & 0 & 0 & 0 & L_{hv} & 0 \\ 0 & 0 & 0 & L_{hv} & 0 & 0 \\ Q_{hv} & Q_{hv} & Q_v & 0 & 0 & 0 \end{bmatrix}$$

□

9.3 A General Solution to the Field Equations in Terms of Quasi-Harmonic Potentials

In this section the differential equation (9.12) is expressed in a simpler form that involves the introduction of quasi-harmonic potentials. To this end, the differential operator \mathcal{L} is inverted by employing its adjoint operator \mathcal{L}^* so as to uncouple the equations in (9.12). The new set of uncoupled differential equations is expressed by a scalar differential operator $|\mathcal{L}|$, representing the determinant of \mathcal{L} .

Factorization of the differential operators is used to show that the solution can be expressed as the sum of six quasi-harmonic functions and that the Almansi theorem can be used to further simplify the differential problem.

These steps are described in detail in the following subsections.

9.3.1 Inversion of the Differential Operator \mathcal{L}

The determinant $|\mathcal{L}|$ of \mathcal{L} can be evaluated by employing its Laplace expansion as a function of the entries of the k th row. Indicating by \mathcal{L}^* the adjoint matrix of \mathcal{L} , we have

$$|\mathcal{L}| = \mathcal{L}_{\bar{k}j} \mathcal{L}_{j\bar{k}}^* \quad (9.18)$$

where index notation has been adopted. Notice that, although the index k is repeated in the previous formula, no summation is executed over k since it is a fixed index; to remind this we adopted a bar above the index letter. Accordingly $\mathcal{L}_{\bar{k}j}$ and $\mathcal{L}_{j\bar{k}}^*$ are the j th components of the vectors $\mathcal{L}_{\bar{k}(\cdot)}$ and $\mathcal{L}_{(\cdot)\bar{k}}^*$, i.e. the k th row and column of \mathcal{L} and \mathcal{L}^* , respectively. Similarly, it is easy to verify that

$$\mathcal{L}_{\bar{l}j} \mathcal{L}_{j\bar{k}}^* = 0 \quad \text{for } l \neq k \quad (9.19)$$

since this is the determinant of a matrix in which the l th row repeats twice. Combining Formulas (9.18) and (9.19) for all values of k and l , one obtains the well known property of the adjoint matrix

$$\mathcal{L} \mathcal{L}^* = \mathbf{I} |\mathcal{L}| \quad (9.20)$$

where \mathbf{I} is the identity matrix.

Let us now indicate by φ_k a scalar function that fulfils the condition

$$|\mathcal{L}| \varphi_k = 0 \quad (9.21)$$

This function is used to express a solution to Eq. (9.12) as

$$\mathbf{f}^{(\bar{k})} = \mathcal{L}_{(\cdot)\bar{k}}^* \varphi_{\bar{k}} \quad (9.22)$$

Actually, substituting (9.22) into (9.12), we have

$$\mathcal{L} \mathbf{f}^{(\bar{k})} = \mathcal{L} \mathcal{L}_{(\cdot)\bar{k}}^* \varphi_{\bar{k}} = \mathbf{0} \quad (9.23)$$

in which (9.18), (9.19) and (9.21) have been used.

Clearly, solution (9.22) is not unique, since a different solution can be generated by changing the value of k . Furthermore, it is easy to verify that any linear combination of the solutions obtained by choosing all values of k is also a solution to Eq. (9.12). Actually, we can set

$$\mathbf{f} = \sum_{\bar{k}} c^{(\bar{k})} \mathbf{f}^{(\bar{k})} = \sum_{\bar{k}} \mathcal{L}_{(\cdot)\bar{k}}^* c^{(\bar{k})} \varphi_{\bar{k}} = \mathcal{L}^* \boldsymbol{\varphi} \quad (9.24)$$

where $c^{(\bar{k})}$ are numerical coefficients and $\boldsymbol{\varphi}$ is the vector collecting the functions $c^{(\bar{k})} \varphi_{\bar{k}}$. It fulfils the condition

$$|\mathcal{L}| \boldsymbol{\varphi} = \mathbf{0} \quad (9.25)$$

since all components of $\boldsymbol{\varphi}$ satisfy Eq. (9.21). Hence, substituting (9.24) into (9.12) we have

$$\mathcal{L} \mathbf{f} = \mathcal{L} \mathcal{L}^* \boldsymbol{\varphi} = \mathbf{I} |\mathcal{L}| \boldsymbol{\varphi} = \mathbf{0} \quad (9.26)$$

in which the property (9.20) and (9.25) have been adopted.

Notice that, having expressed the solution of (9.12) by means of (9.24), the problem of computing \mathbf{f} has been transformed into the problem of evaluating the vector function $\boldsymbol{\varphi}$ by solving (9.25). Although the number of unknowns is unchanged, the differential form (9.25) is advantageous since it is expressed by a scalar differential operator.

The evaluation of the adjoint matrix \mathcal{L}^* and of the determinant $|\mathcal{L}|$ is a key aspect of the presented solution strategy. A Mathematica script for their evaluation is reported in Sect. 9.4.

9.3.2 Factorization of the Differential Equation $|\mathcal{L}| \boldsymbol{\varphi} = \mathbf{0}$

The differential operator $|\mathcal{L}|$ is computed as the determinant of \mathcal{L} , yielding

$$|\mathcal{L}| = \mathcal{L}_K \mathcal{L}_G (p_1 \partial_h^8 + p_2 \partial_h^6 \partial_z^2 + p_3 \partial_h^4 \partial_z^4 + p_4 \partial_h^2 \partial_z^6 + p_5 \partial_z^8) \quad (9.27)$$

where \mathcal{L}_K is defined in (9.17)₃, $\mathcal{L}_G = G_{hh} \partial_h^2 + G_{hv} \partial_z^2$, while p_1, \dots, p_5 are scalar parameters computed as a function of the constitutive parameters (9.5)–(9.9), see, e.g. Sect. 9.4.1.

Equation (9.27) is substituted into (9.24) and the resulting equation is factorized to obtain the equivalent equation

$$|\mathcal{L}|\varphi = \mathbf{0} \Leftrightarrow \mathcal{D}_1 \mathcal{D}_2 \mathcal{D}_3 \mathcal{D}_4 \mathcal{D}_5 \mathcal{D}_6 \varphi = \prod_{i=1}^6 \mathcal{D}_i \varphi = \mathbf{0} \quad (9.28)$$

in which the entire set of equations has been expressed by means of the six differential operators

$$\mathcal{D}_i = \partial_h^2 + \partial_{z_i}^2 = \partial_h^2 + s_i^2 \partial_z^2 \quad i = 1, \dots, 6 \quad (9.29)$$

where $z_i = z/s_i$ and the parameters $s_i, i = 1, \dots, 6$ are the roots of the characteristic polynomial equation

$$\left(s^2 - \frac{G_{hv}}{G_{hh}}\right) \left(s^2 - \frac{k_v}{k_h}\right) (p_1 s^8 - p_2 s^6 + p_3 s^4 - p_4 s^2 + p_5) = 0 \quad (9.30)$$

The procedure for obtaining (9.28)₂ is detailed below. However, written in this form, the set of differential equations can be solved by employing the generalized Almansi's theorem (Almansi 1899; Wang and Xu 1990). Accordingly, the vector function φ can be expressed by means of up to six vector functions Ψ_i as

$$\varphi = \sum_{i=1}^{n_r} \sum_{j=1}^{m_i} z^{m_i-j} \varphi_i \quad (9.31)$$

where n_r is the number of distinct roots of (9.30) and m_i is the multiplicity of the i th root. The potential functions Ψ_i are quasi-harmonic since they are required to fulfil the conditions

$$\mathcal{D}_i \varphi_i = \mathbf{0} \quad i = 1, \dots, n_r \quad (9.32)$$

In order to obtain the factorization of Eq. (9.24), one first divides it by k_v and G_{hv} , respectively. This operation gives the first two operators \mathcal{D}_1 and \mathcal{D}_2 as equivalent to \mathcal{L}_K and \mathcal{L}_G when the roots of the first two factors of (9.30) are employed. The remaining operators $\mathcal{D}_i, i = 2, \dots, 5$, are obtained in a similar way by factorizing the eighth degree differential operator in (9.27) as

$$\begin{aligned} & p_1 \partial_h^8 + p_2 \partial_h^6 \partial_z^2 + p_3 \partial_h^4 \partial_z^4 + p_4 \partial_h^2 \partial_z^6 + p_5 \partial_z^8 \\ & = p_1 (\partial_h^2 + s_a^2 \partial_z^2) (\partial_h^2 + s_b^2 \partial_z^2) (\partial_h^2 + s_c^2 \partial_z^2) (\partial_h^2 + s_d^2 \partial_z^2) \end{aligned} \quad (9.33)$$

in which s_a, s_b, s_c and s_d are the roots of the third factor in equation (9.30).

Formula (9.33) can be verified by expanding the product on the right-hand side, obtaining:

$$\begin{aligned} & p_1 \partial_h^8 + p_1 (s_a^2 + s_b^2 + s_c^2 + s_d^2) \partial_h^6 \partial_z^2 + p_1 (s_a^2 s_b^2 + s_a^2 s_c^2 + s_b^2 s_c^2 + s_a^2 s_d^2 + s_b^2 s_d^2 \\ & + s_c^2 s_d^2) \partial_h^4 \partial_z^4 + p_1 (s_a^2 s_b^2 s_c^2 + s_a^2 s_b^2 s_d^2 + s_a^2 s_c^2 s_d^2 + s_b^2 s_c^2 s_d^2) \partial_h^2 \partial_z^6 + p_1 s_a^2 s_b^2 s_c^2 s_d^2 \partial_z^8 \end{aligned} \quad (9.34)$$

Comparing the previous expression with the left-hand side of equation (9.33), we obtain the following system of equations:

$$\begin{cases} p_1 (s_a^2 + s_b^2 + s_c^2 + s_d^2) - p_2 = 0 \\ p_1 (s_a^2 s_b^2 + s_a^2 s_c^2 + s_b^2 s_c^2 + s_a^2 s_d^2 + s_b^2 s_d^2 + s_c^2 s_d^2) - p_3 = 0 \\ p_1 (s_a^2 s_b^2 s_c^2 + s_a^2 s_b^2 s_d^2 + s_a^2 s_c^2 s_d^2 + s_b^2 s_c^2 s_d^2) - p_4 = 0 \\ p_1 s_a^2 s_b^2 s_c^2 s_d^2 - p_5 = 0 \end{cases} \quad (9.35)$$

which needs to be solved to obtain s_a , s_b , s_c and s_d . Hereafter we are going to solve (9.35) so as to derive a condition that s_a has to fulfil in order to be used in the factorization (9.33). The same procedure can be followed for s_b , s_c and s_d .

With the objective of isolating all terms containing s_a , we can rewrite (9.35)₃ as

$$p_1 s_b^2 s_c^2 s_d^2 = -p_1 (s_a^2 s_b^2 s_c^2 + s_a^2 s_b^2 s_d^2 + s_a^2 s_c^2 s_d^2) + p_4 \quad (9.36)$$

which can be substituted in (9.35)₄ to obtain

$$[-p_1 (s_a^2 s_b^2 s_c^2 + s_a^2 s_b^2 s_d^2 + s_a^2 s_c^2 s_d^2) + p_4] s_a^2 - p_5 = 0 \quad (9.37)$$

that is

$$-p_1 (s_b^2 s_c^2 + s_b^2 s_d^2 + s_c^2 s_d^2) s_a^4 + p_4 s_a^2 - p_5 = 0 \quad (9.38)$$

Similarly, isolating all terms containing s_a in (9.35)₂, we have

$$p_1 (s_b^2 s_c^2 + s_b^2 s_d^2 + s_c^2 s_d^2) = -p_1 (s_a^2 s_b^2 + s_a^2 s_c^2 + s_a^2 s_d^2) + p_3 \quad (9.39)$$

Substituting the previous formula into (9.37)₂ we obtain

$$-[-p_1 (s_a^2 s_b^2 + s_a^2 s_c^2 + s_a^2 s_d^2) + p_3] s_a^4 + p_4 s_a^2 - p_5 = 0 \quad (9.40)$$

which gives

$$p_1 (s_b^2 + s_c^2 + s_d^2) s_a^6 - p_3 s_a^4 + p_4 s_a^2 - p_5 = 0 \quad (9.41)$$

Finally, from (9.35)₁ we have

$$p_1 (s_b^2 + s_c^2 + s_d^2) = -p_1 s_a^2 + p_2 \quad (9.42)$$

which is used in (9.40)₂ to get

$$(-p_1 s_a^2 + p_2) s_a^6 - p_3 s_a^4 + p_4 s_a^2 - p_5 = 0 \quad (9.43)$$

that is

$$p_1 s_a^8 - p_2 s_a^6 + p_3 s_a^4 - p_4 s_a^2 + p_5 = 0 \quad (9.44)$$

The previous equation represents the condition that s_d has to fulfil in order to be used in (9.33); it is equivalent to (9.30). Similarly one can verify that the same condition has to be fulfilled by s_b , s_c , and s_d . In conclusion, all the parameters $s_{(i)}$ used in the polynomial factorization (9.33) are the roots of the polynomial (9.30).

9.4 Automatic Evaluation of $|\mathcal{L}|$ and \mathcal{L}^* and Relevant Coefficients

Although the evaluation of $|\mathcal{L}|$ and \mathcal{L}^* is not conceptually difficult, a series of manipulations are required due to the great amount of constitutive parameters which are involved. Furthermore, the resulting expressions are rather long and difficult to be transcribed in a computer code for numerical applications; for their generation we furnish below two Mathematica scripts so that the interested reader can convert the desired expressions into C and Fortran codes by employing the functions **CForm** and **FortranForm** available in Mathematica.

9.4.1 Evaluation of $|\mathcal{L}|$

For the evaluation of $|\mathcal{L}|$, the differential operator \mathcal{L} is first input

```
L={ {Mh*x^2+Ghh*y^2+Ghv*z^2, (1hh+Ghh)*x*y, (1hv+Ghv)*x*z,
      (Nhv+Ehv)*x*z, (Lhv+Qhv)*x*z, -bh*x },
      { (1hh+Ghh)*x*y, Ghh*x^2+Mh*y^2+Ghv*z^2, (1hv+Ghv)*y*z,
      (Nhv+Ehv)*y*z, (Lhv+Qhv)*y*z, -bh*y },
      { (1hv+Ghv)*x*z, (1hv+Ghv)*y*z, Ghv*h^2+Mv*z^2,
      Nhv*h^2+Ev*z^2, Lhv*h^2+Qv*z^2, -bv*z },
      { (Nhv+Ehv)*x*z, (Nhv+Ehv)*y*z, Nhv*h^2+Ev*z^2, -Dh*h^2-Dv*z^2,
      -ah*h^2-av*z^2, pv*z },
      { (Lhv+Qhv)*x*z, (Lhv+Qhv)*y*z, Lhv*h^2+Qv*z^2, -ah*h^2-av*z^2,
      -mh*h^2-mv*z^2, 1v*z },
      { 0, 0, 0, 0, 0, kh*h^2+kv*z^2 } };
lhh=Mh-2*Ghh;
Print [ ' 'L= ' ',L// MatrixForm ]
```

where the differential operators ∂_x , ∂_y , ∂_z and ∂_h^2 are treated as algebraic quantities denoted by x , y , z , and h^2 , respectively. Also, within the previous code, Formula (9.9) has been used to reduce the number of constitutive parameters in \mathcal{L} .

The determinant of \mathcal{L} is then computed and Formula (9.17)₄ is used to simplify its expression

```
DetL=Det [ L ];
DetL= Simplify [ Collect [ DetL, { h^2, z^2, x^2+y^2 }, Simplify ] /.
      (x^2+y^2)->h^2];
Print [ ' ' |L|= ' ', DetL ]
```


Such a code generates an expression of $|\mathcal{L}|$ which is difficult to be handled. However, displaying the list of factors of $|\mathcal{L}|$ one can verify that the last factor is a long combination of constitutive parameters and differential operators, i.e. ∂_h^2 and ∂_z^2 . This is done by the code

```
FactorOfDetL=Simplify [ FactorList [ DetL ] ];
Print [ ' ' Factors of |L|= ' ', FactorOfDetL // TableForm ]
```

In order to simplify the expression of $|\mathcal{L}|$, the coefficients of ∂_h^2 and ∂_z^2 are isolated and substituted by a series of factors p_i , expressed as a combination of constitutive coefficients. This task is accomplished by the function **FactorDet** defined by the following code:

```
FactorDet [ det_ , np_ , pi_ , pa_ ] := (
  FactOfDet=Simplify [ FactorList [ det ] ];
  NFactOfDet=Dimensions [ FactOfDet ] [[1]];
  MyFactOfDet=FactOfDet [[1,1]]^FactOfDet [[1,2]]*
    FactOfDet [[NFactOfDet,1]]^FactOfDet [[NFactOfDet,2]];
  Ai=CoefficientList [ MyFactOfDet , { h^2 , z^2 } ];
  NewMyFactOfDet=0;
  nps=np+1;
  npi=np;
  pii=pi;
  Do [ { If [ Not [ TrueQ [ Simplify [ Ai [[ i , j ] ] ] == 0 ] ] ,
    { npi=npi+1 ,
      pii [[ npi ] ] = Simplify [ Ai [[ i , j ] ] ] ,
      iq=npi ,
      Do [ If [ Simplify [ pii [[ npi ] ] - pii [[ nqi ] ] ] == 0 ,
        { iq=nqi ,
          pii [[ npi ] ] = 0 ,
          npi=npi-1 ,
          Break [ ]
        }
      ] ,
      { nqi , npi - 1 }
    ] ,
    NewMyFactOfDet=NewMyFactOfDet+
      pa [[ iq ] ] * h^(2*(i-1)) * z^(2*(j-1))
  ]
  ] ,
  { j , Dimensions [ Ai ] [[2]] } ,
  { i , Dimensions [ Ai ] [[1]] }
];
NewDet=NewMyFactOfDet;
Do [ NewDet=NewDet*FactOfDet [[ i , 1 ] ] ^ FactOfDet [[ i , 2 ] ] ,
  { i , 2 , NFactOfDet - 1 } ];
Print [ NewDet ];
Print [ ' ' where : ' ' ];
If [ nps <= npi , Do [ Print [ ' ' p [ ' ' , i , ' ' ] = ' ' , pii [[ i ] ] ] , { i , nps , npi } ];
Return [ { { NewDet } , { pii } , { npi } } ];
);
```

The function **FactorDet** outputs an array containing the input variable det , that is \mathcal{L} , and the coefficients p_i used therein.

The function is conceived in such a way that the list of coefficients is updated, without repetitions, each time the function is called. Thus, at the first call of the function, the number of coefficient, the array of coefficients and the array of their names needs to be initialized.

```
np=0;
pi=Array[0&,1000];
pa=Array[p,1000];
```

Hence the simplified expression of $|\mathcal{L}|$ can be obtained by typing:

```
Print['' Determinant of L: ''];
FDetL=FactorDet[DetL,np,pi,pa];
DetL=FDetL[[1,1]];
pi=FDetL[[2,1]];
np=FDetL[[3,1]];
```

Finally, the expression (9.27) of $|\mathcal{L}|$ is output, together with the following coefficients

$$\begin{aligned}
p_1 &= M_h [D_h (L_{hv}^2 + G_{hv} \mu_h) - \alpha_h^2 G_{hv} - 2\alpha_h L_{hv} N_{hv} + \mu_h N_{hv}^2] \\
p_2 &= -2D_h \lambda_{hv} L_{hv}^2 - 2D_h G_{hv} \lambda_{hv} \mu_h - D_h \lambda_{hv}^2 \mu_h + E_{hv}^2 (L_{hv}^2 + G_{hv} \mu_h) \\
&\quad + D_v L_{hv}^2 M_h + D_v G_{hv} \mu_h M_h + D_h G_{hv} M_h \mu_v + D_h \mu_h M_h M_v + \alpha_h^2 (2G_{hv} \lambda_{hv} \\
&\quad + \lambda_{hv}^2 - M_h M_v) - 2\alpha_v L_{hv} M_h N_{hv} + 2E_v \mu_h M_h N_{hv} - 2\lambda_{hv} \mu_h N_{hv}^2 \\
&\quad + M_h \mu_v N_{hv}^2 - 2D_h \lambda_{hv} L_{hv} Q_{hv} + D_h G_{hv} Q_{hv}^2 + N_{hv}^2 Q_{hv}^2 - 2E_{hv} N_{hv} (\lambda_{hv} \mu_h \\
&\quad + L_{hv} Q_{hv}) + 2D_h L_{hv} M_h Q_v + 2\alpha_h (E_{hv} \lambda_{hv} L_{hv} - \alpha_v G_{hv} M_h - E_v L_{hv} M_h \\
&\quad + 2\lambda_{hv} L_{hv} N_{hv} - E_{hv} G_{hv} Q_{hv} + \lambda_{hv} N_{hv} Q_{hv} - M_h N_{hv} Q_v) \\
p_3 &= -2E_{hv} E_v L_{hv}^2 - 2D_v \lambda_{hv} L_{hv}^2 - 2E_{hv} E_v G_{hv} \mu_h - 2E_{hv} E_v \lambda_{hv} \mu_h \\
&\quad - 2D_v G_{hv} \lambda_{hv} \mu_h - D_v \lambda_{hv}^2 \mu_h - \alpha_v^2 G_{hv} M_h + E_v^2 \mu_h M_h + E_{hv}^2 G_{hv} \mu_v \\
&\quad - 2D_h G_{hv} \lambda_{hv} \mu_v - D_h \lambda_{hv}^2 \mu_v + D_v G_{hv} M_h \mu_v - \alpha_h^2 G_{hv} M_v + D_h L_{hv}^2 M_v \\
&\quad + E_{hv}^2 \mu_h M_v + D_h G_{hv} \mu_h M_v + D_v \mu_h M_h M_v + D_h M_h \mu_v M_v - 2E_v \lambda_{hv} \mu_h N_{hv} \\
&\quad - 2E_{hv} \lambda_{hv} \mu_v N_{hv} + 2E_v M_h \mu_v N_{hv} + 2E_{hv} \mu_h M_v N_{hv} - 2\lambda_{hv} \mu_v N_{hv}^2 \\
&\quad + \mu_h M_v N_{hv}^2 - 2E_{hv} E_v L_{hv} Q_{hv} - 2D_v \lambda_{hv} L_{hv} Q_{hv} + 2D_h L_{hv} M_v Q_{hv} \\
&\quad + 2E_v L_{hv} N_{hv} Q_{hv} + D_v G_{hv} Q_{hv}^2 + D_h M_v Q_{hv}^2 + 2E_v N_{hv} Q_{hv}^2 + 2E_{hv}^2 L_{hv} Q_v \\
&\quad - 2D_h \lambda_{hv} L_{hv} Q_v + 2D_v L_{hv} M_h Q_v + 2E_{hv} L_{hv} N_{hv} Q_v - 2D_h G_{hv} Q_{hv} Q_v \\
&\quad - 2D_h \lambda_{hv} Q_{hv} Q_v - 2E_{hv} N_{hv} Q_{hv} Q_v - 2N_{hv}^2 Q_{hv} Q_v + D_h M_h Q_v^2 \\
&\quad + 2\alpha_v (E_{hv} \lambda_{hv} L_{hv} - E_v L_{hv} M_h + 2\lambda_{hv} L_{hv} N_{hv} - E_{hv} G_{hv} Q_{hv} + \lambda_{hv} N_{hv} Q_{hv} \\
&\quad - M_h N_{hv} Q_v) + 2\alpha_h \{ \alpha_v (2G_{hv} \lambda_{hv} + \lambda_{hv}^2 - M_h M_v) - E_{hv} L_{hv} M_v \\
&\quad - L_{hv} M_v N_{hv} - E_{hv} M_v Q_{hv} - M_v N_{hv} Q_{hv} + E_{hv} G_{hv} Q_v + E_{hv} \lambda_{hv} Q_v \\
&\quad + \lambda_{hv} N_{hv} Q_v + E_v [G_{hv} Q_{hv} + \lambda_{hv} (L_{hv} + Q_{hv}) - M_h Q_v] \}
\end{aligned}$$

$$\begin{aligned}
p_4 = & -2D_v G_{hv} \lambda_{hv} \mu_v - D_v \lambda_{hv}^2 \mu_v + D_v L_{hv}^2 M_v \\
& + D_v G_{hv} \mu_h M_v + E_{hv}^2 \mu_v M_v + D_h G_{hv} \mu_v M_v + D_v M_h \mu_v M_v + \alpha_v^2 (2G_{hv} \lambda_{hv} \\
& + \lambda_{hv}^2 - M_h M_v) + 2E_{hv} \mu_v M_v N_{hv} + \mu_v M_v N_{hv}^2 + 2D_v L_{hv} M_v Q_{hv} \\
& + D_v M_v Q_{hv}^2 - 2D_v \lambda_{hv} L_{hv} Q_v - 2D_v G_{hv} Q_{hv} Q_v - 2D_v \lambda_{hv} Q_{hv} Q_v \\
& + E_v^2 (L_{hv}^2 + G_{hv} \mu_h + M_h \mu_v + 2L_{hv} Q_{hv} + Q_{hv}^2) \\
& + E_{hv}^2 Q_v^2 + D_h G_{hv} Q_v^2 + D_v M_h Q_v^2 + 2E_{hv} N_{hv} Q_v^2 + N_{hv}^2 Q_v^2 \\
& + 2\alpha_v \{ E_{hv} G_{hv} Q_v - \alpha_h G_{hv} M_v - E_{hv} L_{hv} M_v - L_{hv} M_v N_{hv} - E_{hv} M_v Q_{hv} \\
& - M_v N_{hv} Q_{hv} + E_{hv} \lambda_{hv} Q_v + \lambda_{hv} N_{hv} Q_v \\
& + E_v [G_{hv} Q_{hv} + \lambda_{hv} (L_{hv} + Q_{hv}) \\
& - M_h Q_v] \} - 2E_v \{ \lambda_{hv} \mu_v N_{hv} + \alpha_h G_{hv} Q_v \\
& + L_{hv} N_{hv} Q_v + N_{hv} Q_{hv} Q_v + E_{hv} [G_{hv} \mu_v + \lambda_{hv} \mu_v \\
& + (L_{hv} + Q_{hv}) Q_v] \} \\
p_5 = & G_{hv} [E_v^2 \mu_v - \alpha_v^2 M_v - 2\alpha_v E_v Q_v + D_v (\mu_v M_v + Q_v^2)]
\end{aligned}$$

9.4.2 Evaluation of \mathcal{L}^*

For the evaluation of the \mathcal{L}^* , the *Combinatorica* package needs to be loaded

```
Needs [ 'Combinatorica' ]
```

so that the cofactor matrix of \mathcal{L} can be computed by the **Cofactor** function and simplified by adopting Formula (9.17)₄.

```
CofL=Table [ Simplify [ Cofactor [ L, { i, j } ], { i, 6 }, { j, 6 } ];
Do [ CofL [ [ i, j ] ] = Simplify [ Collect [ CofL [ [ i, j ] ], { h^2, z^2, x^2+y^2 },
Simplify ] /. ( x^2+y^2 ) -> h^2 ],
{ i, 1, Dimensions [ CofL ] [ [ 1 ] ] },
{ j, 1, Dimensions [ CofL ] [ [ 2 ] ] }
];
AdjL=Transpose [ CofL ];
Print [ 'L*=' , AdjL // MatrixForm ]
```

Likewise $|\mathcal{L}|$, each term of \mathcal{L}^* appears as the product of a set of factors whose last term is characterized by having a very long expression. In order to simplify the final expression of \mathcal{L}^* we employ a procedure, called **FactorAdj**, similar to the one adopted for $|\mathcal{L}|$.

```
FactorAdj [ adj_ , np_ , pi_ , pa_ ] := (
NewAdj=Array [ 0 & , Dimensions [ adj ] ];
nps=np+1;
npi=np;
pii=pi;
Do [ { If [ Not [ TrueQ [ Simplify [ adj [ [ r, s ] ] ] ] ] ] = 0 } ],
```

```

{ FactOfAdj=Simplify [ FactorList [ adj [[ r , s ] ] ] ];
Print [ ' ' Factors of component [ ' ', r , ' ' , ' ' , s , ' ' ] : ' ' ];
Print [ FactOfAdj // TableForm ];
NFactOfAdj=Dimensions [ FactOfAdj ];
LastFactOfAdj=FactOfAdj [[ 1 , 1 ] ] ^ FactOfAdj [[ 1 , 2 ] ] *
      FactOfAdj [[ NFactOfAdj [[ 1 ] ] , 1 ] ] ^
      FactOfAdj [[ NFactOfAdj [[ 1 ] ] , 2 ] ];
Ai=CoefficientList [ LastFactOfAdj , { x , y , h^2 , z^2 } ];
NewLastFactOfAdj=0;
Do [ { If [ Not [ TrueQ [ Simplify [ Ai [[ i , j , k , 1 ] ] ] ] == 0 ] ] ,
      { npi=npi+1 ,
        pii [[ npi ] ] = Simplify [ Ai [[ i , j , k , 1 ] ] ] ,
        iq=npi ,
        Do [ If [ Simplify [ pii [[ npi ] ] - pii [[ nqi ] ] ] == 0 ,
              { iq=nqi ,
                pii [[ npi ] ] = 0 ,
                npi=npi-1 ,
                Break [ ]
              }
            ] ,
        { nqi , 1 , npi-1 }
      ] ,
      NewLastFactOfAdj=NewLastFactOfAdj+pa [[ iq ] ] *
      x^(i-1)*y^(j-1)*
      z^(2*(k-1))*h^(2*(1-1))
    }
  ] ,
  { 1 , 1 , Dimensions [ Ai ] [[ 4 ] ] } ,
  { k , 1 , Dimensions [ Ai ] [[ 3 ] ] } ,
  { j , 1 , Dimensions [ Ai ] [[ 2 ] ] } ,
  { i , 1 , Dimensions [ Ai ] [[ 1 ] ] }
];
NewAdj [[ r , s ] ] = NewLastFactOfAdj ;
Do [ NewAdj [[ r , s ] ] = NewAdj [[ r , s ] ] * FactOfAdj [[ i , 1 ] ] ^
      FactOfAdj [[ i , 2 ] ] ,
      { i , 2 , NFactOfAdj [[ 1 ] ] - 1 } ];
Print [ ' ' Component [ ' ', r , ' ' , ' ' , s , ' ' ] : ' ' , NewAdj [[ r , s ] ] ];
}
]
} ,
{ s , 1 , Dimensions [ adj ] [[ 2 ] ] } ,
{ r , 1 , Dimensions [ adj ] [[ 1 ] ] }
];
Print [ ' ' where : ' ' ];
If [ nps <= npi , Do [ Print [ ' ' p [ ' ' , i , ' ' ] = ' ' , pii [[ i ] ] ] , { i , nps , npi } ] ];
Return [ { { NewAdj } , { pii } , { npi } } ];
);

```

Thus, since the vector of coefficients p_i is updated up to p_5 , the simplified expression of \mathcal{L}^* is obtained by typing:

```
Print [''djoint matrix of L:'']
FAdjL=FactorAdj [AdjL , np , pi , pa ];
AdjL=FAdjL [[ 1 , 1]];
pi=FAdjL [[ 2 , 1]];
np=FAdjL [[ 3 , 1]];
```

which returns the terms of \mathcal{L}^* the additional coefficients. Their expressions are not reported here for brevity.

9.5 Conclusion

The behaviour of magneto-electro-thermo-elastic materials is governed by a set of differential equations, e.g. see Formula (9.10). The relevant differential operator \mathcal{L} is expressed as a 6×6 matrix of scalar operators as in Formulas (9.12)–(9.17). This system of equations can be simplified by uncoupling the equations and expressing the solution as the sum of up to six quasi-harmonic functions as in Formula (9.31). Actually, these functions are required to fulfil a series of modified Laplace equations, see, e.g. Eq. (9.32), in which the differential operator \mathcal{D}_i is expressed by (9.29) as a function of the roots of the characteristic polynomial (9.30) associated with the original set of governing equations. Due to the large number of constitutive parameters involved in this procedure, we have provided a Mathematica script that computes the coefficients of the characteristic polynomial associated with the magneto-electro-thermo-elastic coupling and the components of the adjoint differential operator employed to express the final solution. Forthcoming papers will be devoted to show how the presented general and complete solution can be specialized to existing solutions taken from the literature. Actually, depending on the existence of distinct, partially, or fully coincident roots of the characteristic polynomial equation, specific solutions already presented in the literature (Wang and Shen 2002; Ding and Jiang 2003; Chen et al. 2004) can be obtained as special cases of the general solution derived in the paper. Interesting extensions of the proposed solution include the effects of higher displacement gradients (Pideri and Seppecher 1997; Camar-Eddine and Seppecher 2001; Alibert et al. 2003; Franciosi et al. 2019) and/or micropolar elasticity (Eremeyev et al. 2012; Abd-alla et al. 2017) with applications to pantographic microstructured materials (Barchiesi et al. 2018; Dell’Isola et al. 2019a, b; De Angelo et al. 2019; Andreaus et al. 2018).

References

- AenN A, Alshaikh F, Del Vescovo D, Spagnuolo M (2017) Plane waves and eigenfrequency study in a transversely isotropic magneto-thermoelastic medium under the effect of a constant angular velocity. *J Thermal Stresses* 40(9):1079–1092
- Alibert JJ, Seppecher P, Dell’Isola F (2003) Truss modular beams with deformation energy depending on higher displacement gradients. *Math Mech Solids* 8(1):51–73

- Almansi E (1899) Sull'integrazione dell'equazione differenziale $\delta 2n = 0$. *Annali di Matematica Pura ed Applicata* (1898–1922) 2(1):1–51
- Andreas U, Spagnuolo M, Lekszycki T, Eugster SR (2018) A Ritz approach for the static analysis of planar pantographic structures modeled with nonlinear euler-bernoulli beams. *Continuum Mech Thermodyn* 30(5):1103–1123
- Ashida F, Noda N, Okumura I (1993) General solution technique for transient thermoelasticity of transversely isotropic solids in cylindrical coordinates. *Acta mechanica* 101(1):215–230
- Barchiesi E, Dell'Isola F, Laudato M, Placidi L, Seppecher P (2018) A 1d continuum model for beams with pantographic microstructure: asymptotic micro-macro identification and numerical results. In: *Advances in mechanics of microstructured media and structures*. Springer, pp 43–74
- Bardzokas DI, Filshitsky ML, Filshitsky LA (2007) *Mathematical methods in electro-magneto-elasticity*, vol 32. Springer Science & Business Media
- Camar-Eddine M, Seppecher P (2001) Non-local interactions resulting from the homogenization of a linear diffusive medium. *Comptes Rendus de l'Académie des Sciences-Series I-Mathematics* 332(5):485–490
- Chen WT (1966) On some problems in transversely isotropic elastic materials. *J Appl Mech* 33(2):347–355
- Chen W (2000) On the general solution for piezothermoelasticity for transverse isotropy with application. *J Appl Mech* 67(4):705–711
- Chen W, Lee KY, Ding H (2004) General solution for transversely isotropic magneto-electro-thermo-elasticity and the potential theory method. *Int J Eng Sci* 42(13–14):1361–1379
- De Angelo M, Spagnuolo M, D'annibale F, Pfaff A, Hoschke K, Misra A, Dupuy C, Peyre P, Dirrenberger J, Pawlikowski M (2019) The macroscopic behavior of pantographic sheets depends mainly on their microstructure: experimental evidence and qualitative analysis of damage in metallic specimens. *Continuum Mech Thermodyn* 31(4):1181–1203
- Dell'Isola F, Seppecher P, Alibert JJ, Lekszycki T, Grygoruk R, Pawlikowski M, Steigmann D, Giorgio I, Andreas U, Turco E et al (2019a) Pantographic metamaterials: an example of mathematically driven design and of its technological challenges. *Continuum Mech Thermodyn* 31(4):851–884
- Dell'Isola F, Turco E, Misra A, Vangelatos Z, Grigoropoulos C, Melissinaki V, Farsari M (2019b) Force-displacement relationship in micro-metric pantographs: experiments and numerical simulations. *Comptes Rendus Mécanique* 347(5):397–405
- di Cosmo F, Laudato M, Spagnuolo M (2018) Acoustic metamaterials based on local resonances: homogenization, optimization and applications. In: *Generalized models and non-classical approaches in complex materials*, vol 1. Springer, pp 247–274
- Ding H, Jiang A (2003) Fundamental solutions for transversely isotropic magneto-electro-elastic media and boundary integral formulation. *Sci China Ser E: Technol Sci* 46(6):607–619
- Ding H, Chen W, Zhang L (2006) *Elasticity of transversely isotropic materials*, vol 126. Springer Science & Business Media
- Eerenstein W, Mathur N, Scott JF (2006) Multiferroic and magnetoelectric materials. *Nature* 442(7104):759–765
- Elliott HA, Mott N (1948) Three-dimensional stress distributions in hexagonal aeolotropic crystals. In: *Mathematical proceedings of the cambridge philosophical society*, vol 44. Cambridge University Press, pp 522–533
- Eremeyev VA, Lebedev LP, Altenbach H (2012) *Foundations of micropolar mechanics*. Springer Science & Business Media
- Fabrikant V (1989) *Applications of potential theory in mechanics: a selection of new results*. Kluwer Academic Publishers, Dordrecht
- Franciosi P, Spagnuolo M, Salman OU (2019) Mean green operators of deformable fiber networks embedded in a compliant matrix and property estimates. *Continuum Mech Thermodyn* 31(1):101–132
- Green A, Zerna W (1968) *Theoretical elasticity*. Clarendon Press, Oxford

- Haojiang D et al (1996) General solutions for coupled equations for piezoelectric media. *Int J Solids Struct* 33(16):2283–2298
- Lekhnitskii S (1940) Symmetrical deformation and torsion of revolution with a special kind of anisotropy. *PPM* 4:43–60
- Lekhnitskii S (1981) *Theory of elasticity of an anisotropic body*. Mir Publishers, Moscow
- Lin W, Kuo C, Keer L (1991) Analysis of a transversely isotropic half space under normal and tangential loadings. *ASME J Tribol* 113:335–338
- Marmo F, Rosati L (2016) A general approach to the solution of Boussinesq's problem for polynomial pressures acting over polygonal domains. *J Elasticity* 122(1):75–112
- Marmo F, Sessa S, Rosati L (2016a) Analytical solution of the Cerruti problem under linearly distributed horizontal loads over polygonal domains. *J Elasticity* 124(1):27–56
- Marmo F, Toraldo F, Rosati L (2016b) Analytical formulas and design charts for transversely isotropic half-spaces subject to linearly distributed pressures. *Meccanica* 51(11):2909–2928
- Marmo F, Toraldo F, Rosati L (2017) Transversely isotropic half-spaces subject to surface pressures. *Int J Solids Struct* 104:35–49
- Marmo F, Toraldo F, Rosati A, Rosati L (2018) Numerical solution of smooth and rough contact problems. *Meccanica* 53(6):1415–1440
- Marmo F, Sessa S, Vaiana N, De Gregorio D, Rosati L (2020) Complete solutions of three-dimensional problems in transversely isotropic media. *Continuum Mech Thermodyn* 32(3):775–802
- Michell J (1900) The stress in an æolotropic elastic solid with an infinite plane boundary. *Proc Lond Mathe Soc* 1(1):247–257
- Milton GW, Seppecher P, Bouchitté G (2009) Minimization variational principles for acoustics, elastodynamics and electromagnetism in lossy inhomogeneous bodies at fixed frequency. *Proc Royal Soc A: Math Phys Eng Sci* 465(2102):367–396
- Nejadsadeghi N, Placidi L, Romeo M, Misra A (2019) Frequency band gaps in dielectric granular metamaterials modulated by electric field. *Mech Res Commun* 95:96–103
- Pan E (2002) Three-dimensional green's functions in anisotropic magneto-electro-elastic bimetals. *Zeitschrift für angewandte Mathematik und Physik ZAMP* 53(5):815–838
- Pan YC, Chou TW (1976) Point force solution for an infinite transversely isotropic solid. *J Appl Mech* 43(4):608–612
- Pan YC, Chou TW (1979) Green's function solutions for semi-infinite transversely isotropic materials. *Int J Eng Sci* 17(5):545–551
- Pideri C, Seppecher P (1997) A second gradient material resulting from the homogenization of an heterogeneous linear elastic medium. *Continuum Mech Thermodyn* 9(5):241–257
- Podil'chuk YN, Sokolovskii YI (1994) Thermostress in an infinite transversally isotropic medium with an internal elliptical crack. *Int Appl Mech* 30(11):834–840
- Rosati L, Marmo F (2014) Closed-form expressions of the thermo-mechanical fields induced by a uniform heat source acting over an isotropic half-space. *Int J Heat Mass Transf* 75:272–283
- Shield R (1951) Notes on problems in hexagonal aeolotropic materials. In: *Mathematical proceedings of the Cambridge philosophical society*, vol 47. Cambridge University Press, pp 401–409
- Sp X, Gao Y, Wang W (2008) Completeness of general solutions for three-dimensional transversely isotropic piezoelectricity. *Int J Solids Struct* 45(18–19):5118–5126
- Wang M, Wang W (1995) Completeness and nonuniqueness of general solutions of transversely isotropic elasticity. *Int J Solids Struct* 32(3–4):501–513
- Wang M, Xu X (1990) A generalization of Almansi's theorem and its application. *Appl Math Modelling* 14(5):275–279
- Wang X, Yp S (2002) The general solution of three-dimensional problems in magneto-electro-elastic media. *Int J Eng Sc* 40(10):1069–1080
- Wang Y, Hu J, Lin Y, Nan CW (2010) Multiferroic magneto-electric composite nanostructures. *NPG Asia Materi* 2(2):61–68
- Zikung W, Bailin Z (1995) The general solution of three-dimensional problems in piezoelectric media. *Int J Solids Struct* 32(1):105–115

Chapter 10

Mathematical Tools for the Seismic Analysis of Reinforced Concrete Structures: A Selected Review



Cristoforo Demartino and Sicheng Zhou

Abstract Response spectrum analysis represents the preferential strategy to analyze and design civil engineering structures subjected to seismic actions. Nevertheless, most structural codes were developed by following hand computation-oriented philosophies so that their prescriptions can be hard to be implemented in finite element frameworks and often prevent the use of innovative strategies. This contribution presents a review of innovative tools focused on reinforced concrete framed structures aiming to establish a possible organic workflow for design procedures. Some pivotal issues typical of such a structural typology are hereby addressed, and particularly, global torsion and capacity checks in the presence of axial force–biaxial bending responses. This has been done by correlating innovative solutions such as torsional spectra, seismic envelopes, and limit analysis and by presenting a numerical procedure capable of performing capacity checks of reinforced concrete cross sections. The presented strategy aims to be a computationally efficient and exhaustive procedure to be used within the framework of finite element analysis.

Keywords Seismic analysis · Reinforced concrete structures · Torsional spectrum · Seismic envelopes · Limit analysis · Finite element

C. Demartino (✉) · S. Zhou
Zhejiang University—University of Illinois at Urbana Champaign Institute (ZJUI),
718 East Haizhou Road, Zhejiang 314400, Haining, PR China
e-mail: cristoforodemartino@intl.zju.edu.cn

S. Zhou
e-mail: sichengzhou@intl.zju.edu.cn

© Springer Nature Switzerland AG 2021
F. Marmo et al. (eds.), *Mathematical Applications in Continuum and Structural Mechanics*, Advanced Structured Materials 127,
https://doi.org/10.1007/978-3-030-42707-8_10

10.1 Introduction

Within the framework of earthquake engineering, response spectrum analysis represents one of the most popular techniques for structural design and it is recommended by several international codes (Chopra 2007), including the Eurocode 8 (EN 1998–1 1998), as the preferred procedure for building design. In spite of this popularity, standard code prescriptions are often not oriented to computer-aided computational analysis so that their implementation in automatic procedures is burdensome and inefficient.

In fact, some provisions were developed in order to facilitate *handmade-oriented* computations in which the human designer is weak in performing large amounts of calculations, while it is highly skilled in making qualitative and theoretical considerations (Zuccaro et al. 2017). On the contrary, in computer-aided design, structural software easily handles great computational efforts, while it is barely reliable in making even simple qualitative choices.

Such drawbacks are even more significant for the case of reinforced concrete structures since computational strategies capable of addressing the nonlinear and compressive-only nature of the material are obviously more complex than those oriented to solve linear structures (Lima et al. 2020). Such an aspect becomes pivotal in a context aiming to assess risk and resilience of existing structures (Chiaia et al. 2019).

A first aspect concerns the global torsion behavior of buildings, consisting in rotations induced by nonuniform seismic motions and structural asymmetries, which is of the most importance in seismic design (Karimiyan et al. 2014). Standard codes often account for torsional effects by enforcing an accidental eccentricity to be applied by shifting the floor masses from their original location (EN 1998–1 1998; NBCC 2005; NZS 1170 2004).

Such a procedure is conceptually very simple; nevertheless, its application turns out to be computationally burdensome because it is necessary to analyze several structural models corresponding to different mass configurations (DeBock et al. 2014).

A further aspect concerns the fact that multicomponent responses play a significant role in capacity check procedures of reinforced concrete structural elements. In fact, their safety depends on the combination of more than a single response, as for the case of biaxial shear (Selna and Lawder 1977) or axial force–biaxial bending (Chen et al. 2001; Marmo et al. 2011) actions in concrete beams.

Such an issue is not directly addressed by the procedures recommended by standard codes. In fact, although combination of multiple responses provided by response spectrum analysis is a well known issue since the late 1977 (Gupta and Singh 1977), code provisions often fail to account for it. Moreover, the definition of multicomponent capacity domains, in general, is addressed by conventionally extending single-response cases (Sessa et al. 2019b).

As a matter of fact, while the scientific community has made a great effort in investigating response spectrum analysis, common design of reinforced concrete

presents a significant gap with respect to the research advancements. In fact, recent developments in concrete analysis and design concern crack propagation (Barchiesi et al. 2020; Contrafatto and Cuomo 2006; Contrafatto et al. 2012, 2016), damage (Placidi et al. 2018, 2019; De Angelo et al. 2019) and viscoelasticity (Cuomo 2017) as well as analysis of isogeometric elements (Cuomo et al. 2014).

This contribution presents a selected review of the latest advancements concerning analysis and design of reinforced concrete structures by response spectrum analysis and proposes a possible synergical and comprehensive strategy. The discussed solutions can be organized in a unique workflow formulated in such a way to allow for computationally efficient procedures.

In this respect, Sect. 10.2 presents an overview of the strategies capable of accounting for global torsion in buildings and analyzes their main benefits and drawbacks. These strategies are introductory to the computation of multicomponent actions in structural elements which is addressed in Sect. 10.3.

Moreover, a review of axial force–biaxial bending capacity surfaces of reinforced concrete beams is introduced in Sect. 10.4 in which recent advancements concerning approximate formulations, limit analysis, and probabilistic assessment are also discussed. Then, an innovative approach to perform capacity checks in beams, based on seismic envelopes (Menun and Der Kiureghian 2000a, b), is presented in Sect. 10.4.1. Finally, conclusions are reported in Sect. 10.5.

10.2 Review of Strategies Accounting for Global Torsion in Buildings

Global torsion induced by earthquake excitation is a well-known problem addressed by several researches over years (Anagnostopoulos et al. 2015). One of the first attempts to propose a systematic strategy was presented by Newmark in 1969 (Newmark 1969). Such an approach interpreted torsional effects as the result of a base motion acting with different phases at different points of the foundation because of wave passage effects and ground inhomogeneities (Chopra and de la Llera 1994a). Nevertheless, the computed torsional spectrum was relevant to recorded response spectra and was not determined by design prescriptions.

The main contribution of Newmark research was the definition of the accidental eccentricity. In fact, since automatic computation was not widespread at the time, structural analysis was performed by means of simplified models defined in terms of center of mass and stiffness so that it was straightforward to conventionally increase the natural eccentricity between these points. The concept of accidental eccentricity has been furtherly investigated in years and, finally, calibrated for design purposes (Chopra and de la Llera 1994b, c).

Despite of its intuitive simplicity, accidental eccentricity does not represent a suitable strategy from a computational point of view since, for the case of three-

dimensional finite element analysis, it is necessary to define more than a single structural models. For this reason, several strategies to overcome such a drawback have been investigated over years.

In order to present a better overview of the available approaches, it is possible to introduce three main classes.

A first family consists in performing seismic analyses by considering the sole translational actions and to conventionally increase the structural responses to indirectly account for torsional effects. In particular, multipliers of the translational responses relevant to a single structural element are determined. They depend on the element's coordinates within the structural model and on a few properties of the analyzed building (Chopra and de la Llera 1995; Goel and Chopra 1993). Such strategies were defined for the case of flexible diaphragms (Basu and Jain 2004; Lin et al. 2001). Nevertheless, they introduce strong hypotheses about the properties of the structural model and cannot be used in conjunction with recent strategies to address the design of concrete sections such as the ones discussed in Sect. 10.3.

Further typologies of computational approaches consist in adopting either recorded or artificial global torsion response spectra and are capable of characterizing ground motions up to six components (Falamarz-Sheikhabadi 2014).

Recent advances in seismology have been focused on recording torsional actions. A popular strategy consists in extracting rotational motions from translational records (Ghayamghamian and Nouri 2007) by analyzing accelerations at different stations (Basu et al. 2013). A further approach relies on direct records by the use of torsional measurement devices (Lee et al. 2009; Nazarov et al. 2015).

Despite of its capability in determining the actual torsional component of the ground motions, such strategies are not capable of determining general purpose design spectra because of the limited quantity of experimental observations.

A more effective approach in structural design consists in determining artificial torsional spectra by processing the translational actions. In such a case, it is possible to adopt the design response spectra of the translational analysis so that such procedures can be applied regardless of the availability of records relevant to the building site.

A promising approach (Shakib 2004) determines the torsional spectrum as the response of a nonlinear mechanical model, calibrated on soil and structural properties, reproducing the behavior of the ground subject to translational actions, while a similar one (Avilés and Suárez 2006) is focused on seismic wave reflection. Both strategies proved to be effective although they require a sophisticated characterization of the soil mechanics as well as an uncommon knowledge of the designer.

One of the simplest solutions to compute artificial spectra characterizing global torsion actions is represented by the Dynamic Equivalent Rotational Spectrum (DERS) (Sessa et al. 2018b), a recently proposed strategy based on the equivalence of two degrees-of-freedom (DOFs) oscillators. Such an approach aims to compute in closed form an artificial torsional spectrum equivalent to the application of the accidental eccentricity provided by standard codes.

Its main benefit consists in the fact that the torsional spectrum is computed by analytical expressions defined in terms of the translational spectrum and of mechanical properties of the structural model.

Table 10.1 Synoptic comparison of existing strategies for buildings sensitive to torsional effects

| Method | Advantages | Disadvantages |
|--|---|--|
| Accidental eccentricity | Intuitive and consolidated strategy | Burdensome for 3D structural analysis |
| Translational response increment (Basu and Jain 2004; Chopra and de la Llera 1995; Goel and Chopra 1993; Lin et al. 2001) | Simple and fast approach, easy to implement | Applicable to a limited number of structural typologies; it usually requires restrictive dynamical features |
| Recorded torsional response spectra (Basu et al. 2013; Ghayamghamian and Nouri 2007; Lee et al. 2009; Nazarov et al. 2015) | Computationally efficient, provides reliable results | Lack of territorial data; it requires complex computations for defining the torsional spectrum. It is not permitted by some building codes |
| Artificial torsional response spectra (Avilés and Suárez 2006; Sessa et al. 2018b; Shakib 2004) | Computationally efficient, provide conservative results. The DERS fulfills the requirements of building codes | They may require a complex characterization of the soil and can be not fully equivalent to the accidental eccentricity prescriptions for multi DOFs structures |

Because of its simplicity, it will be used in the sequel to account for global torsion, although the designer can choose to adopt alternative formulations or recorded spectra; for this reason, it is summarized in Sect. 10.2.1.

As a general consideration, torsional spectra, regardless of their recorded or artificial nature, represent the best strategy to account for global torsion. In fact, response spectrum analysis performed in the combination of modal analysis consists in superimposing the structural responses relevant to each spectrum of the seismic excitation.

For the case of hand computations, a further response spectrum results in an increased computational burden, while the adoption of an increment of the natural eccentricity is a straightforward strategy. On the contrary, when spectral analysis is performed by automatic computations, a further component of the seismic action is not burdensome to perform since it results in redundant calculations.

For the reader's convenience, Table 10.1 reports a summary of the strategies described in this sections specifying a synoptic comparison of their main advantages and drawbacks.

10.2.1 Review of the Dynamic Equivalent Rotational Spectrum

The analytical definition of the DERS presented in Sessa (2018b) is based on the outcomes of a modal analysis in which structural responses are computed in terms of

modes of vibration, each one relevant to a natural pulsation. The artificial spectrum is computed by enforcing the equivalence between two oscillators, each one having two DOFs, modeling the response of each vibration mode.

Specifically, the response of a generic vibration mode, with pulsation ω , is modeled by means of a linear oscillator presenting a translational u_χ and a rotational u_θ displacements.

We also denote by ε the value of the structural eccentricity, by r the inertial radius of gyration of the structural model about the vertical axis and by Ω the frequency ratio, i.e., the ratio between the translational and rotational natural frequencies of the structural model.

Under these assumptions, the equation of motion of the two DOFs oscillator is ruled by the equation of motion:

$$\begin{bmatrix} \ddot{u}_\chi \\ r\ddot{u}_\theta \end{bmatrix} + \begin{bmatrix} \omega^2 & \frac{\omega^2\varepsilon}{r} \\ \frac{\omega^2\varepsilon}{r} & \omega^2\Omega^2 + \frac{\varepsilon^2}{r^2} \end{bmatrix} \begin{bmatrix} u_\chi \\ ru_\theta \end{bmatrix} = - \begin{bmatrix} a_\chi(t) \\ ra_\theta(t) \end{bmatrix}, \quad (10.1)$$

where a_χ is the value of the modal acceleration of the translational action, while a_θ is the value of an unknown global torsion acceleration.

Such a general oscillator can be specialized in two subcases. A *coupled oscillator*, in which the value of the eccentricity is set equal to the quantity enforced by standard codes and the global torsion acceleration is set to zero, and an *uncoupled oscillator* in which there is no eccentricity and the (unknown) torsional acceleration is not null.

By enforcing equivalence between the responses of both oscillators, the torsional acceleration a_θ is the sole unknown quantity of the problem. As a consequence, if the translational acceleration is defined by means of response spectrum, it is possible to compute the relevant value of an artificial rotational spectrum providing the very same response of the standard code eccentricity.

Such a problem can be solved in closed form by introducing some auxiliary variables:

$$c = \omega^2 \frac{1 + \Omega^2 + \varepsilon^2/r^2}{2}; \quad R = \frac{\omega^2}{2} \sqrt{(\Omega^2 + \varepsilon^2/r^2 - 1)^2 + 4\varepsilon^2/r^2} \quad (10.2)$$

$$T_1 = \frac{2\pi}{\sqrt{c - R}}; \quad T_2 = \frac{2\pi}{\sqrt{c + R}} \quad (10.3)$$

representing the two natural periods of the coupled oscillator,

$$c_1 = (\omega^2\varepsilon/r)^2; \quad c_2 = (-\omega^2 + c - R)^2 \quad (10.4)$$

and, finally, computing the value of the artificial torsional spectrum $D_\theta (T/\Omega)$ as

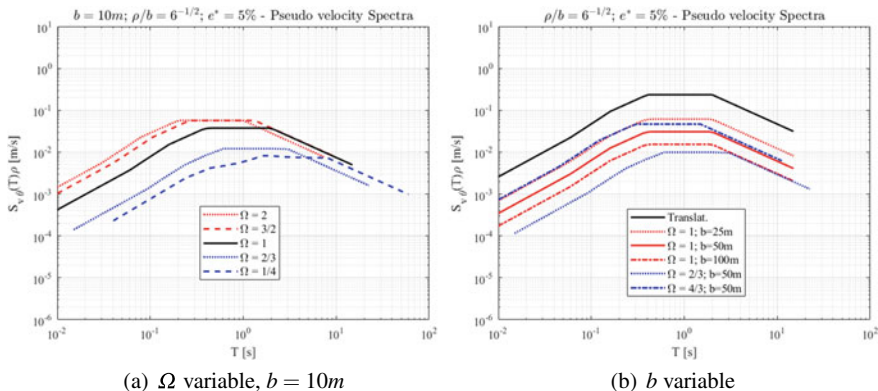


Fig. 10.1 Global torsion response spectra

$$D_{\theta}(T/\Omega) = \frac{c_1 c_2}{r [c_1 + c_2]} \sqrt{D_{\chi,1}^2 - D_{\chi,2}^2 - D_{\chi,1} D_{\chi,2} \rho_{1,2}} \tag{10.5}$$

where $T = 2\pi/\omega$ is the natural period of the considered vibration mode, $D_{\chi,1}$ and $D_{\chi,2}$ are the values of the translational response spectrum relevant to periods T_1 and T_2 and $\rho_{1,2}$ is the modal correlation coefficient of the coupled oscillator.

The latter can be easily computed by the complete quadratic combination (Smeby and Der Kiureghian 1985) as

$$\rho_{1,2} = \frac{8\xi^2 (T_2/T_1)^{3/2}}{(1 + T_2/T_1) [(1 - T_2/T_1)^2 + 4\xi^2 (T_2/T_1)]} \tag{10.6}$$

in which ξ is the damping ratio associated with the vibration mode.

We emphasize that response spectra have been reported in terms of displacements. The corresponding pseudo-acceleration and pseudo-velocity spectra can be easily computed as

$$S_{a\theta,\chi}(S_{\chi}, T) = D_{\theta}(T/\Omega) \omega^2; \quad S_{v\theta,\chi}(S_{\chi}, T) = D_{\theta}(T/\Omega) \omega \tag{10.7}$$

Figure 10.1a and b present some examples of pseudo-velocity global torsion spectra in which the accidental eccentricity has been set $\varepsilon = 0.05b$ with b representing the generic width of the structural model and the radius of gyration is $r = b/\sqrt{6}$.

We emphasize that such artificial spectra can be quite different from recorded ones since the DERS is not representative of any real ground motion. However, it represents an easy procedure to account for global torsion by adopting a single structural model.

10.3 Computation of Multicomponent Actions by Seismic Envelopes

Response spectrum analysis computes the peak value of a structural quantity of interest by superimposing the outcomes of different vibration modes relevant to a set of seismic components.

It is worth being emphasized that each structural response due to a seismic action is, in general, a quantity that varies in time and spectral analysis is not capable of determining the instant at which each peak occurs.

More generally, if capacity checks depend on more than a single response, such as for the case of axial force–biaxial bending capacity of reinforced concrete beams, the peaks of different components of the response are not necessarily synchronous.

Moreover, outcomes of the spectral analysis are computed by the superposition of the responses relevant to each seismic components which is usually defined by means of quadratic forms. Thus, the algebraic sign of these responses is undefined.

Importance of a proper combination of different response components is a well-established problem whose importance was highlighted in the late '70s by Gupta and Singh (1977). Their approach introduced a rectangular envelope, determined by assigning to the response components all possible combinations of the algebraic sign.

Although simple, such an approach is not very accurate, presents some drawbacks in accounting for seismic actions with unknown input directions and does not accounts for the correlation between the response components.

A theoretical solution overcoming these drawbacks was proposed by Menun and Der Kiureghian (2000a, b), and later extended to perform capacity checks of reinforced concrete beam sections (Sessa et al. 2015). Such an approach is based on the fact that multi-component responses computed by the response spectrum procedure can be conveniently represented by tensor analysis (Lebedev et al. 2010).

To fix the ideas, let us consider the space determined by the components of the structural response of interest. For the case of axial force–biaxial bending capacity checks the response is defined by the axial force P acting on a cross section and two bending moments M_1 and M_2 about the section reference axes. The Supreme Envelope determines a boundary surface which encompasses all possible values that the multi-component response can attain during the seismic motion.

To compute the Supreme Envelope expression, it is necessary to determine the vibration modes of the structural models. Specifically, each mode presents three components of the response which can be arranged in the following matrix:

$$\Psi = \begin{bmatrix} P^1 & \dots & P^i & \dots & P^n \\ M_1^1 & \dots & M_1^i & \dots & M_1^n \\ M_2^1 & \dots & M_2^i & \dots & M_2^n \end{bmatrix} \quad (10.8)$$

where n is the number of the considered modes.

To account for seismic actions, it is useful to introduce two sets of $n \times n$ diagonal matrices \mathbf{D}_k and $\mathbf{\Gamma}_k$. Index k denotes the component of the seismic action with $k = 1, 2$ corresponding to the horizontal components, $k = 3$ to the vertical one, and $k = 4$ to the global torsion one defined in Sect. 10.2. Elements $D_{i,i,k}$ and $\Gamma_{i,i,k} = \gamma_i^k$, belonging to the principal diagonals of \mathbf{D} and $\mathbf{\Gamma}$ denote, respectively, the values of the displacement spectrum and of the participating factor of mode i with respect to the seismic component k .

Modal superposition adopts cross-correlation coefficients of the Complete Quadratic Combination (CQC) procedure (Wilson et al. 1981) which are arranged in the square matrix \mathbf{R} whose element $\rho_{i,j}$ denotes the correlation coefficient between modes i and j .

Denoting by \mathbf{f}_d the structural response vector produced by static forces and by $\mathbf{X}_S(\boldsymbol{\alpha})$ a 3×3 matrix depending on modal and spectral quantities (Menun and Der Kiureghian 2000a), the relationship determining the Supreme Envelope is defined as follows:

$$\mathbf{f}(\boldsymbol{\alpha}) = \mathbf{f}_d + \frac{\mathbf{X}_S(\boldsymbol{\alpha})\boldsymbol{\alpha}}{[\boldsymbol{\alpha}^T \mathbf{X}_S(\boldsymbol{\alpha})\boldsymbol{\alpha}]^{0.5}} \quad (10.9)$$

where vector $\mathbf{f}(\boldsymbol{\alpha})$ denotes a generic point of the envelope boundary, while $\boldsymbol{\alpha}$ is a unit vector used as parameter.

Matrix $\mathbf{X}_S(\boldsymbol{\alpha})$ is computed by combining modal responses and spectral quantities by the equation:

$$\mathbf{X}_S(\boldsymbol{\alpha}) = \left[\mathbf{Z}_1 + \frac{1}{2}\mathbf{Z}_2 - \frac{1}{2}\mathbf{Z}_2 P_2(\boldsymbol{\alpha}) + \frac{1}{2}\mathbf{Z}_3 P_3(\boldsymbol{\alpha}) \right] \quad (10.10)$$

where:

$$\mathbf{Z}_1 = \boldsymbol{\Psi} \left[\sum_{k=1}^4 \mathbf{\Gamma}_k \mathbf{D}_k \mathbf{R} \mathbf{D}_k^T \mathbf{\Gamma}_k^T \right] \boldsymbol{\Psi}^T \quad (10.11)$$

$$\mathbf{Z}_2 = \boldsymbol{\Psi} \left[- \sum_{k=1}^2 \sum_{l=1}^2 (-1)^k \mathbf{\Gamma}_l \mathbf{D}_k \mathbf{R} \mathbf{D}_k^T \mathbf{\Gamma}_l^T \right] \boldsymbol{\Psi}^T \quad (10.12)$$

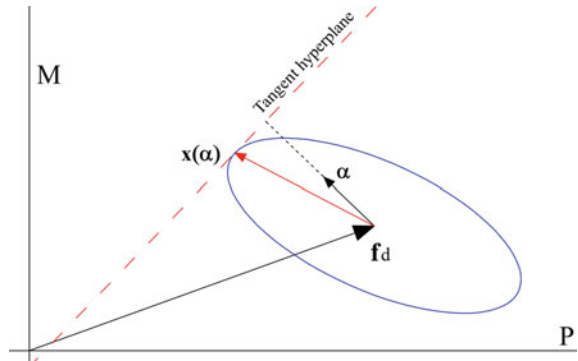
$$\mathbf{Z}_3 = \boldsymbol{\Psi} \left[\sum_{k=1}^2 (-1)^k \mathbf{\Gamma}_1 \mathbf{D}_k \mathbf{R} \mathbf{D}_k^T \mathbf{\Gamma}_2^T + \mathbf{\Gamma}_2 \mathbf{D}_k \mathbf{R} \mathbf{D}_k^T \mathbf{\Gamma}_1^T \right] \boldsymbol{\Psi}^T \quad (10.13)$$

$$P_2(\boldsymbol{\alpha}) = - \frac{\boldsymbol{\alpha}^T \mathbf{Z}_2 \boldsymbol{\alpha}}{H(\boldsymbol{\alpha})}; \quad P_3(\boldsymbol{\alpha}) = \frac{\boldsymbol{\alpha}^T \mathbf{Z}_3 \boldsymbol{\alpha}}{H(\boldsymbol{\alpha})} \quad (10.14)$$

and:

$$H(\boldsymbol{\alpha}) = \left[(\boldsymbol{\alpha}^T \mathbf{Z}_2 \boldsymbol{\alpha})^2 + (\boldsymbol{\alpha}^T \mathbf{Z}_3 \boldsymbol{\alpha})^2 \right]^{0.5} \quad (10.15)$$

Fig. 10.2 Example of a 2D Supreme Envelope, unit vector α , and the relevant point of the envelope $\mathbf{f}(\alpha)$



To better understand the role of α as parameter, it is useful to introduce its physical interpretation. Specifically, α is the unit vector normal to the hyperplane tangent to the envelope boundary at $\mathbf{f}(\alpha)$; Fig. 10.2 presents a 2D example for simplicity. In order to obtain a large set of points belonging to the envelope, it is possible to assume different orientations of α by making it span the whole space of the actions and obtain all corresponding responses $\mathbf{f}(\alpha)$.

It is worth being emphasized that, despite of their apparent complex form, such relationships consist in combining quadratic forms of square matrices and these have been obtained by combining in a suitable way spectral and modal outcomes usually employed in classic response spectrum analysis. In this respect, all calculations are easy to be implemented into an automatic algorithm processing the outcomes of a finite element analysis.

Moreover, it is interesting to analyze the sum of Eq. (10.11) in which matrices \mathbf{D}_k , containing the response spectrum values relevant to each mode and to each seismic components, are multiplied by the ones containing the participation factors and the correlation coefficients.

The presence of the global torsion response spectrum, corresponding to the fourth component, simply determines a further sum, a fast and easy task to be performed by a numerical algorithm. We emphasize that the classical mass-shifting strategy to account for the accidental eccentricity would compromise the whole procedure since different mass locations would not permit the computation of a univocal matrix Ψ containing the modal responses of the structure. Hence, it is apparent that the adoption of a torsional spectrum turns out to be a procedure by far easier to be implemented than strategies dealing with mass locations.

Figure 10.3 presents the Supreme Envelope (in blue) computed by Eq. (10.9) relevant to a reinforced concrete cross section compared with the corresponding rectangular envelope computed by the procedure (Gupta and Singh 1977). Note that, in such a peculiar case, the latter turns out to be non-conservative with respect to the Supreme Envelope.

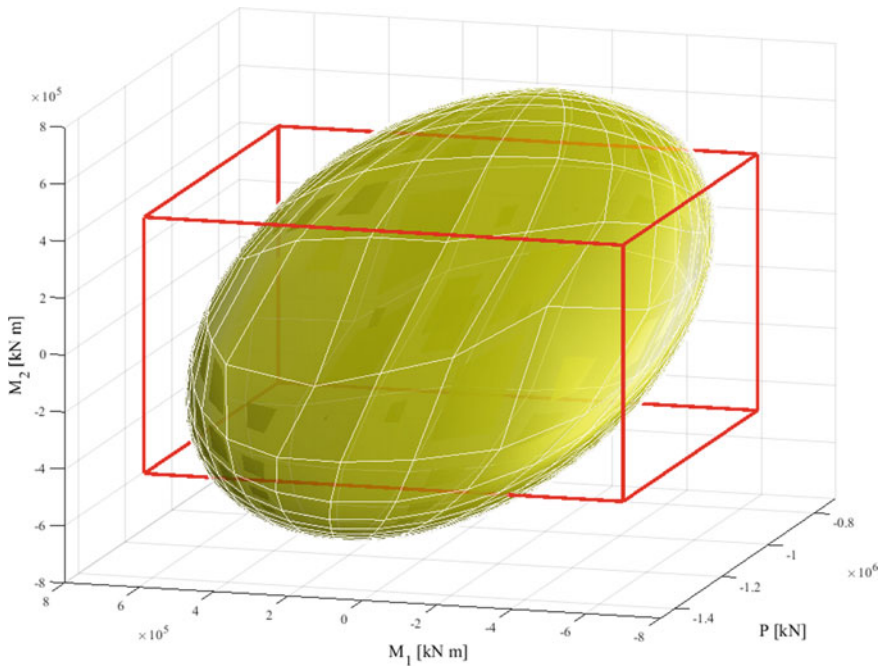


Fig. 10.3 Example of the Supreme Envelope (yellow) and of the Rectangular Envelope of a reinforced concrete column section

Such an issue is due to the fact that, while the rectangular envelope and, in general, the classic response spectrum strategy computes the peak responses relevant to a single seismic input direction, the Supreme Envelope accounts for its randomness.

10.4 Capacity Checks of Reinforced Concrete Beams

A significant step in the structural design of reinforced concrete structures consists in the determination of the capacity domain of each cross section. In fact, the seismic actions computed by the strategies described in Sect. 10.3, in particular the Supreme Envelope, must be fully contained within a closed surface representing the boundary between a safe and a collapse region, namely, the Capacity Surface.

Making reference to the ultimate limit state strategy, such a boundary is relevant to all states for which either a point of the concrete region of the cross section or one of the reinforcement bars attains its limit state.

Standard codes, such as Eurocode 2 (EN 1992-1-1 1992), define limit states of materials in terms of maximum normal strain ε_z , where z represents the axis normal to the cross-sectional plane. Moreover, constitutive relationships of both the concrete and reinforcement bar materials usually present a nonlinear behavior. In particular,

in Eurocode 2, steel is assumed to be elastic–perfectly plastic, while concrete can be modeled by a Parabola–Rectangle compressive-only relationship.

Strain field is assumed to be linear over the cross section; thus, points of the capacity surface are defined by internal actions for which the strain field attains the limit state in at least a point of the section. In this context, the values of the axial force and of the two bending moments relevant to a strain distributions are computed by means of integrals of the stress over the cross section.

Such a problem, although efficiently addressed for the case of rectangular sections (Papanikolaou and Sextos 2016), in common practice needs to be performed for arbitrarily shaped elements. Besides of the intuitive strategy of adopting a fiber discretized description of the cross section, integrals can be computed by a large variety of different strategies such as superposition of elementary-shaped section (Silva et al. 2009) and incremental iterative approaches (Chiorean 2010, 2013).

Interesting approaches are focused on the use of boundary integrals to get exact solutions (Matuszak and Pluciński 2014) and proved to be more accurate than fiber-oriented procedures both numerically (Matuszak 2017) and experimentally (Koziański and Winnicki 2016).

One of the most promising ones is a fiber-free algorithm (Alfano et al. 2007) based on a polygonal description of the cross section in which its boundary is expressed as function of the coordinates of the vertices. Fixed a strain field for which the ultimate limit state is reached, the corresponding values of the axial force and of the bending moments are computed in closed form by applying the Gauss–Green theorem and by adopting exact integrals of the elastic–plastic responses of steel and concrete (Marmo et al. 2008).

Such a strategy proved to be very effective in providing exact results and it was applied to pre-stressed concrete sections (Marmo et al. 2011) as well as to evaluate the response of reinforced concrete elements within the framework of finite element analysis (Marmo and Rosati 2012, 2013).

It is worth being emphasized that limit state analysis has a conventional nature; thus, its results can be not significant of the actual physical behavior of reinforced concrete beams. Moreover, the determination of the capacity surface is not provided in closed form but is defined by a set of discretized points.

The first issue has been recently investigated from a probabilistic point of view. In particular, it has been shown in Sessa (2019b) that the conventional ultimate limit state procedure was developed for axial force–uniaxial bending actions. Hence, its results, although conservative, turn out to be quite inaccurate for the case of biaxial bending. The distribution of the collapse probability over the capacity surface is far to be regular and uniform, as it would be recommendable. On the contrary, it turns out to be over-conservative for most of its regions.

Moreover, recent investigations compared the capacity domains of reinforced concrete sections, computed by such a fiber-free approach, and the capacity surfaces determined by limit analysis (Sessa et al. 2018a). The latter strategy represents an appealing tool since it is based on the well-known safe theorem and is less compu-

tationally demanding than traditional limit state analyses. It has been shown that, as long as a sufficient ductility is ensured, limit analysis provides accurate estimations of the capacity surface.

Use of limit analysis (Malena and Casciaro 2008) was first developed for shake-down analyses of 3D frames (Casciaro and Garcea 2002) and has been enhanced to account for Eurocode 8-compliant load combinations (Leonetti et al. 2015). Such a strategy reduces the computational burden by reducing redundant constraints (Simon and Weichert 2012; Spiliopoulos and Panagiotou 2017) and introduces the possibility of representing the domain boundaries by approximate formulations. In particular, capacity surface can be represented by a Minkowsky sum of ellipsoids (Yan and Chirikjian 2015), a mathematical tool representing multidimensional surfaces as a function of their gradient.

For the case of axial force–biaxial bending domains, the Minkowsky sum of ellipsoids can be determined either by optimization (Bleyer and Buhan 2013) or by a reduction approach. The latter consists in dividing the reinforced concrete section in triangles and rectangles, whose theoretical contribution to the overall capacity can be computed in closed form, and then by superimposing such contributions to obtain a global capacity surface (Magisano et al. 2018).

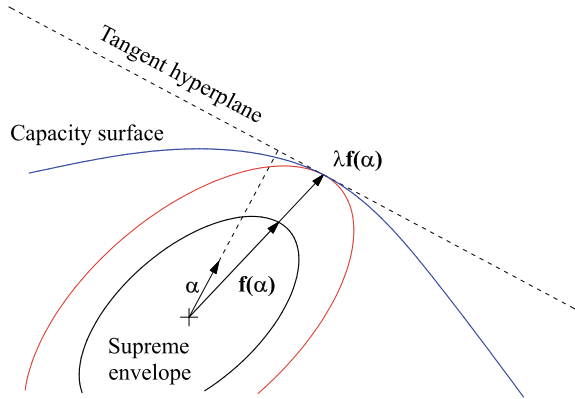
It is worth being emphasized that the most suitable approach to determine the capacity surface of reinforced concrete cross sections is strongly dependent on the peculiar problem. For example, limit analysis approaches are effective for the case of new buildings for which code prescriptions require a sufficient ductility. On the contrary, they cannot be easily used for the case of existing buildings.

Solutions based on the exact computation of the capacity of rectangular subsections are suitable if the cross-sectional geometry fulfills some geometrical conditions, while the fiber-free approach (Alfano et al. 2007) can address sections of arbitrary shape but its employment can result burdensome if used in conjunction with the Supreme Envelope described in Sect. 10.3.

A further aspect concerns the fact that, in common design, a single section can be subject to a large set of different actions and it is convenient to determine its capacity surface only once what is often done by means of a discretized set of points.

Referring to the cited works for the details concerning the capacity surfaces, the following subsection proposes an approximate strategy capable of performing capacity checks by combining actions defined in terms of the Supreme Envelope and a capacity surface defined by means of discrete points. Such an approach aims to propose a general procedure which permits to the designer the choice of the most suitable capacity surface formulation, thus taking advantage of the large variety of solutions provided by the literature.

Fig. 10.4 Example of 2D capacity check performed by the Supreme Envelope and a capacity surface



10.4.1 A General Algorithm to Perform Capacity Checks by the Supreme Envelope

Capacity checks performed by formulating the seismic action by the Supreme Envelope and by adopting a capacity surface aim to determine the *critical multiplier* λ of the seismic response spectra which makes the Supreme Envelope to become tangent to the capacity surface.

For simplicity, Fig. 10.4 shows a 2D example in which the capacity surface has been plotted in blue while the Supreme Envelope corresponding to the actual seismic excitation has been reported in black. The Supreme Envelope amplified by the critical load multiplier λ has been reported in red.

Note that the amplified envelope and the capacity surface present the same tangent hyperplane at the point $\lambda \mathbf{f}(\boldsymbol{\alpha})$ with normal unit vector $\boldsymbol{\alpha}$.

Determination of $\boldsymbol{\alpha}$ and λ is not straightforward and, in general, cannot be performed in closed form. Numerical algorithms have been proposed to address such an issue, although the one proposed in Menun (2004b) assumes a simplified formulation of the capacity surface not suitable for reinforced concrete sections while the numerical algorithm presented in Sessa (2015) requires the computation of the fiber free surface (Alfano et al. 2007) and is computationally demanding if the cross section is subject to several actions.

In order to permit efficient capacity checks regardless of the strategy adopted for determining the capacity domain of the section, let us assume that the capacity surface \mathcal{D} is defined by means of a sufficiently dense set of discretized points whose i th element is:

$$\mathbf{d}_i = [P_i, M_{1,i}, M_{2,i}]^T \quad (10.16)$$

where P_i denotes the axial force while $M_{1,i}$ and $M_{2,i}$ are the two bending components.

Representation of a continue surface approximating a set of discrete point can be conveniently performed by defining a *Minkowski sum of ellipsoids* which is capable

of defining n -dimensional surfaces by means of a superposition of ellipsoids (Yan and Chirikjian 2015), as illustrated before.

The surface is defined by means of the *support function*, representing the distance of the tangent hyperplane at \mathbf{t} from the origin, which is:

$$\pi(\mathbf{t}) = [\boldsymbol{\alpha}(\mathbf{t})^T \mathbf{M}^{-1} \boldsymbol{\alpha}(\mathbf{t})]^{0.5} = [\mathbf{M}^{-1} \boldsymbol{\alpha}(\mathbf{t}) \cdot \boldsymbol{\alpha}(\mathbf{t})]^{0.5} \quad (10.17)$$

where $\boldsymbol{\alpha}$ is the unit vector normal to the tangent hyperplane.

Matrix \mathbf{M} is numerically calibrated by means of a least-square minimization algorithm so that the surface approximates the set of discretized points belonging to the capacity domain. Hence, the vector $\boldsymbol{\alpha}$ can be used as a parameter for computing any point of the ellipsoids by the relationship:

$$\mathbf{t}(\boldsymbol{\alpha}) = \frac{\mathbf{M}^{-1} \boldsymbol{\alpha}}{[\boldsymbol{\alpha}^T \mathbf{M}^{-1} \boldsymbol{\alpha}]^{0.5}} \quad (10.18)$$

More complex shapes can be properly approximated by the superposition of several ellipsoids. Specifically, denoting as \mathbf{M}_i , $i = 1 \dots m$, the canonic matrices of m ellipsoids and as \mathbf{t}_0 the vector locating the domain center with respect to the origin, the Minkowski sum is defined as:

$$\mathbf{t}(\boldsymbol{\alpha}) = \mathbf{t}_0 + \sum_{i=1}^m \frac{\mathbf{M}_i^{-1} \boldsymbol{\alpha}}{[\boldsymbol{\alpha}^T \mathbf{M}_i^{-1} \boldsymbol{\alpha}]^{0.5}} \quad (10.19)$$

Figure 10.5 presents an illustrative Minkowski sum (represented by the black mesh) of three ellipsoids (represented in yellow, green and blue), approximating the capacity domain of a RC cross section, represented by the red bullets.

It is worth being emphasized that the expression determining the approximated domain of Eq. (10.19) is very similar to Eq. (10.9) representing the seismic Supreme Envelope.

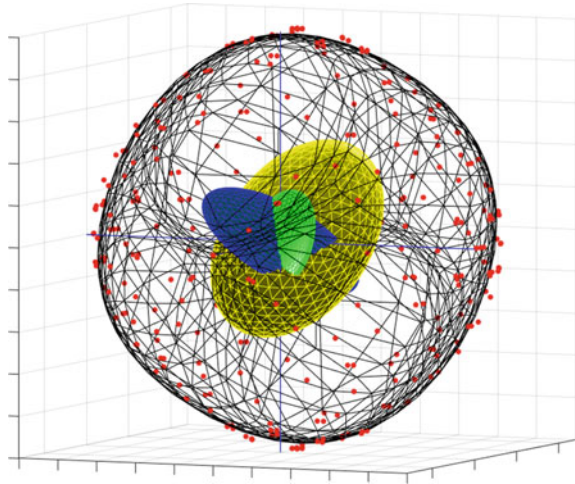
In this sense, the condition for which the Supreme Envelope is tangent to the capacity domain turns out to be:

$$\mathbf{f}_d - \mathbf{t}_0 + \lambda \frac{\mathbf{X}_S(\boldsymbol{\alpha}) \boldsymbol{\alpha}}{[\boldsymbol{\alpha}^T \mathbf{X}_S(\boldsymbol{\alpha}) \boldsymbol{\alpha}]^{0.5}} - \sum_{i=1}^m \frac{\mathbf{M}_i^{-1} \boldsymbol{\alpha}}{[\boldsymbol{\alpha}^T \mathbf{M}_i^{-1} \boldsymbol{\alpha}]^{0.5}} = 0 \quad (10.20)$$

where λ is a multiplier of the seismic action.

For this reason, the capacity check relevant to a single cross section consists in determining parameters λ and $\boldsymbol{\alpha}$ fulfilling Eq. (10.20) which can be easily computed by several numerical algorithms.

Fig. 10.5 Illustrative
3-ellipsoids Minkowski sum



The described procedure provides approximate although conservative results since the Minkowski sum of ellipsoids is always contained within the actual capacity surface. We emphasize once more that such a procedure aims to perform capacity checks for common design purposes with limited computational burden. Hence, as long as the capacity surface is discretized in a sufficient number of points, approximations will be affordable. Moreover, in contrast with the capacity check procedure described in Sessa (2015), the proposed strategy does not involve burdensome computations provided that the capacity check is limited to numerically solve a single nonlinear equation.

10.5 Conclusions

A review of recent developments concerning seismic analysis of reinforced concrete structures by response spectrum has been presented. The discussed strategies represent some of the most advanced contributions for performing structural analysis and design within the finite element framework.

To this end, a classification of the available approaches for properly modeling the effects of global torsion in buildings has been discussed. The presented strategies have been selected in order to ensure easy implementations in structural analysis software, particularly in finite element frameworks, proving that the most effective strategy consists in adopting global torsion response spectra.

Within this context, a selected state of the art concerning available formulations of torsional spectra has been reported and a recent strategy for defining an artificial torsional spectrum has been presented. Such an approach, defined as Dynamic Equivalent Rotational Spectrum (DERS), provides a global torsion action, as func-

tion of the mechanical properties of the structure and of the translational action, whose response is equivalent to the effects of the accidental eccentricity prescribed by standard codes.

The problem of multi-component structural responses, pivotal for the case of axial force—biaxial bending actions in reinforced concrete frames, has been addressed by means of seismic envelopes. Such a strategy takes into account the correlation between all components of the seismic response acting on a cross section and properly considers the randomness of the direction of propagation of earthquakes.

In order to analyze the characterization of the structural capacity of reinforced concrete beam elements, a comparison between different formulations of axial force—biaxial bending capacity domains has been presented. The discussed approaches are relevant to different theories such as the classical ultimate limit state analysis, adopted by standard codes, and recent results obtained by the limit analysis theory and the application of the Safe Theorem.

Finally, a numerical strategy for performing capacity checks by using seismic envelopes has been proposed. Such a procedure needs the capacity surface to be defined by a set of discretized points and determines an approximate capacity surface defined by means of a Minkowski sum of ellipsoids. A critical multiplier of the seismic load, defined as the scalar coefficient that makes the seismic Supreme Envelope to be tangent to the boundary, can therefore be computed by a numerical algorithm solving a vectorial equation.

In conclusion, the presented tools aim to represent a rational workflow for the analysis and design of reinforced concrete beam structures. The organic use of the discussed strategies permits an easy and computationally efficient implementation of a unique strategy consistent with the most common procedures of the finite element analysis.

Future challenges about the use of seismic envelopes in analyzing reinforced concrete structures are particularly focused on shell structural elements (Altenbach and Eremeyev 2009; Altenbach et al. 2009, 2010). In particular, an envelope formulation, based on the Mohr's circle and capable of addressing elastic shell elements, is already available (Menun 2004a), although it needs to be extended to nonlinear elements in order to address complex and curved structures (Eremeyev and Zubov 2007; Marmo et al. 2019). Effective extensions to address the nonlinear behavior of concrete should properly include reinforcements in nonlinear elements (Caggegi et al. 2018; Valoroso et al. 2014, 2015; Salman et al. 2019) and confinement (Serpiery et al. 2018; Sessa et al. 2017a, b, 2019a). Further developments concern the use of explicit solutions (Marmo et al. 2016, 2020) in order to take into account the stiffness of the foundation soil as well as the use of innovative beam models accounting for shear and torque (Paradiso et al. 2020, 2021).

References

- Alfano G, Marmo F, Rosati L (2007) An unconditionally convergent algorithm for the evaluation of the ultimate limit state of RC sections subject to axial force and biaxial bending. *Int J Numer Methods Eng* 72:924–963. <https://doi.org/10.1002/nme.2033>
- Altenbach H, Eremeyev V (2009) On the linear theory of micropolar plates. *ZAMM J Appl Math Mech/Zeitschrift für Angewandte Mathematik und Mechanik* 89:242–256. <https://doi.org/10.1002/zamm.200800207>
- Altenbach H, Eremeyev V, Morozov N (2009) Linear theory of shells taking into account surface stresses. *Dokl Phys* 54:531–535. <https://doi.org/10.1134/S1028335809120039>
- Altenbach J, Altenbach H, Eremeyev V (2010) On generalized cosserat-tape theories of plates and shells: a short review and bibliography. *Arch Appl Mech* 80:73–92. <https://doi.org/10.1007/s00419-009-0365-3>
- Anagnostopoulos S, Kyrkos M, Stathopoulos K (2015) Earthquake induced torsion in buildings: critical review and state of the art. *Earthquakes and Structures* 8:305–377. <https://doi.org/10.12989/eas.2015.8.2.305>
- Avilés J, Suárez M (2006) Natural and accidental torsion in one-storey structures on elastic foundation under non-vertically incident sh-waves. *Earthq Eng Struct Dyn* 35(7):829–850
- Barchiesi E, Hua Y, Tran C, Placidi L, Mueller W (2020) Computation of brittle fracture propagation in strain gradient materials by the fenics library. *Math Mech Solids* 26(108128652095):451. <https://doi.org/10.1177/1081286520954513>
- Basu D, Jain S (2004) Seismic analysis of asymmetric buildings with flexible floor diaphragms. *J Struct Eng-ASCE* 130. [https://doi.org/10.1061/\(ASCE\)0733-9445\(2004\)130:8\(1169\)](https://doi.org/10.1061/(ASCE)0733-9445(2004)130:8(1169))
- Basu D, Whittaker A, Constantinou M (2013) Extracting rotational components of earthquake ground motion using data recorded at multiple stations. *Earthq Eng Struct Dyn* 42. <https://doi.org/10.1002/eqe.2233>
- Bleyer J, Buhan P (2013) Yield surface approximation for lower and upper bound yield design of 3d composite frame structures. *Comput Struct* 129:86–98. <https://doi.org/10.1016/j.compstruc.2013.08.011>
- Caggegi C, Sciuto D, Cuomo M (2018) Experimental study on effective bond length of basalt textile reinforced mortar strengthening system: contributions of digital image correlation. *Measurement* 129. <https://doi.org/10.1016/j.measurement.2018.07.003>
- Casciaro R, Garcea G (2002) An iterative method for shakedown analysis. *Comput Methods Appl Mech Eng* 191(49):5761–5792. [https://doi.org/10.1016/S0045-7825\(02\)00496-6](https://doi.org/10.1016/S0045-7825(02)00496-6)
- Chen S, Teng J, Chan SL (2001) Design of biaxially loaded short composite columns of arbitrary section. *J Struct Eng-ASCE* 127. [https://doi.org/10.1061/\(ASCE\)0733-9445\(2001\)127:6\(678\)](https://doi.org/10.1061/(ASCE)0733-9445(2001)127:6(678))
- Chiaia B, Barchiesi E, De Biagi V, Placidi L (2019) A novel worst-case-based structural resilience index: definition, computation and applications to portal frame structures. *Mech Res Commun* 99. <https://doi.org/10.1016/j.mechrescom.2019.03.007>
- Chiorean C (2010) Computerised interaction diagrams and moment capacity contours for composite steel-concrete cross-sections. *Eng Struct* 32:3734–3757. <https://doi.org/10.1016/j.engstruct.2010.08.019>
- Chiorean C (2013) A computer method for nonlinear inelastic analysis of 3d semi-rigid steel frameworks. *Eng Struct* 57:125–152
- Chopra A (2007) Elastic response spectrum: a historical note. *Earthq Eng Struct Dyn* 36:3–12. <https://doi.org/10.1002/eqe.609>
- Chopra AK, de la Llera JC (1994a) Accidental torsion in buildings due to base rotational excitation. *Earthq Eng Struct D* 23:1003–1021
- Chopra AK, de la Llera JC (1994b) Evaluation of code accidental-torsion provisions from building records. *J Struct Eng* 120:597–616
- Chopra AK, de la Llera JC (1994c) Using accidental eccentricity in code-specified static and dynamic analyses of buildings. *Earthq Eng Struct D* 23:947–967

- Chopra AK, de la Llera JC (1995) Estimation of accidental torsion effects for seismic design of buildings. *J Struct Eng* 121:102–114
- Contrafatto L, Cuomo M (2006) A framework of elastic-plastic damaging model for concrete under multiaxial stress states. *Int J Plasticity* 22:2272–2300. <https://doi.org/10.1016/j.ijplas.2006.03.011>
- Contrafatto L, Cuomo M, Fazio F (2012) An enriched finite element for crack opening and rebar slip in reinforced concrete members. *Int J Fract* 178:33–50. <https://doi.org/10.1007/s10704-012-9723-1>
- Contrafatto L, Cuomo M, Gazzo S (2016) A concrete homogenisation technique at meso-scale level accounting for damaging behaviour of cement paste and aggregates. *Comput Struct* 173. <https://doi.org/10.1016/j.compstruc.2016.05.009>
- Cuomo M (2017) Forms of the dissipation function for a class of viscoplastic models. *Math Mech Complex Syst* 5:217–237. <https://doi.org/10.2140/memocs.2017.5.217>
- Cuomo M, Contrafatto L, Greco L (2014) A variational model based on isogeometric interpolation for the analysis of cracked bodies. *Int J Eng Sci* 80:173–188. <https://doi.org/10.1016/j.ijengsci.2014.02.017>
- De Angelo M, Spagnuolo M, D'Annibale F, Pfaff A, Hoschke K, Misra A, Dupuy C, Peyre P, Dirrenberger J, Pawlikowski M (2019) The macroscopic behavior of pantographic sheets depends mainly on their microstructure: experimental evidence and qualitative analysis of damage in metallic specimens. *Continuum Mech Thermodyn* 31. <https://doi.org/10.1007/s00161-019-00757-3>
- DeBock D, Liel A, Haselton C, Hooper J, Henige R (2014) Importance of seismic design accidental torsion requirements for building collapse capacity. *Earthq Eng Struct Dyn* 43:831–850. <https://doi.org/10.1002/eqe.2375>
- EN 1992-1-1 (1992) Design of concrete structures—part 1-1: general rules and rules for buildings. Standard, CEN
- EN 1998-1 (1998) Design of structures for earthquake resistance. Part I: General rules, seismic actions and rules for buildings. Standard, CEN
- Eremeyev VA, Zubov LM (2007) On constitutive inequalities in nonlinear theory of elastic shells. *J. Appl. Math. Mech./Zeitschrift für Angewandte Mathematik und Mechanik* 87(2):94–101. <https://hal.archives-ouvertes.fr/hal-00835648>
- Falamarz-Sheikhabadi MR (2014) Simplified relations for the application of rotational components to seismic design codes. *Eng Struct* 59:141–152. <https://doi.org/10.1016/j.engstruct.2013.10.035>
- Ghayamghamian M, Nouri G (2007) On the characteristics of ground motion rotational components using chiba dense array data. *Earthq Eng Struct D* 36:1407–1429
- Goel R, Chopra AK (1993) Seismic code analysis of buildings without locating centers of rigidity. *J Struct Eng-ASCE* 119:3039–3055
- Gupta A, Singh M (1977) Design of column sections subjected to three components of earthquake. *Nucl Eng Des* 41:129–133
- Karimiyan S, Kashan A, Karimiyan M (2014) Progressive collapse vulnerability in 6-story RC symmetric and asymmetric buildings under earthquake loads. *Earthq Struct* 6:473–494
- Koziński K, Winnicki A (2016) Experimental research and analysis of load capacity and deformability of slender high strength concrete columns in biaxial bending. *Eng Struct* 107:47–65. <https://doi.org/10.1016/j.engstruct.2015.10.025>
- Lebedev L, Cloud M, Eremeyev V (2010) Tensor analysis with applications in mechanics. <https://doi.org/10.1142/7826>
- Lee W, Igel H, Trifunac M (2009) Recent advances in rotational seismology. *Seismol Res Lett* 80:479–490. <https://doi.org/10.1785/gssrl.80.3.479>
- Leonetti L, Casciaro R, Garcea G (2015) Effective treatment of complex static and dynamical load combinations within shakedown analysis of 3d frames. *Comput Struct* 158(C):124–139, <https://doi.org/10.1016/j.compstruc.2015.06.002>
- Lima C, Angiolilli M, Barbagallo F, Belletti B, Bergami A, Camata G, Cantagallo C, Di Domenico M, Fiorentino G, Ghersi A, Gregori A, Lavorato D, Luciano R, Marino E, Martinelli E, Nuti C, Ricci P, Rosati L, Ruggieri S, Verderame G (2020) Nonlinear modeling approaches for existing

- reinforced concrete buildings: the case study of De Gasperi-Battaglia School Building in Norcia, pp 82–95
- Lin WH, Chopra A, de la Llera J (2001) Accidental torsion in buildings: analysis versus earthquake motions. *J Struct Eng-ASCE* 127. [https://doi.org/10.1061/\(ASCE\)0733-9445\(2001\)127:5\(475\)](https://doi.org/10.1061/(ASCE)0733-9445(2001)127:5(475))
- Magisano D, Liguori FS, Leonetti L, Garcea G (2018) Minkowski plasticity in 3d frames: decoupled construction of the cross-section yield surface and efficient stress update strategy: Minkowski plasticity in 3d frames. *Int J Numer Methods Eng* 116:435–464. <https://doi.org/10.1002/nme.5931>
- Malena M, Casciaro R (2008) Finite element shakedown analysis of reinforced concrete 3d frames. *Comput Struct* 86:1176–1188
- Marmo F, Rosati L (2012) Analytical integration of elasto-plastic uniaxial constitutive laws over arbitrary sections. *Int J Numer Methods Eng* 91:990–1022. <https://doi.org/10.1002/nme.4316>
- Marmo F, Rosati L (2013) The fiber-free approach in the evaluation of the tangent stiffness matrix for elastoplastic uniaxial constitutive laws. *Int J Numer Methods Eng* 94:868–894. <https://doi.org/10.1002/nme.4484>
- Marmo F, Rosati L, Sessa S (2008) Exact integration of uniaxial elasto-plastic laws for nonlinear structural analysis. *AIP Conf Proc* 1020:1219–1226
- Marmo F, Serpieri R, Rosati L (2011) Ultimate strength analysis of prestressed reinforced concrete sections under axial force and biaxial bending. *Comput Struct* 89:91–108. <https://doi.org/10.1016/j.compstruc.2010.08.005>
- Marmo F, Sessa S, Rosati L (2016) Analytical solution of the cerruti problem under linearly distributed horizontal loads over polygonal domains. *J Elasticity* 124. <https://doi.org/10.1007/s10659-015-9560-3>
- Marmo F, Sessa S, Vaiana N, De Gregorio D, Rosati L (2020) Complete solutions of three-dimensional problems in transversely isotropic media. *Continuum Mech Thermodyn* 32. <https://doi.org/10.1007/s00161-018-0733-8>
- Marmo F, Demartino C, Candela G, Sulpizio C, Briseghella B, Spagnuolo R, Xiao Y, Vanzi I, Rosati L (2019) On the form of the Musmeci's bridge over the basento river. *Eng Struct* 191:658–673. <https://doi.org/10.1016/j.engstruct.2019.04.069>
- Matuszak A (2017) Errors of stress numerical integration for cross-sections with straight and curved boundaries. *Comput Assisted Methods Eng Sci* 22(2):153–176. <https://ames.ippt.pan.pl/index.php/ames/article/view/34>
- Matuszak A, Pluciński P (2014) Accuracy of cross-section stress numerical integration by boundary integration formulae, pp 111–120. <https://doi.org/10.1201/b16513-16>
- Menun C (2004a) An envelope for Mohr's circle in seismically excited three-dimensional structures. *Earthq Eng Struct D* 33:981–998
- Menun C (2004b) Strategies for identifying critical seismic response combinations. *Earthq Spectra* 20. <https://doi.org/10.1193/1.1806148>
- Menun C, Der Kiureghian A (2000a) Envelopes for seismic response vectors. I: Theory. *J Struct Eng-ASCE* 126. [https://doi.org/10.1061/\(ASCE\)0733-9445\(2000\)126:4\(467\)](https://doi.org/10.1061/(ASCE)0733-9445(2000)126:4(467))
- Menun C, Der Kiureghian A (2000b) Envelopes for seismic response vectors. II: Application. *J Struct Eng-ASCE* 126. [https://doi.org/10.1061/\(ASCE\)0733-9445\(2000\)126:4\(474\)](https://doi.org/10.1061/(ASCE)0733-9445(2000)126:4(474))
- Nazarov Y, Poznyak E, Filimonov A (2015) A brief theory and computing of seismic ground rotations for structural analyses. *Soil Dyn Earthq Eng* 71:31–41. <https://doi.org/10.1016/j.soildyn.2015.01.013>
- NBCC (2005) National building code of Canada (NBCC). Standard, National Research Council of Canada, Ottawa, Canada
- Newmark NM (1969) Torsion in symmetrical buildings. *Proc 4th World Conf Earthq Eng* 3:19–32
- NZS 1170, (2004) Structural design actions, Part 5: Earthquake actions. Standard, New Zealand
- Papanikolaou V, Sextos A (2016) Design charts for rectangular R/C columns under biaxial bending: a historical review toward a eurocode-2 compliant update. *Eng Struct* 115:196–206. <https://doi.org/10.1016/j.engstruct.2016.02.033>

- Paradiso M, Vaiana N, Sessa S, Marmo F, Rosati L (2020) A BEM approach to the evaluation of warping functions in the saint Venant theory. *Eng Anal Boundary Elements* 113:359–371. <https://doi.org/10.1016/j.enganabound.2020.01.004>
- Paradiso M, Sessa S, Vaiana N, Marmo F, Rosati L (2021) Shear properties of isotropic and homogeneous beam-like solids having arbitrary cross sections. *Int J Solids Struct* 216. <https://doi.org/10.1016/j.ijsolstr.2021.01.012>
- Placidi L, Barchiesi E, Misra A (2018) A strain gradient variational approach to damage: a comparison with damage gradient models and numerical results. *Math Mech Complex Syst* 6:77–100. <https://doi.org/10.2140/memocs.2018.6.77>
- Placidi L, Misra A, Barchiesi E (2019) Simulation results for damage with evolving microstructure and growing strain gradient moduli. *Continuum Mech Thermodyn* 31. <https://doi.org/10.1007/s00161-018-0693-z>
- Salman O, Francois P, Spagnuolo M (2019) Mean green operators of deformable fiber networks embedded in a compliant matrix and property estimates. *Continuum Mech Thermodyn* 31. <https://doi.org/10.1007/s00161-018-0668-0>
- Selna LG, Lawder JH (1977) Biaxial inelastic frame seismic behavior. *Publ SP Am Concr Inst SP-53. Am Concr Inst Annu Conv, San Francisco, Calif* 53:439–461
- Sessa S, Marmo F, Rosati L (2015) Effective use of seismic response envelopes for reinforced concrete structures. *Earthq Eng Struct D* 44(14):2401–2423
- Sessa S, Serpieri R, Rosati L (2017a) A continuum theory of through-the-thickness jacketed shells for the elasto-plastic analysis of confined composite structures: theory and numerical assessment. *Comp Part B Eng* 113. <https://doi.org/10.1016/j.compositesb.2017.01.011>
- Sessa S, Serpieri R, Rosati L (2017b) Probabilistic assessment of historical masonry walls retrofitted with through-the-thickness confinement devices. *AIMETA 2017— Proc 23rd Conf Italian Ass Th App Mech* 3:2324–2332
- Sessa S, Marmo F, Rosati L, Leonetti L, Garcea G, Casciaro R (2018a) Evaluation of the capacity surfaces of reinforced concrete sections: Eurocode versus a plasticity-based approach. *Meccanica* 53(6):1493–1512
- Serpieri R, Sessa S, Rosati L (2018) A MITC-based procedure for the numerical integration of a continuum elastic-plastic theory of through-the-thickness-jacketed shell structures. *Comput Struct* 191:209–220
- Sessa S, Marmo F, Vaiana N, Rosati L (2018b) A computational strategy for eurocode 8-compliant analyses of reinforced concrete structures by seismic envelopes. *J Earthq Eng* 25:1–34. <https://doi.org/10.1080/13632469.2018.1551161>
- Sessa S, Marmo F, Vaiana N, De Gregorio D, Rosati L (2019a) Strength hierarchy provisions for transverse confinement systems of shell structural elements. *Comp Part B Eng* 163:413–423. <https://doi.org/10.1016/j.compositesb.2019.01.018>
- Sessa S, Marmo F, Vaiana N, Rosati L (2019b) Probabilistic assessment of axial force-biaxial bending capacity domains of reinforced concrete sections. *Meccanica* 54. <https://doi.org/10.1007/s11012-019-00979-4>
- Shakib H (2004) Evaluation of dynamic eccentricity by considering soil-structure interaction: a proposal for seismic design codes. *Soil Dyn Earthq Eng* 24:369–378. <https://doi.org/10.1016/j.soildyn.2004.01.003>
- Silva V, Barros H, Júlio E, Ferreira C (2009) Closed form ultimate strength of multi-rectangle reinforced concrete sections under axial load and biaxial bending. *Comput Concrete* 6:505–521. <https://doi.org/10.12989/cac.2009.6.6.505>
- Simon JW, Weichert D (2012) Shakedown analysis with multidimensional loading spaces. *Comput Mech* 49. <https://doi.org/10.1007/s00466-011-0656-8>
- Smeby W, Der Kiureghian A (1985) Modal combination rules for multicomponent earthquake excitation. *Earthq Eng Struct D* 13(1):1–12
- Spiliopoulos K, Panagiotou K (2017) An enhanced numerical procedure for the shakedown analysis in multidimensional loading domains. *Comput Struct* 193:155–171. <https://doi.org/10.1016/j.compstruc.2017.08.008>

- Valoroso N, Marmo F, Sessa S (2014) Limit state analysis of reinforced shear walls. *Eng Struct* 61:127–139. <https://doi.org/10.1016/j.engstruct.2013.12.032>
- Valoroso N, Marmo F, Sessa S (2015) A novel shell element for nonlinear pushover analysis of reinforced concrete shear walls. *Bull Earthq Eng* 13:2367–2388. <https://doi.org/10.1007/s10518-015-9724-3>
- Wilson E, Der Kiureghian A, Bayo E (1981) A replacement for the SRSS method in seismic analysis. *Earthq Eng Struct D* 9(2):187–192
- Yan Y, Chirikjian G (2015) Closed-form characterization of the Minkowski sum and difference of two ellipsoids. *Geometriae Dedicata* 177:103–128
- Zuccaro G, Dato F, Cacace F, Gregorio D, Sessa S (2017) Seismic collapse mechanisms analyses and masonry structures typologies: a possible correlation. *Ingegneria Sismica* 34:121–149

Chapter 11

Form Finding of Shell Structures by Using Membrane Theory



Francesco Marmo  and Nicolás Vaiana

Abstract A two-step form-finding strategy for determining the heights of a shell of a given plan-form is presented. The shell heights are determined in such a way that the structure can equilibrate applied loads by pure membrane actions. To this end, a set of algebraic equations are obtained by applying the finite difference method to the differential equations derived from the membrane theory of shells. The two-step procedure amounts to compute a distribution of projected membrane stresses that fulfil assigned boundary conditions and to compute shell heights as a function of the membrane stresses computed at the previous step. In case the loads are known in advance, the shell heights are computed in closed form, while the procedure is iterative if loads are expressed as a function of the shell heights. Two numerical examples show the feasibility of the proposed approach.

Keywords Shell structures · Membrane theory · Form finding · Finite difference method

11.1 Introduction

The state of stress in shell structures can be described by means of stress resultants (or internal forces). Their components can be grouped into three categories, i.e., membrane (or tangential), out-of-plane shear and bending-twisting stress resultants (Calladine 1989). When the shell structure is constituted by a uniform material, membrane stress resultants are associated with an even distribution of stresses along the transversal direction of the shell, while out-of-plane shear and bending-twisting

F. Marmo (✉) · N. Vaiana
Department of Structures for Engineering and Architecture, University
of Naples Federic II, via Claudio 21, 80124 Napoli, Italy
e-mail: f.marmo@unina.it

N. Vaiana
e-mail: nicolo.vaiana@unina.it

© Springer Nature Switzerland AG 2021
F. Marmo et al. (eds.), *Mathematical Applications in Continuum
and Structural Mechanics*, Advanced Structured Materials 127,
https://doi.org/10.1007/978-3-030-42707-8_11

internal forces cause higher values of stress near the shell mid-surface and at the extremities of the shell thickness, respectively (Ventsel et al. 2002).

An interesting design strategy for shell structures is that of fostering suitable employment of material by determining a structural form such that a specific design load produces only membrane stress resultants and null out-of-plane shear and bending-twisting internal forces. Such a design approach, nowadays referred to as *form finding* of shells, has a long tradition in the history of structural engineering. Actually, it finds practical applications for the design of one- and two- dimensional structural elements having curved geometry and unilateral material constitution, such as masonry arches and vaults, concrete shells, cable networks and fabric tensile structures.

Although these concepts were not mature in the classical and mediaeval ages, the geometry of masonry and concrete arches and vaults was determined by following simple thumb rules and adopting scale rigid block models with the goal of mitigating and verifying the admissibility of bending internal forces (Huerta Fernández 2006). The design of the shape of these structures started having a scientific foundation after the introduction of the catenary principle (Block et al. 2006). Physical hanging chain models and static graphic constructions based on the use of the funicular polygon were employed since the Renaissance throughout the contemporary era. Famous applications are the networks of hanging strings employed by Huerta (2006) for designing his breathtaking architectural wonders.

In the mid-twentieth century, the catenary principle was translated to that of a funicular membrane by, among others, Addis et al. (2013), who employed hanging cloth models for determining the form of elegant and audacious reinforced concrete shell roofs, and Marmo et al. (2019a), who used soap film and neoprene sheet models to design the bearing structure of a 300 m-long bridge in Southern Italy.

During the same years, computational tools for structural analysis were being developed Clough (2004) and, a few decades later, the same happened for numerical form-finding methods (Bradshaw 2005).

Among the first numerical form-finding methods is the so-called *grid method* (Siev and Eidelman 1964), formulated for the stress analysis cable networks composed of a grid of rod elements. An alternative approach, based on the Dynamic Relaxation Method (DRM), solved form-finding problems by analysing the dynamic equilibrium of a system of springs and masses (Day and Bunce 1970). Its computational efficiency is reached by avoiding matrix assemblage and by employing fictitious damping properties so as to expedite convergence to a steady-state solution.

It was the need of accuracy and efficiency required by the design of the tension structure of the Olympic Park in Tomlow (2016) that pushed the development of more effective computational form-finding tools. On this occasion, Argyris and coworkers (1974) proposed a formulation based on Finite Element Method (FEM) consisting of static analysis of elastic rods in large displacements. Meanwhile, involved in the design of the same structure, Linkwitz and Schek (1971; 1974) formulated the so-called Force Density Method (FDM). Their method computes the nodal coordinates of a network subjected to nodal forces as a function of the ratio between axial forces and lengths, namely *force density*, associated with each branch. The method

is extremely efficient for determining suitable structural forms since it is sufficient to solve a system of linear algebraic equations corresponding to the equilibrium of nodes. However, the method becomes non-linear when additional constraints are added in order to control the distance between nodes or assign a specified value of force in some elements.

In order to deal with the need of assigning non-intuitive quantities such as force densities, a two-stage solving procedure that uses separately horizontal and vertical equilibrium equations can be employed. First, the former equations are used to compute a distribution of force densities as a function of the horizontal components of nodal coordinates, while the latter are employed to evaluate nodal heights as a function of the force densities computed at the first stage of the analysis. This approach, namely the Thrust Network Analysis (TNA), was originally proposed for the limit analysis of masonry vaults (O'Dwyer 1999; Marmo and Rosati 2017; Marmo et al. 2018, 2019b; Fraddosio et al. 2020; Foti et al. 2016; Fraddosio et al. 2019b), and was successfully employed for form-finding compressed shells (Block and Ochsendorf 2007; Fraddosio et al. 2019a) and used to design modern stone vaults (Rippmann et al. 2016).

Since pioneering proposals, which were applicable only to cable networks (Greco et al. 2014), mentioned approaches have further developed by including two-dimensional elements. These have been employed in FEM-based approaches (Tabarrok and Qin 1992), as well as in FDM (Maurin and Motro 1998; Pauletti and Pimenta 2008; Marmo and Rosati 2018), TNA (Marmo and Rosati 2018) and DRM (Barnes 1999, 1988) formulations. Newer formulations combine mentioned approaches with the tools of the isogeometric analysis (Alic and Persson 2016; Philipp et al. 2016).

Methods that employ two-dimensional elements are based on the membrane theory of shells although the relationship between numerical tools and their theoretical foundation is seldom described. This theory represents a theoretical framework in which the height of the shell mid-surface and the membrane resultant components are related by a unique differential equation (Pucher 1934). Several authors have used this equation to find the following forms of compressed shells: Musmeci et al. (1977) employed the Finite Difference Method to solve a simplified version of the basic equation; Fund (2008) developed an FEM-based solution strategy under the hypothesis of isotropic, compressive projected membrane resultants; analytical solutions were proposed by Olivieri et al. (2021) to develop a parametric design of compressed shells; the procedure proposed by Xia et al. (2019) uses an isogeometric analysis approach to design shells subjected to predefined projected membrane resultants.

The mentioned methods employ the membrane theory of shells by assigning a predefined field of projected membrane stress resultants in the form of Airy stress potential function. In addition to being a limitative choice, the arbitrary assignment of the working stresses can sometimes hide the violation of trivial equilibrium conditions. For instance, Xia et al. (2019) presented a series of results obtained by assigning constant projected membrane stresses on the entire shell, even at the free edges of the structure, where thrust has to be null in order to fulfil equilibrium at the free boundary.

The approach proposed below keeps the internal distribution of membrane stress resultants unknown. It is computed by assigning only the projected membrane stress resultants at the boundary of the covered area. These correspond to the design thrusts that the shell is expected to transmit to its supports. Hence, the user can control these quantities and assign them as a system of self-equilibrated actions.

After recalling the membrane theory of shells (Sect. 11.2), a form-finding algorithm based on the Finite Difference Method is formulated in Sect. 11.3. Two numerical examples are presented in Sect. 11.4 to illustrate the validity of the proposed approach. Finally, conclusions and further enhancements of the proposed approach are drawn in Sect. 11.5.

11.2 The Membrane Theory of Shells

A historic overview of the literature about the membrane theory of shells is reported in the bibliography of the book by Flügge (2013). However, among the many proposals listed therein, the most adapt to solve form-finding problems is the formulation by Pucher (1934), holding for shells of general shape. According to Pucher's formulation, the shell is represented by its mid-surface \mathcal{S} subjected to distributed loads \mathbf{p} , defined as forces per unit area of the shell, and to internal actions, represented by the membrane stress (resultants) tensor \mathbf{N} . Equilibrium equations for the points of \mathcal{S} are obtained by considering all forces acting on an infinitesimal element of \mathcal{S} , which, at this scale, can be approximated by the plane \mathcal{P} tangent to \mathcal{S} at the considered point. These equations express, in differential form, the relationship between \mathbf{N} and the shape of the shell mid-surface.

For the reader's convenience, the derivation of Pucher's equilibrium equation is described in full detail below. However, instead of invoking the Airy stress potential, as usual in the classical approach, the components of the membrane stress resultants are kept explicit in the presented formulation. This allows the form-finding algorithm to control the value of the membrane actions at the boundary of \mathcal{S} .

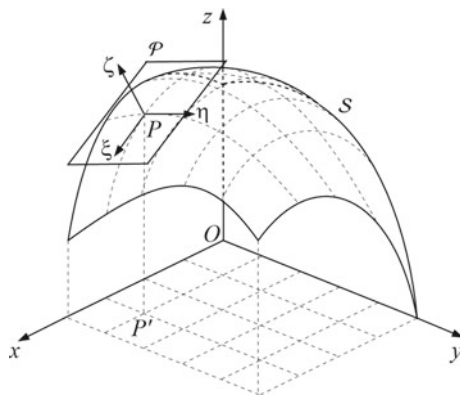
11.2.1 Global and Local Reference Frames

The shell mid-surface \mathcal{S} is defined in a Cartesian reference frame of origin O and axes x , y and z , which have base vectors $\mathbf{x} = (1, 0, 0)$, $\mathbf{y} = (0, 1, 0)$ and $\mathbf{z} = (0, 0, 1)$; see, e.g., Fig. 11.1. The equation that defines \mathcal{S} reads

$$z = f(x, y) \tag{11.1}$$

f being a real-valued function of class C^2 . A generic point of \mathcal{S} has coordinates $P = (x_P, y_P, f(x_P, y_P))$, while its projection on the $x - y$ plane is indicated by $P' = (x_P, y_P, 0)$. Here and below, projections are intended to take place along z .

Fig. 11.1 Global and local reference frames



The plane \mathcal{P} , tangent to S at P , has the equation

$$z = f(x_P, y_P) + f_{,x}(x_P, y_P)(x - x_P) + f_{,y}(x_P, y_P)(y - y_P) \quad (11.2)$$

where the right-hand side corresponds to the first-order Taylor series expansion of f at P' . Projections of the vectors \mathbf{x} and \mathbf{y} on \mathcal{P} give the vectors $\boldsymbol{\xi} = (1, 0, f_{,x})$ and $\boldsymbol{\eta} = (0, 1, f_{,y})$, which are tangent to S at P . Their components are obtained by transforming \mathbf{x} and \mathbf{y} by means of (11.2). The vectors $\boldsymbol{\xi}$, $\boldsymbol{\eta}$ and $\boldsymbol{\zeta} = \boldsymbol{\xi} \times \boldsymbol{\eta} = (-f_{,x}, -f_{,y}, 1)$ form the basis of a local reference frame of axes ξ , η and ζ , centred at P . Notice that being orthogonal to $\boldsymbol{\xi}$ and $\boldsymbol{\eta}$, $\boldsymbol{\zeta}$ is perpendicular to \mathcal{P} and S at P . However, $\boldsymbol{\xi}$ and $\boldsymbol{\eta}$ are neither mutually orthogonal nor of unit length. The vector $\boldsymbol{\zeta}$ as well is not a unit vector. Being used to describe quantities pertaining to an infinitesimal neighbourhood of P , the reference frame (P, ξ, η, ζ) will be referred to as local to distinguish it from the orthonormal reference frame (O, x, y, z) that will be termed global since it will be used to describe an arbitrary quantity referred to the entire shell mid-surface.

While it is convenient to consider membrane stress components in the local reference ξ , η and ζ , loads are more easily assigned in the global reference x , y and z . Additionally, the solution of the set of equilibrium equations is more efficiently obtained in the global reference frame. Hence, prior to writing the local equilibrium equations, i.e., the equilibrium of the shell infinitesimal element, it is useful to obtain the transformation formulas between infinitesimal lengths and areas defined within the mentioned reference frames.

11.2.2 Transformation Formulas for Lengths and Areas

Infinitesimal increments along x and y have components $d\mathbf{x} = (dx, 0, 0)$ and $d\mathbf{y} = (0, dy, 0)$, respectively. Their projection onto \mathcal{P} can be obtained by trans-

forming dx and dy by means of (11.2), which gives $d\xi = (dx, 0, f_{,x} dx)$ and $d\eta = (0, dy, f_{,y} dy)$, respectively. Their norms

$$d\xi = |d\xi| = \sqrt{1 + f_{,x}^2} dx \quad \text{and} \quad d\eta = |d\eta| = \sqrt{1 + f_{,y}^2} dy \quad (11.3)$$

can be used to transform lengths between the local and the global reference frames.

An infinitesimal rectangular region of the $x - y$ plane having sides dx and dy has area $dA' = dx dy$. Its projection on \mathcal{P} corresponds to an infinitesimal parallelogram of sides $d\xi$ and $d\eta$, whose area is

$$dA = |d\xi \times d\eta| = \sqrt{f_{,x}^2 + f_{,y}^2 + 1} dx dy = \sqrt{f_{,x}^2 + f_{,y}^2 + 1} dA' \quad (11.4)$$

This formula transforms areas between considered reference frames.

Within an infinitesimal neighbourhood of P the shell mid-surface \mathcal{S} and its tangent plane \mathcal{P} are indistinguishable. For this reason, transformation formulas for infinitesimal lengths and areas can equivalently be employed for quantities defined either on \mathcal{P} or \mathcal{S} . In particular, this correspondence will be used hereafter for computing the resultants of distributed loads and membrane stresses.

11.2.3 Distributed Loads and Stress Components

Loads applied to the shell mid-surface are modelled as forces per unit area of the shell and are indicated as $\mathbf{p} = (p_x, p_y, p_z)$. The resultant of \mathbf{p} over an infinitesimal region of \mathcal{S} having area dA is

$$\mathbf{p} dA = \mathbf{p} \sqrt{f_{,x}^2 + f_{,y}^2 + 1} dx dy = \mathbf{q} dA' \quad (11.5)$$

where

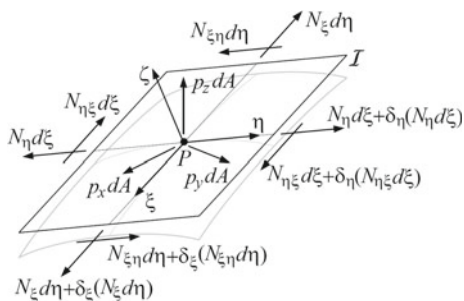
$$\mathbf{q} = \mathbf{p} \sqrt{f_{,x}^2 + f_{,y}^2 + 1} \quad (11.6)$$

takes the meaning of a force per unit projected area and is referred to as projected load.

All components of the membrane stress tensor \mathbf{N} lie within the plane \mathcal{P} . In Fig. 11.2 is represented an infinitesimal neighbourhood \mathcal{I} of P of quadrilateral shape with the opposite sides parallel to ξ and η . These sides have length $d\xi$ and $d\eta$, respectively, and are subjected to the corresponding components of the membrane stress tensor \mathbf{N} , i.e., the membrane stresses denoted as N_ξ , N_η and $N_{\xi\eta} = N_{\eta\xi}$. Accordingly, \mathbf{N} is represented by the matrix

$$\mathbf{N} = \begin{bmatrix} N_\xi & N_{\xi\eta} \\ N_{\xi\eta} & N_\eta \end{bmatrix} \quad (11.7)$$

Fig. 11.2 Load and membrane stress resultants



in the local reference.

The component N_ξ , for instance, acting along ξ , on the side of length $d\eta$, has resultant $N_\xi d\eta$. Employing formulas (11.3)₂, its norm is computed as

$$N_\xi d\eta = N_\xi \sqrt{1 + f_{,y}^2} dy \tag{11.8}$$

in the global reference frame.

The direction of such a stress resultant is represented by the vector $\xi/|\xi|$, which has a unitary norm in the global reference. Hence, according to (11.3), its components in the global reference frame are given by

$$N_\xi d\eta \xi/|\xi| = \left(\frac{\sqrt{1 + f_{,y}^2}}{\sqrt{1 + f_{,x}^2}} N_\xi, 0, \frac{\sqrt{1 + f_{,y}^2}}{\sqrt{1 + f_{,x}^2}} N_\xi f_{,x} \right) dy = (N_x, 0, N_x f_{,x}) dy \tag{11.9}$$

where

$$N_x = \frac{\sqrt{1 + f_{,y}^2}}{\sqrt{1 + f_{,x}^2}} N_\xi \tag{11.10}$$

assumes the meaning of a projected membrane stress component for obvious reasons and represents the first element of the matrix associated with \mathbf{N} in the global reference.

The force $N_\xi d\eta$ is expected to have a variation $\delta_\xi(N_\xi d\eta)$ when moving to the opposite side of \mathcal{I} ; see, e.g., Fig. 11.2. Likewise $N_\xi d\eta$, such a variation has direction $\xi/|\xi|$, so that its components are

$$\delta_\xi(N_\xi d\eta \xi/|\xi|) = [(N_x, 0, N_x f_{,x}) dy]_{,\xi} d\xi = [(N_x, 0, N_x f_{,x}) dy]_{,x} dx \tag{11.11}$$

where formula (11.3)₁ and the chain rule have been applied to express $(\cdot)_{,\xi} d\xi = (\cdot)_{,x} dx$. Thus, the components of $\delta_\xi(N_\xi d\eta)$ in the global reference frame are finally computed as

$$[(N_x, 0, N_x f_{,x}) dy]_{,x} dx = (N_{x,x}, 0, N_{x,x} f_{,x} + N_x f_{,xx}) dx dy \quad (11.12)$$

The same approach can be followed for computing the resultants and the variations of the remaining components of \mathbf{N} . Such resultants have global components

$$\begin{aligned} N_{\xi\eta} d\eta \boldsymbol{\eta}/|\boldsymbol{\eta}| &= (0, N_{xy}, N_{xy} f_{,y}) dy \\ N_{\eta\xi} d\xi \boldsymbol{\xi}/|\boldsymbol{\xi}| &= (N_{yx}, 0, N_{yx} f_{,x}) dx \\ N_{\eta} d\xi \boldsymbol{\eta}/|\boldsymbol{\eta}| &= (0, N_y, N_y f_{,y}) dx \end{aligned} \quad (11.13)$$

where the additional projected membrane stresses

$$N_y = \frac{\sqrt{1 + f_{,x}^2}}{\sqrt{1 + f_{,y}^2}} N_{\eta} \quad \text{and} \quad N_{xy} = N_{yx} = N_{\xi\eta} = N_{\eta\xi} \quad (11.14)$$

have been introduced. The corresponding stress variations are

$$\begin{aligned} \delta_{\xi}(N_{\xi\eta} d\eta \boldsymbol{\eta}/|\boldsymbol{\eta}|) &= (0, N_{xy,x}, N_{xy,x} f_{,y} + N_{xy} f_{,xy}) dx dy \\ \delta_{\eta}(N_{\eta\xi} d\xi \boldsymbol{\xi}/|\boldsymbol{\xi}|) &= (N_{yx,y}, 0, N_{yx,y} f_{,x} + N_{yx} f_{,xy}) dx dy \\ \delta_{\eta}(N_{\eta} d\xi \boldsymbol{\eta}/|\boldsymbol{\eta}|) &= (0, N_{y,y}, N_{y,y} f_{,y} + N_y f_{,yy}) dx dy \end{aligned} \quad (11.15)$$

11.2.4 Equilibrium

Equilibrium equations of \mathcal{I} can be obtained by considering all loads, membrane stress components and relevant variations computed above. Hence, equilibrium along x yields

$$q_x dx dy - N_x dy + N_x dy + N_{x,x} dx dy - N_{yx} dx + N_{yx} dx + N_{yx,y} dx dy = 0 \quad (11.16)$$

Cancelling out opposite addends, employing (11.14)₂ to substitute N_{yx} with N_{xy} , and dividing by $dx dy$, one obtains

$$N_{x,x} + N_{xy,y} + q_x = 0 \quad (11.17)$$

By the same procedure, one can obtain the equilibrium equations along y

$$N_{y,y} + N_{xy,x} + q_y = 0 \quad (11.18)$$

and z

$$N_{x,x}f_{,x} + N_x f_{,xx} + N_{xy,x}f_{,y} + N_{xy,y}f_{,x} + 2N_{xy}f_{,xy} + N_{y,y}f_{,y} + N_y f_{,yy} + q_z = 0 \quad (11.19)$$

where $f_{,yx} = f_{,xy}$ by Shwartz' theorem.

The previous three equations are combined to derive a unique differential equation that represents the complete equilibrium of an infinitesimal element of the shell mid-surface. The classical approach for combining previous equations employs the analogy between formulas (11.17) and (11.18) and the equilibrium equations of a plane stress problem. Accordingly, the horizontal equilibrium equations can be solved by introducing the Airy stress function Φ . Thus, the membrane stress components

$$N_x = \Phi_{,yy} - \int q_x dx \quad N_y = \Phi_{,xx} - \int q_y dy \quad N_{xy} = -\Phi_{,xy} \quad (11.20)$$

solve Eqs. (11.17) and (11.18). Use of previous positions into (11.19) yields

$$\Phi_{,yy}f_{,xx} - 2\Phi_{,xy}f_{,xy} + \Phi_{,xx}f_{,yy} = q_x f_{,x} + \int q_x dx f_{,xx} + q_y f_{,y} + \int q_y dy f_{,yy} - q_z \quad (11.21)$$

which is the definitive equilibrium equation of the membrane theory of shells.

The previous equation replaces the set of three differential equations (11.17)–(11.19). For this reason, it is easier to handle when the stress field is unknown. Actually, all membrane stress components are here substituted by a unique unknown stress function Φ . Instead, in form-finding analyses, it is preferable to control working membrane stresses. Hence, it is convenient to consider the original set of differential equations, which is explicitly expressed as a function of membrane stress components.

However, Eq. (11.19) can be rewritten in a simpler form by obtaining $N_{xy,x}$ and $N_{xy,y}$ from (11.17) and (11.18),

$$N_{xy,y} = -N_{x,x} - q_x \quad N_{xy,x} = -N_{y,y} - q_y \quad (11.22)$$

and then substituting these two derivatives into (11.19) to get

$$N_x f_{,xx} + 2N_{xy}f_{,xy} + N_y f_{,yy} - q_x f_{,x} - q_y f_{,y} + q_z = 0 \quad (11.23)$$

which replaces (11.19).

Accordingly, Eqs. (11.17), (11.18) and (11.23) can be used to determine the height f of a shell mid-surface in such a way that applied loads can be equilibrated by pure membrane stresses. The problem can be solved in two phases: first, a suitable distribution of projected membrane stresses is assigned, then the height of the shell mid-surface is computed as a function of the assigned membrane stresses. In more complicated situations, projected values of loads are a function of the shell height. In this case, the previous two phases are iterated.

11.3 Form-Finding Algorithm

The proposed form-finding algorithm employs Eqs. (11.17) and (11.18) to define an equilibrated distribution of projected membrane stresses N_x , N_y and N_{xy} . However, these equations are not sufficient to determine a unique distribution of projected membrane stresses; hence, an additional equation is required. To this end, the proposed methodology makes use of the analogy between Eqs. (11.17) and (11.18) and the equilibrium equations of a plane stress problem. Accordingly, the compatibility equation associated with isotropic plane stress problems (Timoshenko and Goodier 1951) is considered. It reads

$$N_{x,xx} + N_{x,yy} + N_{y,xx} + N_{y,yy} = -(1 - \nu)(q_{x,x} + q_{y,y}) \quad (11.24)$$

and, together with (11.17) and (11.18), it is used to define a suitable distribution of projected membrane stresses.

Once projected membrane stresses are defined, the form-finding analysis proceeds with the evaluation of the value assumed by function f . It is computed from Eq. (11.23) and relevant boundary conditions.

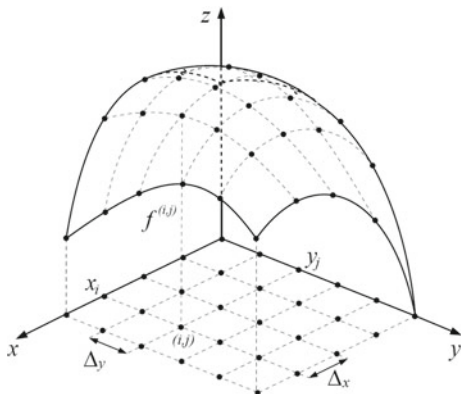
In more general cases, projected values of loads are not given in advance. This is the case, for example, in which distributed loads represent the shell self-weight. In this case, the value of projected loads can be computed only after the height of shell mid-surface is determined. For this reason, an iterative procedure is required. It amounts to computing the projected membrane stresses \mathbf{N} and the shell mid-surface height f at each iteration for a tentative distribution of projected loads. Then the corresponding value of projected loads is updated according to the last estimate of f . The procedure is iterated until two successive estimates of f differ by less than a given tolerance.

The phases of the form-finding analysis described above are solved by specific algorithms that will be illustrated below in full detail. However, these algorithms amount to solve one or more differential equations corresponding to the projected equilibrium equation of the membrane theory of shells and the compatibility equation of isotropic plane stress. Hence, prior to describing each algorithm, the discretization of such differential equations by the Finite Difference Method is recalled hereafter.

11.3.1 Discretization of the Equilibrium Equations by the Finite Difference Method

The differential equations (11.17), (11.18), (11.23) and (11.24) are converted into a set of algebraic equations by employing the finite difference method. Accordingly, these equations are written for a discrete set of points positioned at the nodes of a rectangular grid defined on the domain of integration, which lies on the $x - y$ plane.

Fig. 11.3 Grid of nodes on the $x - y$ plane



For simplicity, grid spacing is assumed constant and equal to Δ_x and Δ_y along the two directions of the reference frame; see, e.g., Fig. 11.3.

The grid is composed of $I \times J$ nodes, each having coordinates (x_i, y_j) and identified by the pair of indices (i, j) . The value assumed by a generic quantity F at the node (i, j) is indicated as $F^{(i, j)} = F(x_i, y_j)$. Hence, Eqs. (11.17), (11.18), (11.23) and (11.24) are rewritten for a generic node as

$$N_{x,x}^{(i, j)} + N_{xy,y}^{(i, j)} + q_x^{(i, j)} = 0 \tag{11.25}$$

$$N_{y,y}^{(i, j)} + N_{xy,x}^{(i, j)} + q_y^{(i, j)} = 0 \tag{11.26}$$

$$N_x^{(i, j)} f_{,xx}^{(i, j)} + 2N_{xy}^{(i, j)} f_{,xy}^{(i, j)} + N_y^{(i, j)} f_{,yy}^{(i, j)} - q_x^{(i, j)} f_{,x}^{(i, j)} - q_y^{(i, j)} f_{,y}^{(i, j)} + q_z^{(i, j)} = 0 \tag{11.27}$$

and

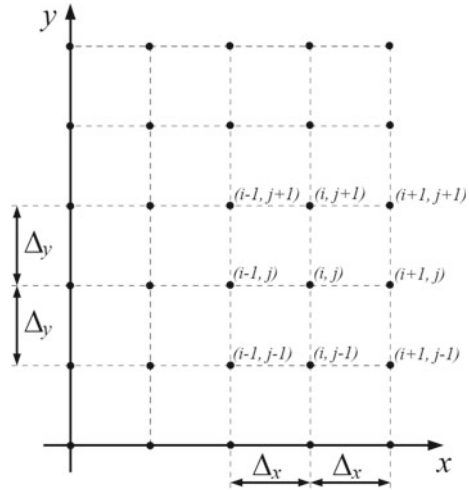
$$N_{x,xx}^{(i, j)} + N_{x,yy}^{(i, j)} + N_{y,xx}^{(i, j)} + N_{y,yy}^{(i, j)} = -(1 - \nu)(q_{x,x}^{(i, j)} + q_{y,y}^{(i, j)}) \tag{11.28}$$

The differential nature of these equations can be eliminated by considering the second-order Taylor series expansion of all differentiated quantities. Actually, a generic function F can be approximated as

$$F(x, y) \approx F^{(i, j)} + (x - x_i)F_{,x}^{(i, j)} + (y - y_j)F_{,y}^{(i, j)} + \frac{(x - x_i)^2}{2}F_{,xx}^{(i, j)} + \frac{(y - y_j)^2}{2}F_{,yy}^{(i, j)} + (x - x_i)(y - y_j)F_{,xy}^{(i, j)} \tag{11.29}$$

This formula can be used to rewrite the derivatives of F at the generic node (i, j) as a function of the values assumed by F at the 8 nodes that surround the considered node; see, e.g., Fig. 11.4.

Fig. 11.4 Node (i, j) and surrounding 8 nodes



Setting $x = x_i + \Delta_x$ and $y = y_j$, the previous formula is used to compute an approximate estimate of $F(x_i + \Delta_x, y_j) = F^{(i+1, j)}$, that is,

$$F^{(i+1, j)} \approx F^{(i, j)} + \Delta_x F_{,x}^{(i, j)} + \frac{\Delta_x^2}{2} F_{,xx}^{(i, j)} \tag{11.30}$$

while, setting $x = x_i - \Delta_x$ and $y = y_j$, one has

$$F^{(i-1, j)} \approx F^{(i, j)} - \Delta_x F_{,x}^{(i, j)} + \frac{\Delta_x^2}{2} F_{,xx}^{(i, j)} \tag{11.31}$$

Subtracting (11.30) from (11.31), one obtains

$$F^{(i+1, j)} - F^{(i-1, j)} \approx 2\Delta_x F_{,x}^{(i, j)} \Leftrightarrow F_{,x}^{(i, j)} \approx \frac{F^{(i+1, j)} - F^{(i-1, j)}}{2\Delta_x} \tag{11.32}$$

while the sum of the same equations yields

$$F^{(i+1, j)} + F^{(i-1, j)} \approx 2F^{(i, j)} + \Delta_x^2 F_{,xx}^{(i, j)} \Leftrightarrow F_{,xx}^{(i, j)} \approx \frac{F^{(i+1, j)} + F^{(i-1, j)} - 2F^{(i, j)}}{\Delta_x^2} \tag{11.33}$$

Similarly, using (11.29) to approximate $F(x_i, y_j + \Delta_y) = F^{(i, j+1)}$ and $F(x_i, y_j - \Delta_y) = F^{(i, j-1)}$, one has

$$F^{(i, j+1)} \approx F^{(i, j)} + \Delta_y F_{,y}^{(i, j)} + \frac{\Delta_y^2}{2} F_{,yy}^{(i, j)}, \quad F^{(i, j-1)} \approx F^{(i, j)} - \Delta_y F_{,y}^{(i, j)} + \frac{\Delta_y^2}{2} F_{,yy}^{(i, j)} \tag{11.34}$$

which can be subtracted or added to get

$$F_{,y}^{(i,j)} \approx \frac{F^{(i,j+1)} - F^{(i,j-1)}}{2\Delta_y}, \quad F_{,xy}^{(i,j)} \approx \frac{F^{(i,j+1)} + F^{(i,j-1)} - 2F^{(i,j)}}{\Delta_y^2} \quad (11.35)$$

For estimating the value of mixed derivative $F_{,xy}^{(i,j)}$, formula (11.29) is used to compute the four values $F(x_i \pm \Delta_x, y_j \pm \Delta_y) = F^{(i\pm 1, j\pm 1)}$ as

$$\begin{aligned} F^{(i+1,j+1)} &\approx F^{(i,j)} + \Delta_x F_{,x}^{(i,j)} + \Delta_y F_{,y}^{(i,j)} + \frac{\Delta_x^2}{2} F_{,xx}^{(i,j)} + \Delta_x \Delta_y F_{,xy}^{(i,j)} + \frac{\Delta_y^2}{2} F_{,yy}^{(i,j)} \\ F^{(i-1,j-1)} &\approx F^{(i,j)} - \Delta_x F_{,x}^{(i,j)} - \Delta_y F_{,y}^{(i,j)} + \frac{\Delta_x^2}{2} F_{,xx}^{(i,j)} + \Delta_x \Delta_y F_{,xy}^{(i,j)} + \frac{\Delta_y^2}{2} F_{,yy}^{(i,j)} \\ F^{(i-1,j+1)} &\approx F^{(i,j)} - \Delta_x F_{,x}^{(i,j)} + \Delta_y F_{,y}^{(i,j)} + \frac{\Delta_x^2}{2} F_{,xx}^{(i,j)} - \Delta_x \Delta_y F_{,xy}^{(i,j)} + \frac{\Delta_y^2}{2} F_{,yy}^{(i,j)} \\ F^{(i+1,j-1)} &\approx F^{(i,j)} + \Delta_x F_{,x}^{(i,j)} - \Delta_y F_{,y}^{(i,j)} + \frac{\Delta_x^2}{2} F_{,xx}^{(i,j)} - \Delta_x \Delta_y F_{,xy}^{(i,j)} + \frac{\Delta_y^2}{2} F_{,yy}^{(i,j)} \end{aligned} \quad (11.36)$$

Subtraction of the last two equations from the sum of the first two furnishes

$$F_{,xy}^{(i,j)} \approx \frac{F^{(i+1,j+1)} + F^{(i-1,j-1)} - F^{(i-1,j+1)} - F^{(i+1,j-1)}}{4\Delta_x \Delta_y} \quad (11.37)$$

Finally, employing formulas (11.32), (11.33), (11.35) and (11.37), one can rewrite the differential equations (11.25), (11.26), (11.27) and (11.28) in the form of algebraic equations as follows:

$$\frac{1}{2\Delta_x} [N_x^{(i+1,j)} - N_x^{(i-1,j)}] + \frac{1}{2\Delta_y} [N_{xy}^{(i,j+1)} - N_{xy}^{(i,j-1)}] + q_x^{(i,j)} = 0 \quad (11.38)$$

$$\frac{1}{2\Delta_y} [N_y^{(i,j+1)} - N_y^{(i,j-1)}] + \frac{1}{2\Delta_x} [N_{xy}^{(i+1,j)} - N_{xy}^{(i-1,j)}] + q_y^{(i,j)} = 0 \quad (11.39)$$

$$\begin{aligned} \frac{N_x^{(i,j)}}{\Delta_x^2} [f^{(i+1,j)} + f^{(i-1,j)} - 2f^{(i,j)}] + \frac{N_y^{(i,j)}}{\Delta_y^2} [f^{(i,j+1)} + f^{(i,j-1)} - 2f^{(i,j)}] + \\ + \frac{N_{xy}^{(i,j)}}{2\Delta_x \Delta_y} [f^{(i+1,j+1)} + f^{(i-1,j-1)} - f^{(i-1,j+1)} - f^{(i+1,j-1)}] + \\ - \frac{q_x^{(i,j)}}{2\Delta_x} [f^{(i+1,j)} - f^{(i-1,j)}] - \frac{q_y^{(i,j)}}{2\Delta_y} [f^{(i,j+1)} - f^{(i,j-1)}] + q_z^{(i,j)} = 0 \end{aligned} \quad (11.40)$$

and

$$\begin{aligned} & \frac{1}{\Delta_x^2} [N_x^{(i+1, j)} + N_y^{(i+1, j)} + N_x^{(i-1, j)} + N_y^{(i-1, j)} - 2N_x^{(i, j)} - 2N_y^{(i, j)}] + \\ & \frac{1}{\Delta_y^2} [N_x^{(i, j+1)} + N_y^{(i, j+1)} + N_x^{(i, j-1)} + N_y^{(i, j-1)} - 2N_x^{(i, j)} - 2N_y^{(i, j)}] + \\ & \frac{1+\nu}{2\Delta_x} [q_x^{(i+1, j)} - q_x^{(i-1, j)}] + \frac{1+\nu}{2\Delta_y} [q_y^{(i, j+1)} - q_y^{(i, j-1)}] = 0 \end{aligned} \quad (11.41)$$

11.3.2 Assigning the Distribution of Projected Membrane Stresses

The distribution of projected membrane stresses is assigned by solving a system of three differential equations corresponding to the horizontal equilibrium (11.17) and (11.18) and the compatibility Eq. (11.24). In order to control thrusts at supports and to impose null stresses on the free edges of the shell, projected tractions \mathbf{Nn} are assigned on the entire boundary of the region covered by the shell, \mathbf{n} being the outward unit vector associated with the boundary. In particular, it is set as $\mathbf{Nn} = \mathbf{0}$ on the free boundary, while \mathbf{Nn} can be set arbitrarily on the supported boundary. These values constitute the boundary conditions holding for the mentioned differential equations.

Following the Finite Difference Method, this set of differential equations is transformed into the corresponding algebraic counterpart (11.38), (11.39) and (11.41). The corresponding set of equations is

$$\mathbf{Dh} = -\mathbf{q}_h \quad (11.42)$$

where \mathbf{D} is a matrix of coefficients, \mathbf{h} is the vector collecting sets of triplets (N_x, N_y, N_{xy}) associated with each node, while \mathbf{q}_h collects known terms. The vector \mathbf{h}_K is split into \mathbf{h}_K , which collects the Known values of projected membrane stress, i.e., those assigned through the boundary conditions, and by \mathbf{h}_U collecting the Unknown ones. The vector \mathbf{q}_h and the coefficient matrix \mathbf{D} are partitioned correspondingly, so that the previous equation is rewritten as

$$\begin{cases} \mathbf{D}_{UU}\mathbf{h}_U + \mathbf{D}_{UK}\mathbf{h}_K = -\mathbf{q}_{hU} \\ \mathbf{D}_{KU}\mathbf{h}_U + \mathbf{D}_{KK}\mathbf{h}_K = -\mathbf{q}_{hK} \end{cases} \quad (11.43)$$

The first equation is used to compute the unknown values of projected membrane stresses as

$$\mathbf{h}_U = -\mathbf{D}_{UU}^{-1}(\mathbf{q}_{hU} + \mathbf{D}_{UK}\mathbf{h}_K) \quad (11.44)$$

Since the second equation is not used, there is no need to assemble equations corresponding to the boundary nodes. Hence, no special treatment is required for equations relevant to these nodes.

11.3.3 Evaluation of the Shell Mid-Surface Height

After the projected membrane stress components are assigned, the height f of the shell mid-surface needs to be computed. This is done by solving the set of algebraic equations corresponding to the vertical equilibrium of each node of the discretized domain of integration, which is represented by Eq. (11.40). In order to account for suitable boundary conditions, the nodes of the boundary are grouped into two sets, respectively, corresponding to i) the nodes where the shell mid-surface has unknown height, and ii) those where f is given.

This first set of nodes correspond to the free boundary of the shell so that, by equilibrium, $\mathbf{Nn} = \mathbf{0}$ at these nodes. Accordingly, the vertical equilibrium equation can be simplified for these nodes. In particular, one has $N_x = N_{xy} = 0$ at nodes pertaining to the free boundary of outward normal $\pm x$. Similarly, one has $N_y = N_{xy} = 0$ on the free boundary of outward normal $\pm y$.

For these nodes, a reformulation of the vertical equilibrium equation is also required since it involves the values that f attains at nodes positioned outside the domain of integration. To this end, the approximate evaluation of the first derivatives, given by formulas (11.32)₂ and (11.35)₁, are substituted by those obtained by truncating the Taylor series expansions (11.30), (11.31) and (11.34) to the linear term. Accordingly, for the nodes pertaining to the free boundaries of outward normal $+x$ and $-x$, one has

$$F_{,x}^{(i,j)} \approx \frac{F^{(i,j)} - F^{(i-1,j)}}{\Delta_x} \quad F_{,x}^{(i,j)} \approx \frac{F^{(i+1,j)} - F^{(i,j)}}{\Delta_x} \quad (11.45)$$

respectively, while the expressions

$$F_{,y}^{(i,j)} \approx \frac{F^{(i,j)} - F^{(i,j-1)}}{\Delta_y} \quad F_{,y}^{(i,j)} \approx \frac{F^{(i,j+1)} - F^{(i,j)}}{\Delta_y} \quad (11.46)$$

are used, respectively, for the nodes of the free boundaries of outward normal $+y$ and $-y$.

Hence, for the nodes of the free boundaries of normal $+x$, $-x$, $+y$ and $-y$, Eq. (11.40) modifies to

$$\begin{aligned} & \frac{N_y^{(i,j)}}{\Delta_y^2} [f^{(i,j+1)} + f^{(i,j-1)} - 2f^{(i,j)}] + \\ & - \frac{q_x^{(i,j)}}{\Delta_x} [f^{(i,j)} - f^{(i-1,j)}] - \frac{q_y^{(i,j)}}{2\Delta_y} [f^{(i,j+1)} - f^{(i,j-1)}] + q_z^{(i,j)} = 0 \end{aligned} \quad (11.47)$$

$$\begin{aligned} & \frac{N_y^{(i,j)}}{\Delta_y^2} [f^{(i,j+1)} + f^{(i,j-1)} - 2f^{(i,j)}] + \\ & - \frac{q_x^{(i,j)}}{\Delta_x} [f^{(i,j)} - f^{(i-1,j)}] - \frac{q_y^{(i,j)}}{2\Delta_y} [f^{(i,j+1)} - f^{(i,j-1)}] + q_z^{(i,j)} = 0 \end{aligned} \quad (11.48)$$

$$\begin{aligned} & \frac{N_x^{(i,j)}}{\Delta_x^2} [f^{(i+1,j)} + f^{(i-1,j)} - 2f^{(i,j)}] + \\ & - \frac{q_x^{(i,j)}}{2\Delta_x} [f^{(i+1,j)} - f^{(i-1,j)}] - \frac{q_y^{(i,j)}}{\Delta_y} [f^{(i,j)} - f^{(i,j-1)}] + q_z^{(i,j)} = 0 \end{aligned} \quad (11.49)$$

and

$$\begin{aligned} & \frac{N_x^{(i,j)}}{\Delta_x^2} [f^{(i+1,j)} + f^{(i-1,j)} - 2f^{(i,j)}] + \\ & - \frac{q_x^{(i,j)}}{2\Delta_x} [f^{(i+1,j)} - f^{(i-1,j)}] - \frac{q_y^{(i,j)}}{\Delta_y} [f^{(i,j+1)} - f^{(i,j)}] + q_z^{(i,j)} = 0 \end{aligned} \quad (11.50)$$

respectively.

Similarly, at the corner nodes, if pertaining to the free boundary, Eq. (11.40) is substituted by

$$- \frac{q_x^{(i,j)}}{\Delta_x} [f^{(i,j)} - f^{(i-1,j)}] - \frac{q_y^{(i,j)}}{\Delta_y} [f^{(i,j)} - f^{(i,j-1)}] + q_z^{(i,j)} = 0 \quad (11.51)$$

for the node positioned at the corner between the boundaries of outward normals $+x$ and $+y$, while

$$- \frac{q_x^{(i,j)}}{\Delta_x} [f^{(i,j)} - f^{(i-1,j)}] - \frac{q_y^{(i,j)}}{\Delta_y} [f^{(i,j+1)} - f^{(i,j)}] + q_z^{(i,j)} = 0 \quad (11.52)$$

$$- \frac{q_x^{(i,j)}}{\Delta_x} [f^{(i+1,j)} - f^{(i,j)}] - \frac{q_y^{(i,j)}}{\Delta_y} [f^{(i,j)} - f^{(i,j-1)}] + q_z^{(i,j)} = 0 \quad (11.53)$$

$$- \frac{q_x^{(i,j)}}{\Delta_x} [f^{(i+1,j)} - f^{(i,j)}] - \frac{q_y^{(i,j)}}{\Delta_y} [f^{(i,j+1)} - f^{(i,j)}] + q_z^{(i,j)} = 0 \quad (11.54)$$

are used for the corners $(+x, -y)$, $(-x, +y)$ and $(-x, -y)$, respectively. From these last four equations, it is clear that, in the case of purely vertical loads, corner nodes cannot pertain to the free boundary.

Conversely, the vertical equilibrium equations of nodes pertaining to the constrained boundary, i.e., where f is given, are not even assembled since they are not used to solve the form-finding problem. Actually, the full set of equations, comprising those relevant to both internal and boundary nodes, is symbolically written as

$$\mathbf{C}\mathbf{f} = -\mathbf{q}_z \quad (11.55)$$

where \mathbf{C} is a matrix of coefficients, while the vectors \mathbf{f} and \mathbf{q}_z collect the nodal values $f^{(i,j)}$ and $q_z^{(i,j)}$, respectively.

Vectors \mathbf{f} and \mathbf{q}_z are split into the sub-vectors \mathbf{f}_U and \mathbf{f}_K , \mathbf{q}_{zU} and \mathbf{q}_{zK} by selecting the elements corresponding to the nodes where f is Unknown, i.e., internal nodes and those pertaining to the free boundary of the shell, and those where f is Known. The coefficient matrix \mathbf{C} is partitioned into four sub-matrices accordingly. Hence, the system of vertical equilibrium equations of nodes is rewritten as

$$\begin{cases} \mathbf{C}_{UU}\mathbf{f}_U + \mathbf{C}_{UK}\mathbf{f}_K = -\mathbf{q}_{zU} \\ \mathbf{C}_{KU}\mathbf{f}_U + \mathbf{C}_{KK}\mathbf{f}_K = -\mathbf{q}_{zK} \end{cases} \quad (11.56)$$

The unknown values of f are computed by solving the first equation as

$$\mathbf{f}_U = -\mathbf{C}_{UU}^{-1}(\mathbf{q}_{zU} + \mathbf{C}_{UK}\mathbf{f}_K) \quad (11.57)$$

while the second equation is not used. Consequently, only the rows of \mathbf{C} corresponding to the nodes where f is unknown are needed. Accordingly, the vertical equilibrium equations of nodes where f is known are not assembled.

11.3.4 Iterative Procedure for Assigning Projected Loads

In many form-finding analyses, the value of projected loads depends on the shell form. Practical examples are those in which the load represents the shell self-weight or the weight of a coating distributed on the shell. In such cases, it is convenient to assign the load as a force per unit area of the shell mid-surface, namely the quantity \mathbf{p} in formula (11.5). Hence, the evaluation of the corresponding projection can be done only after the height of the shell is evaluated.

Actually, if the load \mathbf{p} keeps its direction independently from the form of the shell, it is sufficient to employ formula (11.5) to evaluate the corresponding projection \mathbf{q} . Of course, this formula can be applied, only after that the shell mid-surface height f has been computed for each node of the model, which in turn depend on the assumed values of the projected load. Hence, an iterative procedure is implemented as described hereafter.

At the generic k th iteration, a tentative value for f is estimated for each node of the model, namely $f_k^{(i,j)}$. At first iteration, the procedure is initiated by assigning $f_1^{(i,j)} = 0$ at all nodes.

These values are then used to evaluate nodal values of projected loads by means of the numerical counterpart of formula (11.5), which is obtained by substituting the derivatives of f by formulas (11.32) and (11.35)₁, according to the Finite Difference Method. This gives the k th estimate of the projected loads

$$\mathbf{q}_k^{(i,j)} = \mathbf{p}^{(i,j)} \sqrt{\frac{\left[f_k^{(i+1,j)} - f_k^{(i-1,j)} \right]^2}{4\Delta_x^2} + \frac{\left[f_k^{(i,j+1)} - f_k^{(i,j-1)} \right]^2}{4\Delta_y^2}} + 1 \quad (11.58)$$

Recall that the previous formula needs to be suitably corrected for boundary nodes, where formulas (11.45) and (11.46) are used in place of (11.32) and (11.35)₁ for the evaluation of the numerical derivatives of f .

Current values of projected loads are then used to assign projected membrane stresses and evaluate a new estimate of nodal heights, that is, $f_{k+1}^{(i,j)}$. These values are then used at the next iteration to repeat the same sequence of operations.

Convergence is reached when the relative difference between successive values of applied projected loads is lower than a given tolerance tol , that is,

$$\left| \mathbf{q}_{k+1}^{(i,j)} - \mathbf{q}_k^{(i,j)} \right| \leq tol \left| \mathbf{q}_k^{(i,j)} \right| \quad \forall i, j \quad (11.59)$$

11.4 Numerical Examples

In order to show the feasibility of the presented form-finding algorithm, we consider the case of two fully compressed shells, both covering a rectangular area of sides $L_x \times L_y = 4m \times 6m$. A grid of 40×60 equally spaced nodes is assumed for discretizing the shell plan-form. The origin of the reference frame is positioned at the centre of the covered area so that the rectangle is defined by $L_x/2 \leq x \leq L_x/2$, $L_y/2 \leq y \leq L_y/2$.

Shells have a constant thickness $t = 0.2m$ and their material has weight per unit volume $d = 24kN/m^3$. Accordingly, assuming that the shell is subjected to its own weight, the vertical load applied to the shell's surface amounts to $p_z = -d \times t = -4.8kN/m^2$.

The difference between the two shells is at their boundaries. The first is supported on three sides, while the boundary of outward normal $+y$ is free. The second is supported only at corners, while central parts of the four sides are free.

11.4.1 Shell with One Free Side

A distribution of boundary thrusts that satisfies the global equilibrium of the shell is assigned. In particular, null thrusts are assigned to the nodes of the free boundary while compressive thrusts are assigned to the sides of outward normal $\pm x$ and $-y$, as follows:

$$\text{Side } -x: N_x = \frac{A}{3} \left(y + \frac{L_y}{2} \right), N_{xy} = -\frac{B}{2} \left(1 - \frac{4y^2}{L_y^2} \right)$$

$$\text{Side } +x: N_x = \frac{A}{3} \left(y + \frac{L_y}{2} \right), N_{xy} = \frac{B}{2} \left(1 - \frac{4y^2}{L_y^2} \right)$$

$$\text{Side } -y: N_y = B \frac{L_y}{L_x} \left(1 - \frac{4x^2}{L_x^2} \right), N_{xy} = 0$$

$$\text{Side } +y: N_y = 0, N_{xy} = 0$$

Numerical parameters A and B have been chosen so as to have a semi-negative definite (compressive) projected membrane resultant tensor \mathbf{N} on the entire shell plan-form. This assignment is done iteratively, by computing the projected membrane resultants by means of formula (11.44) for some given values of A and B and then correcting these tentative values in order to have compressive principal projected stress resultants on the entire domain. This condition is fulfilled when $A = 2B = 2p_z$. The corresponding principal values and directions of the projected membrane stresses are represented in Fig. 11.5. Segments drawn in this figure are parallel to the principal directions of \mathbf{N} , and lengths are proportional to the corresponding principal values. Red and blue colours are used for negative and positive principal values, respectively, and, as shown, no tensile principal stress resultants have been computed.

This distribution of projected stress resultants is then used to compute nodal heights according to the iterative procedure described in Sect. 11.3.4. Assuming a tolerance $tol = 10^{-3}$, convergence is reached after 6 iterations and the corresponding shell form is reported in Fig. 11.6, where an isometry and two side views of the solution are drawn.

11.4.2 Shell Supported at Corners

A shell supported at corners has been selected as a second example. Only a small region of each side of the covered area is supported, that is, a portion $\Delta = 0.25 m$ wide, next to each corner. Boundary horizontal thrusts are assigned as a function of the distance δ between the considered node and corners. Accordingly, for the nodes near the south-west corner, the following thrusts are applied:

$$\text{SW corner } (\delta \leq \Delta), \text{ Side } -x: N_y = -1.25 C(\Delta - \delta), N_{xy} = -C(\Delta - \delta)$$

$$\text{SW corner } (\delta \leq \Delta), \text{ Side } -y: N_x = -C(\Delta - \delta), N_{xy} = -C(\Delta - \delta)$$

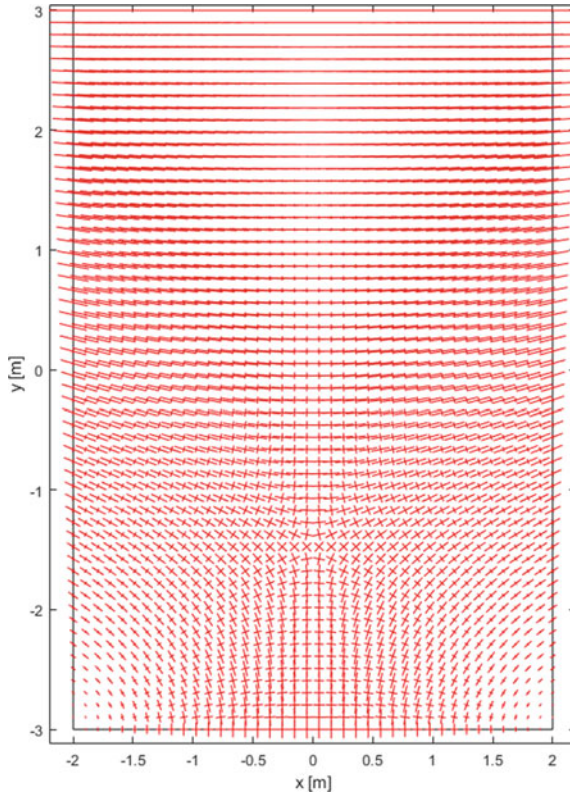


Fig. 11.5 Principal values and directions of the projected stress resultants for the shell with one free side

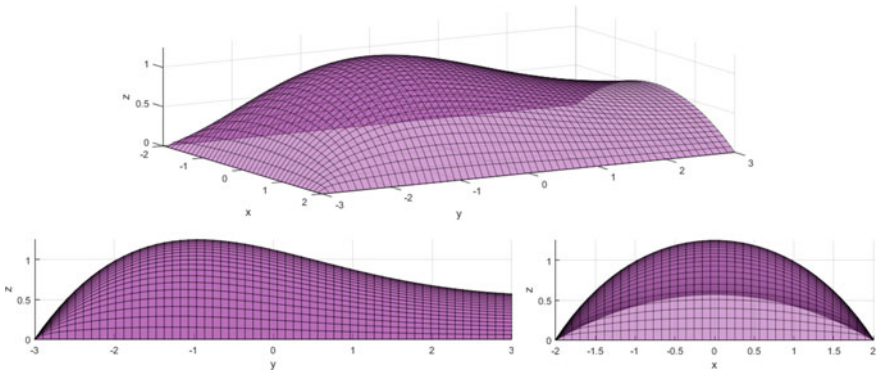


Fig. 11.6 Isometry and side views of the form-found shell with one free side

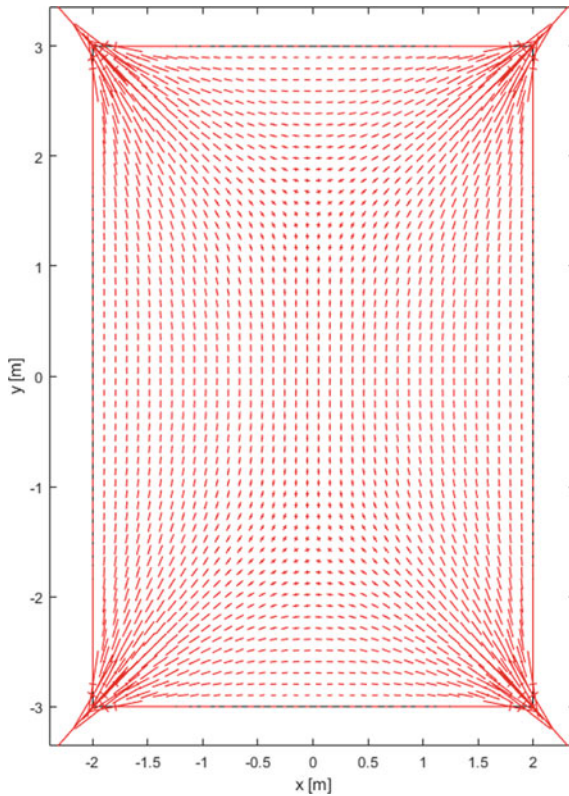


Fig. 11.7 Principal values and directions of the projected stress resultants for the shell supported at corners

Similar boundary conditions, modified in sign in order to guarantee compressive thrusts, are assigned at nodes pertaining to the portion of the boundary near the other corners of the covered area. The numerical parameter C is assigned in such a way that the maximum height of the form-found shell is slightly below 1.5 m . Accordingly, C has been assumed equal to $C = 90p_z$. The corresponding distribution of projected stress resultants is reported in Fig. 11.7.

The computed distribution of \mathbf{N} generates the nodal heights depicted in Fig. 11.8 when the iterative procedure described in Sect. 11.3.4 is employed. This form has been obtained after 6 iterations by setting a tolerance $tol = 10^{-3}$.

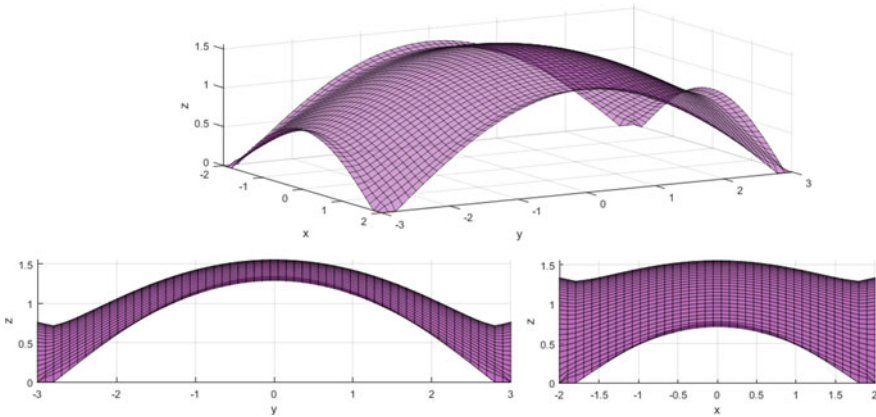


Fig. 11.8 Isometric and side views of the form-found shell supported at corners

11.5 Conclusion

A form-finding algorithm based on the membrane theory of shells has been presented. The numerical implementation of the equilibrium equations is obtained by the Finite Difference Method. In order to avoid any predefined distribution of projected membrane stresses, an additional equation corresponding to the compatibility condition of plane stress problems has been employed. The proposed approach employs an iterative procedure in order to adjust the initially unknown distribution of projected load components. Two numerical examples show the feasibility of the presented method which is capable to find the form of compressed shells having a rectangular plan.

Further enhancements of the presented approach will regard the following issues:

(i) The compatibility equation used by the presented form-finding procedure is relevant to plane stress elasticity problems defined on the horizontal plane, while the stress state is plane on the shell mid-surface. Hence, the feasibility of such an equation needs to be further investigated. In this regards, it is useful to adopt the approach followed in (Flügge and Geyling 1957) to derive a more suitable equation that will substitute the one employed in the presented approach.

(ii) A more general optimization of the shell form can be achieved by introducing an additional unknown function representing the shell thickness. Consequently, a modification of the presented iterative procedure is required since distributed loads representing the shell self-weight need to be modified accordingly.

(iii) The employment of the Finite Difference Method to discretize the basic differential equations restricts the field of application of the presented method to shells having a rectangular plan. In this regard, improved implementations of the Finite Difference Method have been presented in the literature; see, e.g., Liszka and Orkisz (1980), which expand the field of applicability of the proposed approach.

(iv) The presented procedure can be used to define the form of the shell mid-surface, but proper algorithms are required for a comprehensive design of this kind of structures. In particular, for reinforced concrete shells, proper modelling techniques are required to account for the complex (Altenbach and Eremeyev 2009; Altenbach et al. 2010; Tran et al. 2020; De Angelo et al. 2019; Andreaus et al. 2018) and the non-linear (Contrafatto and Cuomo 2006; Valoroso et al. 2014, 2015; Placidi et al. 2018) behaviour of materials, transverse interaction (Sessa et al. 2017; Serpieri et al. 2018; Sessa et al. 2019; Abd-alla et al. 2017), surface stresses (Altenbach et al. 2009) and finite deformations (Eremeyev and Zubov 2007; Barchiesi et al. 2020a, b; Franciosi et al. 2019).

References

- AenN Abd-alla, Alshaikh F, Del Vescovo D, Spagnuolo M (2017) Plane waves and eigenfrequency study in a transversely isotropic magneto-thermoelastic medium under the effect of a constant angular velocity. *J Therm Stress* 40(9):1079–1092
- Addis B et al (2013) Toys that save millions: a history of using physical models in the design of building structures. *SESOC J* 26(2):28
- Alic V, Persson K (2016) Form finding with dynamic relaxation and isogeometric membrane elements. *Comput Methods Appl Mech Eng* 300:734–747
- Altenbach H, Eremeyev VA (2009) On the linear theory of micropolar plates. *ZAMM-J Appl Math Mech/Zeitschrift für Angewandte Mathematik und Mechanik* 89(4):242–256
- Altenbach H, Eremeyev V, Morozov N (2009) Linear theory of shells taking into account surface stresses. *Doklady Phys* 54:531–535
- Altenbach J, Altenbach H, Eremeyev VA (2010) On generalized cosserat-type theories of plates and shells: a short review and bibliography. *Archive Appl Mech* 80(1):73–92
- Andreaus U, Spagnuolo M, Lekszycki T, Eugster SR (2018) A ritz approach for the static analysis of planar pantographic structures modeled with nonlinear euler-bernoulli beams. *Continuum Mech Thermodyn* 30(5):1103–1123
- Argyris JH, Angelopoulos T, Bichat B (1974) A general method for the shape finding of lightweight tension structures. *Comput Methods Appl Mech Eng* 3(1):135–149
- Barchiesi E, dell’Isola F, Hild F, Seppacher P (2020a) Two-dimensional continua capable of large elastic extension in two independent directions: asymptotic homogenization, numerical simulations and experimental evidence. *Mech Res Commun* 103(103):466
- Barchiesi E, Eugster SR, Dell’isola F, Hild F (2020b) Large in-plane elastic deformations of bi-pantographic fabrics: asymptotic homogenization and experimental validation. *Math Mech Solids* 25(3):739–767
- Barnes MR (1988) Form-finding and analysis of prestressed nets and membranes. *Comput Struct* 30(3):685–695
- Barnes MR (1999) Form finding and analysis of tension structures by dynamic relaxation. *Int J Space Struct* 14(2):89–104
- Block P, Ochsendorf J (2007) Thrust network analysis: a new methodology for three-dimensional equilibrium. *J Int Assoc Shell Spatial Struct* 48(3):167–173
- Block P, DeJong M, Ochsendorf J (2006) As hangs the flexible line: equilibrium of masonry arches. *Nexus Netw J* 8(2):13–24
- Bradshaw RR (2005) History of the analysis of cable net structures. In: *Structures congress 2005: metropolis and beyond*, pp 1–11
- Calladine CR (1989) *Theory of shell structures*. Cambridge University Press

- Clough RW (2004) Early history of the finite element method from the view point of a pioneer. *Int J Numer Methods Eng* 60(1):283–287
- Contrafatto L, Cuomo M (2006) A framework of elastic-plastic damaging model for concrete under multiaxial stress states. *Int J Plastic* 22(12):2272–2300
- Day A, Bunce J (1970) Analysis of cable networks by dynamic relaxation. *Civil Eng Public Works Rev* 4:383–386
- De Angelo M, Spagnuolo M, D’annibale F, Pfaff A, Hoschke K, Misra A, Dupuy C, Peyre P, Dirrenberger J, Pawlikowski M, (2019) The macroscopic behavior of pantographic sheets depends mainly on their microstructure: experimental evidence and qualitative analysis of damage in metallic specimens. *Continuum Mech Thermodyn* 31(4):1181–1203
- Eremeyev V, Zubov L (2007) On constitutive inequalities in nonlinear theory of elastic shells. *ZAMM-J Appl Math Mech/Zeitschrift für Angewandte Mathematik und Mechanik: Applied Mathematics and Mechanics* 87(2):94–101
- Flügge W (2013) *Stresses in shells*. Springer
- Flügge W, Geyling F (1957) A general theory of deformations of membrane shells. *Int Assoc Bridg Struct Eng* 17:23
- Foti P, Fraddosio A, Lepore N, Piccioni MD (2016) Three-dimensional lower-bound analysis of masonry structures. In: *Proceeding of the third international conference on structures and architecture*, Guimaraes, Portugal
- Fraddosio A, Lepore N, Piccioni MD (2019a) Further refinement of the corbelling theory for the equilibrium analysis of corbelled domes. *Curved Layer Struct* 6(1):30–40
- Fraddosio A, Lepore N, Piccioni MD (2019b) Lower bound limit analysis of masonry vaults under general load conditions. In: *Structural analysis of historical constructions*, Springer, pp 1090–1098
- Fraddosio A, Lepore N, Piccioni MD (2020) Thrust surface method: An innovative approach for the three-dimensional lower bound limit analysis of masonry vaults. *Eng Struct* 202(109):846
- Franciosi P, Spagnuolo M, Salman OU (2019) Mean green operators of deformable fiber networks embedded in a compliant matrix and property estimates. *Continuum Mech Thermodyn* 31(1):101–132
- Fund AI (2008) *Form-finding structures*. PhD thesis, Massachusetts Institute of Technology
- Greco L, Impollonia N, Cuomo M (2014) A procedure for the static analysis of cable structures following elastic catenary theory. *Int J Solids Struct* 51(7–8):1521–1533
- Huerta S (2006) *Structural design in the work of Gaudi*. *Architec Sci Rev* 49(4):324–339
- Huerta Fernández S (2006) *Geometry and equilibrium: the gothic theory of structural design*. *Struct Eng* 84(2):23–28
- Linkwitz K, Schek HJ (1971) Einige bemerkungen zur berechnung von vorgespannten seilnetzkonstruktionen. *Ingenieur-Archiv* 40(3):145–158
- Liszka T, Orkisz J (1980) The finite difference method at arbitrary irregular grids and its application in applied mechanics. *Comput Struct* 11(1–2):83–95
- Marmo F, Rosati L (2017) Reformulation and extension of the thrust network analysis. *Comput Struct* 182:104–118
- Marmo F, Rosati L (2018) Form finding of compressed shells by the thrust membrane analysis. In: *Proceedings of IASS annual symposia, international association for shell and spatial structures (IASS)*, vol 2018, pp 1–6
- Marmo F, Masi D, Rosati L (2018) Thrust network analysis of masonry helical staircases. *Int J Architec Heritage* 12(5):828–848
- Marmo F, Demartino C, Candela G, Sulpizio C, Briseghella B, Spagnuolo R, Xiao Y, Vanzi I, Rosati L (2019a) On the form of the musmeci’s bridge over the basento river. *Eng Struct* 191:658–673
- Marmo F, Ruggieri N, Toraldo F, Rosati L (2019b) Historical study and static assessment of an innovative vaulting technique of the 19th century. *Int J Archit Heritage* 13(6):799–819
- Maurin B, Motro R (1998) The surface stress density method as a form-finding tool for tensile membranes. *Eng Struct* 20(8):712–719
- Musmeci S, et al (1977) *Ponte sul basento a patenza*. L’industria Italiana del Cemento

- O'Dwyer D (1999) Funicular analysis of masonry vaults. *Comput Struct* 73(1–5):187–197
- Olivieri C, Angelillo M, Gesualdo A, Iannuzzo A, Fortunato A (2021) Parametric design of purely compressed shells. *Mech Mater* 155(103):782
- Pauletti RM, Pimenta PM (2008) The natural force density method for the shape finding of taut structures. *Comput Methods Appl Mech Eng* 197(49–50):4419–4428
- Philipp B, Breitenberger M, D'Auria I, Wüchner R, Bletzinger KU (2016) Integrated design and analysis of structural membranes using the isogeometric b-rep analysis. *Comput Method Appl Mech Eng* 303:312–340
- Placidi L, Misra A, Barchiesi E (2018) Two-dimensional strain gradient damage modeling: a variational approach. *Zeitschrift für angewandte Mathematik und Physik* 69(3):1–19
- Pucher A (1934) Über den spannungszustand in gekrümmten flächen. *Beton und Eisen* 33:298
- Rippmann M, Van Mele T, Popescu M, Augustynowicz E, Méndez Echenagucia T, Calvo Barentin CJ, Frick U, Block P (2016) The armadillo vault: Computational design and digital fabrication of a freeform stone shell. *Adv Architect Geometry* 2016:344–363
- Schek HJ (1974) The force density method for form finding and computation of general networks. *Comput Methods Appl Mech Eng* 3(1):115–134
- Serpieri R, Sessa S, Rosati L (2018) A mitc-based procedure for the numerical integration of a continuum elastic-plastic theory of through-the-thickness-jacketed shell structures. *Compos Struct* 191:209–220
- Sessa S, Serpieri R, Rosati L (2017) A continuum theory of through-the-thickness jacketed shells for the elasto-plastic analysis of confined composite structures: Theory and numerical assessment. *Compos Part B Eng* 113:225–242
- Sessa S, Marmo F, Vaiana N, De Gregorio D, Rosati L (2019) Strength hierarchy provisions for transverse confinement systems of shell structural elements. *Compos Part B Eng* 163:413–423
- Siev A, Eidelman J (1964) Stress analysis of prestressed suspended roofs. *J Struct Div* 90(4):103–121
- Tabarrok B, Qin Z (1992) Nonlinear analysis of tension structures. *Comput Struct* 45(5–6):973–984
- Timoshenko S, Goodier J (1951) *Theory of elasticity*, 1951. New York 412:108
- Tomlow J (2016) Designing and constructing the Olympic roof (Munich 1972). *Int J Space Struct* 31(1):62–73
- Tran CA, Gołaszewski M, Barchiesi E (2020) Symmetric-in-plane compression of polyamide pantographic fabrics-modelling, experiments and numerical exploration. *Symmetry* 12(5):693
- Valoroso N, Marmo F, Sessa S (2014) Limit state analysis of reinforced shear walls. *Eng Struct* 61:127–139
- Valoroso N, Marmo F, Sessa S (2015) A novel shell element for nonlinear pushover analysis of reinforced concrete shear walls. *Bull Earthq Eng* 13(8):2367–2388
- Ventsel E, Krauthammer T, Carrera E (2002) Thin plates and shells: theory, analysis, and applications. *Appl Mech Rev* 55(4):B72–B73
- Xia Y, Mantzafaris A, Jüttler B, Pan H, Hu P, Wang W (2019) Design of self-supporting surfaces with isogeometric analysis. *Comput Method Appl Mech Eng* 353:328–347

Chapter 12

Influence of Non-structural Components on Equivalent Linearization of Buildings



Salvatore Sessa  and Luciano Rosati

Abstract Influence of non-structural elements on the seismic response of nonlinear systems is hereby investigated. In particular, tail-equivalent linearization has been adopted because of its capability of determining the statistics of stochastic response processes in order to characterize secondary excitation. A random vibration analysis determined a parameter range, characterizing the dynamic properties of non-structural components, for which the linearized system is not influenced by the presence of such devices. Numerical results show that tail equivalent linearization is an appealing strategy for the characterization of secondary seismic excitations.

Keywords Equivalent linearization · Seismic analysis · Nonlinear systems · Tail-equivalent linearization · Stochastic response · Vibration analysis

12.1 Introduction

Seismic events recently occurred worldwide have drawn attention on the influence of non-structural devices on the seismic response of nonlinear buildings. To this end, such secondary devices have been classified in several typologies and classes (FEMA 1994) in order to evaluate secondary seismic actions by means of dynamic filters.

Moreover, such a topic is of particular importance in assessing structural resilience (Chiaia et al. 2019) as well as for the case of seismic protection of cultural heritage artifacts exposed in museums (Calio and Marletta 2003) or of archaeological vestiges. In the latter cases, several elements, such as balustrades, roofs, or ruins, can be not part of the main structure although they be an essential part to be preserved by proper analyses adopting secondary excitations. At the same time, presence of such devices

S. Sessa (✉) · L. Rosati
University of Naples Federico II, via Claudio 21, Napoli, Italy
e-mail: salvatore.sessa2@unina.it

L. Rosati
e-mail: rosati@unina.it

may strongly influence the dynamic response of the main structure and, subsequently, the secondary excitation.

Given the importance of properly account for nonlinearity of structures subject to dynamic loads, several approaches have been proposed in the last decades including variational strategies (Barchiesi and Khakalo 2019) and Lagrangian methods (Turco et al. 2019, 2020; Andreus et al. 2018).

Within the context of equivalent linearization approaches, the Tail-Equivalent Linearization Method, proposed by Fujimura and Der Kiureghian (2007), is a particularly effective strategy which defines a linearized system by means of a collection of response functions in the time or frequency domain (Garrè and Der Kiureghian 2010).

Compared to traditional linearization strategies, such an approach proved to be more accurate (Kiureghian and Fujimura 2009) and is capable to address multicomponent (Broccardo and Der Kiureghian 2016) and multisupport (Wang and Der Kiureghian 2016) seismic actions as well as multi-objective responses (Sessa 2010). More in general, a representation of structural responses in frequency and time domain is a very powerful technique which can be also used to characterize even more complex problems (Alibert et al. 2003; Barchiesi et al. 2018; Dell'Isola et al. 2019).

Since the dynamic response of a nonlinear system can be significantly adulterated by non-structural devices (Badillo-Almaraz et al. 2007; Milton et al. 2009; Villaverde 1997), the definition of the linearized system should properly account for their presence within the mechanical system. Unfortunately, common procedures of structural design are not sufficiently detailed to model non-structural parts which are merely introduced as additional masses and loads. On the contrary, a proper computation of the linearized system and of secondary excitations must properly account for the dynamic behavior of secondary devices.

The present research investigates the influence of non-structural devices on the tail-equivalent linearized system of nonlinear buildings by introducing a parametrized secondary oscillator in the structural system.

Specifically, a brief review of the TELM is reported in Sect. 12.2 while Sect. 12.3 presents the computation of the linearized system and Sect. 12.3.1 discusses the response sensitivity with respect to the mass and stiffness properties of the secondary devices.

Moreover, statistics of the random process representing the peak response is computed in Sect. 12.3.2 by means of first excursion probability in order to determine boundary intervals of the properties of non-structural devices for which their influence on the structural response is negligible.

Numerical results prove that such an interval includes several typologies of secondary devices so that they can be neglected in performing tail equivalent analysis.

12.2 Brief Review of Tail-Equivalent Linearization

Conceptually, the Tail-Equivalent Linearization Method (TELM) determines a linearized system by equating the tail probability of its response with the first-order approximation of the tail probability relevant to the nonlinear structure for a fixed threshold.

Let F be a discretized representation of a stochastic excitation:

$$F(t) = \sum_{i=1}^n s_i(t)u_i = \mathbf{s}(t)\mathbf{u} \quad (12.1)$$

where $s_i(t)$ are deterministic functions depending on the covariance of the seismic random process and u_i are n random variables defined in the standard normal space.

Denoted by $X(\hat{t})$ the response of the nonlinear structure, its tail probability relevant to a threshold of interest x^* and to an instant-in-time \hat{t} is defined by

$$\Pr[X(\hat{t}) \leq x^*]$$

and its first-order approximation is associated with the solution \mathbf{u}^* (or *performance point*) of the optimization problem:

$$\mathbf{u}^*(\hat{t}, x^*) = \arg \min [\|\mathbf{u}\| \mid x^* - X(\hat{t}) = 0] \quad (12.2)$$

which can be computed by the First-Order Reliability Method (FORM) (Ditlevsen and Madsen 1996).

The dynamic response $X_l(\hat{t})$ of a linear oscillator can be computed by means of a convolution integral:

$$X_l(\hat{t}) = \int_0^{\hat{t}} h(\tau) \sum_{i=1}^n s_i(\tau)u_i d\tau = \mathbf{a}(\hat{t}) \cdot \mathbf{u} \quad (12.3)$$

where $h(\tau)$ represents the Impulse Response Function (IRF) of a linear system.

Enforcing an equivalence condition between the linear and nonlinear response at the performance point permits to compute a deterministic vector $a_j(\hat{t})$ as

$$\mathbf{a}(\hat{t}) = \frac{x^*}{\|\mathbf{u}^*(x^*, \hat{t})\|} \frac{\mathbf{u}^*(x^*, \hat{t})}{\|\mathbf{u}^*(x^*, \hat{t})\|} \quad (12.4)$$

whose components are associated with the IRF of the linear system:

$$a_j(\hat{t}) = \sum_{j=1}^n h(\hat{t} - \tau_j) s_i(\tau_j) \Delta t \quad (12.5)$$

Therefore, the impulse response function $\hat{h}(t, \hat{t}, x^*)$ of a linearized system associated with the threshold x^* and at time \hat{t} can be computed by inverting Equation (12.5) which represents a linear system of equations.

It is worth being emphasized that the explicit dependency of the IRF on the threshold and time is due to the fact that, for different values of x^* and \hat{t} , the nonlinear structure provides a distinct response and subsequently it is associated with a different linearized system.

A Tail-Equivalent Linearized System can be defined by computing the IRFs associated with an array of thresholds x_k^* . Such functions proved to be insensitive to amplitude and frequency content of the base excitation (Fujimura and Der Kiureghian 2007).

In order to use the TELS within the context of random vibration analysis, it is useful to define the Frequency Response Functions (FRFs) as the Fourier transforms of the IRFs:

$$H(f, \hat{t}, x_k^*) = \int_0^\infty \hat{h}(\tau, \hat{t}, x_k^*) \exp(-i\omega\tau) d\tau \quad (12.6)$$

where $\omega = 2\pi f$ denotes the pulsation and f is the frequency.

The stationary response X of the linearized system can be characterized by its power spectral density $\Phi_{XX}(f, \hat{t}, x_k^*)$ computed as

$$\Phi_{XX}(f, \hat{t}, x_k^*) = \Phi_{FF}(f, \hat{t}, x_k^*) |H(f, \hat{t}, x_k^*)|^2 \quad (12.7)$$

where Φ_{FF} is the power spectral density of the base excitation.

12.3 Influence of Secondary Devices on TELS

In order to investigate the influence of non-structural devices on the response of the global structural system, a case study consisting of a 4-storey building is defined. It has been analyzed in OpenSees, a finite-element object-oriented framework (Mazzoni et al. 2006), capable of performing TELM analyses.

According to Fujimura and Der Kiureghian (2007), the system has been modeled by defining the interaction between adjacent floors by means of a Bouc-Wen nonlinear relationship (Baber and Noori 1985). Specifically, the inter-story shear force $R(t)$ is defined by

$$R(t) = \alpha k_0 v(t) + (1 - \alpha) k_0 z(t) \quad (12.8)$$

where $v(t)$ is the inter-story drift, k_0 is the initial stiffness, α is the yield ratio, and $z(t)$ is a nonlinear inter-story drift whose first time-derivative is

$$\dot{z}(t) = \dot{v}(t) \{A_0 - [\beta \text{sign}(\dot{v}(t)) |z(t)|^{n-1} z(t) + \gamma |z(t)|^n]\} \quad (12.9)$$

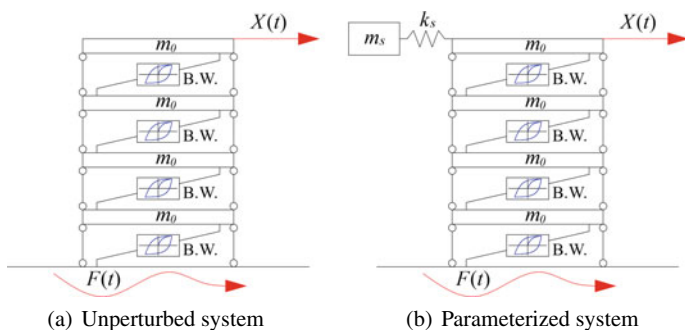


Fig. 12.1 Structural schemes of the unperturbed and parameterized structural systems

Each floor has mass $m_0 = 3 \cdot 10^5$ kg; constitutive parameters have been assumed $\alpha = 0.05$, $A_0 = 2$, $n = 1$. Stiffness k_0 is computed so that a linear oscillator with mass m_0 has natural frequency of 5 Hz and finally $\gamma = \beta = 1/(2\nu_y)$ where $\nu_y = 0.0182$ m is the equivalent yield inter-story drift.

Figure 12.1a shows the model representing the main structure where the structural response of interest $X(t)$ is the horizontal displacement at the top floor. Note that in such a model no secondary device has been introduced; thus, it will be referred to as *unperturbed system*.

The *perturbed system*, shown in Fig. 12.1b, is defined by introducing in the unperturbed model a linear oscillator representing the non-structural devices. Such a Parametrized Oscillator (PO) is constrained at the top floor and is defined by means of mass m_s and frequency f_s so that its stiffness turns out to be $k_s = (2\pi f_s)^2 m_s$.

Tail-Equivalent linearization is performed for both the structural models in order to compare the linearized systems associated with the perturbed and unperturbed structure. To this end, a set of parameters characterizing the secondary device have been adopted. In particular, the oscillator mass m_s spans within the interval $[0.01m_0, m_0]$ while its natural frequency belongs to the interval $[0.5, 30.0]$ Hz plus the further limit case of $f_s = \infty$.

Linearized systems have been determined by means of the frequency response functions $H_U(f, x^*)$ and $H_P(f, x^*, m_s, f_s)$ relevant to the unperturbed and parameterized structure, respectively. For the latter case, dependency of the FRFs on m_s and f_s has been explicitly reported.

12.3.1 Frequency Content Comparison

A first comparison between the parameterized and unperturbed system can be made in terms of frequency response functions in order to investigate the influence of the PO on the frequency content of the system.

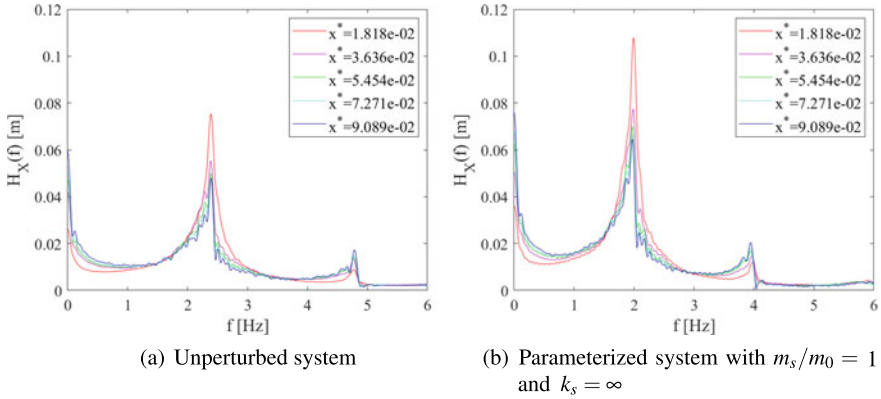


Fig. 12.2 TELS frequency response functions depending on the threshold x^*

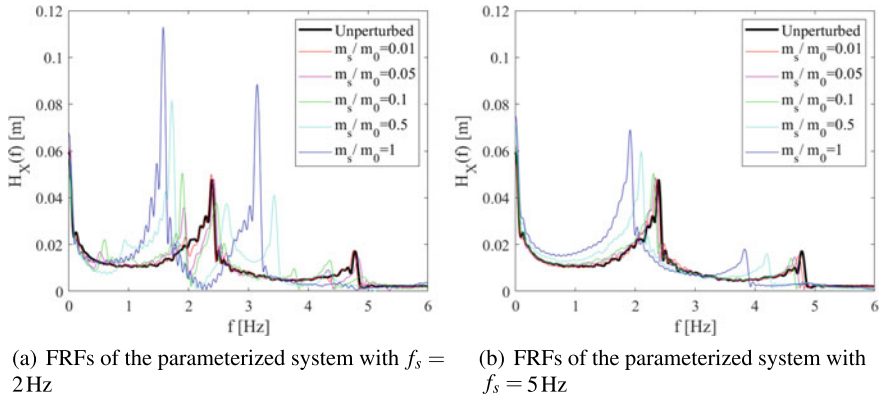
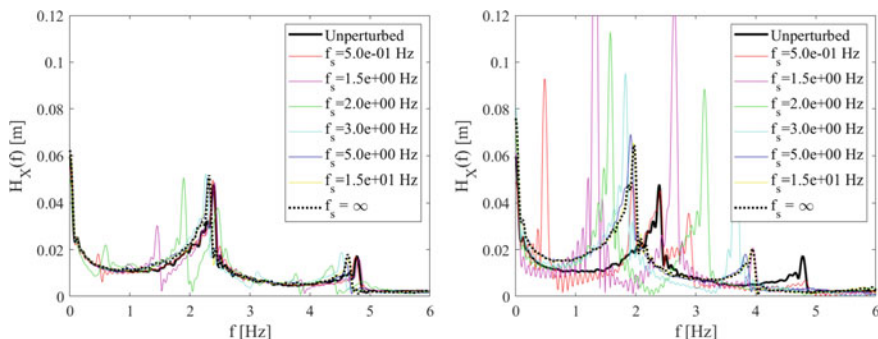


Fig. 12.3 TELS frequency response functions at threshold $x^* = 45.45$ mm depending on the PO mass m_s

Figure 12.2a reports the FRFs of the unperturbed system associated with thresholds x^* . The dominant structural frequency occurs at about 2.5 Hz; moreover, both the peak amplitude and the dominant frequency of the FRFs are inversely proportional to the threshold value.

Frequency response functions relevant to the parametrized system with $f_s = \infty$ and $m_s/m_0 = 1$ are reported in Fig. 12.3b. Such a model represents a limit case since the mass of the secondary device is equal to the floor mass and the PO is infinitely stiff meaning that its mass is perfectly constrained to the top floor. In particular, such modeling assumptions correspond to a structural design which introduces the secondary devices in the model merely as masses and loads.

Functions reported in Fig. 12.2b show that the peaks are significantly higher than the corresponding ones of the unperturbed model and occur at lower frequencies



(a) FRFs of the parameterized system with $m_s/m_0 = 0.1$ (b) FRFs of the parameterized system with $m_s/m_0 = 1$

Fig. 12.4 TELS frequency response functions at threshold $x^* = 45.45$ mm depending on the PO frequency f_s

meaning that the model is stiffer. As a consequence, a random vibration analysis would compute very different response statistics for the considered models.

In general, such a limit case is not frequent in common practice; hence, it is essential to investigate the dependency of the structural response with respect to the mass m_s of the secondary device. To this end, Fig. 12.3a and b report the FRFs at threshold $x^* = 45.45$ mm associated with frequencies $f_s = 2$ Hz and $f_s = 5$ Hz, respectively.

In both the cases, amplitude of the FRFs associated with low mass ratios remains almost unaltered meaning that the influence of the secondary device is limited. Moreover, higher values of m_s turn out to significantly influence the frequency content of the model since the FRFs present a further peak nearby the natural frequency of the PO.

Such an issue is significant for the case of $f_s = 2$ Hz; in particular, for $m_s/m_0 > 0.1$ FRFs present multi-mode behavior and peaks significantly shifted from their unperturbed location. On the contrary, influence of the PO on the functions relevant to $f_s = 5$ Hz, reported in Fig. 12.3b, turns out to be less significant.

The different sensitivity of such FRFs is due to the fact that the value $f_s = 2$ Hz is very close to the dominant frequency of the main structure so that the system presents resonance phenomena. On the contrary, the value $f_s = 5$ Hz implies that the PO behaves as a sort of mass damper reducing the frequency of the system.

Frequency response functions reported in Fig. 12.4a and b, relevant to secondary oscillators with varying natural frequency and mass ratios $m_s/m_0 = 0.1$ and $m_s/m_0 = 1$, respectively, confirm the qualitative behavior deduced by comparing Fig. 12.3a and b.

In particular, Fig. 12.4a shows that the effects of oscillators with limited mass on the structural response are significant only if the dominant frequencies of the secondary oscillator and of the main structure are similar. Specifically, for $f_s = 2$ Hz

and $f_s = 3$ Hz, resonance is triggered while for different values of f_s the curves present limited differences from the unperturbed case.

A further aspect can be observed by analyzing curves relevant to $m_s/m_0 = 1$ reported in Fig. 12.4b. Structural frequency response is strongly adulterated by the presence of a significant mass. For $f_s \geq 3$ Hz, although peaks move to the lower frequencies and increase in amplitude, the shape of the function remains almost unaltered. Such an issue is due to the fact that a stiff secondary oscillator results in a mere increment of the structural mass and is even more visible for frequencies of $f_s = 5$ Hz and $f_s = 15$ Hz which progressively tend to the response relevant to $f_s = \infty$.

On the contrary, for low values of f_s , the response is very close to the unperturbed one although it has a further peak at $f = f_s$. Hence, the secondary oscillator induces a narrow band response uncorrelated to the one of the main structure. This is confirmed by observing curves relevant to $f_s = 0.5$ Hz and $f_s = 1.5$ Hz.

12.3.2 First Excursion Probability Comparison

In order to investigate the influence of the non-structural components on the seismic vulnerability of the main structure, it is convenient to determine the First Excursion Probability (FEP) over a time interval. Such a quantity is defined as the probability that the response of interest $X(t)$ crosses a fixed bound x during the time interval $[0, t_{fp}]$ and is defined as

$$F_X(x, t_{fp}) = \Pr[\max(|X(x, \tau)|; \forall \tau \in [0, t_{fp}]) \geq x] \tag{12.10}$$

where a double-bound $\pm x$ is assumed.

Referring to the original paper (Kiureghian and Fujimura 2009) for the details, TELM takes advantage of the linearization by determining the FEP relevant to each threshold by means of Vanmarcke’s extreme peak distribution:

$$F_X(x, t_{fp}) = \left[1 - \exp\left(-\frac{x^2}{2}\right) \right] \exp\left[-\nu_X(0^+) t_{fp} \frac{1 - \exp(-\sqrt{2}\delta^{1.2}x)}{\exp(0.5x^2) - 1}\right] \tag{12.11}$$

where ν_X denotes the mean up-crossing rate and δ is the regularity factor. Denoting by $\Phi_{XX}(\omega)$ the power spectral density of the structural response $X(t)$, δ and ν_X can be computed as

$$\lambda_m = \int_0^\infty 2\omega^m \Phi_{XX}(\omega) d\omega; \quad \delta = \sqrt{1 - \frac{\lambda_1^2}{\lambda_0\lambda_2}}; \quad \nu_X(x^+, t_{fp}) = \frac{1}{2\pi} \sqrt{\frac{\lambda_2}{\lambda_0}} \exp\left[-\frac{x^2}{2\lambda_0}\right] \tag{12.12}$$

in which λ_m is the m th spectral moment, x^+ denotes the up-crossing of threshold x , and $\omega = 2\pi f$ is the pulsation.

Statistics of the response relevant to the unperturbed and parametrized systems have been computed for a stationary excitation consisting of a filtered white noise with intensity $\sigma_0 = 0.0448 \text{ m/s}^2$ filtered by a linear oscillator with natural frequency of $f_{FF} = 1.5 \text{ Hz}$ and damping $\zeta_{FF} = 0.3$.

Moreover, a comparison between the response statistics is performed by means of the rate F and its envelope \hat{F} defined as:

$$F(t_{fp}, x^*, f_s, m_s) = \left| \frac{F_X^p(x^*, t_{fp}, f_s, m_s) - F_X^u(x^*, t_{fp})}{F_X^u(x^*, t_{fp})} \right| \quad (12.13)$$

$$\hat{F}(t_{fp}, x^*) = \max \{F(t_{fp}, x^*, f_s, m_s) \mid \forall f_s \in [0.5, 30] \text{ Hz}, \forall (m_s/m_0) \in [0.01, 1]\} \quad (12.14)$$

where $F_X^u(x, t_{fp})$ and $F_X^p(x, t_{fp}, f_s, m_s)$ are the FEP of the unperturbed and parametrized system, respectively.

Colormaps of FEP-rates relevant to six secondary oscillators and depending by threshold x^* and time interval t_{fp} are reported in Fig. 12.5a–f. Note that white regions are associated with negligible error values $F(t_{fp}, x^*, f_s, m_s) \leq 10^{-4}$.

It is worth being emphasized that FEP-rate is higher for short time intervals and high thresholds. Specifically, for $x^* < 0.055 \text{ m}$ the first excursion probabilities of the unperturbed and parametrized systems tend to coincide if sufficiently lasting time intervals are adopted.

Such a phenomenon is due to the transient phase of the extreme peak process. In fact, because of stationarity, at high thresholds (i.e., $x^* > 0.055 \text{ m}$) the rates present a constant trend independently by the assumed t_{fp} . This physically means that both systems reached stationarity with different response peak values.

Furthermore, comparison between Fig. 12.5a and f proves that the FEP-ratio is more sensitive to the mass m_s of the non- structural components than to the PO frequency f_s .

In order to provide a complete overview of the investigated phenomenon, the FEP-rate envelope $\hat{F}(t_{fp}, x^*)$, defined by Eq. (12.14), is reported in Fig. 12.6a and b by means of a 3D surface and of a colormap, respectively.

A very interesting issue consists in the fact that, for all the considered values of m_s and f_s , the first passage probabilities are sensitive to the threshold rather than to the time interval. In particular, for sufficiently lasting intervals with $t_{fp} \geq 15 \text{ s}$ and at thresholds $x^* < 0.055 \text{ m}$, the extreme peak processes of the unperturbed and of the parametrized structure converge to the same tail probability.

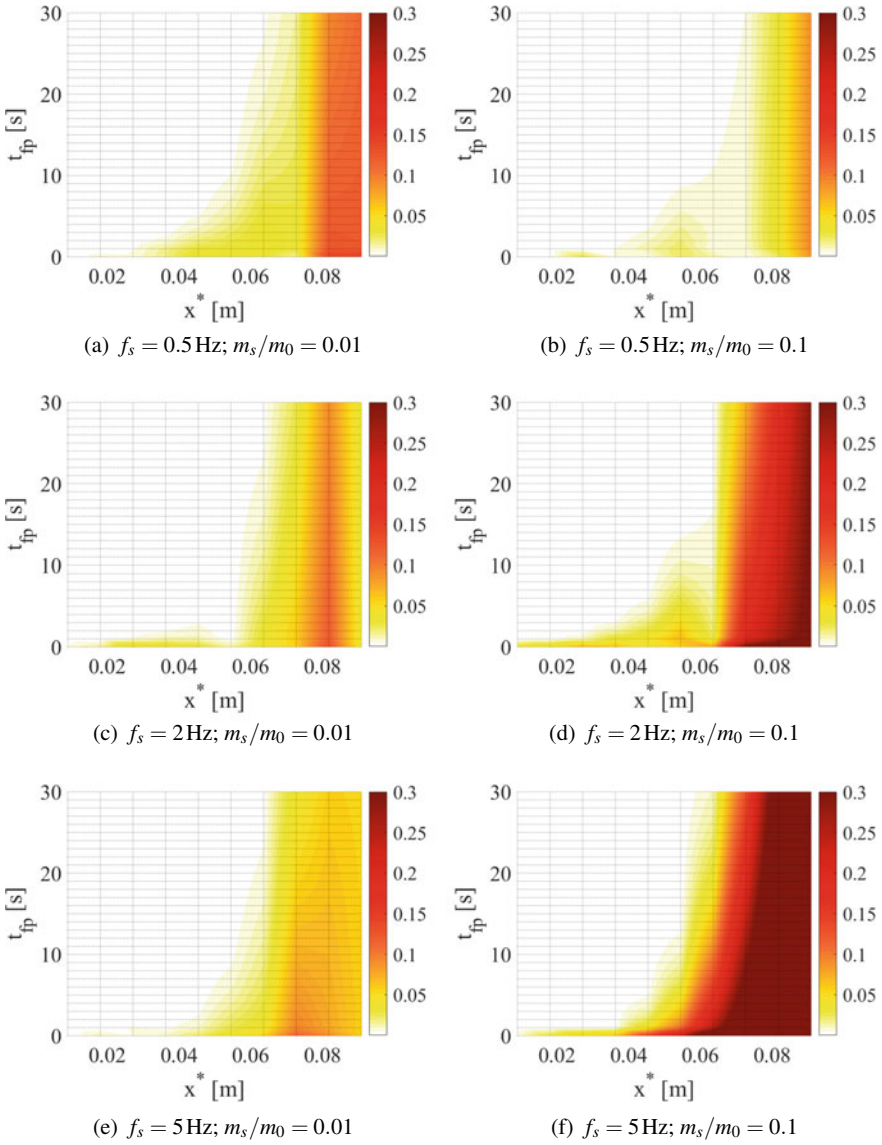


Fig. 12.5 First excursion probability rate F as function of the time interval t_{fp} and threshold x^* (In white regions $F(t_{fp}, x^*, f_s, m_s) \leq 10^{-4}$)

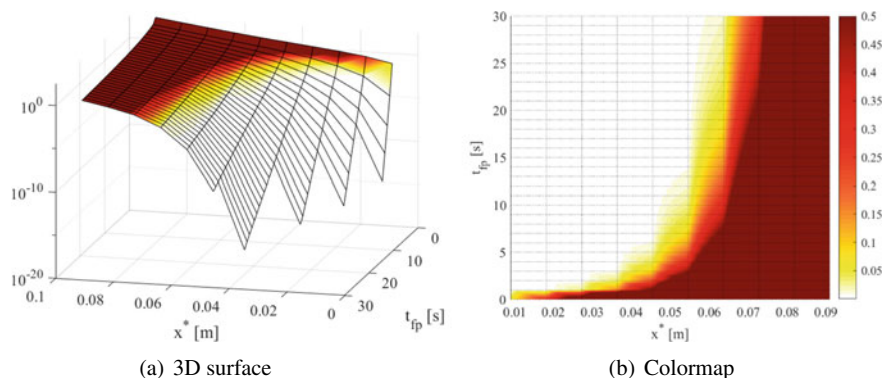


Fig. 12.6 First excursion probability rate envelope \hat{F} as function of the time interval t_{fp} and threshold x^* (In white regions $\hat{F}(t_{fp}, x^*) \leq 10^{-4}$)

12.4 Conclusion

Influence of non-structural components on the response of a structural system is investigated and discussed. To this end, the Tail-Equivalent Linearization Method, providing a linearized equivalent system by means of response functions, has been adopted.

A comparison between the frequency content of an *unperturbed* structure, in which the presence of non-structural devices is neglected, and of a *parameterized* model, where a secondary, parametrized oscillator is introduced, proved that structural responses are strongly influenced by resonance phenomena.

Despite of the fact that non-structural components dramatically adulterate the response in time of the model, their influence on the first excursion probability turns out to be more limited.

In particular, for sufficiently lasting time intervals and moderate thresholds, the peak response of the parametrized model tends to coincide with the one of the unperturbed structure independently of the dynamical properties of the secondary oscillator.

Such an aspect becomes pivotal if the linearized system aims to be used for determining secondary excitations. In fact, in such a case, the selected thresholds cannot overcome the values for which the main structure becomes irretrievably damaged: it could be meaningless to characterize a seismic excitation to be used for non-structural components if the main structure collapsed.

In this sense, the presented results are very appealing and open a new perspective on the possible applications of Tail-Equivalent linearization.

Future research directions will be focused on the characterization of secondary excitation processes. Within the framework of protection of cultural heritage artifacts and archaeological vestiges, such investigations may include isolation of statues (Vaiana et al. 2017) by introducing a biaxial characterization of the nonlinear model

(Vaiana et al. 2021) and appropriate integration procedures (Greco et al. 2018). Moreover, significant improvements consist in extending tail-equivalent linearization to more complex structural models including shell elements (Altenbach et al. 2009, 2010; Cuomo et al. 2014) damage (Contrafatto and Cuomo 2006; Franciosi et al. 2019), viscoelasticity (Cuomo 2017), metamaterials (De Angelo et al. 2019; di Cosmo et al. 2018; Abd-alla et al. 2017), and reinforced concrete (Contrafatto et al. 2012, 2016).

Acknowledgements The present research was supported by the University of Naples Federico II and the Compagnia di San Paolo, which are gratefully acknowledged by the authors, as part of the Research Project *MuRA— Multi-risk assessment and structural protection of archaeological vestiges in volcanic scenarios*, FRA grants, CUP E69C21000250005.

References

- AenN Abd-alla, Alshaikh F, Del Vescovo D, Spagnuolo M (2017) Plane waves and eigenfrequency study in a transversely isotropic magneto-thermoelastic medium under the effect of a constant angular velocity. *J Therm Stress* 40(9):1079–1092
- Alibert JJ, Seppecher P, Dell’Isola F (2003) Truss modular beams with deformation energy depending on higher displacement gradients. *Math Mech Solids* 8(1):51–73
- Altenbach H, Eremeyev V, Morozov N (2009) Linear theory of shells taking into account surface stresses. *Doklady Phys* 54:531–535
- Altenbach J, Altenbach H, Eremeyev VA (2010) On generalized cosserat-type theories of plates and shells: a short review and bibliography. *Arch Appl Mech* 80(1):73–92
- Andreas U, Spagnuolo M, Lekszycki T, Eugster SR (2018) A Ritz approach for the static analysis of planar pantographic structures modeled with nonlinear Euler-Bernoulli beams. *Contin Mech Thermodyn* 30(5):1103–1123
- Baber TT, Noori MN (1985) Random vibration of degrading, pinching systems. *J Eng Mech* 111(8):1010–1026
- Badillo-Almaraz H, Whittaker AS, Reinhorn AM (2007) Seismic fragility of suspended ceiling systems. *Earthq Spectra* 23(1):21–40
- Barchiesi E, Khakalo S (2019) Variational asymptotic homogenization of beam-like square lattice structures. *Math Mech Solids* 24(10):3295–3318
- Barchiesi E, Dell’Isola F, Laudato M, Placidi L, Seppecher P (2018) A 1d continuum model for beams with pantographic microstructure: asymptotic micro-macro identification and numerical results. In: *Advances in mechanics of microstructured media and structures*. Springer, pp 43–74
- Broccardo M, Der Kiureghian A (2016) Multicomponent nonlinear stochastic dynamic analysis by tail-equivalent linearization. *J Eng Mech* 142(3):04015,100
- Calio I, Marletta M (2003) Passive control of the seismic rocking response of art objects. *Eng Struct* 25(8):1009–1018
- Chiaia B, Barchiesi E, De Biagi V, Placidi L (2019) A novel structural resilience index: definition and applications to frame structures. *Mech Res Commun* 99:52–57
- Contrafatto L, Cuomo M (2006) A framework of elastic-plastic damaging model for concrete under multiaxial stress states. *Int J Plast* 22(12):2272–2300
- Contrafatto L, Cuomo M, Fazio F (2012) An enriched finite element for crack opening and rebar slip in reinforced concrete members. *Int J Fract* 178(1–2):33–50
- Contrafatto L, Cuomo M, Gazzo S (2016) A concrete homogenisation technique at meso-scale level accounting for damaging behaviour of cement paste and aggregates. *Comput Struct* 173:1–18

- di Cosmo F, Laudato M, Spagnuolo M (2018) Acoustic metamaterials based on local resonances: homogenization, optimization and applications. In: *Generalized models and non-classical approaches in complex materials*, 1. Springer, pp 247–274
- Cuomo M (2017) Forms of the dissipation function for a class of viscoplastic models. *Math Mech Complex Syst* 5(3):217–237
- Cuomo M, Contrafatto L, Greco L (2014) A variational model based on isogeometric interpolation for the analysis of cracked bodies. *Int J Eng Sci* 80:173–188
- De Angelo M, Spagnuolo M, D’annibale F, Pfaff A, Hoschke K, Misra A, Dupuy C, Peyre P, Dirrenberger J, Pawlikowski M, (2019) The macroscopic behavior of pantographic sheets depends mainly on their microstructure: experimental evidence and qualitative analysis of damage in metallic specimens. *Contin Mech Thermodyn* 31(4):1181–1203
- Dell’Isola F, Turco E, Misra A, Vangelatos Z, Grigoropoulos C, Melissinaki V, Farsari M (2019) Force-displacement relationship in micro-metric pantographs: Experiments and numerical simulations. *Comptes Rendus Mécanique* 347(5):397–405
- Ditlevsen O, Madsen HO (1996) *Structural reliability methods*, vol 178. Wiley, New York
- FEMA (1994) *Fema e-74, reducing the risks of nonstructural earthquake damage-a practical guide*
- Franciosi P, Spagnuolo M, Salman OU (2019) Mean green operators of deformable fiber networks embedded in a compliant matrix and property estimates. *Contin Mech Thermodyn* 31(1):101–132
- Fujimura K, Der Kiureghian A (2007) Tail-equivalent linearization method for nonlinear random vibration. *Prob Eng Mech* 22(1):63–76
- Garrè L, Der Kiureghian A (2010) Tail-equivalent linearization method in frequency domain and application to marine structures. *Marine Struc* 23(3):322–338
- Greco F, Luciano R, Serino G, Vaiana N (2018) A mixed explicit-implicit time integration approach for nonlinear analysis of base-isolated structures. *Annals Solid Struct Mech* 10(1):17–29
- Kiureghian AD, Fujimura K (2009) Nonlinear stochastic dynamic analysis for performance-based earthquake engineering. *Earthq Eng Struct Dyn* 38(5):719–738
- Mazzoni S, McKenna F, Scott MH, Fenves GL et al (2006) *OpenSees command language manual*. Pacific Earthq Eng Res (PEER) Center 264
- Milton GW, Seppecher P, Bouchitté G (2009) Minimization variational principles for acoustics, elastodynamics and electromagnetism in lossy inhomogeneous bodies at fixed frequency. *Proc R Soc A Math Phys Eng Sci* 465(2102):367–396
- Sessa S (2010) Multiobjective non-linear random vibration analysis for performance-based earthquake engineering. In: *Proceedings of reliability and optimization of structural systems*, pp 185–192
- Turco E, Dell’Isola F, Misra A (2019) A nonlinear Lagrangian particle model for grains assemblies including grain relative rotations. *Int J Num Anal Methods Geomech* 43(5):1051–1079
- Turco E, Barchiesi E, Giorgio I, Dell’Isola F (2020) A Lagrangian hencky-type non-linear model suitable for metamaterials design of shearable and extensible slender deformable bodies alternative to timoshenko theory. *Int J Non-Linear Mech* 123(103):481
- Vaiana N, Spizzuoco M, Serino G (2017) Wire rope isolators for seismically base-isolated lightweight structures: experimental characterization and mathematical modeling. *Eng Struct* 140:498–514
- Vaiana N, Losanno D, Ravichandran N (2021) A novel family of multiple springs models suitable for biaxial rate-independent hysteretic behavior. *Comput Struct* 244(106):403
- Villaverde R (1997) Seismic design of secondary structures: state of the art. *J Struct Eng* 123(8):1011–1019
- Wang Z, Der Kiureghian A (2016) Tail-equivalent linearization of inelastic multisupport structures subjected to spatially varying stochastic ground motion. *Journal of Engineering Mechanics* 142(8):04016,053

Chapter 13

Do We Really Need Pantographic Structures?



Mario Spagnuolo  and Emilio Barchiesi 

Abstract This chapter attempts to provide a comprehensive answer to the challenging question: do we really need pantographic structures? This question may arise spontaneously given the recent proliferation of contributions on this type of metamaterial in the literature. A reasoned answer to this question may be crucial for the future development and orientation of research concerning this metamaterial. More generally, we show the context from which the studies that led to the development of pantographic structures originated and observe how an excessively orthodox view of Continuum Mechanics may prevent interesting developments. Within the framework of generalised theories and second-gradient models, pantographic structures assume an important role.

Keywords Pantographic structures · Metamaterials · Continuum mechanics · Second gradient theory · Microstructure · Variational principles

13.1 Introduction

Recently, the literature has seen a proliferation of scientific contributions concerning so-called pantographic structures (dell’Isola et al. 2016; Boutin et al. 2017; Eremeyev et al. 2018, 2019; Giorgio et al. 2019; Rahali et al. 2015; Andreaus et al. 2018; Barchiesi et al. 2019a; Scerrato and Giorgio 2019). The mechanical properties of such objects are reported to be exotic and very high-performance. In this short chapter, we

M. Spagnuolo (✉)

Dipartimento di Ingegneria Civile, Ambientale e Architettura (DICAAR), Università degli Studi di Cagliari, Cagliari, Italy
e-mail: mario.spagnuolo@unica.it

M. Spagnuolo · E. Barchiesi

International Research Center for the Mathematics and Mechanics of Complex Systems, University of L’Aquila, L’Aquila, Italy

E. Barchiesi

École Nationale d’Ingénieurs de Brest, ENIB, UMR CNRS 6027, IRDL, 29200 Brest, France

© Springer Nature Switzerland AG 2021

F. Marmo et al. (eds.), *Mathematical Applications in Continuum and Structural Mechanics*, Advanced Structured Materials 127, https://doi.org/10.1007/978-3-030-42707-8_13

253

would like to attempt to answer the insistent question that is asked by some scholars when topics related to pantographic structures are presented at scientific congresses: do we really need pantographic structures?

In order to answer this question, we will need to retrace in an organic manner the path that led to the formulation of the theory governing these objects. We will have to give a clear and agreeable definition of what a metamaterial is Barchiesi et al. (2019b), Abali and Yang (2019), Carcaterra et al. (2015), dell’Isola and Steigmann (2020), Eugster et al. (2019), Giorgio et al. (2020), Yang et al. (2018). In the end, we will have to show, as in any worthwhile theory, what is the real theoretical necessity behind the existence of such devices.

As we will see specifically, the environment in which pantographic structures have been developed has to be researched back to the split that originated in the nineteenth century, when the school of Continuum Mechanics related to Cauchy, Navier and Poisson prevailed over that of Lagrangian, D’Alembertian and Piolan inspiration (Lagrange 1853, 1806; dell’Isola et al. 2014, 2019, 2015a).

In order to be able to address this study in a consistent and self-contained manner, it is necessary to specify, at least in brief, what a pantographic structure is. A pantographic structure consists of a planar grid made up of two families of continuous fibres oriented orthogonally and interconnected by hinges located at the intersections. From a purely theoretical point of view, the mechanical behaviour of pantographic structures is treated in the formal context of higher gradient continua, i.e. continua whose deformation energies depend on higher gradients of the displacement field, as opposed to the Cauchy continuum in which the deformation energy is only a function of the first gradient of displacement.

13.2 **Metamaterials Are (Natural) Materials *on Demand***

In its formulation due mainly to Lagrange, Continuum Mechanics studies how the equilibrium shapes of a continuum body are modified by external interactions. A given body is assumed to consist, at each of its material points, of a specific material. The actual shape of such a body is mathematically modelled by means of a placement function and, in its elastic deformation range, by the corresponding deformation energy density, which objectively depends on the placement gradient. Further constitutive functions and kinematic descriptors can be introduced for the modelling of damage (Cuomo 2019; Misra and Poorsolhjouy 2020; Placidi 2015; Placidi et al. 2018; Spagnuolo et al. 2017) and plastic phenomena (Altenbach and Eremeyev 2014; Bertram 2015). The adoption of the above mathematical context is important in order to generalise the concepts of Continuum Mechanics to non-standard materials generally referred to as artificial or non-natural. Such a change of perspective, in fact, makes the expression “natural material” completely meaningless. In fact, from a purely modelling point of view, we can only speak of materials with a simple microstructure and materials with a complex microstructure. In the context of Continuum Mechanics based on the definition of the deformation energy density

associated with a given material, every material that can exist is natural by definition and what changes is only its mechanical behaviour, which is questioned if it can be described by certain constitutive functions.

To answer the question that underlies this chapter, we are interested in placing pantographic structures, or pantographic material as it is often referred to, in the proper context of generalised theories in Continuum Mechanics. For this reason, we are interested in discussing the positioning of theories concerning metamaterials in Continuum Mechanics. To this end, the definition given of a metamaterial is of fundamental importance. A definition that is often found in the literature and that, for what we have said so far, seems paradoxical consists in defining the theory of metamaterials as the theory of those materials that are not natural: but, we have already pointed out, all materials are by definition natural. Another possibility also often found in the literature (Seppecher et al. 2011) is to define metamaterials as those materials whose mechanical behaviour is “exotic”. This definition, however, is also easily attacked. Indeed, it is necessary to specify what we mean by exotic mechanical behaviour. It seems reasonable to argue that exotic mechanical behaviour is a type of behaviour that has not yet been experimentally observed. Of course, what is exotic at one point in time may become standard at another. For example, Lamé, Navier, Cauchy, Poisson, all regarded a material with a negative Poisson’s ratio as very exotic, and some scholars of their time even believed that such a material was not physical and could not exist. However, auxetic metamaterials do exist and play an important role in modern engineering (Evans 1991; Evans and Alderson 2000).

The cited approach to the theory of metamaterials produces several misunderstandings that can lead the scientific investigation to results completely detached from reality. Indeed, claiming that a given mechanical behaviour is standard as opposed to another implies that one is confusing a mathematical model for a material with the physical material itself, and that one is implicitly assuming that particular assumptions accepted to describe particular phenomena are universally valid in every physical situation. This attitude, as well as being unscientific, does not lead to any advancement in scientific research and is, therefore, to be avoided. The confusion between model and modelled object has led over time to conceptual statements that are completely cacophonous. The example we want to give here consists of the assumption that “materials described by second-gradient models do not exist because the materials used in engineering do not show their properties and the standard theoretical framework does not envisage them”. Those who agree with the above statement are clearly confusing first gradient models (model belonging to a symbolic-mathematical description) with materials existing in nature (physical object describable by a model). Exaggerating this non-scientific attitude to its extreme consequences, one may come to believe that, without having a theory to describe it, one cannot use a material even though he has it in his hands, and may even believe that a certain material does not exist. This is maybe the main reason for which we need a metamaterial as the pantographic one: its existence demonstrates by itself that the first gradient continua do not model every existing material.

In view of what has been said so far, we can now try to give an operational definition of what a metamaterial is. A metamaterial is a material on demand: we

establish a priori the mechanical behaviour we wish to observe in such a material, and only secondarily we search for a microstructure that, following a homogenisation procedure, can present the required mechanical behaviour at a macroscopic level.

13.3 Second Gradient Theories

As we have observed, in the self-proclaimed standard school of Continuum Mechanics there is no place for theories other than those studied in the tradition of Cauchy, Navier and Poisson. Gabrio Piola introduced in 1848 a generalised continuum model by means of deformation energies dependent on the n th gradient of the placement (Piola 1846). However, this type of model did not fit into the orthodox formulation of Continuum Mechanics à la Cauchy. Paradigmatic, in this context, is the unanimous agreement by Cauchy and his acolytes of the so-called “Cauchy postulate”, which asserts that the contact forces, within continua, can only be forces per unit area depending only on the normal to the Cauchy cuts.

In Cauchy’s version of Continuum Mechanics some ad hoc restrictions are included, among which is the fact that the deformation energy of a continuum medium can only depend on the first gradient of the displacement field. A priori, nothing would prevent a dependence on higher order gradients, but the simplest choice, coherent with the phenomenology shown by Cauchy’s continuum model, is to restrict to the first gradient of the displacement. Piola, on the other hand, introduces, for a mere rational demand, the higher gradients of displacement in the calculation of the deformation energy, arguing for characterising those microstructures for which the homogenised models must be of this more general type. In Alibert et al. (2003), Seppacher et al. (2011), dell’Isola and Seppacher (1995, 1997), Pideri and Seppacher (1997), Seppacher (1989, 2000) it is shown that models in which the second gradient of displacement takes on a non-negligible role, at the macroscopic level, are obtained by homogenisation from a microstructure, or architecture, at a lower scale in a continuum medium where high stiffness contrasts are present.

From what we have said, it seems clear that in order to be able to evaluate and observe experimentally effects that can be assimilated to a description by means of the second gradient of the displacement field, it is necessary to have a technology capable of producing a microstructured material (Spagnuolo et al. 2019; Altenbach and Eremeyev 2014; Eremeyev et al. 2012) and, above all, a material whose microstructure shows the appropriate highly contrasted stiffness fields, so that, at the macroscopic level, the terms used by Piola appear in the deformation energy. In the following we will shortly show how Paul Germain demonstrates that the presence of a microstructure can determine, at the macroscopic level, the necessity of using a second-gradient model (Germain 1973, 2020; Epstein and Smelser 2020).

The technological capacity of an era can also block its scientific development. As long as technology does not reach a sufficient level to test the results introduced in the new theories, the new theories will remain blocked, ignored and, certainly, unusable. The absurdity of the contemporary situation consists in the fact that regardless of the

technological ability to produce materials whose behaviour is described by Piola's theory (and cannot be described within the framework of Cauchy's models), there are actually still scholars who insist on denying its usefulness.

Stressing a concept we have already mentioned before, this last remark partly answers the question we asked at the beginning of this chapter: do we really need pantographic structures? From a purely theoretical point of view, the answer is clearly affirmative, because pantographic structures have been expressly designed as a material that can be described fundamentally in terms of a second-gradient theory: if we can fabricate a material that can be described by means of a given theory and not by means of the theory generally adopted in the description of materials, then this theory becomes indispensable and it is absolutely inconceivable that it should not be applicable.

13.4 Microstructure in Continuum Mechanics

At present, with recently developed and improved techniques, the fabrication of materials with complex microstructures is not as implausible as before. As we have specified above, due to the advancements in the field of additive manufacturing, it is now possible to produce microstructured metamaterials exhibiting mechanical properties that cannot be described in the context of Cauchy's Continuum Mechanics.

Here we also want to address an issue concerning the terminology adopted in the field of metamaterials. Some scholars claim that the term microstructure cannot be used because it refers to a scale of micrometres, whereas it is more appropriate to refer to architecture. However, in our opinion, this associates the metamaterial with an artefact connotation that is not of fundamental interest in the theory. More specifically, the relevant point is to understand what determines the mechanical properties of the so-called standard or natural materials: clearly the difference between a cubic material and a tetragonal one, just to give an example, is in the geometry according to which the "particles" that compose it are arranged, i.e. in its microstructure. Now some people refer to architecture in the case of metamaterials because the present technological capabilities do not yet allow manufacture on scales comparable to those currently existing in nature. But the idea is the same as that underlying the differences between the mechanical behaviour of cubic and tetragonal materials: the mechanical behaviour of a metamaterial is determined by the geometric arrangement of its elementary constituents. This is why, in our opinion, distinguishing architecture from microstructure is only misleading.

As we have seen above, Piola was the first to study continuum models in which the deformation energy depends on higher gradients of the displacement field. Later, in the twentieth century, this kind of models was also studied and reformulated by various authors. Among others, we mention in particular two pioneering studies presented by Mindlin (1965) and by Germain (1973, 2020); Epstein and Smelser (2020). A very interesting aspect that emerges from these studies, and of course from others, is that they show how the existence of the microstructure in some cases could induce

higher order terms in the equilibrium equations of the material under consideration. Unlike classical homogenisation techniques, equations containing terms dependent on second or higher order derivatives of the displacement are obtained in this case, thus introducing higher gradient theories in a logical way.

Germain shows in general that, by applying the Principle of Virtual Power (analogous to the Principle of Virtual Work), the classical equations of the Continuum Mechanics are easily obtained. When considering a microstructured continuum, these equations have terms that depend on the second gradient of the displacement field. In this context, it is crucial to assign the right kinematics. Therefore, in the case of a usual continuum, this is considered to consist of a continuum distribution of particles geometrically represented by a material point and its velocity components. When considering the microstructure, from a macroscopic point of view each particle is still represented by a material point, but its kinematics must be defined more precisely. The main feature of the method explained by Germain is that, having assigned the required kinematics, the associated continuum theory can be deduced immediately through the Principle of Virtual Work. He shows that the kinematics due to the presence of the microstructure generates a second-gradient continuum at the macroscopic level. We refer to the original work by Germain for the technical details (Germain 1973, 2020; Epstein and Smelser 2020).

This can be considered the starting point in the study of pantographic structures. A certain microstructure is chosen to get a second-gradient continuum as simple as possible and then homogenisation techniques are used to determine this appropriate macroscopic continuum model.

13.4.1 The Synthesis Problem

The real mathematical challenge facing us today, therefore, is to design metamaterials that can be described within the framework of a generalised theory (Maugin 2011; Altenbach et al. 2010; Altenbach and Eremeyev 2010, 2013; Altenbach et al. 2013; Auffray 2015; dell'Isola et al. 2009; Eremeyev and dell'Isola 2018). Thus, the fundamental problem in the theory of metamaterials consists in the problem of the synthesis of microstructures that produce a certain desired macro-behaviour (Rahali et al. 2015; Placidi et al. 2020; Khakalo and Niiranen 2020; Abdoul-Anziz et al. 2019). As we have seen briefly, in this context, the most complex problem to address from a mathematical point of view is to link microstructures and macro-behaviours. This is done in terms of mathematical procedures called homogenisation: starting from the elementary constituents and the basic cell of the chosen microstructure, one must link this microstructure to the given macroscopic theory (appropriate action functions and consequent stationarity conditions) chosen a priori, and this, in order to be of some general use, must be approached in an algorithmic manner, thus allowing generalisation.

The basic ideas in the field of metamaterial synthesis can be deduced by analogy from the theory of analogue circuit synthesis. In this theory, it can be shown that any

passive linear element can be synthesised algorithmically using inductors, capacitors, resistors and transformers (Bloch 1944, 1945; Kron 1945; Mablekos and Weidmann 1968). The main challenge is to conjecture that this method can also be applied to the synthesis of non-linear (and multiphysical) mechanical systems (Spagnuolo 2020; Spagnuolo and Scerrato 2020).

13.5 Why We Really Need Pantographic Structures

Up to now we have tried to exhibit the background needed to answer a question often repeated as a result of the enormous development of literature on pantographic structures: do we really need pantographic structures? For what purpose do they serve? There are many arguments advanced on this topic which are commonly referred against second and higher gradient models: some scholars observe that the extremely formal mathematical investigation required to formulate the theory underlying this type of metamaterial is unnecessarily over-discussed and studied, and that there are no practical applications of the object studied; others point out that, on the contrary, from a theoretical point of view it is not necessary to introduce second-gradient theories, because they are useless mathematical complications, but that the classical Cauchy theory on its own is able to explain and represent all the phenomenology observed in Continuum Mechanics; finally, some argue that there are many other metamaterials much more interesting than the pantographic one. We limit ourselves to observe that one of the most cited works in the field of metamaterials (Bertoldi et al. 2010), the work of researchers belonging to the Harvard intelligentsia, seems to us to be rather weak and basically a patchwork of experimental results obtained for a microstructure that produces a material with auxetic mechanical behaviour.

But it is not our purpose to comment on the null and void scientific contribution of the various power groups of the moment. Instead, we are interested in precisely defining the reasons why pantographic structures are actually worth studying. Basically, we can divide the positive scientific contributions resulting from the development of this type of metamaterials into four areas: theoretical, practical, methodological and multiphysical.

13.5.1 *The Existence of Pantographic Metamaterial Motivates the Need of Second Gradient Theories*

From a theoretical and methodological point of view, the importance of pantographic structures seems indisputable. In fact, consider the fundamental objection that has historically been made to second-gradient theories: they are not necessary, since the materials can be very well described within the framework of the classical Cauchy first gradient theory, possibly by adding *ad hoc* corrections. If, then, we are able

to show a material not describable by means of a first gradient theory, but only by invoking a second-gradient one, then this is enough to motivate the necessity of such theories. We want, accordingly, to postulate the existence of such a material by writing its governing equations, i.e. its deformation energy, which should be dependent of the second gradient of displacement. We subsequently ask which microstructure can produce this macroscopic deformation energy after homogenisation. This approach is methodologically the reverse of that used in the majority of works on metamaterials, including the aforementioned (Bertoldi et al. 2010). We therefore ask what characteristics a microstructure must have in order to produce a second-gradient continuum at the macroscopic level.

Methodologically we start from the following observation, which is certainly superficial, but definitely indicative to try to define a microstructure suitable to produce a second-gradient mechanical behaviour: if we consider an Euler-Bernoulli beam, even a linear one, its deformation energy can be separated into two components, elongation and bending. The elongation energy depends on the first derivative of the longitudinal displacement, while the bending energy depends on the second derivative of the transverse displacement. In a sense, we can say that the Euler-Bernoulli beam is first gradient in extension and second gradient in bending. We want to produce a second-gradient material at extension. We can therefore conceive an assembly of beams such that a macroscopic extension action corresponds to a bending action from a microscopic point of view. In other words, by extending or compressing the metamaterial we are flexing the fibres that make up its microstructure. In this way, the deformation energy of the metamaterial subjected to extensional load should correspond to a “microscopic” bending energy and consequently to a second-gradient energy. This is how the pantographic microstructure has been originated.

13.5.2 *A Mechanical Diode*

From a practical point of view, we would like to highlight just one aspect that seems extremely promising with respect to the possible applications of the pantographic metamaterial. Consider that, due to the peculiar microstructure chosen, from the point of view of mechanical behaviour, we observe a phenomenology similar to that presented by the diode in the analysis of electrical circuits. The diode is a circuit element that exhibits an extremely particular voltage-current response. In various applications of interest, the voltage-current behaviour of an ideal diode, under static conditions, can be approximated by a linear piecewise function. In this approximation, the current can be considered to be zero if the voltage between anode and cathode is less than or equal to a certain threshold value V_γ ; if, on the contrary, the voltage is higher, the diode can be approximated to a voltage generator, whose current is imposed by the circuit to which it is subordinated. In the field of mechanics, a response formally identical to that exhibited by the diode in electrical circuits is shown by the pantographic metamaterial. If the hinges connecting the fibres of

the two families are perfect, and therefore no deformation energy is associated with them, then considering a bias-extension test of a pantographic structure the following response will be observed in terms of a force-displacement measurement: up to a certain imposed displacement a very low value of the reaction force will be measured; after a threshold value of the displacement, the force will begin to increase considerably. The shape of the observed curve is reminiscent of the voltage-current diagram of the diode. In this sense, one can refer to the pantographic metamaterial as a kind of mechanical diode.

This mechanical behaviour can be useful when one wants to insert a mechanical element into a structure which does not function directly as a spring, but only exhibits linear elastic behaviour after a certain elongation threshold value (at least for deformations not too far beyond the threshold value).

The explanation for this unusual mechanical behaviour lies in the deformation of the microstructure: in a bias-extension test, in a first phase the predominantly observed deformation corresponds to the bending of the fibres clamped at the ends of the pantographic structure (whereas the unclamped fibres are simply free to rotate). This bending is concentrated in very precise areas of the pantographic structure and gives rise, from a theoretical point of view, to the bending term modelled by means of the second gradient of placement. It is common experience that a beam is easier to bend than to stretch, so it is easy to agree that the bending energy of the pantographic structure (beam assembly) is certainly lower than the elongation energy. However, since the extension test is conducted along a direction in which the fibres are biased, then the first mechanism to occur corresponds to the bending of the fibres, whereas their elongation only begins when the rotating fibres touch (which corresponds to the threshold value above which the measured force begins to increase significantly). One can refer to Spagnuolo (2020), Spagnuolo and Scerrato (2020) for more details.

13.5.3 An Iterative Algorithm for Synthesising Metamaterials

From a methodological-theoretical point of view, we want to underline an important aspect recalled in Alibert et al. (2003), Seppecher et al. (2011). Once the pantographic microstructure has been obtained, which at the macroscopic level produces the required second-gradient behaviour by means of a suitable homogenisation, one can think of generalising this procedure to the production of metamaterials described by energies dependent on higher displacement gradients. In Alibert et al. (2003), Seppecher et al. (2011) it is shown how, by using a Warren bridge microstructure in association with a pantographic microstructure, it is possible to obtain a third gradient-in-bending material. With an iterative procedure it is suggested that one can proceed from $(2n + 1)$ -th gradient-in-bending materials to $(2n + 2)$ -th gradient-in-extension materials. This problem, only mentioned in Alibert et al. (2003), Seppecher et al. (2011), turns out to be of utmost importance in the synthesis of new metamaterials.

13.6 Conclusion

In this chapter, we have briefly discussed some of the fundamental motivations behind the development of pantographic metamaterial. We have established that studies of this metamaterial are strongly motivated from several points of view: from a theoretical point of view, it demonstrates the necessity of the introduction of second-gradient models; from a practical point of view, this metamaterial possesses extremely peculiar characteristics and, therefore, is worthy of detailed study; from a methodological point of view, it offers a useful example in the field of procedures for the synthesis of new metamaterials.

These reasons that we have listed and discussed lead us to believe that pantographic structures may provide a new class of materials worth studying in depth. In fact, there are several indications that the phenomenology of this metamaterial is very variegated. Here we limit ourselves to a few cases of extreme interest: the observation of Poynting reversal effects for torsion tests conducted on pantographic structures (Misra et al. 2018; Auger et al. 2020); the observation of wave phenomena in the case of very dense mesh structures of sufficiently large length (dell'Isola et al. 2015b); the study of the distribution of displacement and velocity fields for high-frequency vibratory phenomena (Laudato et al. 2018; Barchiesi et al. 2018; Laudato and Barchiesi 2019; Laudato et al. 2020); the extremely non-standard phenomenology in the case of three-point bending tests (Yildizdag et al. 2020).

The enormous amount of phenomenology and experimental observations obtained on pantographic structures require the development of precise methods of analysis, such as those based on Digital Image Correlation, already applied to the case of this metamaterial with good results (Hild et al. 2020; Barchiesi et al. 2020b, a), and of numerical implementation of theoretical models in order to conduct precise model validation. This also requires the development of numerical methods capable of simulating the cases of interest (Cazzani and Atluri 1993; Cazzani and Lovadina 1997; Cazzani et al. 2016c, b, a, 2020; Cuomo et al. 2014; Greco and Cuomo 2013, 2014; Maurin et al. 2019; Capobianco et al. 2018; Turco et al. 2017, 2018, 2019b, a; Turco and Barchiesi 2019; Schulte et al. 2020; Hesch et al. 2017; Capobianco and Eugster 2018; Eugster and Glocker 2013; Huang et al. 2020, 2021; Barchiesi et al. 2020c; Yang et al. 2019; Jafarzadeh et al. 2020; Namnabat et al. 2020; Rahbar et al. 2020). The methods and reasoning developed for pantographic structures may also be interesting for other applications, such as civil engineering (Vaiana et al. 2021, 2019; Serpieri et al. 2018; Sessa et al. 2019a, 2017, 2018a, 2019b, 2018b, 2015; Cricri et al. 2015; Greco et al. 2018; Perricone et al. 2020; Marmo et al. 2018a, b, 2019; Vaiana et al. 2017; Paradiso et al. 2019).

Acknowledgements Il presente articolo é stato realizzato nell'ambito del progetto di ricerca finanziato con le risorse del P.O.R. SARDEGNA F.S.E. 2014–2020—Asse III “Istruzione e Formazione, Obiettivo Tematico: 10, Obiettivo Specifico: 10.5, Azione dell'accordo di Partenariato: 10.5.12” Avviso di chiamata per il finanziamento di Progetti di ricerca—Anno 2017

References

- Abali BE, Yang H (2019) Parameter determination of metamaterials in generalized mechanics as a result of computational homogenization. In: Indeitsev D, Krivtsov A (eds) *Advanced problems in mechanics. APM 2019. Lecture Notes in Mechanical Engineering*. Springer, Cham, Switzerland, pp 22–31
- Abdoul-Anziz H, Seppecher P, Bellis C (2019) Homogenization of frame lattices leading to second gradient models coupling classical strain and strain-gradient terms. *Math Mech Solids* 24(12):3976–3999
- Alibert JJ, Seppecher P, dell’Isola F (2003) Truss modular beams with deformation energy depending on higher displacement gradients. *Math Mech Solids* 8(1):51–73
- Altenbach H, Eremeyev V (2014) Strain rate tensors and constitutive equations of inelastic micropolar materials. *Int J Plas* 63:3–17
- Altenbach H, Eremeyev VA (2010) On the theories of plates based on the Cosserat approach. In: *Mechanics of generalized continua*. Springer, pp 27–35
- Altenbach H, Eremeyev VA (2013) Cosserat media. In: Eremeyev VA, Altenbach H (ed) *Generalized continua from the theory to engineering applications*. Springer, pp 65–130
- Altenbach H, Birsan M, Eremeyev VA (2013) Cosserat-type rods. In: *Generalized continua from the theory to engineering applications*. Springer, pp 179–248
- Altenbach J, Altenbach H, Eremeyev VA (2010) On generalized Cosserat-type theories of plates and shells: a short review and bibliography. *Arch Appl Mech* 80(1):73–92
- Andreus U, Spagnuolo M, Lekszycki T, Eugster SR (2018) A Ritz approach for the static analysis of planar pantographic structures modeled with nonlinear Euler-Bernoulli beams. *Contin Mech Thermodyn* 30(5):1103–1123
- Auffray N (2015) On the algebraic structure of isotropic generalized elasticity theories. *Math Mech Solids* 20(5):565–581
- Auger P, Lavigne T, Smaniotto B, Spagnuolo M, dell’Isola F, Hild F (2020) Poynting effects in pantographic metamaterial captured via multiscale DVC. *J Strain Anal Eng Design* 0309324720976625
- Barchiesi E, Laudato M, Di Cosmo F (2018) Wave dispersion in non-linear pantographic beams. *Mechan Res Commun* 94:128–132
- Barchiesi E, Ganzosch G, Liebold C, Placidi L, Grygoruk R, Müller WH (2019a) Out-of-plane buckling of pantographic fabrics in displacement-controlled shear tests: experimental results and model validation. *Contin Mech Thermodyn* 31(1):33–45
- Barchiesi E, Spagnuolo M, Placidi L (2019b) Mechanical metamaterials: a state of the art. *Math Mech Solids* 24(1):212–234
- Barchiesi E, dell’Isola F, Hild F, Seppecher P (2020a) Two-dimensional continua capable of large elastic extension in two independent directions: asymptotic homogenization, numerical simulations and experimental evidence. *Mech Res Commun* 103(103):466
- Barchiesi E, Eugster SR, dell’Isola F, Hild F (2020b) Large in-plane elastic deformations of bi-pantographic fabrics: asymptotic homogenization and experimental validation. *Math Mech Solids* 25(3):739–767
- Barchiesi E, Yang H, Tran C, Placidi L, Müller WH (2020c) Computation of brittle fracture propagation in strain gradient materials by the fenics library. *Math Mech Solids* 1081286520954513
- Bertoldi K, Reis PM, Willshaw S, Mullin T (2010) Negative Poisson’s ratio behavior induced by an elastic instability. *Adv mater* 22(3):361–366
- Bertram A (2015) Finite gradient elasticity and plasticity: a constitutive mechanical framework. *Contin Mech Thermodyn* 27(6):1039–1058
- Bloch A (1944) XXXVIII. A new approach to the dynamics of systems with gyroscopic coupling terms. *London, Edinburgh, and Dublin Philosoph Mag J Sci* 35(244):315–334
- Bloch A (1945) Electromechanical analogies and their use for the analysis of mechanical and electromechanical systems. *J Instit Electric Eng Part I Gener* 92(52):157–169
- Boutin C, Giorgio I, Placidi L et al (2017) Linear pantographic sheets: asymptotic micro-macro models identification. *Math Mech Complex Syst* 5(2):127–162

- Capobianco G, Eugster S (2018) Time finite element based moreau-type integrators. *Int J Numer Methods Eng* 114(3):215–231
- Capobianco G, Eugster SR, Winandy T (2018) Modeling planar pantographic sheets using a non-linear Euler–Bernoulli beam element based on B-spline functions. *PAMM* 18(1):e201800,220
- Carcatera A, dell’Isola F, Esposito R, Pulvirenti M (2015) Macroscopic description of microscopically strongly inhomogeneous systems: A mathematical basis for the synthesis of higher gradients metamaterials. *Arch Rational Mech Anal* 218(3):1239–1262
- Cazzani A, Atluri S (1993) Four-noded mixed finite elements, using unsymmetric stresses, for linear analysis of membranes. *Comput Mech* 11(4):229–251
- Cazzani A, Lovadina C (1997) On some mixed finite element methods for plane membrane problems. *Comput Mech* 20(6):560–572
- Cazzani A, Malagù M, Turco E (2016a) Isogeometric analysis of plane-curved beams. *Math Mech Solids* 21(5):562–577
- Cazzani A, Malagù M, Turco E, Stochino F (2016b) Constitutive models for strongly curved beams in the frame of isogeometric analysis. *Math Mech Solids* 21(2):182–209
- Cazzani A, Stochino F, Turco E (2016c) An analytical assessment of finite element and isogeometric analyses of the whole spectrum of Timoshenko beams. *ZAMM J Appl Math Mech/Zeitschrift für Angewandte Mathematik und Mechanik* 96(10):1220–1244
- Cazzani A, Serra M, Stochino F, Turco E (2020) A refined assumed strain finite element model for statics and dynamics of laminated plates. *Contin Mech Thermodyn* 32(3):665–692
- Cricri G, Perrella M, Sessa S, Valoroso N (2015) A novel fixture for measuring mode III toughness of bonded assemblies. *Eng Fract Mech* 138:1–18
- Cuomo M (2019) Continuum damage model for strain gradient materials with applications to 1d examples. *Contin Mech Thermodyn* 31(4):969–987
- Cuomo M, Contrafatto L, Greco L (2014) A variational model based on isogeometric interpolation for the analysis of cracked bodies. *Int J Eng Sci* 80:173–188
- dell’Isola F, Seppecher P (1995) The relationship between edge contact forces, double forces and interstitial working allowed by the principle of virtual power. *Comptes rendus de l’Académie des sciences Série II, Mécanique, physique, chimie, astronomie* 321(8):303–308
- dell’Isola F, Seppecher P (1997) Edge contact forces and quasi-balanced power. *Meccanica* 32(1):33–52
- dell’Isola F, Steigmann DJ (2020) *Discrete and continuum models for complex metamaterials*. Cambridge University Press, Cambridge. <https://doi.org/10.1017/9781316104262>
- dell’Isola F, Sciarra G, Vidoli S (2009) Generalized Hooke’s law for isotropic second gradient materials. *Proc R Soc A Math Phys Eng Sci* 465(2107):2177–2196
- dell’Isola F, Maier G, Perego U, et al (2014) *The complete works of Gabrio Piola: Volume I (Advanced structured materials, vol 38)*. Springer, Berlin
- dell’Isola F, Andreaus U, Placidi L (2015a) At the origins and in the vanguard of peridynamics, non-local and higher-gradient continuum mechanics: an underestimated and still topical contribution of Gabrio Piola. *Math Mech Solids* 20(8):887–928
- dell’Isola F, Giorgio I, Andreaus U (2015b) Elastic pantographic 2d lattices: a numerical analysis on the static response and wave propagation. *Proc Estonian Acad Sci* 64(3):219
- dell’Isola F, Giorgio I, Pawlikowski M, Rizzi NL (2016) Large deformations of planar extensible beams and pantographic lattices: heuristic homogenization, experimental and numerical examples of equilibrium. *Proc R Soc A Math Phys Eng Sci* 472(2185):20150,790
- dell’Isola F, Maier G, Perego U et al (2019) *The complete works of Gabrio Piola, vol II*. Springer, Cham
- Epstein M, Smelser R (2020) An appreciation and discussion of Paul Germain’s “The method of virtual power in the mechanics of continuous media, I: second-gradient theory”. *Math Mech Complex Syst* 8(2):191–199

- Eremeyev VA, dell'Isola F (2018) A note on reduced strain gradient elasticity. In: Altenbach H., Pouget J., Rousseau M., Collet B., Michelitsch T. (eds) *Generalized models and non-classical approaches in complex materials 1. Advanced structured materials*, vol 89. Springer, Cham, pp 301–310
- Eremeyev VA, Lebedev LP, Altenbach H (2012) *Foundations of micropolar mechanics*. Springer, Heidelberg
- Eremeyev VA, dell'Isola F, Boutin C, Steigmann D (2018) Linear pantographic sheets: existence and uniqueness of weak solutions. *J Elast* 132(2):175–196
- Eremeyev VA, Alzahrani FS, Cazzani A, dell'Isola F, Hayat T, Turco E, Konopińska-Zmysłowska V (2019) On existence and uniqueness of weak solutions for linear pantographic beam lattices models. *Contin Mech Thermodyn* 31(6):1843–1861
- Eugster S, dell'Isola F, Steigmann D (2019) Continuum theory for mechanical metamaterials with a cubic lattice substructure. *Math Mech Complex Syst* 7(1):75–98
- Eugster SR, Glocker C (2013) Constraints in structural and rigid body mechanics: a frictional contact problem. *Annals Solid Struct Mech* 5(1–2):1–13
- Evans KE (1991) Auxetic polymers: a new range of materials. *Endeavour* 15(4):170–174
- Evans KE, Alderson A (2000) Auxetic materials: functional materials and structures from lateral thinking!. *Adv Mater* 12(9):617–628
- Germain P (1973) The method of virtual power in continuum mechanics. Part 2: Microstructure. *SIAM J Appl Math* 25(3):556–575
- Germain P (2020) The method of virtual power in the mechanics of continuous media, I: second-gradient theory. *Math Mechan Complex Syst* 8(2):153–190
- Giorgio I, Rizzi NL, Andreaus U, Steigmann DJ (2019) A two-dimensional continuum model of pantographic sheets moving in a 3D space and accounting for the offset and relative rotations of the fibers. *Math Mech Complex Syst* 7(4):311–325
- Giorgio I, Ciallella A, Scerrato D (2020) A study about the impact of the topological arrangement of fibers on fiber-reinforced composites: some guidelines aiming at the development of new ultra-stiff and ultra-soft metamaterials. *Int J Solids Struct* 203:73–83
- Greco F, Luciano R, Serino G, Vaiana N (2018) A mixed explicit-implicit time integration approach for nonlinear analysis of base-isolated structures. *Annals Solid Struct Mech* 10(1):17–29
- Greco L, Cuomo M (2013) B-Spline interpolation of Kirchhoff-Love space rods. *Comput Methods Appl Mech Eng* 256:251–269
- Greco L, Cuomo M (2014) An implicit G1 multi patch B-spline interpolation for Kirchhoff-Love space rod. *Comput Methods Appl Mech Eng* 269:173–197
- Hesch C, Schuß S, Dittmann M, Eugster S, Favino M, Krause R (2017) Variational space-time elements for large-scale systems. *Comput Methods Appl Mech Eng* 326:541–572
- Hild F, Misra A, dell'Isola F (2020) Multiscale DIC applied to pantographic structures. *Exper Mech*
- Huang J, Boisse P, Hamila N, Zhu Y (2020) Simulation of wrinkling during bending of composite reinforcement laminates. *Materials* 13(10):2374
- Huang J, Boisse P, Hamila N, Gnaba I, Soulat D, Wang P (2021) Experimental and numerical analysis of textile composite draping on a square box, influence of the weave pattern. *Compos Struct* 113844
- Jafarzadeh H, Farrahi GH, Levitas VI, Javanbakht M (2020) Phase field theory for fracture at large strains including surface stresses. *arXiv preprint arXiv:201113324*
- Khakalo S, Niiranen J (2020) Anisotropic strain gradient thermoelasticity for cellular structures: Plate models, homogenization and isogeometric analysis. *J Mech Phys Solids* 134(103):728
- Kron G (1945) Numerical solution of ordinary and partial differential equations by means of equivalent circuits. *J Appl Phys* 16(3):172–186
- Lagrange JL (1806) *Traité de la résolution des équations numériques de tous les degrés: avec des notes sur plusieurs points de la théorie des équations algébriques*. chez Courcier
- Lagrange JL (1853) *Mécanique analytique*, vol 1. Mallet-Bachelier, Paris

- Laudato M, Barchiesi E (2019) Non-linear dynamics of pantographic fabrics: modelling and numerical study. In: *Wave dynamics, mechanics and physics of microstructured metamaterials*. Springer, pp 241–254
- Laudato M, Manzari L, Barchiesi E, Di Cosmo F, Göransson P (2018) First experimental observation of the dynamical behavior of a pantographic metamaterial. *Mech Res Commun* 94:125–127
- Laudato M, Manzari L, Scerrato D, Göransson P, Giorgio I (2020) Spectral properties of 2d pantographic metamaterial: experimental results. *Mech Res Commun* 109(103):613
- Mablekos E, Weidmann H (1968) Realization of negative impedance inverter using Kron's mesh primitive-branch approach. *J Franklin Instit* 286(1):59–75
- Marmo F, Masi D, Rosati L (2018a) Thrust network analysis of masonry helical staircases. *Int J Architec Heritage* 12(5):828–848
- Marmo F, Ruggieri N, Toraldo F, Rosati L (2018b) Historical study and static assessment of an innovative vaulting technique of the 19th century. *Int J Architec Heritage*
- Marmo F, Demartino C, Candela G, Sulpizio C, Briseghella B, Spagnuolo R, Xiao Y, Vanzi I, Rosati L (2019) On the form of the musmeci's bridge over the basento river. *Eng Struct* 191:658–673
- Maugin GA (2011) A historical perspective of generalized continuum mechanics. In: Altenbach H, Maugin G, Erofeev V (eds) *Mechanics of generalized continua*. Advanced structured materials, vol 7. Springer, Berlin, Heidelberg, pp 3–19
- Maurin F, Greco F, Desmet W (2019) Isogeometric analysis for nonlinear planar pantographic lattice: discrete and continuum models. *Contin Mech Thermodyn* 31(4):1051–1064
- Mindlin RD (1965) Second gradient of strain and surface-tension in linear elasticity. *Int J Solids Struct* 1(4):417–438
- Misra A, Poorsolhjouy P (2020) Granular micromechanics model for damage and plasticity of cementitious materials based upon thermomechanics. *Math Mech Solids* 25(10):1778–1803
- Misra A, Lekszycki T, Giorgio I, Ganzosch G, Müller WH, Dell'Isola F (2018) Pantographic metamaterials show atypical poynting effect reversal. *Mech Res Commun* 89:6–10
- Namnabat MS, Barzegar A, Barchiesi E, Javanbakht M (2020) Nonlinear buckling analysis of double-layered graphene nanoribbons based on molecular mechanics. *Carbon Lett* 1–16
- Paradiso M, Marmo F, Rosati L (2019) Consistent derivation of a beam model from the saint Venant's solid model. *Int J Solids Struct* 159:90–110
- Perricone V, Grun T, Marmo F, Langella C, Carnevali MDC (2020) Constructional design of echi-noid endoskeleton: main structural components and their potential for biomimetic applications. *Bioinspiration Biomimetics*
- Pideri C, Seppecher P (1997) A second gradient material resulting from the homogenization of an heterogeneous linear elastic medium. *Contin Mech Thermodyn* 9(5):241–257
- Piola G (1846) *Intorno alle equazioni fondamentali del movimento di corpi qualsivogliono, considerati secondo la naturale loro forma e costituzione: memoria*, vol 10282. BD Camera
- Placidi L (2015) A variational approach for a nonlinear 1-dimensional second gradient continuum damage model. *Contin Mech Thermodyn* 27(4–5):623–638
- Placidi L, Barchiesi E, Misra A (2018) A strain gradient variational approach to damage: a comparison with damage gradient models and numerical results. *Math Mech Complex Syst* 6(2):77–100
- Placidi L, dell'Isola F, Barchiesi E (2020) Heuristic homogenization of Euler and pantographic beams. In: Picu C, Ganghoffer JF (eds) *Mechanics of fibrous materials and applications*. CISM International Centre for Mechanical Sciences (Courses and Lectures), vol 596. Springer, Cham, pp 123–155
- Rahali Y, Giorgio I, Ganghoffer J, dell'Isola F (2015) Homogenization à la Piola produces second gradient continuum models for linear pantographic lattices. *Int J Eng Sci* 97:148–172
- Rahbar H, Javanbakht M, Ziaei-Rad S, Reali A, Jafarzadeh H (2020) Finite element analysis of coupled phase-field and thermoelasticity equations at large strains for martensitic phase transformations based on implicit and explicit time discretization schemes. *Mech Adv Mater Struct* 1–17
- Scerrato D, Giorgio I (2019) Equilibrium of two-dimensional cycloidal pantographic metamaterials in three-dimensional deformations. *Symmetry* 11(12):1523

- Schulte J, Dittmann M, Eugster S, Hesch S, Reinicke T, Dell'Isola F, Hesch C (2020) Isogeometric analysis of fiber reinforced composites using kirchhoff-love shell elements. *Comput Methods Appl Mech Eng* 362(112):845
- Seppacher P (1989) Etude des conditions aux limites en théorie du second gradient: cas de la capillarité. *Comptes rendus de l'Académie des sciences Série 2, Mécanique, Physique, Chimie, Sciences de l'univers, Sciences de la Terre* 309(6):497–502
- Seppacher P (2000) Second-gradient theory: application to Cahn-Hilliard fluids. In: Maugin G.A., Drouot R., Sidoroff F. (eds) *Continuum thermomechanics. Solid mechanics and its applications*, vol 76. Springer, Dordrecht, pp 379–388
- Seppacher P, Alibert JJ, dell'Isola F (2011) Linear elastic trusses leading to continua with exotic mechanical interactions. *J Phys Conf Series* 319(1):012,018
- Serpieri R, Sessa S, Rosati L (2018) A mitc-based procedure for the numerical integration of a continuum elastic-plastic theory of through-the-thickness-jacketed shell structures. *Compos Struct* 191:209–220
- Sessa S, Marmo F, Rosati L (2015) Effective use of seismic response envelopes for reinforced concrete structures. *Earthq Eng Struct Dyn* 44(14):2401–2423
- Sessa S, Serpieri R, Rosati L (2017) A continuum theory of through-the-thickness jacketed shells for the elasto-plastic analysis of confined composite structures: Theory and numerical assessment. *Compos Part B Eng* 113:225–242
- Sessa S, Marmo F, Rosati L, Leonetti L, Garcea G, Casciaro R (2018a) Evaluation of the capacity surfaces of reinforced concrete sections: Eurocode versus a plasticity-based approach. *Meccanica* 53(6):1493–1512
- Sessa S, Marmo F, Vaiana N, Rosati L (2018b) A computational strategy for eurocode 8-compliant analyses of reinforced concrete structures by seismic envelopes. *J Earthq Eng* 1–34
- Sessa S, Marmo F, Vaiana N, De Gregorio D, Rosati L (2019a) Strength hierarchy provisions for transverse confinement systems of shell structural elements. *Compos Part B Eng* 163:413–423
- Sessa S, Marmo F, Vaiana N, Rosati L (2019b) Probabilistic assessment of axial force-biaxial bending capacity domains of reinforced concrete sections. *Meccanica* 54(9):1451–1469
- Spagnuolo M (2020) Circuit analogies in the search for new metamaterials: phenomenology of a mechanical diode. In: Altenbach H, Eremeyev V, Pavlov I, Porubov A (eds) *Nonlinear wave dynamics of materials and structures. Advanced structured materials*, vol 122. Springer, Cham, pp 411–422
- Spagnuolo M, Scerrato D (2020) The mechanical diode: on the tracks of James Maxwell employing mechanical–electrical analogies in the design of metamaterials. In: Abali B, Giorgio I (eds) *Developments and novel approaches in biomechanics and metamaterials. Advanced structured materials*, vol 132. Springer, Cham, pp 459–469
- Spagnuolo M, Barcz K, Pfaff A, dell'Isola F, Franciosi P (2017) Qualitative pivot damage analysis in aluminum printed pantographic sheets: numerics and experiments. *Mech Res Commun* 83:47–52
- Spagnuolo M, Peyre P, Dupuy C (2019) Phenomenological aspects of quasi-perfect pivots in metallic pantographic structures. *Mech Res Commun* 101(103):415
- Turco E, Barchiesi E (2019) Equilibrium paths of Hencky pantographic beams in a three-point bending problem. *Math Mech Complex Syst* 7(4):287–310
- Turco E, Giorgio I, Misra A, Dell'Isola F (2017) King post truss as a motif for internal structure of (meta) material with controlled elastic properties. *R Soc Open Sci* 4(10):171,153
- Turco E, Misra A, Pawlikowski M, dell'Isola F, Hild F (2018) Enhanced Piola-Hencky discrete models for pantographic sheets with pivots without deformation energy: numerics and experiments. *Int J Solids Struct* 147:94–109
- Turco E, Dell'Isola F, Misra A (2019a) A nonlinear Lagrangian particle model for grains assemblies including grain relative rotations. *Int J Numer Anal Methods Geomech* 43(5):1051–1079
- Turco E, Misra A, Sarikaya R, Lekszycki T (2019b) Quantitative analysis of deformation mechanisms in pantographic substructures: experiments and modeling. *Contin Mech Thermodyn* 31(1):209–223

- Vaiana N, Spizzuoco M, Serino G (2017) Wire rope isolators for seismically base-isolated lightweight structures: experimental characterization and mathematical modeling. *Eng Struct* 140:498–514
- Vaiana N, Sessa S, Marmo F, Rosati L (2019) Nonlinear dynamic analysis of hysteretic mechanical systems by combining a novel rate-independent model and an explicit time integration method. *Nonlinear Dyn* 98(4):2879–2901
- Vaiana N, Capuano R, Sessa S, Marmo F, Rosati L (2021) Nonlinear dynamic analysis of seismically base-isolated structures by a novel openseees hysteretic material model. *Appl Sci* 11(3):900
- Yang H, Ganzosch G, Giorgio I, Abali BE (2018) Material characterization and computations of a polymeric metamaterial with a pantographic substructure. *Zeitschrift für angewandte Mathematik und Physik* 69(4):105
- Yang H, Abali BE, Timofeev D, Müller WH (2019) Determination of metamaterial parameters by means of a homogenization approach based on asymptotic analysis. *Contin Mech Thermodyn* 1–20
- Yildizdag ME, Barchiesi E, dell’Isola F (2020) Three-point bending test of pantographic blocks: numerical and experimental investigation. *Math Mech Solids* 25(10):1965–1978